

# **Radiation Damage Analysis of the Swept Charge Device for the C1XS Instrument**

Thesis submitted for the degree of  
Doctor of Philosophy  
at Brunel University

by

Jason Peter David Gow  
Centre for Sensors and Instrumentation  
School of Engineering and Design  
Brunel University

16<sup>th</sup> September 2009

## Abstract

This thesis is concerned with ensuring high energy resolution from the swept charge device (SCD) CCD54, essentially a non-pixelated version of the charge coupled device (CCD), for use in the Chandrayaan-1 X-ray Spectrometer (C1XS). Of particular interest is the effect on performance due to the radiation damage, caused by protons, the CCD54s used in C1XS will receive during the transfer to the Moon and during the two years in lunar orbit. Chapter 2 reviews the atomic structure, the formation and detection of X-rays, and the operation of a CCD. Chapter 3 discusses the space radiation environment and the damaging effects it has on CCDs, for example increasing dark current and charge transfer inefficiency. Chapter 4 presents the basic laboratory equipment and procedure used during the experimental work, and details the initial optimisation and characterisation, the pre-flight characterisation of devices available for use in C1XS, the measurement of the depletion depth, and quantum efficiency of the CCD54. Chapter 5 details the results of the initial proton irradiation study, intended to demonstrate the ability of the CCD54 to provide excellent scientific data over the two years at the Moon. Chapter 6 describes a second irradiation study covering a more detailed investigation of the damage effects, investigating dark current, trap energy levels, and charge transfer inefficiency. Chapter 7 describes work conducted to assist the C1XS science team in the development of an X-ray fluorescence model, to be used with X-ray spectra provided by the X-ray solar monitor and the spectra detected by C1XS, to provide elemental abundance information of the lunar surface. It also presents the initial C1XS results from the Moon, and a brief comparison of the CCD54 with other semiconductor X-ray fluorescence detectors. Chapter 8 describes the final conclusions and recommendations for further work, including a study of the radiation damage effects during the two years at the Moon and the future development of SCD detectors for use in space.

## Declaration

I hereby declare that no part of this thesis has been previously submitted to this or any other university as part of the requirement for a higher degree. The work described herein was conducted solely by the undersigned except for those colleagues and other workers acknowledged in the text.

Jason Peter David Gow

16<sup>th</sup> September 2009

## Dedication

To my mother, father and my little one

## Acknowledgments

I would like to acknowledge and thank a large number of people who have helped and encouraged me over the duration of this thesis.

Thanks to my supervisors David Smith and Andrew Holland for their technical support and the occasional prod in the right direction when I had taken a wrong turn.

Thanks to David Burt and Mark Robbins for their support with CCD operation and the radiation damage effects, with a large number of stories at a complete tangent thrown in.

Thanks to Chris Howe for his assistance in understanding C1XS operation and providing me with some of the devices that have allowed me to undertake this work.

Thanks to Barry Kellett, Ian Crawford, Katie Joy, Shoshana Weider, and Shyama Narendranath for providing C1XS data, explaining the importance of rocks, and providing the lunar regolith simulant.

Thanks to Peter Pool, Bertrand de Monte, John Kemp, and James Endicott at e2v technologies for their help with devices, equipment and information.

Thanks to the past and present members of the cei and ISTA Neil Murray, David Hall, Amir Intisar, Thomas Grieg, Ben Dryer, James Tutt, Billy Kinchin, Richard Ingley, John Osmond, George Seabroke, Gopal Jeyesundra, and Ian Hutchinson who provided friendship, great memories, and made the whole experience even more enjoyable.

I would like to gratefully acknowledge the financial support received from the Science and Technology Facilities Council and e2v technologies during my research studentship.

Finally, another large thank you to David Smith for his uncanny ability to detect the wrong font and the inclusion of too many spaces at twenty paces, Neil for his suggestions on keeping the laboratory above 11 °C over a cold Easter, and last but not least Brunel University for providing the added fiscal incentive of submitting within four years.

# Table of Contents

---

Abstract .....	ii
Declaration .....	iii
Dedication.....	iv
Acknowledgements .....	iv
Contents .....	v
<b>Chapter 1: Introduction.....</b>	<b>1</b>
1.1    The Moon .....	1
1.2    Semiconductor Technology for Space Applications .....	3
1.3    SMART-1 and D-CIXS .....	5
1.4    Chandrayaan-1 and CIXS .....	7
1.5    Research Goals .....	9
1.6    Thesis Organisation .....	10
1.7    Publications .....	11
<b>Chapter 2: The Swept Charge Device and X-ray Interactions .....</b>	<b>13</b>
2.1    Introduction .....	13
2.2    Atomic Structure, the Crystal Lattice and Silicon.....	13
2.2.1    X-ray Fluorescence.....	15
2.2.2    Intrinsic Material and Crystalline Lattice Structure .....	16
2.2.3    Extrinsic Material .....	17
2.3    The Principal Components of a CCD.....	18
2.3.1    The p-n Junction .....	19
2.3.2    Metal-Oxide-Semiconductor .....	19
2.3.3    Buried Channel Potential Well.....	20
2.3.4    Principles of Charge Transfer.....	21
2.3.5    The MOSFET .....	22
2.3.6    The Output Circuit.....	23
2.4    CCD Fabrication, Structure and Operation .....	24
2.4.1    The CCD Structure and Read-out.....	27
2.4.1.1    Charge Transfer Efficiency .....	28

2.4.2	The SCD CCD54 Structure and Read-out.....	28
2.5	Sources of Noise within the CCD and Signal Processing .....	29
2.5.1	Dark and Leakage Current.....	30
2.5.1.1	Surface Generated Dark Current .....	31
2.5.1.2	Dither Mode Clocking.....	33
2.5.1.3	Bulk Generated Dark Current.....	34
2.5.1.4	Dark Current Summary .....	35
2.5.2	Dark Shot Noise .....	36
2.5.3	Dark Current Spikes .....	36
2.5.4	Impact Ionisation and Clock Induced Charge .....	37
2.5.5	Transistor Noise.....	38
2.5.6	Reset (kT/C) Noise .....	39
2.5.7	Transfer Noise .....	39
2.5.8	Transient Noise.....	40
2.5.9	Read Noise, System Noise and Signal Processing .....	41
2.6	X-ray Detection, Measurement and Analysis.....	42
2.6.1	Interaction of X-rays with Matter.....	43
2.6.1.1	X-ray Photon Shot Noise (Fano Noise).....	44
2.6.1.2	X-ray Absorption.....	44
2.6.2	Measurement and Analysis.....	45
2.6.2.1	Spatial Resolution.....	47
2.6.2.2	Energy Resolution .....	48
2.6.2.3	Quantum Efficiency.....	48
2.7	Other Semiconductor Detectors.....	50
2.7.1	Silicon PIN Diode.....	50
2.7.2	Silicon Lithium Detector .....	51
2.7.3	Silicon Drift Detector .....	52
2.7.4	CMOS APS .....	53
2.8	Chapter Summary .....	53
<b>Chapter 3: The Space Environment and its Effects on CCDs.....</b>		<b>55</b>
3.1	Introduction .....	55
3.2	The Space Radiation Environment.....	55
3.2.1	Trapped Radiation .....	56
3.2.1.1	The South Atlantic Anomaly and the Auroral Horns .....	59

3.2.2	Non-Trapped.....	60
3.2.2.1	Cosmic Rays.....	60
3.2.2.2	Solar Flares and Solar Proton Events.....	61
3.3	Other Source of Radiation.....	63
3.3.1	Artificial Sources.....	63
3.3.2	Atmospheric and Spacecraft Secondaries.....	64
3.4	Shielding.....	64
3.5	Modelling the Space Radiation Environment.....	65
3.5.1	Non-Ionising Energy Loss Function.....	66
3.6	Radiation Damage Mechanisms.....	67
3.6.1	Ionisation Damage and its Effects.....	68
3.6.1.1	Flat-Band Voltage Shift.....	71
3.6.2	Displacement Damage and its Effects.....	71
3.6.2.1	Increased Charge Transfer Inefficiency.....	74
3.7	Chapter Summary.....	76
<b>Chapter 4: Optimisation and Flight Device Screening.....</b>		<b>77</b>
4.1	Introduction.....	77
4.2	Voltage and Clock Optimisation.....	77
4.2.1	Experimental Arrangement.....	78
4.2.2	Experimental Procedure.....	79
4.2.3	I-Clock.....	81
4.2.4	Reset Drain Voltage $V_{rd}$ .....	84
4.2.5	Reset Clock.....	86
4.2.6	Output Drain Voltage $V_{od}$ .....	87
4.2.7	Substrate Voltage $V_{ss}$ .....	88
4.2.8	Integration Time and Delays.....	90
4.2.9	Conclusion.....	91
4.3	Pre-Flight Device Characterisation.....	92
4.3.1	Experimental Arrangement.....	92
4.3.2	Experimental Procedure.....	93
4.3.3	Summary of Results.....	96
4.3.4	Conclusion.....	99
4.4	X-ray Detection.....	100
4.5	Quantum Efficiency Analysis.....	103

4.5.1	Experimental Arrangement .....	103
4.5.2	Experimental Procedure .....	104
4.5.3	Experimental Results.....	106
4.5.4	Conclusion.....	109
4.6	Chapter Summary .....	109
<b>Chapter 5: CCD54 Proton Radiation Damage Assessment.....</b>		<b>111</b>
5.1	Introduction .....	111
5.2	Chandrayaan-1 Radiation Environment .....	111
5.3	Experimental Arrangement .....	115
5.4	Experimental Procedure .....	115
5.4.1	Cosmetic Quality Pre-Irradiation Testing .....	115
5.4.2	CCD54 Proton Irradiation .....	115
5.4.3	Post-Irradiation Laboratory Procedure .....	116
5.5	Increase in Dark Current .....	117
5.6	CCD54 Performance Degradation.....	118
5.7	Damage to the Charge Collection Area and Central Transport Channels.....	120
5.8	Increased On Chip Sample Binning .....	122
5.9	Effect of Increased X-ray Flux .....	124
5.10	Energy Resolution Model of Experimental Data .....	126
5.11	C1XS Review and Recommendations.....	127
5.12	Chapter Summary .....	131
<b>Chapter 6: Radiation Damage Study and Analysis Methods.....</b>		<b>133</b>
6.1	Introduction .....	133
6.1.1	Chandrayaan-1 Radiation Environment October 2008 Launch .....	133
6.2	Experimental Arrangement and Procedure.....	135
6.2.1	Laboratory Experimental Arrangement.....	135
6.2.2	Laboratory Test Procedure .....	137
6.2.3	The Accelerator Facility and Dosimetry .....	138
6.2.4	Irradiation of the CCD54 Module .....	140
6.3	Noise.....	142
6.4	Dark Current.....	143
6.5	X-ray Detection .....	146
6.5.1	Threshold of Event Selection .....	146

6.5.2	Energy Calibration.....	147
6.5.3	Linearity Testing .....	148
6.6	X-ray Spectroscopy Degradation.....	149
6.6.1	The Dominant Source of Performance Loss .....	150
6.6.2	Comparison with Previous Irradiation and Predictions.....	154
6.6.3	Lunar Regolith Simulant and Mg, Al, Si Spectra.....	155
6.7	Radiation Damage Model.....	156
6.8	Chapter Summary .....	159
<b>Chapter 7: XRF Modelling, C1XS Initial Results, and a XRF Detector Comparison</b>		<b>160</b>
.....		
7.1	Introduction .....	160
7.1.1	Rocks, the History Books of the Universe .....	160
7.1.2	Extra Terrestrial X-ray Fluorescence .....	161
7.2	Experimental Arrangement and Procedure.....	164
7.2.1	X-ray Beam Profile.....	164
7.2.2	Geological Samples and Surface Type and Particle Size Comparison .....	167
7.2.3	Varying the Incident X-ray Beam Intensity .....	168
7.3	XRF Modelling Code Development.....	169
7.3.1	Spectrum as a Function of Surface and Particle Size .....	169
7.3.2	Spectra as a Function of Incident X-ray Beam.....	171
7.3.3	Initial Results from the XRF modelling code.....	172
7.4	Chandrayaan-1 Launch and Initial Results.....	173
7.5	X-ray Fluorescence Detector Comparison .....	176
7.6	Chapter Summary .....	178
<b>Chapter 8: Conclusions and Further Work</b> .....		<b>180</b>
8.1	Optimisation and Screening .....	180
8.2	CCD54 Proton Radiation Damage Assessment .....	180
8.3	Radiation Damage Study and Analysis Methods .....	181
8.4	XRF Modelling, C1XS Initial Results, and a XRF Detector Comparison.....	183
<b>Bibliography</b> .....		<b>184</b>

## Chapter 1: Introduction

Since the dawn of the space age the ability to capture images from orbit and deep space missions has proved invaluable. Interference caused by the Earth's atmosphere is bypassed, thus allowing for the detailed observation of distant and faint objects that would be hard to detect using ground based observatories. However, this method introduces a number of new problems, these include placing the spacecraft into a viable and suitable orbit, pointing stability, data retrieval, power consumption, and problems associated with the vacuum of space, micrometeoroids, orbital debris, and the thermal and radiation environment.

The focus of this thesis is concerned with ensuring high energy resolution from the swept charge devices (SCDs), essentially a non-pixellated version of the charge coupled device (CCD), for use in the Chandrayaan-1 X-ray Spectrometer (C1XS). C1XS, launched onboard Chandrayaan-1, was designed to detect the X-ray fluorescence, caused by solar flares, from the lunar surface. To ensure the instrument was a success a radiation damage study was performed, making recommendations on device operating conditions, instrument design and the future development of the SCD. A full device characterisation and the assistance provided to the C1XS science team are also discussed.

The thesis is organised into 8 chapters. Chapter 1 describes the origin and significance of the Moon, the historical development of semiconductor technology and its role in space missions, and the Development of a Compact Imaging X-ray Spectrometer (D-CIXS) instrument, on which C1XS is based. The initial research goals are then presented, followed by a chapter overview.

### 1.1 The Moon

The Moon, our closest extraterrestrial neighbour, has played a significant role in the evolution of life on the Earth. An example being through the tidal forces that have stabilised the Earth's tilt [Asimov 1975]. The Lunar surface was first observed in detail by Galileo in 1609 [Galileo 1610]. He recorded the surface to be rough and mountainous with four key features. The dominant feature is the 'terrae', from the Latin for land, often referred to as the 'highlands', these lightly coloured regions are what remain of the original lunar crust [Spudis 2004]. The highlands are scarred by impact craters; the largest, measuring 2,500 km in diameter, is found at the south pole-Aitken basin [Spudis 2004]. The craters are filled with dark regions called 'maria', from the Latin for sea, where basaltic lava has solidified after an impact. Debris thrown up during large impacts and from micrometeorites forms a blanket over much of the lunar surface known as the 'regolith'. The thickness of this layer ranges from 3-5 m in the maria, and from 10-20 m in the highlands [Heiken

*et al.* 1991]. The depth has been linked to the passage of time allowing the surface to be dated [Shkuratova and Bondarenkob 2001].

The formation of the Moon has long been a subject of much contention, the three classical theories are presented below:

- **Binary fission:** The Moon was once part of the Earth, which became separated. Compositional similarities between the Earth's mantle and the surface of the Moon support this [Binder 1984]. However, the Earth would have had to achieve a significant angular velocity for part of it to be ejected.
- **Capture:** The Moon was formed elsewhere in the solar system and then captured in the Earth's gravitational well [Singer 1984]. However, the similar composition of the lunar surface and the Earth's mantle makes this process unlikely.
- **Co-accretion:** The Moon and Earth formed at the same time from the same debris field [Weidenschilling *et al.* 1984]. However, the high angular momentum of the Earth-Moon system and the resulting small amount of iron on the Moon raise questions over the validity of this model.

The prevailing theory today is that the Moon formed as a result of the impact of a large body named '*Theia*', also known as the 'impact trigger' or 'giant impact hypothesis' [Hartmann and Davis 1975]. The impact ejected debris into orbit around the Earth, where it underwent accretion which caused it to form the proto-Moon [Morishima and Watanabec 2004]. As a result of the energy involved in this transformation a magma ocean existed on the surface of the Moon [Warren 1985]. The magma ocean cooled, causing light minerals such as Al rich silicates (plagioclase) to come to the surface to form the crust. Heavier minerals (pyroxene, olivine) descended to form the lunar mantle, while some remained in location, at the surface, where they crystallised [Yongliao *et al.* 2004]. Incompatible elements (those that prefer a liquid state during crystallisation) find it harder to enter the lattices of the main silicate materials, resulting in the formation of potassium rare earth elements and phosphorus (KREEP) rocks at the crust mantle interface [Warren and Wasson 1979]. During this formation phase of the magma ocean cooling the Moon was 15 times closer to the Earth than it is today, enhancing the gravitational pull experienced by the Moon. It now orbits with a semi-major axis of  $0.3844 \times 10^6$  km at an inclination of between  $18.28^\circ$  to  $28.58^\circ$ , and an orbital eccentricity of 0.0549, drifting 3.8 cm from the Earth each year [Williams 2006].

The 380 kg of lunar rock that was returned to the Earth by the six Apollo lander missions, and two unmanned lunar missions, re-vitalised the debate surrounding the formation of the Moon. These rocks included those found within the maria regions, and demonstrated a similarity with terrestrial

volcanic basalt, and KREEP rocks collected from material ejected around craters found on Earth. The material composition and density of 15-20% of the lunar surface has been studied [Spudis 1998]. The lunar crust is believed to have changed little since its formation, as it does not suffer erosion due to plate movement and the elements as the Earth does. The result is a perfectly preserved record of events in the inner solar system over the last 4 billion years, through the craters left by asteroids and meteorites that cover the lunar surface.

Material can escape from the Moon during a large impact, so far around sixty lunar meteorites have been identified with the largest being the Kalahari 009, at 13.5 kg, found in Botswana [Russell *et al.* 2005]. These meteorites provide a geological history of impacts. The composition of the lunar surface can also be used to enforce formation models, however, it is essential that the whole lunar surface is investigated. Large variations were observed in the studied rocks [Spudis 1998] which covered only 9% of the surface around the equatorial regions [Clark and Adler 1978]. Robotic missions can only cover small areas, while manned missions can cover large areas but are complex and costly. The solution would appear to come from an orbital spacecraft which can fly over the entire surface repeatedly allowing a detailed study to be conducted using, for example, X-ray fluorescence or gamma-ray spectrometry.

## 1.2 Semiconductor Technology for Space Applications

The CCD was initially developed at the Bell Laboratories in 1966, as a semiconductor alternative to the magnetic ‘bubble’ memory, then being used for digital storage, other analogue and imaging applications were also envisaged. Through combining these technologies, George Smith and Willard Boyle created the first practical imaging CCD in 1969 at Bell Laboratories, leading to the first CCD camera in 1970 [Boyle and Smith 1970]. Space missions of the time were using vidicon tubes for imaging, for example the deep space Voyager missions and the Mars lander Viking mission. A vidicon is a cathode ray tube where low energy electrons are scanned across a photoconductive surface, recording the charge collected during an exposure to create a digital image. The CCD had the potential to provide a stable pixel structure, much lower mass, power, noise and, most importantly, far higher reliability.

The National Aeronautics and Space Administration (NASA) Jet Propulsion Laboratory (JPL) led the way in developing the CCD into a scientific imager suitable for use in space. Whereas the initial CCDs were designed to transport signal charge across the surface of the device, Fairchild developed a 100 by 100 pixel array which used ‘buried channels’ to give higher transfer efficiency and lower noise [Kim *et al.* 1972]. In 1976 Texas Instruments developed and tested a back illuminated 400 by 400 pixel array, also using buried channel technology, it was plagued by yield

issues arising from short circuits in the aluminium electrode structure. To combat this, a more reliable polysilicon electrode structure was used, as had already been adopted by Fairchild [Anteliffé 1975], and this is still the preferred technique for devices produced today.

The year 1976 also saw the announcement of a back-illuminated 800 by 800 buried channel pixel array for use on the 1989 Galileo mission to Jupiter, which in turn pioneered CCD technology in space with its launch. It may be noted that the state of this early technology, was such that several thousand attempts were necessary to produce the final two flight quality devices. These were produced using a specialised ‘virtual phase’ technology offering good blue response with front illumination. A more standard three phase device was planned, however, the radiation environment meant the applied voltages could not be adequately controlled [Yeates 1985]. The rapid development of the CCD resulted in it being adopted for use in the wide field camera on the Hubble space telescope launched in 1990 [Smith and Tatarewicz 1985]. The Hubble camera used eight three phase back-illuminated CCDs, and resulted in a number of high quality solar and deep space images. Since the early 1990s the CCD has been the dominant imager used on space missions, covering a large majority of the electromagnetic spectrum from infrared to X-rays, for example; XMM, Swift, and in the future GAIA.

A more recent development in semiconductor technology is that of the complementary metal-oxide-semiconductor (CMOS) active pixel sensor (APS), developed at JPL in 1992 [Fossum 1998]. The idea was first conceived in 1968 [Noble 1968]. It was predicted that the technology would provide a small size, low cost, and low powered alternative to the CCD, which in many instances it has, for example star trackers [Fossum *et al.* 1994]. The performance of an APS does not suffer from the radiation induced decrease to charge transfer efficiency to which CCDs are susceptible [Hopkinson *et al.* 2004] (discussed in Chapter 3), making it more tolerant to radiation damage. However, when compared to a CCD, currently the higher thermal and 1/f noise, lower fill factor, and lower quantum efficiency (QE) make it less suitable for scientific and space imaging.

The SCD was developed in 1997 at e2v technologies plc. [CCD54 design details 1997], then EEV ltd., under the UK IMPACT program, as a possible replacement for the PIN diode detector in X-ray spectroscopy applications [Holland and Hutchinson 1998]. The SCD, e2v designation CCD54, collects X-ray generated charge packets in the active area under a similar electrode structure to that of a conventional CCD. The main difference being that the SCD does not provide a pixellated image and is essentially a continuously-clocked linear CCD with a large detection area, as discussed in Chapter 2. The SCD was first flown in space onboard SMART-1 (Small Missions for Advanced Research in Technology), a European Space Agency (ESA) technology demonstrator, launched in 2003 [Grande *et al.* 2003], in the Demonstration of a Compact Imaging X-ray

Spectrometer (D-CIXS) instrument provided by the Rutherford Appleton Laboratory (RAL). This instrument concept has now been extended for use on the Indian Space Research Organisation (ISRO) mission, Chandrayaan-1, in the CIXS instrument.

### 1.3 SMART-1 and D-CIXS

SMART-1 was an ESA technology demonstration mission containing a number of miniaturised instruments, including D-CIXS, using an ion propulsion engine to propel the spacecraft into a lunar orbit [Foing *et al.* 2002]. It was launched in September 2003 and took around 18 months to reach lunar orbit (n.b. the Apollo missions took around 4 days). During this time the spacecraft was repeatedly exposed to high levels of trapped and solar protons. The mission ended on the 3<sup>rd</sup> of September 2006 when the spacecraft was impacted into the lunar surface.

The aim of the D-CIXS instrument, illustrated in Figure 1.1, was to provide high quality spectroscopic mapping of the lunar surface [Grande *et al.* 2003]; while at the same time demonstrating the abilities of a small instrument, using a previously un-flown X-ray spectroscopy technology in the form of the CCD54. The instrument aimed to determine the global distribution of Mg, Al and Si to investigate the evolution of the lunar surface. For example, the magma ocean model would result in Mg-suite rocks being found as part of the crust which exhibit specific relationships to other rock types, e.g. KREEP rocks [Grande *et al.* 2003]. The target energy resolution was around 250 eV at 6 keV, to distinguish between Mg, Al, Si, K, Ca (and Fe if solar activity permitted). The D-CIXS instrument consisted of 6 modules with 4 CCD54 devices on each as shown in Figure 1.1. The collimators allowed 42 km spatial resolution images, at an altitude of 300 km, to be taken. The collimators form the support structure for a 4000 Å thick Al filter on facets 1 and 2, and a Mg filter on facet 3, each on a 4000 Å polyimide structure to remove unwanted UV and electron exposure [Grande 2001].



**Figure 1.1:** Image of the D-CIXS instrument undergoing testing at RAL

During the flight to the Moon, the initial six months and final three months were reserved for spacecraft propulsion operations, while the intervening time was available for cruise testing. On the 16<sup>th</sup> of July 2004 during an X-class solar flare terrestrial argon was observed at 2.89 keV, the expected value for the Ar-K $\alpha$  line is 2.96 keV. At this stage the Fe<sup>55</sup> calibration source gave the energy resolution to be 380 eV at 5.89 keV, with the decrease in performance attributed to damage caused while travelling through the Earth's radiation belts [Grande *et al.* 2007]. On the 15<sup>th</sup> of January 2005 during an X2.6 solar flare SMART-1 was flying over the Luna landing sites, the ground track for facets 1 and 3 are shown in Figure 1.2, the average result from detector facets 1 and 3 over a period of approximately two minutes is shown in Figure 1.3. The Fe peak in facet 3 was interpreted as emanating from the Mare Crisium, while both facets show the detection of Ca emission at 3.69 keV, representing the first ever unambiguous remote sensing of Ca on the Moon [Grande *et al.* 2007]. The data supported the findings from samples collected by the Soviet Luna 20 and Luna 24 landers, and the Clementine and Lunar Prospector orbiter missions.

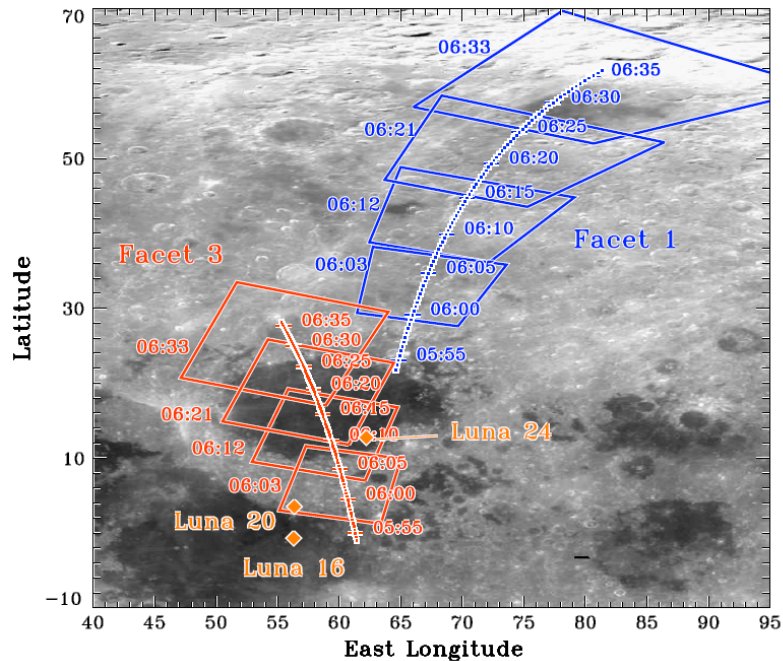


**Figure 1.2:** Groundtracks of D-CIXSs facets 1 and 3 superimposed on areas of the Moon flown over during the 15<sup>th</sup> of January 2005. The landing site of three Soviet Luna robotic landers are also marked [Grande *et al.* 2007]

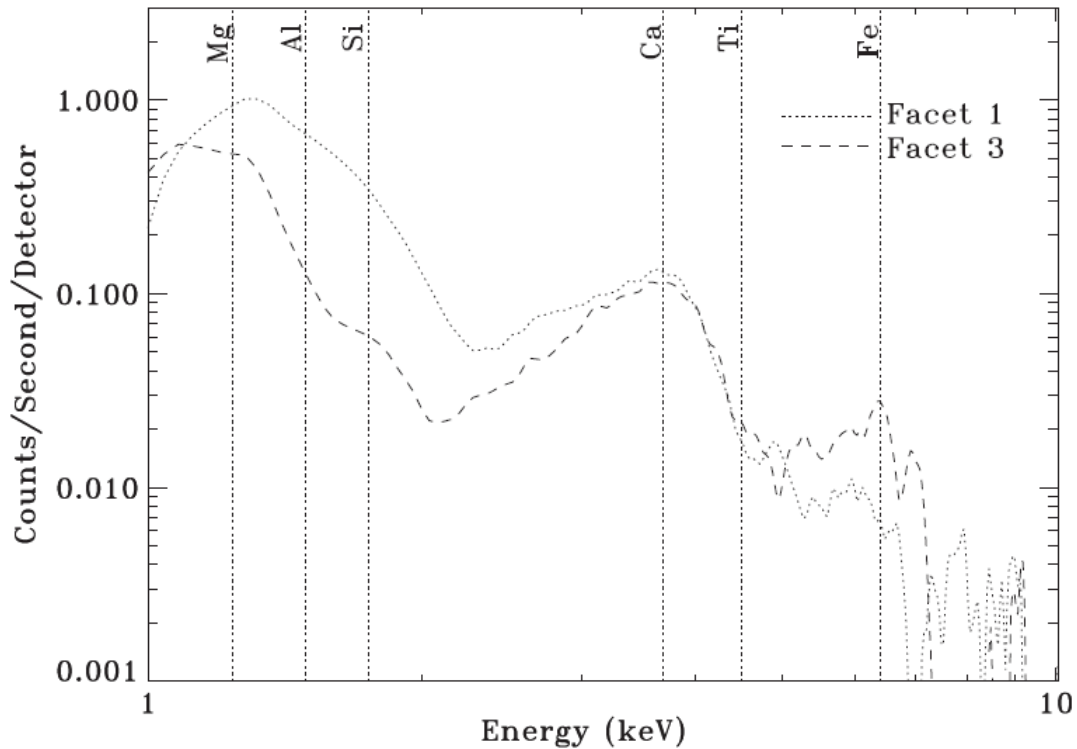


**Figure 1.3:** Instantaneous spectra from facets 1 and 3, showing the emission from Ca, Fe, Mg, Al, and Si obtained over  $\sim 2$  minutes centred at 06:15 UT. Facet 3 was over the centre of Mare Crisium. Facet 1 was observing the highlands to the north east of Crisium [Grande *et al.* 2007]

#### 1.4 Chandrayaan-1 and C1XS

Chandrayaan-1 was originally due to be launched in February 2008, however after delays the launch was postponed to the 22<sup>nd</sup> of October 2008. The spacecraft has now been placed into a  $\sim 100$  km circular polar orbit for two years. The payload, illustrated in Figure 1.4, consists of:

- **Terrain Mapping Camera (TMC):** Creating high resolution maps of the lunar surface [Kumar and Chowdhury 2005].
- **Hyper Spectral Imager (HySI):** Providing Mineralogical mapping in the 400-900 nm band [Goswami *et al.* 2006].
- **C1XS:** Its primary mission objective to map the lunar surface over the energy range of 1-10 keV, to find the distribution of elements such as Mg, Al, Si, K, Ca, Ti and Fe.
- **High Energy X-ray/ $\gamma$ -ray spectrometer (HEX):** Measuring over the energy range of 20-250 keV using a CdZnTe solid-state detector, to map U, Th, Pb, Rn [Goswami *et al.* 2006].
- **Lunar Laser Ranging Instrument (LLRI):** Using an Nd-Yag laser to provide surface topography to a resolution of better than 5m [Goswami *et al.* 2006].
- **Miniature imaging radar instrument (Mini-SAR):** Exploring the polar regions looking for the presence of water ice [Goswami *et al.* 2006].

- **Spectrometer InfraRed 2 (SIR)** and the **Moon Mineral Mapper (MMM)**: Infrared spectrometers, SIR 1 was launched onboard SMART-1 [Goswami *et al.* 2006].
- **Sub-keV atom reflecting analyser (SARA)**: Mapping the composition of the solar wind based on sputtered low energy neutral atoms from the lunar surface [Goswami *et al.* 2006].
- **Moon Impact Probe (MIP)**: Developed by ISRO to impact into the lunar surface carrying a mass spectrometer, an S-band altimeter and a video camera [ISRO data sheet 2009].
- **RADOM-7**: Mapping the radiation environment around the Moon [Goswami *et al.* 2006].

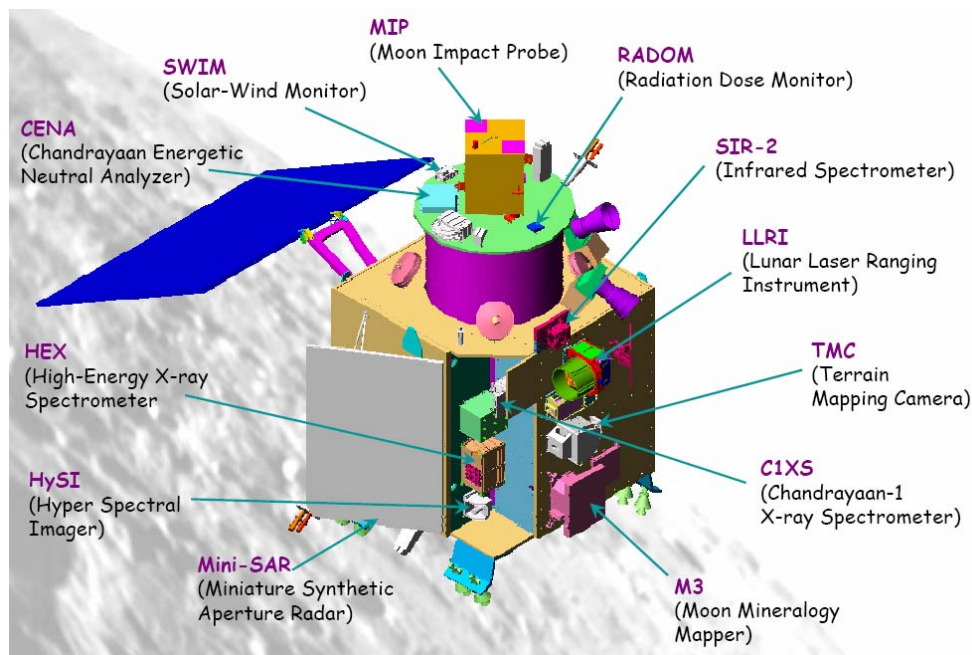


**Figure 1.4:** Schematic of the Chandrayaan-1 spacecraft [ISRO]

C1XS was the next generation of X-ray spectrometer produced at RAL, and over the past three years the author has been involved as it developed from D-C1XS into an almost entirely different instrument.

The detector consisted of 24 CCD54 devices arranged in 6 modules of 4; an example module is shown as Figure 1.5. The modules are mounted on a 3 mm Cu cold finger and have a 6 mm Ta radiation shield inside a 4 mm thick Al instrument case. While on route to the Moon the instrument door shown in the CAD diagram in Figure 1.6 was closed, providing 4 mm of Al door structure and 3 mm of Al calibration source holder, holding twenty four  $\text{Fe}^{55}$  sources for detector calibration. The Cu collimators, which cause a 17% signal loss (compared with 30% loss in D-C1XS), provide an angular acceptance of  $28^\circ$  (i.e.  $\pm 14^\circ$ ) from the 100 km altitude orbit of Chandrayaan-1, the C1XS field of view being equivalent to  $50 \text{ km}^2$  on the surface of the Moon. The detectors were mounted behind Al filters to remove the optical background and low energy electrons [Howe *et al.* 2009].

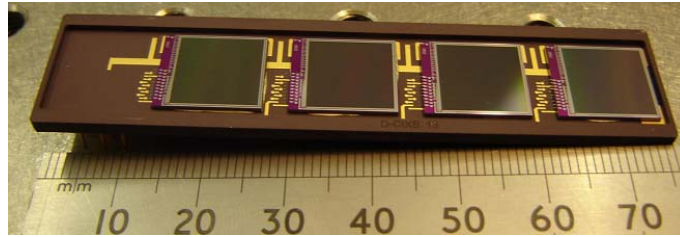


**Figure 1.5:** SCD module, used in both D-CIXS and C1XS, composed of four CCD54 devices

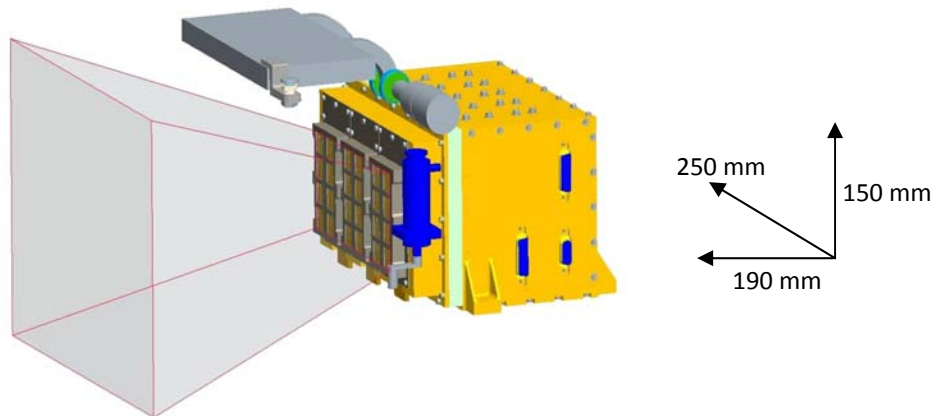


**Figure 1.6:** CAD image of the C1XS instrument, highlighting the  $14^\circ$  field of view [image courtesy of RAL]

## 1.5 Research Goals

The work comprised within this thesis was carried out in support of the C1XS instrument developed at RAL, provided by ESA to ISRO, and launched onboard Chandrayaan-1 in late 2008. The overall goal was to improve upon the results obtained from D-CIXS through improved pre- and post-irradiation performance by understanding the effect of proton damage over the two year mission duration. The work can be divided into three studies.

The initial study was to improve instrument performance by conducting an optimisation study to record the effect of operating the SCD under different voltages, timings and temperatures. The device quantum efficiency (QE) was measured over the energy range of 1,487 to 8,904 eV, the energies of interest for C1XS ranging from 1,000 to 9,000 eV. The work also included the characterisation of a selection of devices available for flight, making a recommendation on those to be used in C1XS.

The second study was a proton irradiation study looking at device performance after receiving 50% and 100% of the expected end of life proton fluence. At the time of this study the mission was due to launch in early February 2008. This work was conducted in order to make recommendations on modifications to the instrument shielding and operating conditions to improve the performance of

the devices used onboard C1XS. The charge collection and charge transport channels of the CCD54 were irradiated separately to identify sensitive areas of the device, allowing recommendations to the development of future SCDs to be made.

The third study was a more detailed radiation study based on the radiation fluence resulting from a revised launch date of September 2008. The whole active areas of two devices were irradiated to provide detailed information of device performance as a function of proton fluence. To demonstrate the possible performance of the CCD54 in C1XS based on the predicted proton flux, investigating energy resolution, charge transfer efficiency, dark current generation, and event detection.

Assistance was also provided to the C1XS science team, working with rocks types of different grain sizes while varying the incident X-ray power. The experimental data was used with code developed by B. Swinyard to find the elemental abundances of data taken from the Lunar surface, allowing the identification of different rock types.

The work carried out in this thesis was funded by a Co-operative Award in Science and Engineering (CASE) studentship from the Science and Technology Facilities Council (STFC) in collaboration with e2v technologies plc. (formerly Marconi, formerly EEV) of Chelmsford, Essex, England.

## 1.6 Thesis Organisation

Chapter 2 briefly describes the principles behind atomic structure, leading to the formation of X-rays and their detection within a semiconductor. The physical operation of a semiconductor detector is described followed by a description of the principal components of a CCD, CCD fabrication and operation, i.e. collecting and transporting charge, sources of noise, and measures of performance. Other commercially available semiconductor detectors, i.e. the silicon lithium detector, silicon drift detector and the CMOS APS, are also described.

Chapter 3 provides information about the space radiation environment and the damaging effects it has on CCDs. This includes a description of the sources of radiation in space, including charge particles in orbit around the Earth's magnetic rings, the solar wind, and solar flares. Finally, the chapter includes a description of the two radiation damage mechanisms, through ionisation and displacement damage, and their effects on semiconductor detectors.

Chapter 4 describes the initial optimisation work conducted on the SCD, including assigning the voltages and clock timings and measuring the QE. The pre-flight characterisation of fourteen modules is discussed, allowing the six most suitable to be recommended as the flight devices.

Chapter 5 details the results of the initial proton irradiation study, intended to demonstrate the ability of the CCD54 to maintain mission performance, over the two year mission of Chandrayaan-1. Two modules were irradiated to 50% and 100% of the end of life proton fluence, based on a February 2008 launch date. Two devices were irradiated to identify the sensitivity to radiation of the charge collection area, and the charge transport channels, one device to highlight the effect of increased dark current, and one of each module held as a control.

Chapter 6 describes a second irradiation study covering a more detailed investigation of the damage effects. Two devices were irradiated to 40%, and 100% of the end of life proton fluence, based on a revised September 2008 launch date. The resulting decrease in performance is discussed, including energy resolution, increased noise, and the effects on charge transfer efficiency and split events across the active area of the SCD. A model is also described which is based on the experimental data, and the physical radiation damage mechanisms involved.

Chapter 7 describes work conducted to provide the C1XS science team with data to input into code designed to identify elemental abundances. The code takes the incident X-ray spectra, provided by the X-ray solar monitor, and based on the angle of incidence and escape and the secondary X-rays, as detected by C1XS, provides the elemental abundance of the C1XS field of view. A brief comparison with other semiconductor X-ray fluorescence detectors is made to demonstrate the performance capabilities of SCD technology.

Chapter 8 describes the final conclusions of this thesis, making recommendations for further work.

## 1.7 Publications

Some of the results in this thesis are contained within the following publications.

D. R. Smith, and **J. Gow** (2009) “The effect of protons on the performance of swept-charge devices”, *Nuclear Instruments and Methods in Physics Research*, **A604**, pp. 177–179

N. J. Murray, A. D. Holland, D. R. Smith, **J. Gow**, P. Pool, D. Burt (2009) “The X-ray quantum efficiency measurement of high resistivity CCDs”, *Nucl. Inst. Meth.*, **A604**, pp. 180-182

C.J. Howe, D. Drummond, R. Edeson, B. Maddison, D. J. Parker, R. Parker, A. Shrivastava, J. Spencer, B. J. Kellett, M. Grande, P. Sreekumar, J. Huovelin, D. R. Smith, **J. Gow**, S. Narendranath, and L. d’Uston (2009) “Chandrayaan-1 X-ray Spectrometer (C1XS)—Instrument design and technical details”, *Planetary and Space Science*, **vol. 57**, Issue 7, pp. 735-743

**J. Gow**, D. R. Smith, A. D. Holland, B. Maddison, C. Howe, P. Sreekumar, J. Huovelin, and M. Grande (2008) “Radiation Study of Swept Charge Devices for the Chandrayaan-1 X-ray Spectrometer (C1XS) instrument”, *Proc SPIE*, **vol. 7021**

S. Z. Weider, **J. Gow**, I. A. Crawford, K. H. Joy, D. R. Smith, A. D. Holland, and B. M. Swinyard (2008) “X-ray Fluorescence Particle Size and Scattering Angle Considerations Preparatory Experiments for the Calibration and Interpretation of C1XS Data”, *Lunar and Planetary Science XXXIX*, **No. 1098**

D. R. Smith, **J. Gow**, and A. D. Holland (2007) “Proton Irradiation of Swept-Charge Devices for the Chandrayaan-1 X-ray Spectrometer (C1XS)”, *Nuclear Instruments and Methods in Physics Research*, **A583**, pp. 270–277

**J. Gow**, D. R. Smith, A. D. Holland, B. Maddison, C. Howe, P. Sreekumar, J. Huovelin, and M. Grande (2007) “Characterisation of Swept-Charge Devices for the Chandrayaan-1 X-ray Spectrometer (C1XS) instrument”, *Proc SPIE*, **vol. 6686**

## Chapter 2: The Swept Charge Device and X-ray Interactions

### 2.1 Introduction

This chapter describes the process of X-ray formation, detection and measurement using semiconductor detectors, primarily the CCD. The principles of device operation, including the formation of potential wells, charge transfer and charge read-out are detailed, leading on to the various sources of noise and the measurement of device performance for X-ray detection. The fabrication and structure of a CCD and the ‘Swept Charge Device’ (SCD) CCD54 are described in detail, with a brief mention of other X-ray sensitive semiconductor detectors. Further details on this subject can be found in Streetman and Banerjee (2000), Janesick (2001), and Lutz (1999).

### 2.2 Atomic Structure, the Crystal Lattice and Silicon

In 1909 Ernest Rutherford bombarded gold foil with alpha particles, he likened what he observed to firing an artillery shell at tissue paper, and the shell rebounding [Rutherford 1911]. The alpha particles were deflected through much larger angles than predicted using the Thompson theory of atomic structure, where the electrons were distributed throughout the atom [Thompson 1904]. Rutherford suggested that the electrons orbited a nucleus. The model was refined in 1913 by Niels Bohr [Bohr 1913]. In Bohr’s model electrons occupied quantised orbits, and could jump up or down provided the absorption or release of specific amounts of energy respectively producing atomic spectra. The Bohr model accurately described the gross features of the hydrogen atomic spectra, however, experimental evidence indicated level-splitting and problems modelling more complicated atoms [Streetman and Banerjee 2000].

The problem was solved through the use of quantum mechanics developed in the late 1920’s by Werner Heisenberg and Erwin Schrödinger. Heisenberg found that it is impossible to describe the position and momentum of a particle at the same time, the ‘uncertainty principle’. The position is described by a probability density function where the particle is described by a wave function given by the Schrödinger equation [Streetman and Banerjee 2000]. The wave function is found to be dependant on four quantum numbers given by:

$$n = 1, 2, 3, \dots \quad (2.1)$$

$$l = 0, 1, 2, \dots (n - 1) \quad (2.2)$$

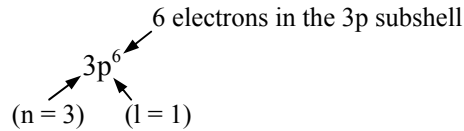
$$m = -l, \dots, -1, 0, +1, +2, \dots +l \quad (2.3)$$

$$s = \pm \frac{1}{2} \frac{h}{2\pi} \quad (2.4)$$

where  $n$  is the principal quantum number,  $l$  the subshell number,  $m$  the magnetic quantum number, and  $s$  the intrinsic angular momentum of an electron. The principal quantum number described the orbit in the Bohr model, whereas due to the uncertainty principle, in the quantum mechanical model it describes the shell number, illustrated for a silicon atom in Figure 2.1. The silicon atom has  $n = 1, 2,$  and  $3,$  representing the K, L and M shells respectively. The electron is said to have positive or negative spin, depending on whether the electron is ‘spin up’ or ‘spin down’. The quantum numbers for silicon are given in Table 2.1. A short hand is often used where the spectral group or subshell value is given by:

$$l = 0, 1, 2, 3, 4, \dots \quad \text{or} \quad l = s, p, d, f, g, \dots$$

the first four are *sharp, principal, diffuse,* and *fundamental,* illustrated in Figure 2.1. Alphabetical order is used above f. The short hand convention follows [Streetman and Banerjee 2000]:



where the short hand for the silicon atom is  $1s^2 2s^2 2p^6 3s^2 3p^2$ .

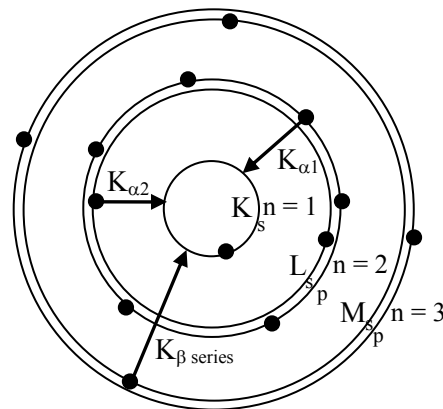


**Figure 2.1:** Illustration of a silicon atom showing the shell numbers and the X-ray fluorescence process resulting in a characteristic  $K_{\alpha 1}$ ,  $K_{\alpha 2}$ , and  $K_{\beta}$  series X-ray photons

$N$	$l$	$m$	$s/h/2\pi$	Electrons in subshell	Electrons in Shell
1 (K)	0	0	$\pm 1/2$	2	2
	0	0	$\pm 1/2$	2	
2 (L)	1	-1	$\pm 1/2$	6	8
		0	$\pm 1/2$		
		1	$\pm 1/2$		
3 (M)	0	0	$\pm 1/2$	2	4
	1	-1	$\pm 1/2$	2	
		0	$\pm 1/2$		
		1	$\pm 1/2$		

**Table 2.1:** Quantum numbers for a silicon atom

### 2.2.1 X-ray Fluorescence

An atom that has lost an inner electron is left in an extremely unstable state and electrons will cascade down from outer shells to fill the hole, as illustrated in Figure 2.1. The energy level of each shell is fixed, depending on only the number of protons in the atomic nucleus. When electrons travel from a higher to a lower level shell, a photon of fixed energy is emitted. This provides a characteristic X-ray response dependant on the target atom, the study of which is known as X-ray fluorescence (XRF) spectroscopy [Lifshin 1999]. The processes involved in the creation of  $K\alpha_1$ ,  $K\alpha_2$ , and  $K\beta$  series X-ray photons in a silicon atom are shown in Figure 2.1.

The fluorescent yield,  $X_Y$  is the measure of the efficiency of characteristic X-ray creation, and is given by:

$$X_Y = \frac{z^4}{A + z^4} \quad (2.5)$$

where  $Z$  is the atomic number of the target atom and  $A$  is a constant of the order  $1 \times 10^6$  for K series and  $1 \times 10^8$  for L series X-rays [Lifshin 1999]. The results over a range of atomic numbers are displayed in Figure 2.2. The reason for the lower efficiency at lower atomic numbers is due to the creation of Auger electrons. This happens when the characteristic X-ray is absorbed by an electron in the outermost shell (i.e. a valence electron), ejecting it from the atom.

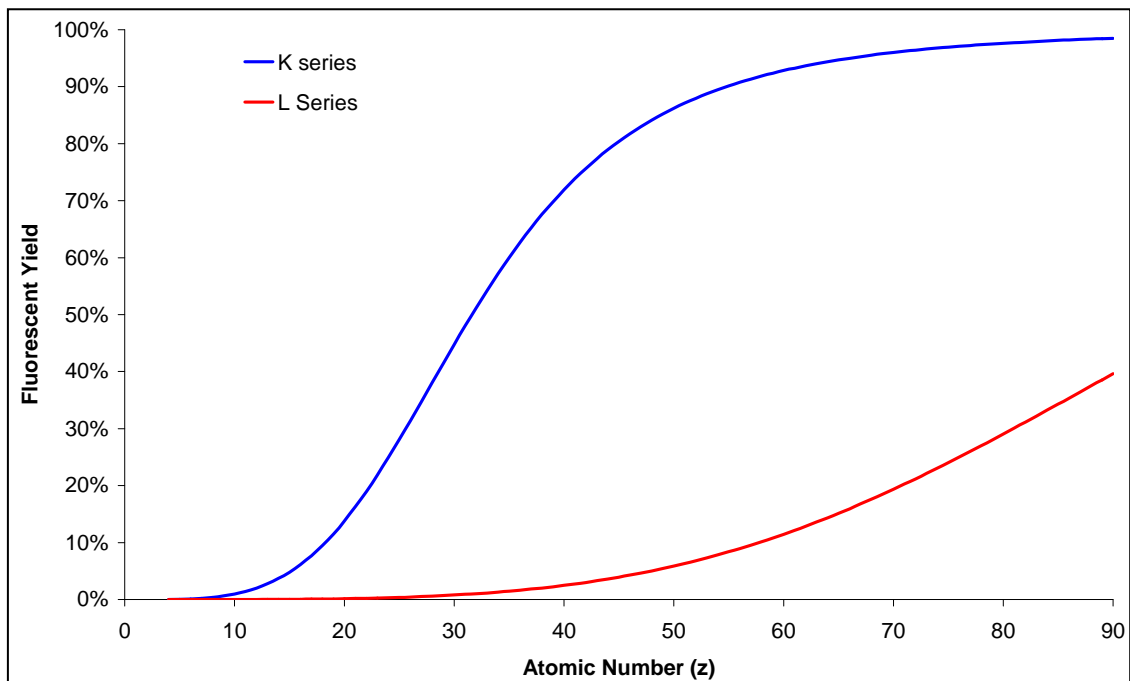


**Figure 2.2:** Atomic number versus the fluorescent yield for K and L series characteristic X-rays

### 2.2.2 Intrinsic Material and Crystalline Lattice Structure

In its pure, intrinsic, form silicon atoms are arranged in a periodic fashion repeated throughout the entire solid, referred to as a crystalline lattice structure, illustrated schematically in Figure 2.3 (n.b. a simplified 2D representation of the 3D structure). Four electrons are required to fill the 3p subshell, therefore the silicon atoms share their valence electrons to achieve a stable subshell, resulting in one silicon atom being locked to four others by the resulting covalent bonds. The energy levels of the silicon atoms within the lattice form continuous bands of energy, but as the inter-atomic spacing decreases the energy levels split into separate bands, beginning with the outer  $n = 3$  shell [Streetman and Banerjee 2000]. This band contains  $8N$  states, where  $N$  is the number of atoms. At equilibrium the band splits in two, separated by an energy gap  $E_g$  (eV) referred to as the ‘forbidden band’ as there are no allowed energy levels within it. The upper band is called the conduction band and the lower band the valence band, with  $4N$  states in each. At 0 K the  $4N$  electrons in the silicon atoms M shells will occupy the valence band as it is the lowest energy state available. The silicon band-gap is given by [Pankove 1971]:

$$E_g = 1.1557 - \frac{7.021 \times 10^{-4} T^2}{1108 + T} \tag{2.6}$$

where T is the absolute temperature (K).

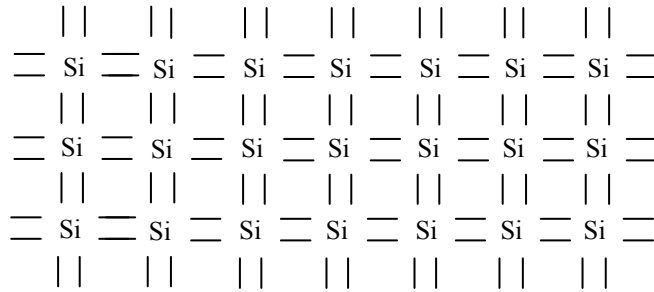


**Figure 2.3:** The lattice structure of intrinsic silicon

Above 0 K there are thermal vibrations within the lattice, each bonded electron has a mean thermal energy of  $\sim kT$ , where  $k$  is Boltzmann’s constant ( $8.62 \times 10^{-5} \text{ eV.K}^{-1}$ ). If an electron possesses an instantaneous energy greater than the band-gap the bond will break and the electron will escape as a free carrier leaving behind a hole. The number of electrons in the conduction band  $n$  ( $\text{e}^-.\text{cm}^3$ ) is equal to the number of holes in the valence band  $p$  ( $\text{h}^+.\text{cm}^3$ ), equal to the intrinsic carrier concentration  $n_i$ . It can be shown that:

$$np = n_i^2 = N_C N_V e^{-E_g/(kT)} \tag{2.7}$$

where  $N_C$  and  $N_V$  are constants relating to the density of states in the conduction and valence bands. Substituting for  $N_C$  and  $N_V$  given by:

$$N_C = 2 \left( \frac{2\pi m_n^* kT}{h^2} \right)^{\frac{3}{2}} \tag{2.8}$$

$$N_V = 2 \left( \frac{2\pi m_p^* kT}{h^2} \right)^{\frac{3}{2}} \tag{2.9}$$

where  $m_n^*$  and  $m_p^*$  are the conductivity of effective mass for electrons and holes respectively, to find:

$$n_i = CT^{1.5} e^{-E_g / (2kT)} \tag{2.10}$$

where  $C = 5.9 \times 10^{15} T^{-3/2}$ . At a temperature of 293 K the intrinsic carrier concentration is  $\sim 7 \times 10^9$  carriers.cm<sup>-3</sup>.

### 2.2.3 Extrinsic Material

Additional carriers of both types can be added, through a process known as doping, to form an extrinsic material. An n-type material has an excess number of electrons, produced with a dopant from group III of the periodic table (e.g. phosphorus), Figure 2.4a, and p-type silicon with excess holes, produced with a dopant from group VI (e.g. boron), Figure 2.4b. The impurities or lattice defects introduced by the dopant atoms create additional energy levels within the band-gap. A phosphorous atom introduces a *donor level* very near the conduction band, where little energy is required to free the electrons, and at temperatures above about 100K virtually all the electrons in the impurity level are ‘donated’ to the conduction band [Streetman and Banerjee 2000]. A boron atom introduces an *acceptor level* very near the valence band, and again at temperatures above about 100 K electrons from the valence band can be excited and ‘accepted’ into this impurity level, leaving behind a hole in the valence band.

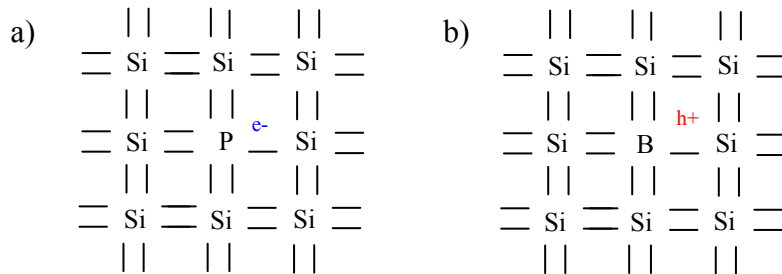


**Figure 2.4:** The lattice structure within n-type (a) and p-type (b) silicon

The Fermi level  $E_F$ , is the energy state that has a 50% probability of being occupied by an electron, found using the equation for the Fermi-Dirac distribution function  $f(E)$ , which gives the probability of occupancy of an available energy state:

$$f(E) = \frac{1}{1 + e^{(E-E_F)/kT}} \quad (2.11)$$

where  $E$  is the available energy state. It should be noted that the Pauli exclusion principle states that ‘no fermions may occupy the same quantum state simultaneously’, and that if there are no available energy states in the band-gap, then there is no possibility of finding an electron there. The Fermi level for p-type and n-type material is illustrated in Figure 2.5a and Figure 2.5b respectively, where  $E_c$  marks the bottom of the conduction band and  $E_v$  marks the top of the valance band.

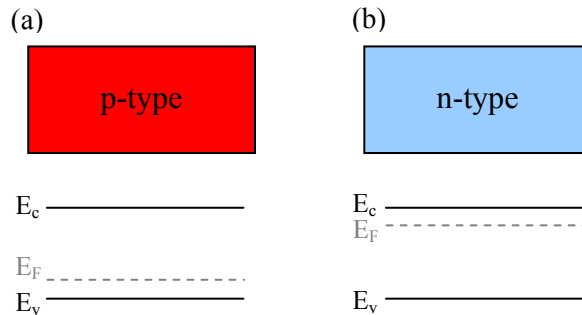


**Figure 2.5:** Cross section of p-type (a) and n-type (b) material and the resulting energy band diagrams with the location of the Fermi level

### 2.3 The Principal Components of a CCD

This section describes the components that make up a CCD. The cross section of a CCD is illustrated in Figure 2.6, showing the electrode/gate structure, the insulating oxide layer, the n-type buried channel and the p-type substrate. The p-n junction, the buried channel, the process of charge storage and transport, and finally, the CCD read-out circuit are all discussed.

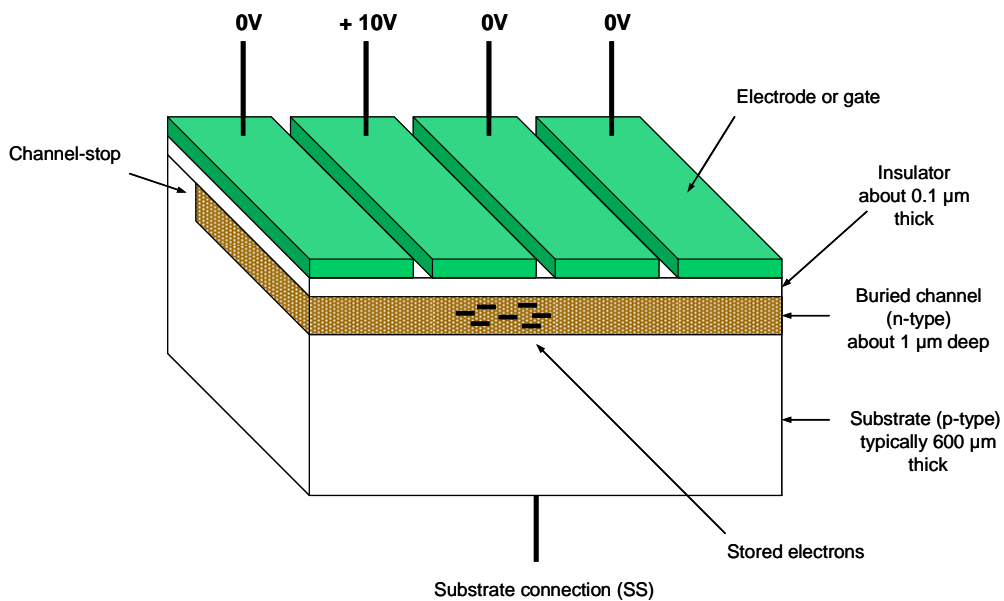


**Figure 2.6:** Illustration of a CCD cross section showing the principal components [Burt 2006]

### 2.3.1 The p-n Junction

The p-n junction created between the buried channel (n-type) and the substrate (p-type) determines the mechanism of charge collection in a CCD and all other semiconductor imaging devices. Initially, electrons that are close to the junction diffuse into the p-type material leaving behind fixed positive charge sites, and holes which are close to the junction diffuse into the n-type material leaving behind fixed negative charge sites, shown in Figure 2.7a. The presence of the fixed charge gives rise to a potential difference  $\phi_{\text{cho}}$  across the junction (called the ‘built-in’ or ‘inbuilt’ potential), which opposes further charge flow [Streetman and Banerjee 2000]. The region occupied by the fixed positive and negative charge sites has a depletion of mobile charge carriers, therefore, it is known as the ‘depletion region’. The resulting energy band diagrams are shown in Figure 2.7b. The extent of the depletion region can be increased through the application of a positive voltage to the n-type material, known as ‘reverse bias’. A negative voltage causes the depletion region to decrease, known as ‘forward bias’.

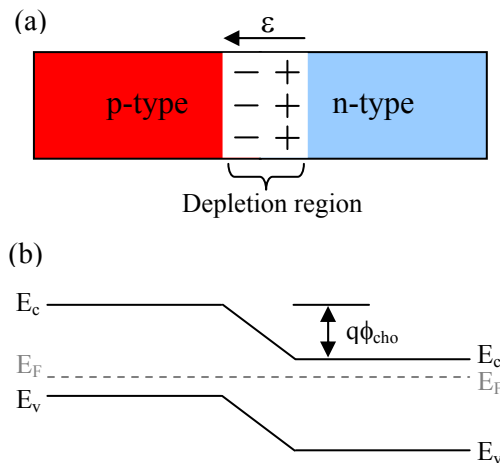


**Figure 2.7:** Cross section of p-n junction (a) and the resulting energy band diagrams (b) showing the formation of the depletion region at equilibrium

### 2.3.2 Metal-Oxide-Semiconductor

The electrode on the oxide layer above the silicon forms a metal-oxide-semiconductor (MOS) capacitor. With no additional voltage, the MOS structure is in the ‘flat-band’ state, as shown in Figure 2.8a, where the Fermi level of the metal  $E_{Fm}$  is the same as that of semiconductor  $E_{Fs}$ . When a negative voltage  $V$  is applied to the metal, the potential drops across the junction raising  $E_{Fm}$  by  $qV$ . Since no current can pass through the MOS structure, there can be no variation in  $E_{Fs}$  resulting in the accumulation of holes at the oxide-semiconductor interface, as shown in Figure 2.8b. Through the application of a positive voltage the potential is raised and  $E_{Fm}$  is lowered by  $qV$ , resulting in the creation of a depletion region shown in Figure 2.8c, comparable with the p-n junction discussed above. If the positive voltage is further increased, the intrinsic level  $E_i$  can bend

below  $E_{Fs}$  creating an inversion and resulting in a large concentration of electrons at the conduction band as shown in Figure 2.8d.

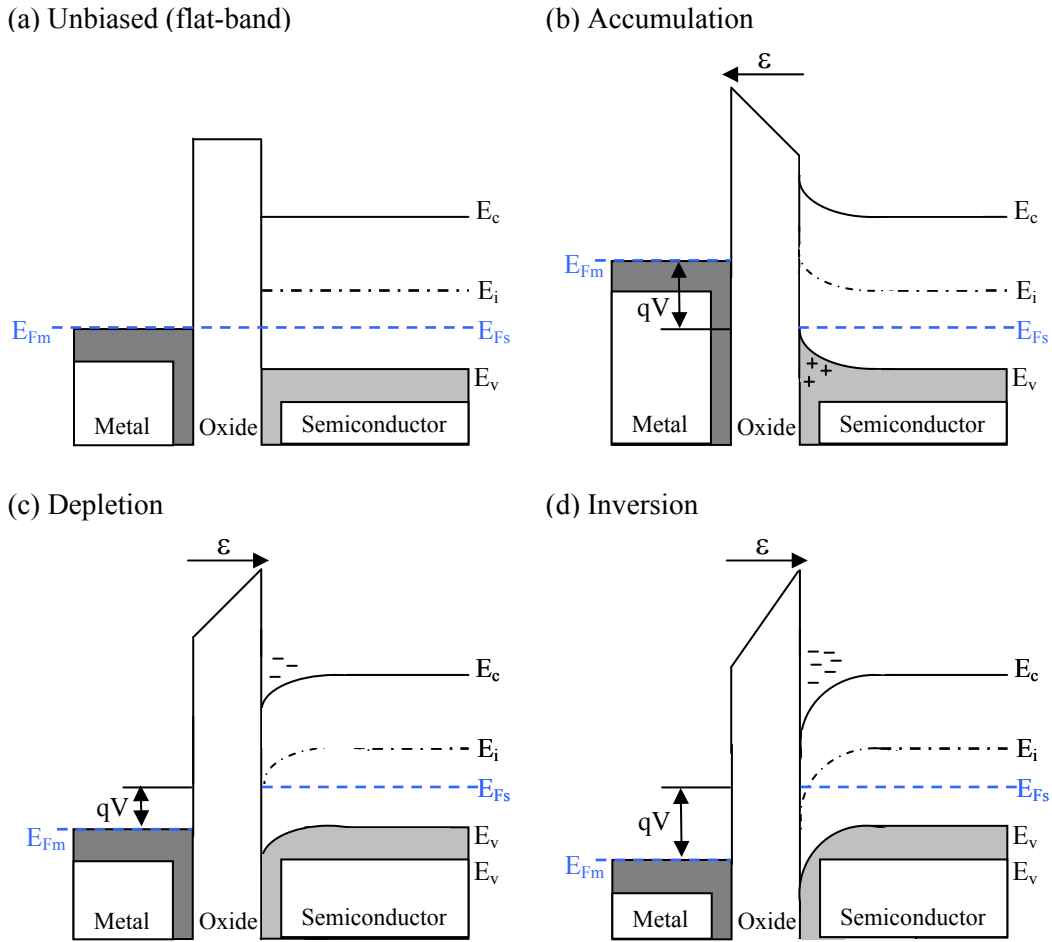


**Figure 2.8:** Band diagrams of MOS structure: (a) unbiased, (b) negative voltage applied causing accumulation, (c) positive voltage applied causing depletion, (d) positive voltage applied causing inversion

### 2.3.3 Buried Channel Potential Well

The buried channel combines both a p-n junction and an MOS capacitor, with the result that the potential maximum is formed below the Si-SiO<sub>2</sub> interface and above the p-n junction. The potential well in Figure 2.9 shows the effect of a gate voltage  $V_1$  at both 0 V and 10 V with positive bias  $V_{SS}$  on the substrate, known as the inverted and collecting phases respectively. The collecting phase used during the charge transfer process is discussed in Section 2.3.4. The inverted phase results in the accumulation of holes at the surface, suppressing the surface component of dark current, also known as ‘pinning’. This is used in ‘dither mode’ clocking, which is discussed in Section 2.5.1.

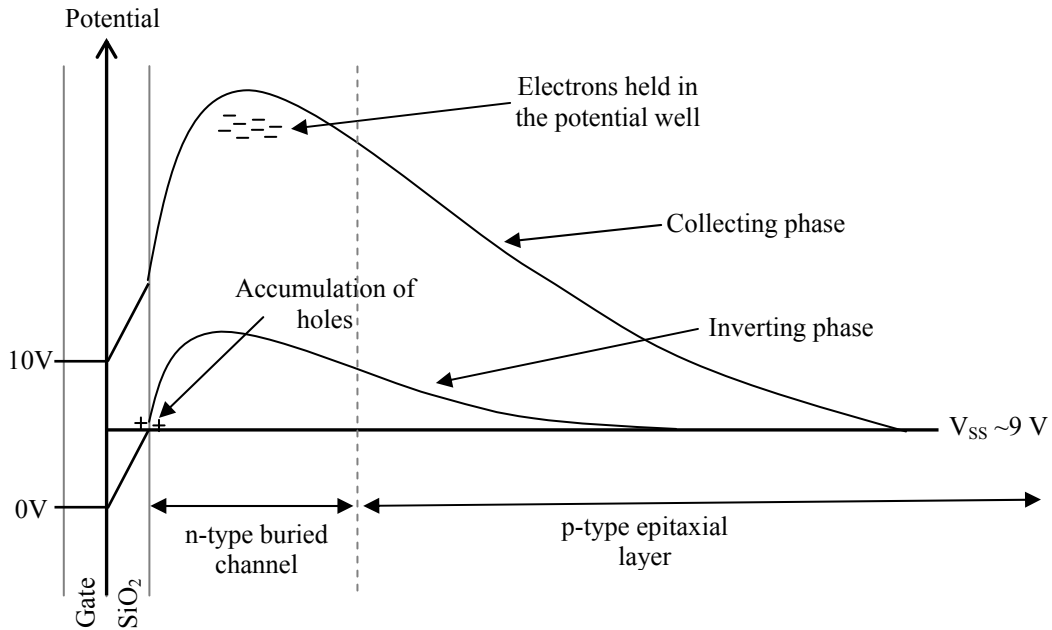


**Figure 2.9:** Buried channel potential well showing the collecting and inverted phases

It should be noted that as the gate voltage is increased, the total depth of depletion increases but the difference between the gate voltage and the potential maximum remains approximately the same. At  $e2v$  this voltage is designated the ‘channel parameter’,  $\phi_{cho}$ , and is typically in the range of 10 to 12 V. There is a second-order effect in that the potential maximum also moves closer to the Si-SiO<sub>2</sub> interface, but this is only significant for very large gate voltages (typically > 40 V).

### 2.3.4 Principles of Charge Transfer

The charge collected within a CCD pixel is referred to as a ‘charge packet’ and this is transferred to another pixel by manipulating the potential wells formed below the three gate electrodes within the pixel, the transfer process being known as ‘clocking’. In a standard CCD the charge is clocked down the device towards the read-out register and output circuit. The process is illustrated in Figure 2.10a where the charge has been shifted from one electrode to the next. The electrodes with an applied voltage (typically 10 V) are marked. The voltages used are called clock waveforms or pulses,  $I\phi_1$ ,  $I\phi_2$ , and  $I\phi_3$  corresponding to the three electrodes within a pixel. The required clock waveform for the transfer in Figure 2.10a is shown in Figure 2.10b. In the first step the charge is held under one electrode, then in step 2 the charge is spread across the potential well formed by two electrodes, and in step 3 the voltage on the first electrode is decreased so the charge well collapses and the charge is shifted to the right. It is vital for the operation of any CCD or SCD that the transfer should be as near perfect as possible, with 100% of charge transferred, but in actual devices a small fraction of the charge packet is generally left behind. This is characterised in terms of the charge transfer efficiency (CTE) or inefficiency (CTI).

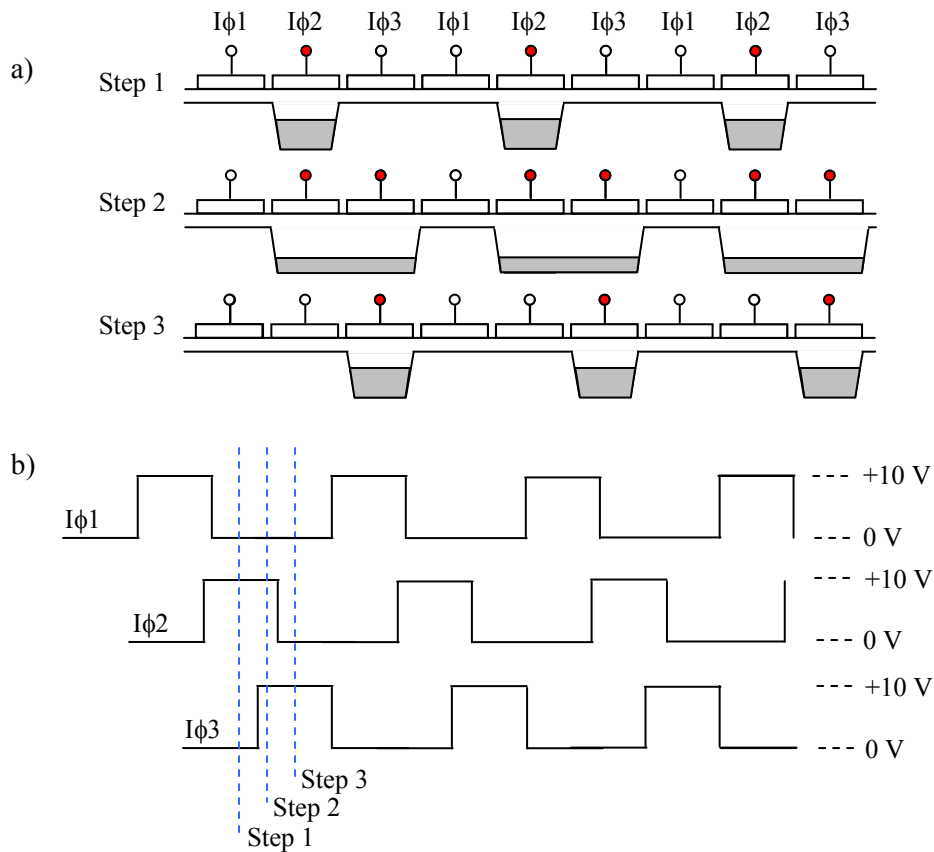


**Figure 2.10:** Illustration of the charge transfer process from one electrode to another (a) and the required clock waveform (b)

### 2.3.5 The MOSFET

A field-effect-transistor (FET) can be used as a signal amplifier and a switch. Essentially, the flow of electrons from the source (S) to the drain (D) is controlled through the electric field created by the voltage applied to the gate (G). The FET used in CCD operation is the MOSFET, the basic structure is shown in Figure 2.11a. At negative or zero voltage  $V_S$  and  $V_D$  are isolated from each other, but as the gate voltage increases an inversion layer will form at the Si-SiO<sub>2</sub> interface, as shown in Figure 2.11b, where the conductivity of this layer is controlled by the gate voltage and to a lesser extent the substrate voltage. The potential difference causing the electrons to move from source to drain is shown in Figure 2.11c. The steeper the gradient, the greater the velocity of the electrons: this is discussed in Section 2.5.2.

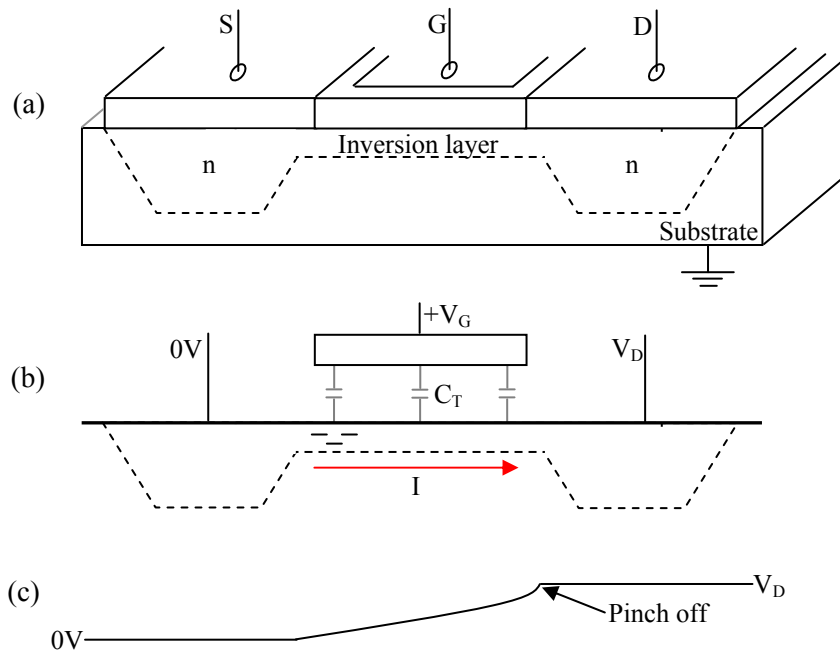


**Figure 2.11:** The metal-oxide semiconductor field-effect-transistor: (a) Basic structure of a MOSFET, (b) Cross-section showing the direction of electron flow and the FET capacitance  $C_o$ , (c) The potential difference felt by electrons as they move to the drain

### 2.3.6 The Output Circuit

The output circuit is shown schematically in Figure 2.12. The components are an output gate biased at fixed voltage  $V_{og}$ , an adjacent n-type region designated the ‘output node’, a reset switch FET using a reset drain  $V_{rd}$  and controlled using the reset gate voltage  $\phi_R$ , and an output FET operated as a source follower with output drain voltage  $V_{od}$ .

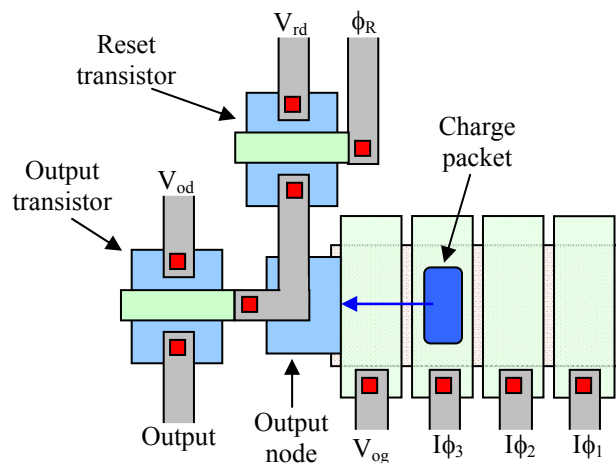


**Figure 2.12:** Illustration of the read-out process of a CCD

In operation the reset FET is ‘turned on’ by applying a suitable gate voltage pulse  $\phi_R$ , which causes the output node to be set to the reference voltage level  $V_{rd}$ . The node then ‘floats’ at  $V_{rd}$  until charge is transferred across the output gate from the last  $I\phi_3$  electrode. The presence of negative signal charge  $\Delta Q$  causes the node voltage to drop by an amount  $\Delta Q/C_T$ , where  $C_T$  is the sum of all the parasitic capacitances at the node, as indicated in Figure 2.13. The source-follower transistor has voltage gain between the gate and source,  $G_{FET}$ , typically 0.65, with the result that the output signal at the source terminal  $\Delta V_{FET}$  is given by the following relationship:

$$\Delta V_{FET} = \frac{\Delta Q}{C_T} G_{FET} \quad (2.12)$$

The ‘responsivity’ of the output circuit is defined as the voltage change arising from a single electron. Actual values are typically in the range of 1 to 10  $\mu\text{V}\cdot\text{electron}^{-1}$ , depending on the device layout and the resulting value for  $C_T$ .

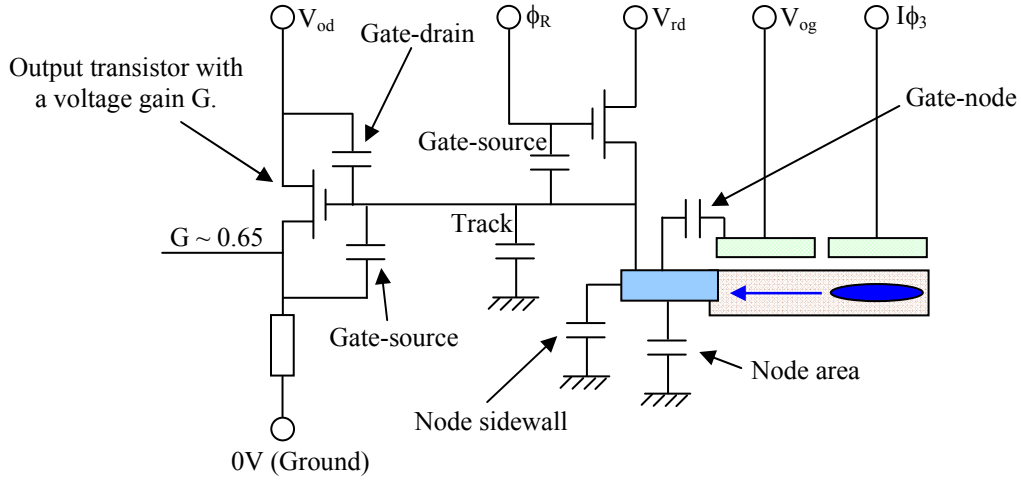


**Figure 2.13:** Schematic of the output circuit, showing the components that form the detection node capacitance  $C_T$

## 2.4 CCD Fabrication, Structure and Operation

The process starts with a silicon wafer, typically 4 to 8 inches in diameter. The silicon wafer forms the highly doped p+ silicon substrate (resistivity of  $< 0.01 \Omega\cdot\text{cm}$ ), acting as an electrical ground and an optically dead region. A layer of silicon pre-doped with boron is grown onto the substrate as shown in Figure 2.14, referred to as epitaxial silicon (from the Greek *epi* meaning ‘above’ and *taxis* meaning ‘in an ordered manner’). Another reason for this structure is that impurities within the epitaxial layer tend to diffuse into the p+ substrate. They are drawn towards faults created by precipitating supersaturated oxygen out of the silicon wafer that act as trap sites for the impurities. This process is known as ‘intrinsic gettering’ and it increases the purity and uniformity of the epitaxial silicon.

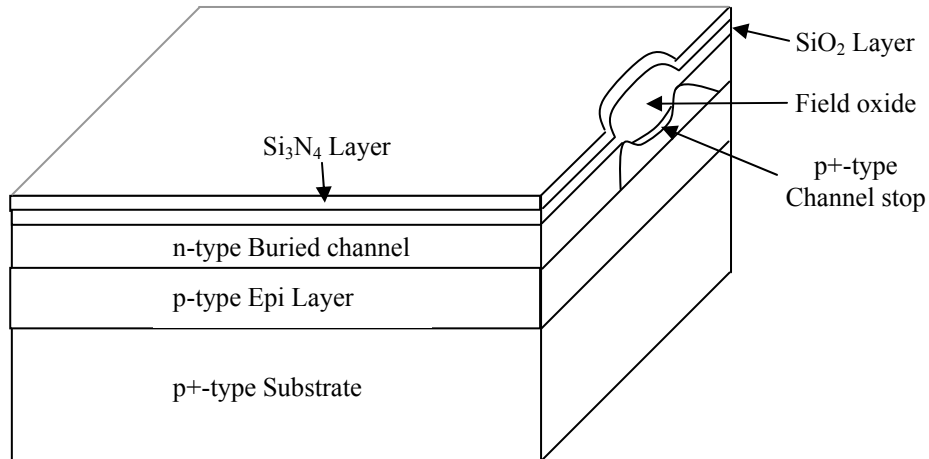


**Figure 2.14:** Cross section of in initial stages of CCD fabrication showing the substrate and the epitaxial layer

The next stage is the use of a process called photolithography. A masking oxide is deposited onto the silicon followed by a photo-resist, a light sensitive material, as shown in Figure 2.15a. A photo-mask or ‘reticle’ is then used to mask the photo-resist from UV light, as shown in Figure 2.15b. The photo-resist used is a negative resist, where the exposed portion remains and the unexposed portion is dissolved. The material is then etched to remove the unwanted oxide and remaining photo-resist to provide windows through which dopants can be applied, as shown in Figure 2.15c. Phosphorus dopant atoms are used to create the n-type buried channel shown in Figure 2.14, introduced using ion implantation shown in Figure 2.15d. Ion implantation causes lattice damage, as discussed in Chapter 3, a high temperature anneal is required to reform the lattice. The  $\sim 0.1 \mu\text{m}$  silicon oxide layer is then re-grown and covered with a  $\sim 0.1 \mu\text{m}$  layer of silicon nitride to prevent further oxidation and to improve the electrical isolation, as shown in Figure 2.14. The Figure also shows the p+ channel stop with the thick field oxide layer above to ensure isolation.

A  $\sim 0.7 \mu\text{m}$  layer of n+ doped polysilicon is deposited onto the layer of silicon nitride using chemical-vapour deposition, and photolithography is used to etch unwanted areas to leave behind the first set of electrodes. The surface of these is then re-oxidised ( $\sim 0.2 \mu\text{m}$ ) and the second  $\sim 0.6 \mu\text{m}$  polysilicon deposition takes place to form the second set of electrodes. This process is repeated to form the final set of  $\sim 0.5 \mu\text{m}$  polysilicon electrodes, resulting in Figure 2.16. The final layer is  $\sim 0.5 \mu\text{m}$  of vapour phase grown oxide (VAPOX) to protect the electrode structure from contamination while the device is in use. The final additions are aluminium bus lines and bond pads to carry the clock voltages. This whole process takes place in class 100 or higher clean conditions to avoid contamination, which could cause shorts and defects within the structure.

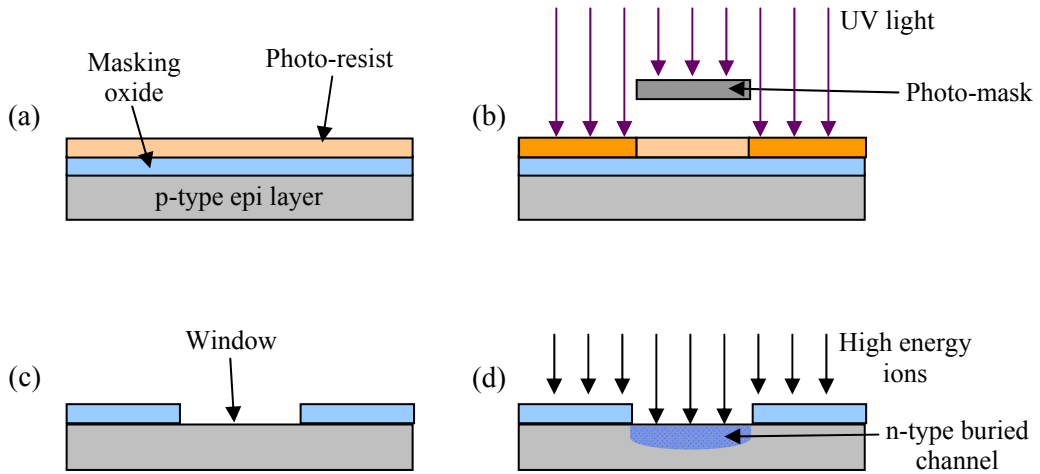


**Figure 2.15:** Illustration of the photolithography process involved in the creation of the n-type buried channel. Negative photo-resist is applied to a masking oxide on the p-type epitaxial layer (a) then exposed to UV light and developed (b). The remaining exposed photo-resist and masking oxide are etched to create a diffusion window (c) through which ion implantation is used (d) to create the n-type buried channel

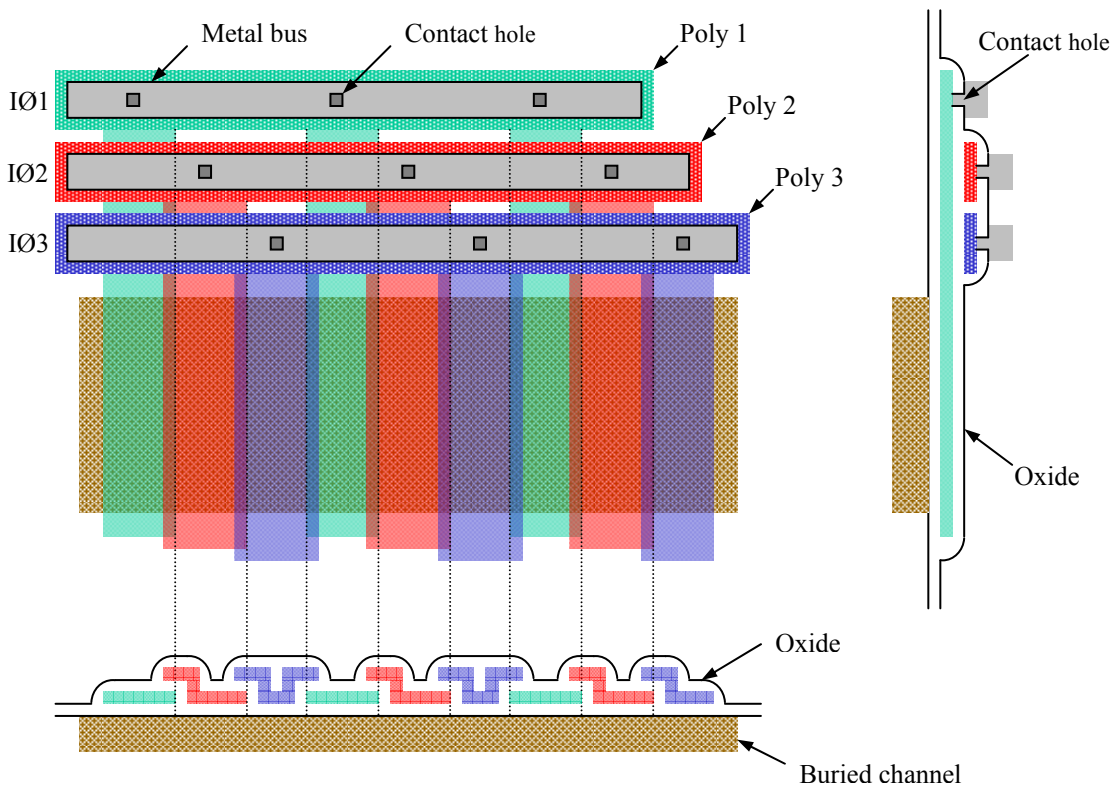


**Figure 2.16:** Top and side view and cross-section of a buried channel CCD [Burt 2006]

### 2.4.1 The CCD Structure and Read-out

A standard CCD consists of rows and columns of electrodes to form an array of pixels, as illustrated in Figure 2.17. Most devices have three electrodes per pixel and are known as ‘three phase devices’. These are the parallel electrodes operated using the image clocks ( $I\phi_1$ ,  $I\phi_2$ , and  $I\phi_3$ ). When an image integration period is set, two of the parallel electrodes are biased high to allow electrons to be collected within the buried channel potential well, as illustrated in Figure 2.9. This is called the collecting phase. The electrode biased at a lower potential is referred to as the barrier phase to stop the spread of signal charge from one row to another. The parallel electrodes are separated by channel stops, illustrated in Figure 2.14, to prevent the spread of signal charge from one column to another.

The charge packet is clocked through the image section towards the read-out register using the image clocks, as illustrated in Figure 2.10. One image clock cycle will cause one parallel transfer, with one row clocked into the read-out register. Before the next image clock cycle the register clocks ( $R\phi_1$ ,  $R\phi_2$ ,  $R\phi_3$ ) are used to clock the charge packets towards the output circuit where the charge to voltage conversion takes place, as illustrated in Figure 2.17. The device is read-out line by line to provide a two dimensional map of photon interactions, where the point of detection within the CCD is known.

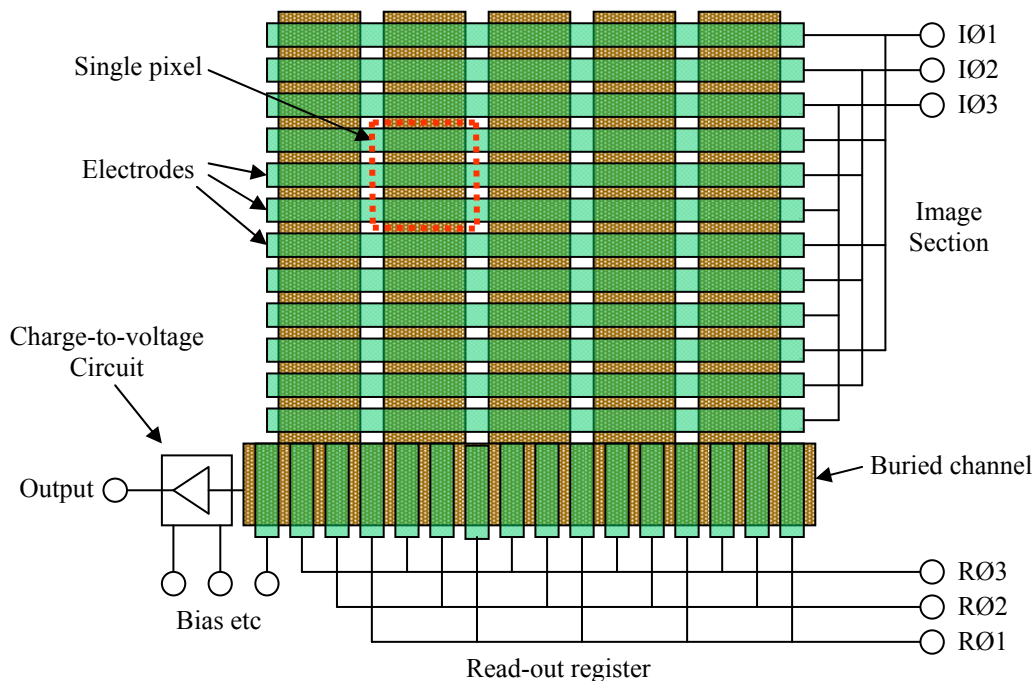


**Figure 2.17:** Schematic of a basic ‘full frame’ array CCD [Burt 2006]

### 2.4.1.1 Charge Transfer Efficiency

The CTE is the fraction of a charge packet that is correctly transferred from one pixel to another. The CTI is the fraction that is left behind, where  $CTI = 1 - CTE$ . Examples are as follows:

In a CCD that requires 575 transfers to read-out the imaging area (as in the CCD54), with a typical CTE of 99.9995 % the charge packet would suffer about 0.3 % loss. If the CCD now suffers from a reduction in CTE to 99.995 %, for example due to radiation damage discussed in Chapter 3, the signal loss from the charge packet would now be around 3 %. The decrease in CTE is as a result of the formation of trap sites with a release time longer than the clock period, as described in Sections 2.5 and 3.6. Smearing, which is one source of split pixel events, is discussed in Section 2.6.2.

The CTI can be measured using a number of techniques, including the extended pixel edge response, the first pixel response and through X-ray analysis, the method discussed here. Based on the location of the X-ray interaction within the CCD, the number of parallel (towards the read-out register) and serial (along the read-out register) transfers can be identified. Using a characteristic X-ray, for example Mn-K $\alpha$ , a known amount of charge is deposited within the CCD, allowing the amount of charge deferred during transport to be found. The CTI is given by [Janesick 2001]:

$$CTI_x = \frac{S_D(e^-)}{X(e^-)n_t} \quad (2.13)$$

where  $S_D(e^-)$  is the average deferred charge,  $X(e^-)$  is the X-ray signal and  $n_t$  is the number of pixels transfers. The limitation is set by the electrons released by high energy X-ray events being collected under multiple pixels. As the CTI is dependent on the mean time between charge packets clocked from one pixel to another and the trap release constant, it is essential to use a low X-ray fluence, as a high fluence would artificially reduce the measured CTI.

### 2.4.2 The SCD CCD54 Structure and Read-out

In the case of the SCD CCD54, the 1.07 cm<sup>2</sup> active area is covered with 1725 diagonal electrodes with the channel stops in the underlying silicon arranged in a herringbone structure, as shown in Figure 2.18. The pitch of the channel stops is 25  $\mu$ m. Charge generated in the triangular sections is clocked through the charge collection area between the channel stops, indicated using solid lines, by means of three-phase clock pulses applied to the overlying electrodes, depicted as dashed lines, towards one of two central read-out channels, one for the top section and one for the lower section. These are combined just before the read-out node. The time it takes any charge to be read-out depends on the point of generation, 575 clock triplets are required to read-out the entire charge collection area. In effect, the mode of operation can be described as that of a pseudo-linear CCD,

with 575 element or samples, each representing the total charge collected in the perpendicular transport channels respectively across the device.

The advantage over a standard two dimensional CCD is the reduction in read-out complexity, and the suppression of surface generated dark current through the use of ‘dither mode’ clocking and the avoidance of an image integration period. The operational temperature can be increased from that used in a standard CCD, typically  $-90\text{ }^{\circ}\text{C}$ , to between  $+5\text{ }^{\circ}\text{C}$  and  $-40\text{ }^{\circ}\text{C}$ . Removing the need for complicated and high powered cooling, allowing for instrument miniaturisation and improved portability.

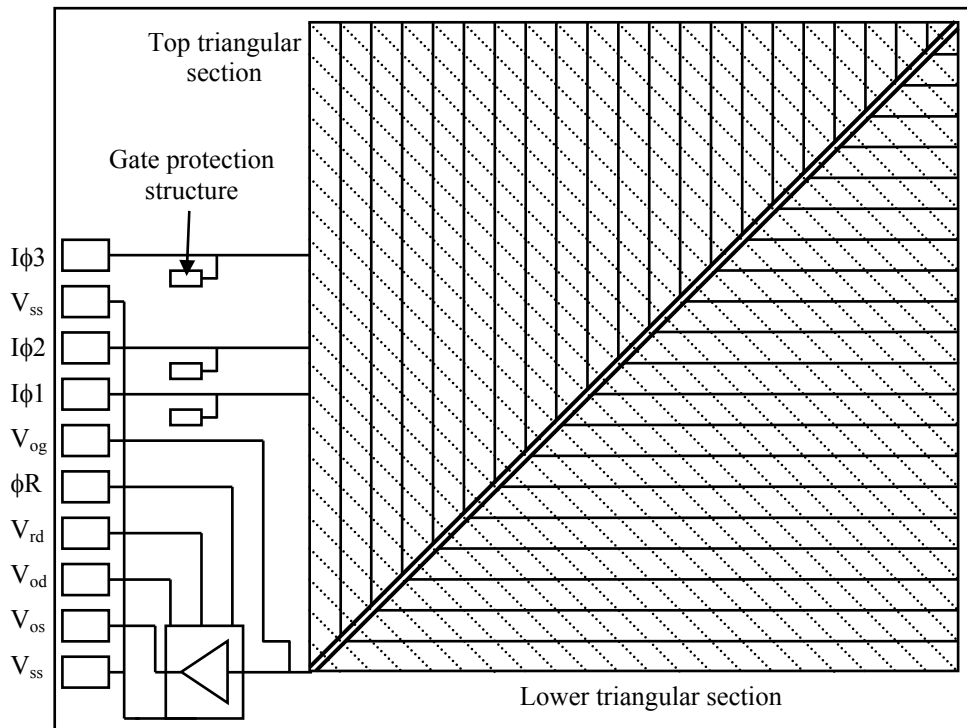


**Figure 2.18:** Schematic of the SCD. The electrodes are depicted as dashed lines, whilst the charge transport channels are indicated using solid lines

The swept charge device does not perform a conventional imaging function but utilises charge transfer to move X-ray generated charge signals under the area of the electrodes to a low noise output circuit. The read-out elements are referred to as ‘samples’ rather than pixels.

## 2.5 Sources of Noise within the CCD and Signal Processing

The next sections will discuss read noise, which includes effects from dark current, reset ( $kT/C$ ) noise, and transistor ( $1/f$ ) noise, together with photon shot noise and transfer noise, which are signal dependant. It will be shown that the noise leads to a reduction in the energy and spatial resolution performance, as discussed in Section 2.6.2.

### 2.5.1 Dark and Leakage Current

Dark current (leakage current when not in the dark) occurs in all semiconductor devices and is the result of thermal generation of free electrons as described in Section 2.2 and by Equation 2.10. The formation of lattice defects introduced by dopants and charged particle radiation damage, discussed in Chapter 3, introduce energy levels within the band-gap as illustrated in Figure 2.19. Most active traps are near the intrinsic level  $E_i$ , and as the energy level position moves away from mid-gap, there is an exponential decrease in generation/recombination rate [Srouf *et al.*2003]. This is because trap sites above  $E_i$  are harder to fill, while traps below are harder to escape from. As illustrated in Figure 2.19 the trap sites can act as ‘stepping stones’ in the transition of electrons between the conduction and valence bands. Where  $np > n_i^2$  the trap sites cause carriers to be held back on charge transfer reducing the CTE, and if  $np < n_i^2$  carriers are generated giving rise to dark current.

The generation of dark current electrons limits the exposure time, as it reduces the time a potential well can exist to collect useful data [Holmes-Siedle 2002]. The avoidance of an image integration period reduces the dark signal detected. Increasing the rate at which the device is read-out using a faster clock cycle also reduces the amount of dark signal detected. This does not change the rate at which dark current is generated. The number of carriers is related to temperature by Equation 2.10. Through cooling the device electrons become frozen into the trap sites, no longer contributing to the detected dark signal.

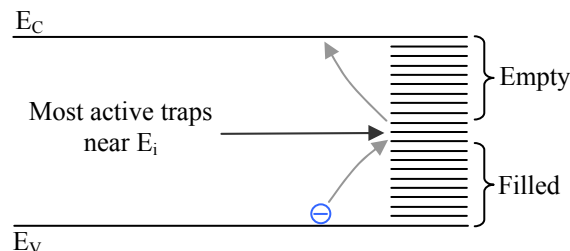


**Figure 2.19:** Silicon band-gap showing the location of the most active trap sites or defect locations

Within a CCD there are three regions that contribute to dark current, as shown in Figure 2.20. These are; (1) neutral bulk material below the potential well, (2) depleted material within the potential well and (3) at the Si-SiO<sub>2</sub> interface. The last of these tends to be the dominant source for a device in non-inverted mode operation (NIMO) [Janesick 2001].

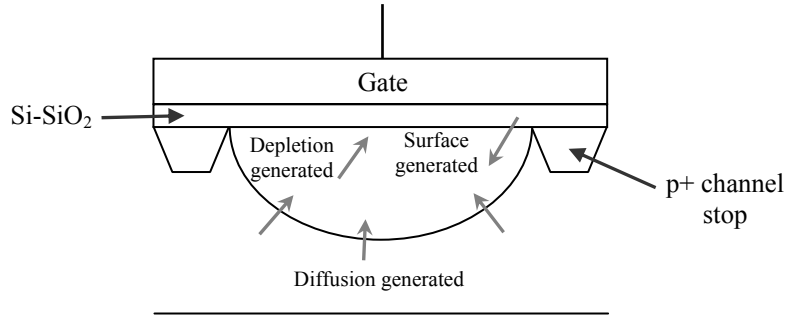


**Figure 2.20:** Source regions of dark current within a CCD [adapted from Janesick 2001]

The net generation or recombination rate  $U$  ( $\text{cm}^{-3}\cdot\text{s}^{-1}$ ) is described by the Shockley/Hall/Read equation given by [Hall 1952, and Shockley and Read 1952]:

$$U = \frac{\sigma_p \sigma_n v_{th} (np - n_i^2) N_t}{\sigma_n \left[ n + n_i \exp\left(\frac{E_t - E_i}{kT}\right) \right] + \sigma_p \left[ p + n_i \exp\left(\frac{E_i - E_t}{kT}\right) \right]} \quad (2.14)$$

Where  $n$  and  $p$  are the electron and hole concentrations ( $\text{cm}^{-3}$ ) in the region of interest,  $\sigma_p$  and  $\sigma_n$  are the electron and hole capture cross-sections ( $\text{cm}^2$ ),  $v_{th}$  is the thermal velocity  $(3kT/m_e^*)^{0.5} \approx 10^7$   $\text{cm}\cdot\text{s}^{-1}$  where  $m_e^*$  is the effective mass of an electron, and  $N_t$  is the concentration of trap sites at energy level  $E_t$  ( $\text{cm}^{-3}$ ). A zero value for  $U$  represents thermal equilibrium, a positive result implies the recombination of electron hole pairs and a negative result implies the generation of electron hole pairs.

A useful assumption is that the cross-section for electron and holes trapping are the same, with  $\sigma = \sigma_n = \sigma_p$ , the net generation rate  $U$  is given by.

$$U = \frac{\sigma v_{th} (np - n_i^2) N_t}{n + p + 2n_i \cosh\left(\frac{E_t - E_i}{kT}\right)} \quad (2.15)$$

### 2.5.1.1 Surface Generated Dark Current

At the Si-SiO<sub>2</sub> interface the lattice structure is a lot less regular than within pure silicon, leading to an increased number of defects, as shown in Figure 2.21. The unpaired electrons, ‘dangling bonds’ can easily break free forming the largest component of dark current, with trap sites distributed across the trap band-gap [Janesick 2001]. The highest probability of a trap location is at  $E_i$ , where  $E_t = E_g/2 = E_i$ , the net surface generation or recombination rate  $U_s$  is given by:

$$U_s = \frac{\sigma_p \sigma_n v_{th} (np - n_i^2) N_t}{\sigma_n [n + n_i] + \sigma_p [p + n_i]} \quad (2.16)$$

under conditions of surface depletion where  $n = p = 0$ , and assuming that the cross sections for electrons and holes are the same,  $U_s$  is given by:

$$U_s = -\frac{\sigma v_{th} n_i N_t}{2} \quad (2.17)$$

The negative sign indicates carrier generation. With an active depth of  $d_s$  and the charge on an electron  $q$  ( $1.60 \times 10^{-19}$  C) the surface generated dark current  $I_s$  ( $\text{A}\cdot\text{cm}^{-2}$ ) is given by:

$$I_s = -q d_s U_s = \frac{q \sigma v_{th} n_i N_{ss}}{2} \quad (2.18)$$

assuming that traps are only effective in very shallow depths such that  $N_t d = N_{ss}$ , where  $N_{ss}$  is the surface state density ( $\text{cm}^{-2}$ ) [Janesick 2001].

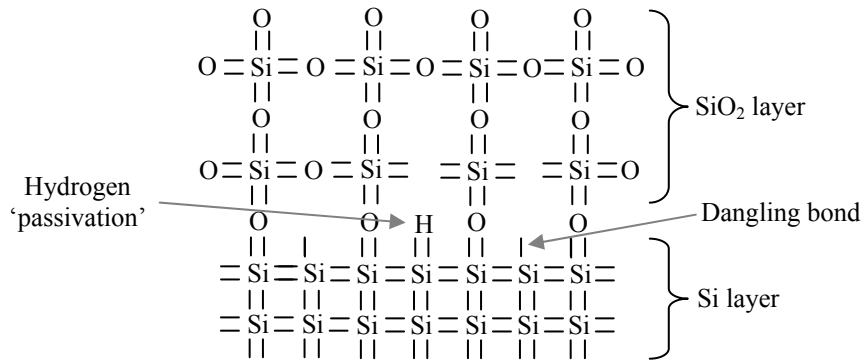


**Figure 2.21:** Si-SiO<sub>2</sub> Interface

The  $N_{ss}$  is reduced through the passivation of the dangling bonds using a 435 °C hydrogen anneal at the end of the processing [Janesick 2001], which effectively attaches hydrogen atoms to the dangling bonds as illustrated in Figure 2.21.

It has been demonstrated [Hynecek 1979, Saks 1980] that the accumulation of holes at the surface, illustrated in Figure 2.9, removes trapped electrons, thereby reducing the surface generated contribution to zero. This operation is described as either 'inversion', because holes are now present in n-type material, or 'pinning', because the holes cause the surface to be at the same potential as the substrate.

If the hole concentration is  $p_s$ , where  $p_s \gg n_i$ , and  $n = 0$ , Equation 2.16 reduces to:

$$U_{si} = -\frac{\sigma v_{th} n_i^2 N_t}{p_s} \quad (2.19)$$

to give the net surface inversion generation or recombination rate  $U_{si}$ . The surface generated dark current while inverted  $I_{si}$  ( $\text{A}\cdot\text{cm}^{-2}$ ) is given by:

$$I_{si} = -qd_s U_{si} = \frac{q\sigma v_{th} n_i^2 N_{ss}}{p_s} = I_s \left( \frac{2n_i}{p_s} \right) \quad (2.20)$$

which is a factor  $p_s/2n_i$  lower than the normal surface component. Typically this factor can be many orders of magnitude. As  $p_s$  is large in relation to  $n_i$  the surface generated dark current is suppressed.

Note that the states at the surface have a range of different energies that span right across the band-gap. The number of states is often described as per  $\text{cm}^2\cdot\text{eV}$ , in which case the number must be multiplied by a factor  $\pi kT$  to obtain  $N_{ss}$ .

### 2.5.1.2 Dither Mode Clocking

Once the surface is taken out of inversion, the traps begin to fill, resulting in an increase in dark current with time, as illustrated in Figure 2.22. The recovery time is dependant on the time constant  $\tau_0 = 1/n_i v_{th} \sigma$  (s), thus for a collection period  $t$ , the mean dark current is given by [Burke and Gajar 1991]:

$$I_s(t) \approx I_s(\infty) \left[ 1 - \exp\left(-\frac{2.7t}{\tau_0}\right) \right] \quad (2.21)$$

where  $\tau_0$  can be approximated to around  $1.9 \times 10^{13} e^{-0.12T}$ . The temperature dependence is clear in Figure 2.22, showing the recovery at  $T_1$  and the cooler  $T_2$ . This process is used in ‘dither mode’ clocking, as now explained.

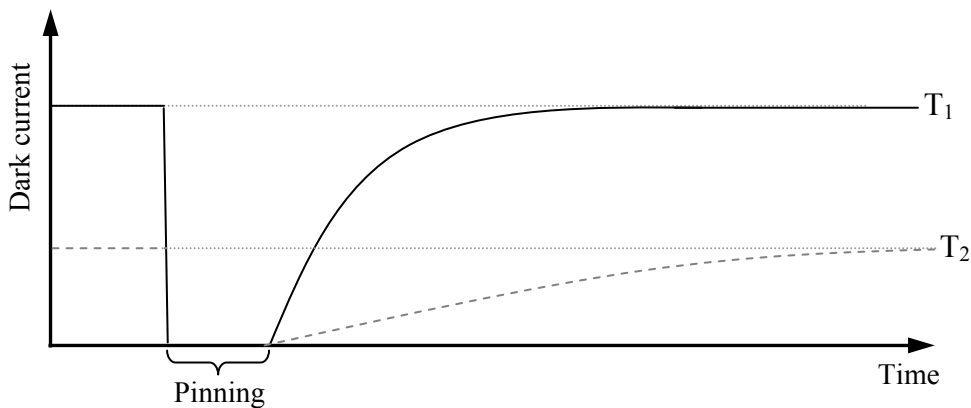


**Figure 2.22:** Illustration of time versus dark current showing the effects of pinning at a temperature  $T_1$  and a lower temperature  $T_2$  [Burt 2008]

The relatively slow build up of dark current can be exploited as follows. With the substrate voltage being such as to pin the electrodes at 0 V clock level, at the beginning of the clock cycle the charge

packet is held under one phase at 10 V with the adjacent phase at 0 V. By switching the voltages from 10 V to 0 V and 0V to 10 V, respectively, the charge is transferred between the phases. The voltages are then switched 0V to 10 V and 10 V to 0 V, respectively, such that the charge returns to the original electrode. This operation, termed ‘dither mode’, is repeated throughout the normal charge collection period. The fact that the periods for which any electrode is out of pinning are relatively short means that the dark current generated during these intervals can be minimal and a small mean total value is typically achieved. [Burke and Gajar 1991]. The same reduction occurs during the normal transfer process, which is therefore termed ‘intrinsic dither mode’ [Holland *et al.* 2004].

The mean dark current is dependant on the switching interval and temperature, fast operation and lower temperature will increase performance. The typical dark current for e2v devices under these conditions is 10 pA.cm<sup>-2</sup> at 20 °C [Burt 2006] an improvement of a factor 100 on normal operation, however, the dark current non-uniformity increases to around 30 % [Burt 2006]. The power dissipation is higher and the full well capacity and depth of depletion are less than with normal three phase clocking, but there is no loss in Quantum efficiency as discussed in section 2.6.2. It can however also lead to increased clock induced charge as a result of charge multiplication. The standard operation for a CCD is non-inverted mode operation (NIMO).

### 2.5.1.3 Bulk Generated Dark Current

The bulk dark current arises from two sources, the depleted and un-depleted regions. In the depletion region  $p = n = 0$  and Equation 2.15 becomes:

$$U_{DEP} = -\frac{\sigma v_{th} n_i N_B}{2 \cosh\left(\frac{E_t - E_i}{kT}\right)} \quad (2.22)$$

where  $U_{DEP}$  is the carrier generation rate in the depletion region (cm<sup>-3</sup>.s<sup>-1</sup>) and  $N_B$  is the bulk state density (cm<sup>-3</sup>). Multiplying by the depletion depth  $x_{Si}$  to give an equation to find the depletion dark current.

$$I_{DEP} = -qx_{Si}U_{DEP} \quad (2.23)$$

Note that whereas traps at the Si-SiO<sub>2</sub> interface are distributed right across the silicon band-gap those in the bulk silicon tend to have discrete energy levels. Hence the use of a single trap energy  $E_t$  in Equation 2.22.

The second source of bulk dark current is from the un-depleted region, below channel stops and potential wells. The carrier concentration is very low just outside the depletion region, any carriers

present would move towards and into the potential well by diffusion, as illustrated in Figure 2.20. This means that the region below the depletion region is largely depleted of carriers and  $n$  tends to 0, therefore the carrier generation rate in the un-depleted region  $U_{UDEP}$  is given by:

$$U_{UDEP} = -\frac{\sigma v_{th} n_i^2 N_B}{p + 2n_i \cosh\left(\frac{E_t - E_i}{kT}\right)} \quad (2.24)$$

in situations where the dominant trap is at mid band-gap and with  $p$  generally much larger than  $2n_i$  the dark signal is a factor  $n_i/p$  smaller than the corresponding depletion layer value.

However, for traps away from mid-band, at low temperatures and with lightly doped substrate material where  $p$  is small the cosh term can be large and the diffusion component is the same as that of the depletion region. In situations where the active thickness is small in comparison with the minority carrier diffusion length  $L_n$ , it is sufficient to assume that all the charge generated within the active depth is collected as dark signal. This is effectively the situation that prevails in the CCD54, as will be shown in Chapter 6. The carrier generation rate in the diffusion region is therefore given by:

$$U_{UDEP} = -\frac{\sigma v_{th} n_i N_B}{2 \cosh\left(\frac{E_t - E_i}{kT}\right)} \quad (2.25)$$

which is exactly the same as equation 2.22. The total dark current from the bulk silicon  $I_{BUL}$ , is then given by:

$$I_{BUL} = -q T_{Si} U_{UDEP} = \frac{\sigma v_{th} n_i N_B q T_{Si}}{2 \cosh\left(\frac{E_t - E_i}{kT}\right)} \quad (2.26)$$

where  $T_{Si}$  the active depth. For devices using epitaxial silicon  $T_{Si}$  is the layer thickness, for back illuminated devices it is the total silicon thickness, and for devices on bulk silicon it is the minority carrier diffusion length  $L_n$ .

#### 2.5.1.4 Dark Current Summary

Dark current provides a limit to device performance, essentially limiting the available integration time. The total dark current per unit area for a device operated in non-inverted mode  $I_{NIMO}$  is dominated by the surface component given by

$$I_{NIMO} = \frac{q \sigma v_{th} n_i N_{ss}}{2} \quad (2.27)$$

under inverted or pinned mode operation the surface component is suppressed and the bulk component is now of significance. The dark current  $I_{IMO}$  is given by:

$$I_{IMO} = \underbrace{\frac{q\sigma v_{th} n_i^2 N_{ss}}{p_s}}_{\text{Si-SiO}_2 \text{ interface}} + \underbrace{\frac{\sigma v_{th} n_i N_B q T_{Si}}{2 \cosh\left(\frac{E_t - E_i}{kT}\right)}}_{\text{Bulk Silicon}} \quad (2.28)$$

since generally  $p_s \gg n_i$ , the first term is very small and only the second bulk term is of significance.

During NIMO the surface and depletion region form the main sources of dark current, the neutral material is negligible [Janesick 2001], both are dependant on the intrinsic carrier concentration  $n_i$  given by Equation 2.10, therefore the general dark current equation is taken as:

$$D_{NIMO}(e^-) = C e^{-E_g/(2kT)} \quad (2.29)$$

where  $D_{NIMO}$  is the average dark current generated ( $e^- \cdot \text{pixel}^{-1} \cdot \text{s}^{-1}$ ), and  $C$  is a constant. The IMO of the SCD results in the suppression of surface generated dark current, therefore the dark current equation becomes:

$$D_{IMO}(e^-) = C e^{-(E_g - E_t)/kT} \quad (2.30)$$

where  $D_{IMO}$  is the average dark current generated ( $e^- \cdot \text{pixel}^{-1} \cdot \text{s}^{-1}$ ).

### 2.5.2 Dark Shot Noise

There is a statistical uncertainty relating to the dark current, described by the dark current ‘shot noise’, as a result of the random fluctuations in the rate of generation [Horowitz and Hill 1989]. The process is governed by Poisson’s statistics which deals with independently occurring events. The shot noise  $N_{DSN}$  ( $e^-$  r.m.s.) is given by [Janesick 2001]:

$$N_{DSN} = \sqrt{I_{AVE}} \quad (2.31)$$

where  $I_{AVE}$  is the average dark current in electrons per pixel. This process occurs throughout the device and will be amplified in the read-out circuit.

### 2.5.3 Dark Current Spikes

Dark current ‘spikes’ are the result of localised (to generally a single pixel) higher-than-average dark current generated during the integration period (as seen as spikes in the video waveform,

hence the name), resulting in bright pixels in a standard CCD. Their origin is probably a result of contamination. Monitoring the signal level within a bright pixel in a two dimensional CCD can give rise to multiple stable levels, this are known as random telegraph signals [Smith *et al.* 2004]. In the case of a SCD dark current spikes should not have a large impact on device performance as any one of the output samples is effectively an average signal over the whole area of the array.

#### 2.5.4 Impact Ionisation and Clock Induced Charge

An electron in an electric field  $E$  moves at a constant velocity  $v_s$ , where the relationship between  $v_s$  and  $E$  is generally as shown in Figure 2.23. It should be remembered that electrons do not travel in straight lines but collide with the lattice and follow a random walk along the direction of the applied electric field with velocity  $v_s$ , the velocity between collisions being the much higher ‘thermal velocity’  $v_{th}$ , i.e. where  $KE = mv_t^2/2 = 3kT/2$ . However, as the electric field is increased the velocity  $v_s$  increases and eventually reaches a saturation value  $v_{Sat}$ , where  $v_{sat} \sim v_t \sim 10^7 \text{ cm.s}^{-1}$ .

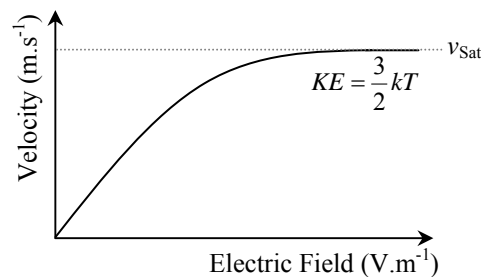


**Figure 2.23:** Illustration of electric field versus the electron velocity showing the saturation velocity  $v_{Sat}$

In regions of very high electric fields (typically  $> 10^4 \text{ V.cm}^{-1}$ ) the velocity between collisions becomes higher than  $v_{Sat}$  and, by virtue of this higher kinetic energy the electrons have a temperature that is higher than the surrounding silicon lattice. Such electrons are said to be ‘hot’. Hot electrons can knock other electrons from the lattice, a process known as ‘impact ionisation’, resulting in charge multiplication and possibly increasing the noise and current fluctuations across the device. With hot electrons at a few thousand Kelvin, as the electrons drop down an energy state, black body radiation is emitted in the form of photons with a long wavelengths tending towards infra red. Holes behave similarly [Burt 2006].

In dither-mode clocking, as the electrode is taken out of pinning some holes are trapped at the surface, as shown in Figure 2.24. When released, the holes can also cause impact ionisation resulting in the generation of electrons. This process is known as ‘clock induced charge’. The generation rate is low but the effect is cumulative with the number of transfers. The rate is increased exponentially with respect to the clock voltage as shown in Figure 2.25, which compares

the clock induced charge of a dither-mode and normal mode device. A lower clock voltage, higher clock rate and good clock overlap all reduce the amount of clock induced charge.

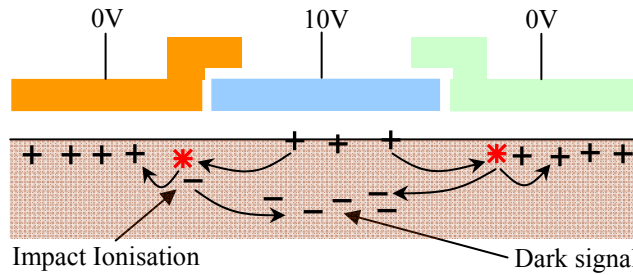


**Figure 2.24:** Cross section of electrode structure showing impact ionisation

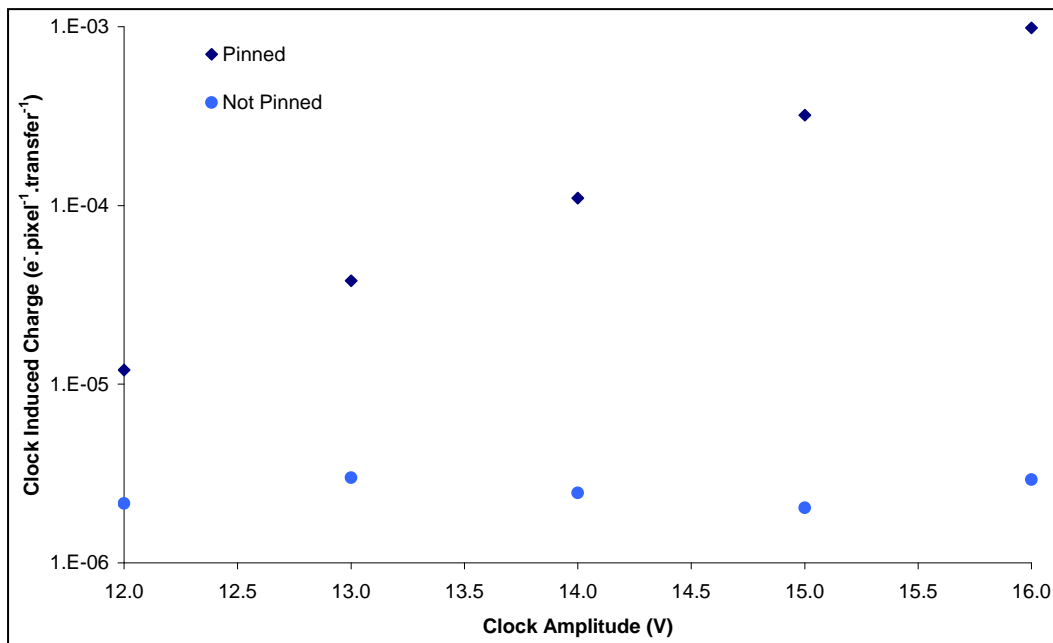


**Figure 2.25:** Clock amplitude versus the clock induced charge for pinned and none pinned operation [Burt 2006]

### 2.5.5 Transistor Noise

With any conductor having a resistance  $R$ , the normal motion of the free electrons gives rise to a fluctuating voltage  $V_n$ , given by:

$$V_n = \sqrt{4kTRB} \tag{2.32}$$

where  $B$  is the system bandwidth, and termed Johnson noise. Caused by Brownian motion, random movement, in the wires it still exists when no current is flowing [Johnson 1928]. In a MOSFET operated in source follower mode such noise is present at the source terminal. At low frequencies there can be additional flicker noise due to the trapping and release of electrons in the channel, also known as  $1/f$  noise due to its spectral distribution which is proportional to  $1/f^\alpha$ , where  $\alpha$  is close to unity [Brophy 1969].  $1/f$  noise decreases by a factor 3.16 for each decade increase in frequency

[Janesick 2001]. The result is illustrated in Figure 2.26, where the mean voltage is denoted by the dashed line and the effect of transistor noise by the solid line.

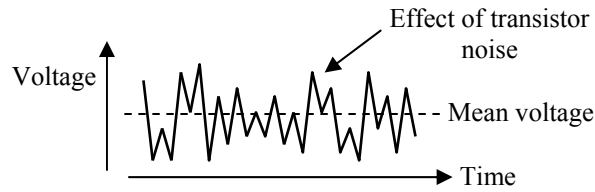


**Figure 2.26:** Illustration of the effect of transistor noise on a mean voltage

### 2.5.6 Reset ( $kT/C$ ) Noise

A feature of resetting the output node voltage ( $V_{rd}$ ) is that Johnson noise associated with the channel resistance of the reset transistor is sampled and held on the node capacitance  $C_F$ . This results in an output-to-output fluctuation in the reset level [Nakamura 2005]. Characterised by the reset noise  $\sigma_{reset}$  (e<sup>-</sup> r.m.s.), given by:

$$\sigma_{reset} = \frac{\sqrt{kTC_F}}{q} \tag{2.33}$$

the effect is illustrated in Figure 2.27. Ideally the reset operation would set the voltage on the output node to exactly  $V_{rd}$ . The noise can be largely removed with the use of ‘correlated double sampling’ discussed in Section 2.5.9.

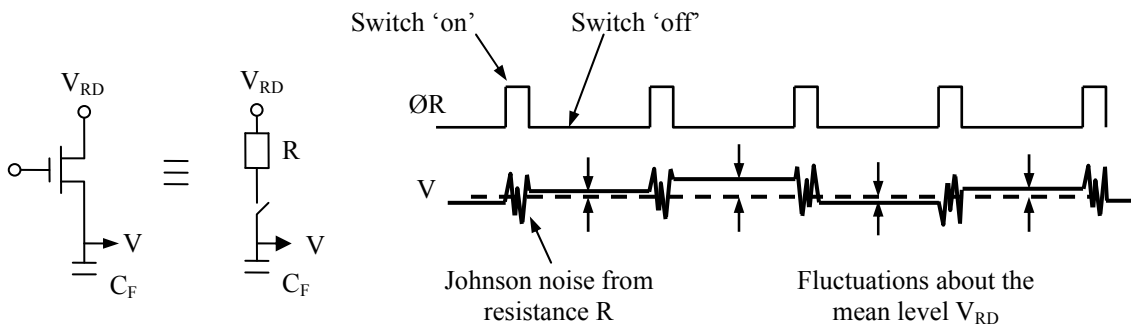


**Figure 2.27:** Illustration of the effect of reset noise arising from Johnson noise within the reset FET [Burt 2006]

### 2.5.7 Transfer Noise

Trap sites are responsible for the loss of charge from the charge packet during clocking, as a result of electron capture and then emission, resulting in an increase in the CTI. The mean electron capture time  $\tau_c$  is strongly dependant on the effective cross-sectional area  $\sigma$  (cm<sup>2</sup>), while the mean

electron emission time  $\tau_e$  is dependant on the trap energy  $E_t$  (eV) and the temperature  $T$  (K). These are given by:

$$\tau_c = \frac{1}{\sigma v_{th} N_t} \quad (2.34)$$

$$\tau_e = \frac{e^{E_t/kT}}{\sigma v_{th} N_t} \quad (2.35)$$

Under steady state conditions the fraction of traps filled  $\Gamma$  in a time  $\Delta t$  is given by (Bond 1996):

$$\Gamma = \frac{1}{\left(1 + \frac{\tau_c}{\tau_e}\right)} \left[ 1 - e^{-\left(\frac{\Delta t}{\tau_c}\right)} e^{-\left(\frac{\Delta t}{\tau_e}\right)} \right] \quad (2.36)$$

The effective lifetime of an electron is  $\sim 10$  to  $100$  ns while the release time is dependent on the trap species and can be of order a few tens of nanoseconds to seconds. If the release time is slow in comparison to the pixel transfer time, the charge will be released in the following pixel, causing smearing and split events.

The transfer noise,  $\sigma_{CTI}$  ( $e^-$ ), generated each time a transfer from one pixel to another takes place, is related to the CTI by:

$$\sigma_{CTI} = \sqrt{CTI X (e^-) n_t} \quad (2.37)$$

where decreasing the signal and the number of transfers will reduce the transfer noise. A typical CCD has a CTI of  $1 \times 10^{-7}$ , therefore Mn-K $\alpha$  X-ray events travelling through 2000 transfers would add  $\sim 0.6 e^-$  r.m.s. to the total noise.

### 2.5.8 Transient Noise

The unwanted signal produced through the interaction of charged particles within the silicon can be a source of transient noise. As any charged particle travels through the silicon, it creates electron-hole pairs along its path of travel ( $\sim 80$  e-h pairs per  $\mu\text{m}$ ), and if it stops within the silicon it can create a large number of additional e-h pairs. X-ray photons typically create between 350 to 4,000 e-h pairs, while a 1 MeV proton will create  $\sim 274,000$  e-h pairs and a 3 MeV alpha particle will create  $\sim 820,000$  e-h pairs. The large amount of charge created by high energy charged particles would thus obscure any X-ray events, and is discussed further in Section 3.14 describing cosmic rays.

### 2.5.9 Read Noise, System Noise and Signal Processing

The complete imaging system comprises the CCD, the drive electronics (i.e. drive pulse generators and dc bias supplies) and the signal processing electronics. All the electronics external to the CCD is located within a ‘drive box’. The total noise consists of the ‘read noise’, arising from the CCD, and the ‘system noise’ arising from within the drive box. The function of the drive box is to pass the voltage signal from the CCD through an analogue to digital converter (ADC) to produce a digitised pixel value for event processing. Prior to entering the ADC the voltage signal requires further amplification. Noise will also be amplified unless it is removed before the signal is amplified. Reset noise, Johnson noise, and flicker noise can be effectively removed using correlated double sampling (CDS).

The function of the signal processing is firstly to minimise the noise and then arrange the signal in a form appropriate for performing analogue-to-digital conversion. The output signal consists of a voltage change produced as a result of X-ray interactions, with superimposed noise and clock feed-through  $V_{FT}$ . The clock feed-through is given by:

$$V_{FT} = \frac{C_{GS}}{C_S + C_{GS}} V_C \quad (2.38)$$

where  $C_S$  is the sense node capacitance (F),  $C_{GS}$  is the gate to source capacitance of the reset MOSFET (F) and  $V_C$  is the clock voltage (V). The output signal of a CCD54 is shown in Figure 2.28. The feed through resulting from the three image clocks is bordered by  $V_{rd}$ , the corresponding clock pulses are shown in Figure 2.28 over the same time scale.

The basic CDS circuit is shown in Figure 2.29, showing the four component parts: (1) preamplifier, (2) two sample and hold amplifiers, (3) a difference amplifier, and (4) the analogue-to-digital converter (ADC) outputting the results in digital number (DN) form. The preamplifier provides an initial low-noise voltage gain before the reference and data signal levels are recorded using the sample and hold amplifiers. To ensure the sampled signals do not contain any clock feed through, delays  $Int^-$  and  $Int^+$  are applied before the reference and data signal voltages are sampled, as illustrated in Figure 2.28. The reference and signal voltages are averaged over a finite time ( $Int$  time). The signal charge is the difference between both levels, found using the difference amplifier [Hopkinson and Lumb 1982].

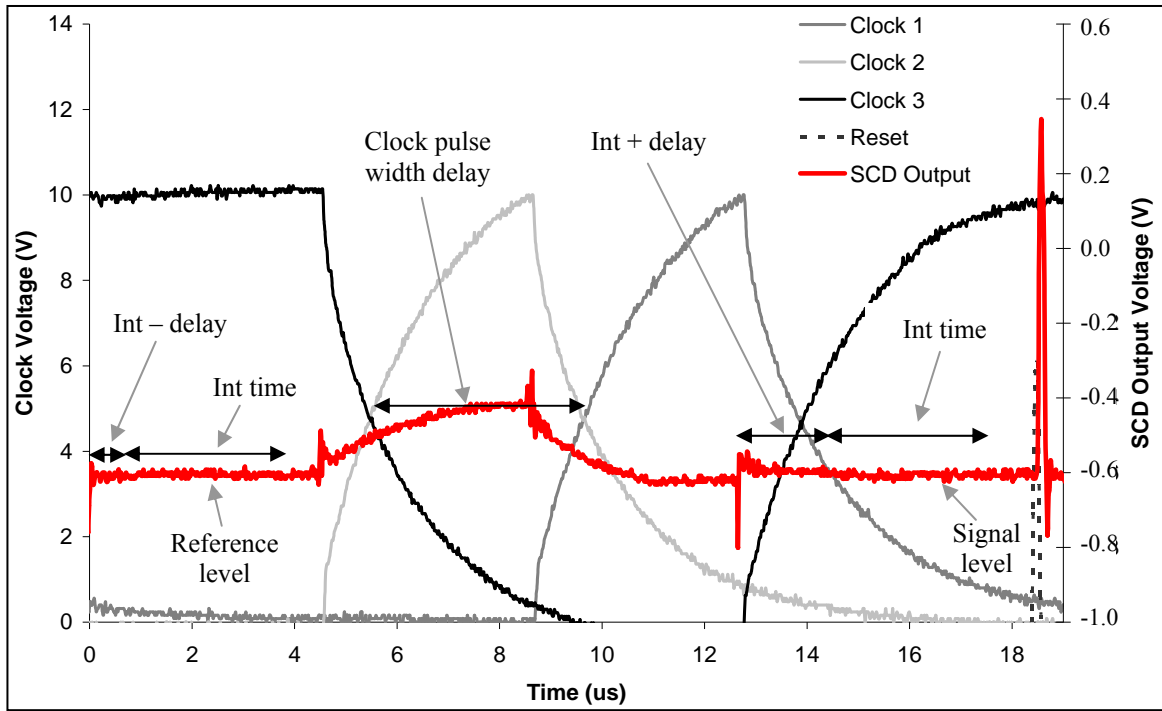


**Figure 2.28:** The CCD54 output trace before entering the drive box and the clock waveform used to drive the device

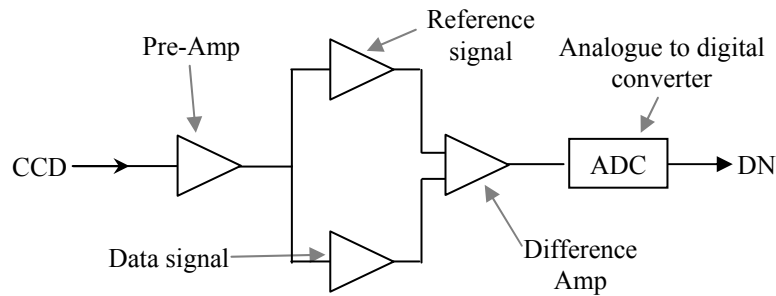


**Figure 2.29:** Basic CDS circuit

## 2.6 X-ray Detection, Measurement and Analysis

To be detected a photon has to travel through the electrode structure shown in Figure 2.16 and interact within the depletion or diffusion region of the bulk silicon. Electrons released in the depletion region experience a strong electric field resulting in direct collection, those electrons released in the lower bulk silicon can be detected if they diffuse to the edge of the depletion region. The process of charge generation and collection is illustrated in Figure 2.30 showing the effect of different X-ray photon energies, where low energy photons have more chance to interact near the surface, while higher energy photons penetrate deeper into the silicon, leading to the charge spreading discussed in Section 2.6.2.

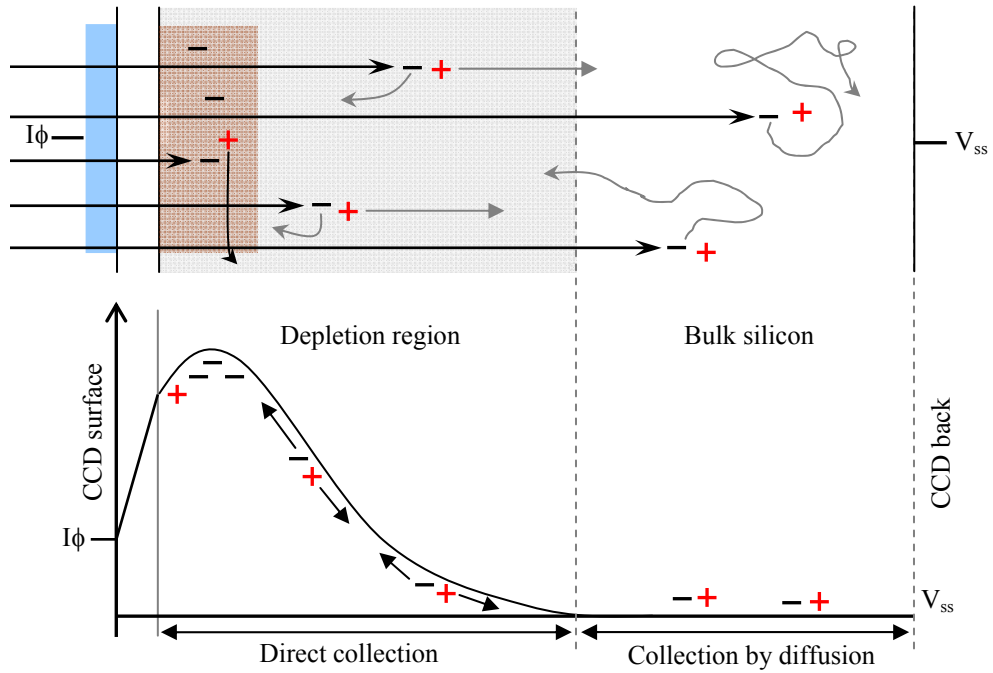


**Figure 2.30:** Illustration of charge generation and collection for a front side illuminated device

### 2.6.1 Interaction of X-rays with Matter

The three most important interactions of photons with matter are the photoelectric effect, Compton scattering and pair production [Krane 1988]. Pair production occurs when the photon interacts with the electric field surrounding a nucleus creating an electron hole pair. This process only occurs above the threshold energy of  $2m_0c^2$  (1.022 MeV). In Compton scattering the energy of the incident photon is split between the recoil electron and the reduced energy photon, allowing the detector to detect a partial energy deposition in a proportion depending on the angle of scatter. It is dominant for photons with an energy range of about 200 keV to 1.5 MeV. The photoelectric effect describes the process when the incident photon transfers all of its energy into a bound electron ejecting it from the lattice atom; it is dominant for photons of energies  $\leq 200$  keV. The photoelectric effect is the dominant process for the interaction of X-rays illustrated in Figure 2.31.

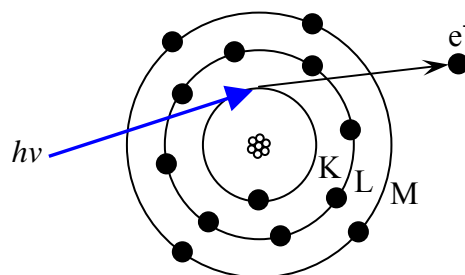


**Figure 2.31:** Illustration of the photoelectric effect showing the atomic K, L and M shells

The number of e-h pairs that an incident X-ray photon will create is dependant on the photon energy and the band-gap, which is described by Equation 2.6. The actual energy required,  $\omega$  is greater due to the production of phonons, where the energy is transferred through optic lattice vibrations, which is observed as heat [Lifshin 1999]. At 173 K  $\omega$  is 3.68 eV and at room temperature it is 3.65 eV [Bertolini and Coche 1968], the number of electron hole pairs produced,  $n_{eh}$ , is given by:

$$n_{eh} = \frac{E_{\gamma}}{\omega} \quad (2.39)$$

where  $E_{\gamma}$  is the energy of an incident X-ray photon (eV).

### 2.6.1.1 X-ray Photon Shot Noise (Fano Noise)

If all the energy of the incident X-ray photon produced e-h pairs there would be no statistical variation in the amount of charge generated, however, some energy is transferred to the silicon lattice (thermal). The uncertainty is described by the Fano factor [Fano 1947] and is dependant on the detector material. The Fano factor  $F_{Si}$  of silicon is taken to be 0.115 (Alig *et al.* 1980). Shot noise arises from the statistical uncertainties involved in the creation of e-h pairs in the silicon. The photon shot noise  $\sigma_{\text{photon shot}}$  (e<sup>-</sup> r.m.s.) is found by:

$$\sigma_{Fano} = \sqrt{F_{Si} n_{eh}} = \sqrt{\frac{F_{Si} E_{\gamma}}{\omega}} \quad (2.40)$$

Thus, if a system is described as being Fano noise limited,  $\sigma_{Fano}$  is larger than other noise sources, e.g. that of the output amplifier.

### 2.6.1.2 X-ray Absorption

The rate of absorption is measured using the linear absorption coefficient  $\mu_L$  (cm<sup>-1</sup>) which is dependant on the density and atomic number of the material in which the X-ray photon is travelling. The intensity of X-ray photons  $I_0$  after travelling through a material is given by:

$$I = I_0 e^{-\mu_L x} \quad (2.41)$$

where  $I$  is the initial intensity, and  $x$  is the thickness of the material. The mass absorption coefficient  $\mu_M$  (cm<sup>2</sup>.g<sup>-1</sup>), where  $\mu_M = \mu_L / \text{density}$ , removes the dependence on material density. The mass absorption coefficient of silicon is displayed in Figure 2.32 from 1 keV to 10 keV, produced using tables in the National Institute of Standards and Technology (NIST) database extracted using the XCOM program. The sharp increase in the coefficient occurs at the minimum energy required for the excitation of a particular electron shell, known as the absorption edge which for silicon is at

1.84 keV. X-rays with a low mass absorption coefficient travel deeper into silicon and will be more likely to be detected over multiple electrode rows, resulting in split events. A useful term is the attenuation length  $x_{Aten}$  or mean free path, this is the depth at which the intensity of X-rays has reduced to 37 % of  $I$ , given by:

$$x_{Aten} = \frac{1}{\mu_L} = \frac{1}{\mu_M \rho} \quad (2.42)$$

where  $\rho$  is the density.

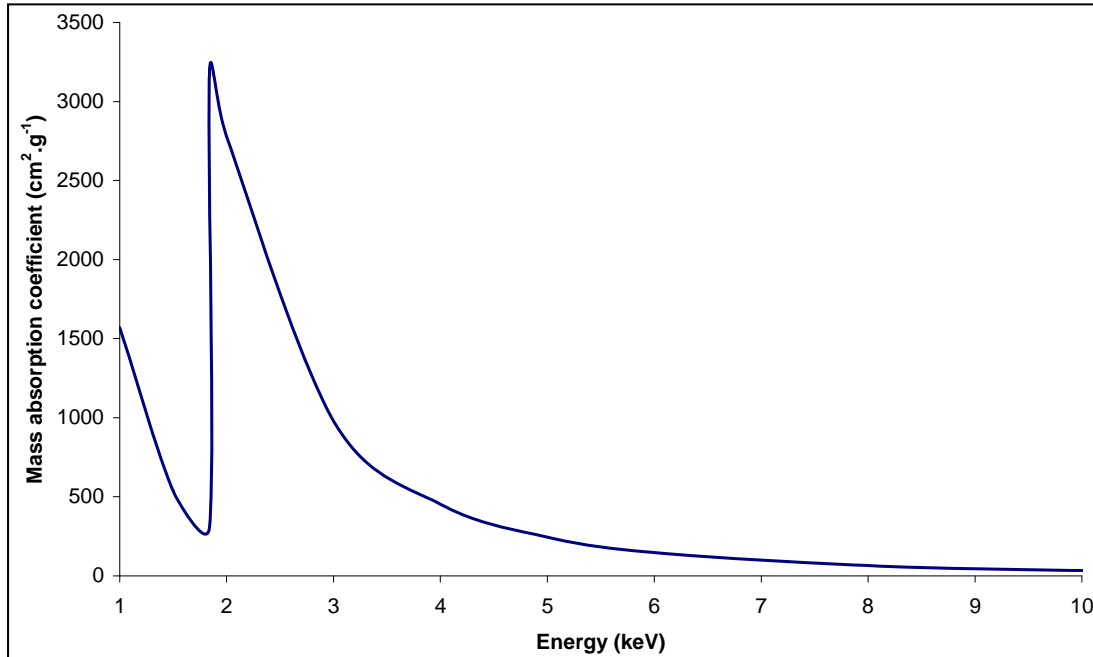


**Figure 2.32:** Mass absorption coefficient of silicon showing the K-edge at 1.84 keV

### 2.6.2 Measurement and Analysis

The first stage of event analysis is to histogram the digitised pixel values to show the relative frequency. An example of the resulting spectrum is given in Figure 2.33. Samples where an X-ray photon was incident are clearly identified above the noise peak. The spectrum in Figure 2.33 is composed of Mn-K $\alpha$  and Mn-K $\beta$  X-rays photons from a  $^{55}\text{Fe}$  source. The other peaks are as a result of the Mn-K $\alpha$  escape peak, the result of XRF taking place within the CCD, and Mn-K $\alpha$  photons detected as split events over two samples. An X-ray photon with energy greater than the absorption edge of a specific shell can eject an electron from the atom, resulting in the production of a characteristic X-ray as described in Section 2.2.1. The silicon K-edge is at 1.84 keV, therefore any incident photons above this energy can cause the silicon to fluoresce, resulting in a Si-K $\alpha$  X-ray and a photon with a reduced energy, called the ‘escape photon’ detected in the escape peak. The

ability of a detector to define X-ray photons of different energies is measured by the energy resolution.

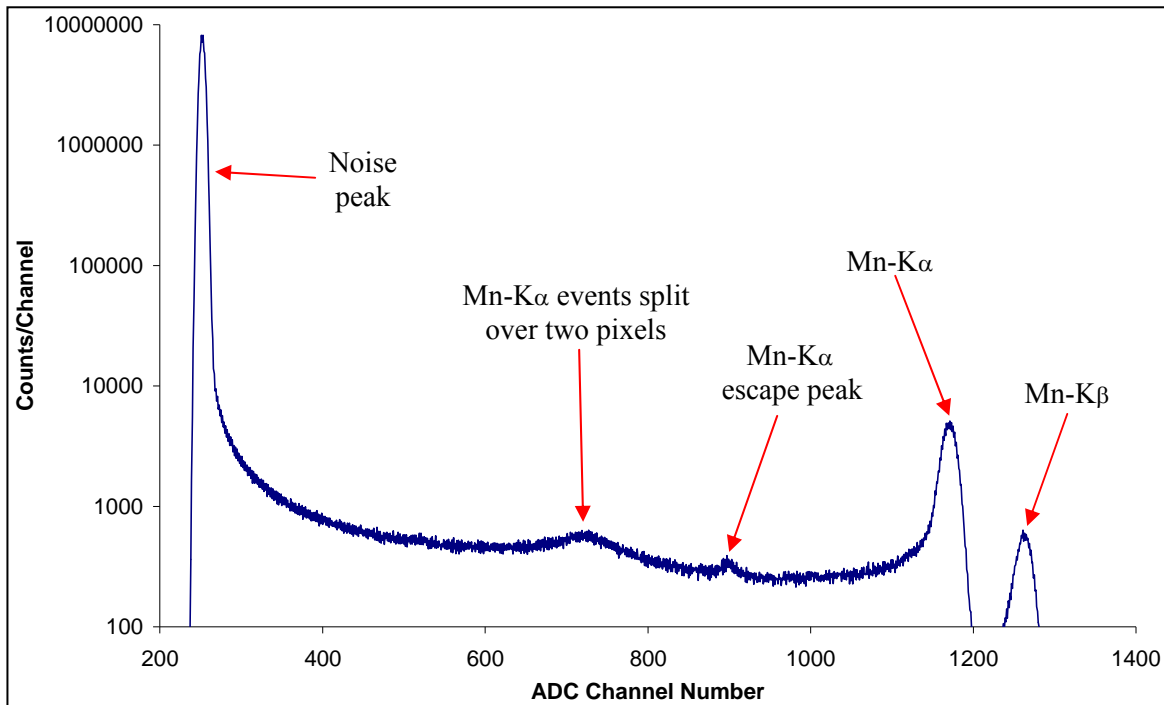


**Figure 2.33:** Raw spectrum produced as a result of Mn-K $\alpha$  and Mn-K $\beta$  X-ray photons, illustrating the noise peak, split events and the Mn-K $\alpha$  escape peak

To provide an energy calibration, the noise peak location and a known X-ray peak location, e.g. Mn-K $\alpha$ , are found and assigned energy values of 0 eV and 5,898 eV respectively, providing an energy calibration in eV per digital number or analogue to digital conversion (ADC) number. The calibrated spectrum is illustrated in Figure 2.34. The next stage of event processing is to remove split events which form the bulk of the continuum between the noise peak and the X-ray photo peaks. This is achieved by setting a threshold condition to remove all samples except those containing isolated events, where the charge packet deposited by the X-ray photon was detected within a single sample. The isolated spectrum is shown in Figure 2.34, clearly showing the Mn-K $\alpha$  and Mn-K $\beta$  escape peaks, and the resulting Si-K $\alpha$  photo peak. Events can also be detected within the same pixel, pile up, producing a peak at two times the energy, 11,796 keV for Mn-K $\alpha$ . These can be accounted for a simple spectrum, or a target of known elemental composition, however, complicated spectrum may result in pile up peaks being obscured. Avoiding pile up limits the detectors maximum count rate, faster read-out allows a higher maximum count rate. Event processing techniques used in the analysis of SCD data are discussed in detail in Section 4.4.

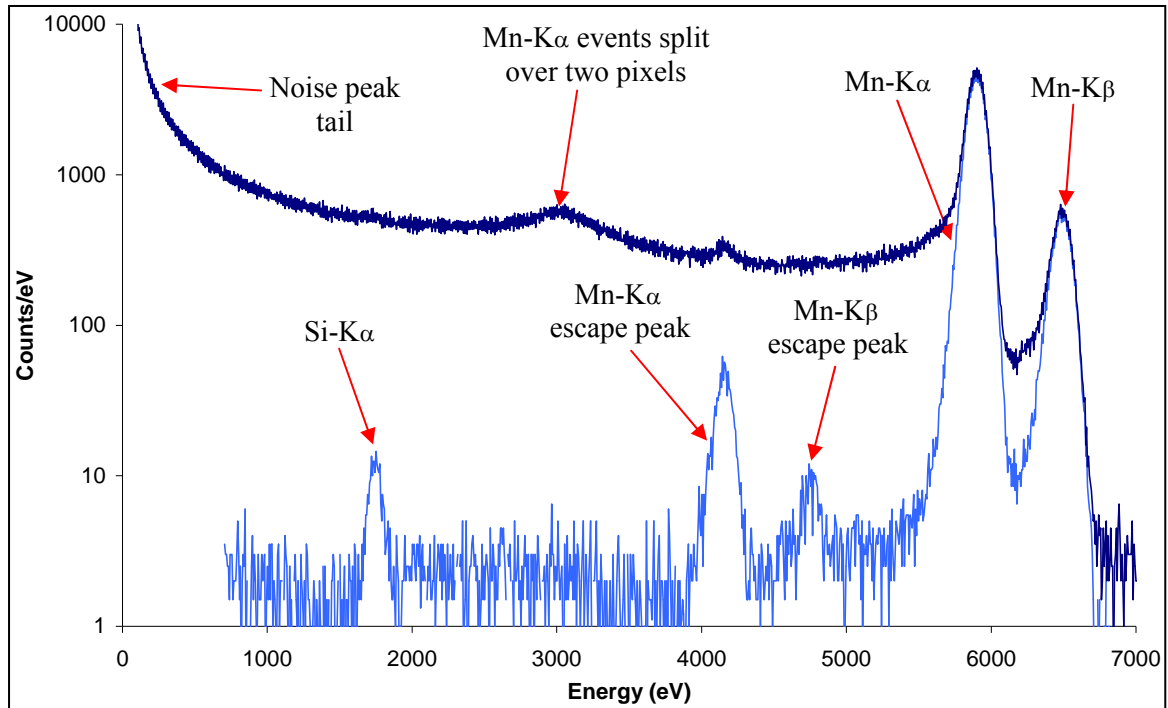


**Figure 2.34:** Calibrated spectrum of all and isolated events produced as a result of Mn-K $\alpha$  and Mn-K $\beta$  X-ray photons, illustrating the noise peak, split events and the Mn-K $\alpha$  escape peak

### 2.6.2.1 Spatial Resolution

The spatial resolution is a measure of charge spreading from one pixel to another, both as a result of poor CTE and charge spreading from X-ray interactions within the bulk silicon, measured by the modulation transfer function (MTF). An X-ray photon interaction is more likely to take place within the epitaxial layer, if the interaction takes place near the sample to sample boundary the charge will be spread over more than one sample. This results in energy spread over a number of read-out cycles, as demonstrated in Figure 2.35a which shows an X-ray detected with an ADC value of 50 as an isolated event (1) and as split events (2 through 5). Due to the read-out mechanism of the SCD the event patterns will be different to that observed in a conventional CCD, illustrated in Figure 2.35a. The resulting SCD read-out from the events in Figure 2.35a are shown in Figure 2.35b. It is unlikely that events will be spread over more than seven pixels on read-out. Also depending on the threshold selected to identify isolated events it could be possible for an event detected as a split event to be recorded as an isolated event, as shown in Figure 2.35(4).

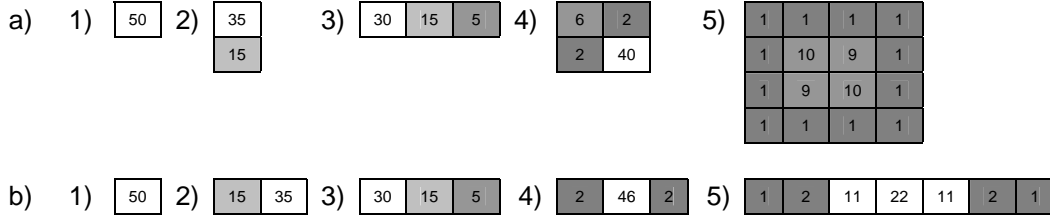


**Figure 2.35:** Pixel array showing possible X-ray interactions within the imaging area of a CCD and SCD (a) and the resulting SCD read-out (b)

### 2.6.2.2 Energy Resolution

The energy resolution of a CCD is measured as the full-width at half maximum (FWHM) calculated by:

$$FWHM = 2.35\sigma_x \quad (2.43)$$

where  $\sigma_x$  is the standard deviation of the X-ray peak. It is clear that higher energy X-ray photons have a greater FWHM, as a result of greater charge spreading. The Fano limited performance can be found using:

$$Fano\ Limited\ FWHM = 2.35\omega\sqrt{n_T^2 + F_{Si}\frac{E_\gamma}{\omega}} \quad (2.44)$$

where  $n_T$  is the total noise (read noise + system noise). A low energy resolution will lead to some energy peaks merging together, for example magnesium (1,254 eV), aluminium (1,487 eV), and silicon (1,740 eV).

### 2.6.2.3 Quantum Efficiency

The sensitivity of a CCD to incident photons is measured through the device's quantum efficiency (QE). This is the percentage of photons that generate useful signal. The QE is dependent on the active thickness of the silicon and the transmission of photons through the electrodes. A large potential well will collect charge more efficiently over a greater energy range than a small one. To avoid the problem of transmission through the surface electrodes the device can be back thinned and the back placed incident to the incoming photons, known as 'back illuminated'.

The theoretical depletion depth,  $x_d$ , in  $\mu\text{m}$  formed by the applied gate voltage is given by [Howes & Morgan 1979]:

$$x_d = 10000\sqrt{\frac{2\epsilon_{Si}V_T}{qN_A}} \quad (2.45)$$

where  $\epsilon_{Si}$  is the permittivity of silicon ( $1.03 \times 10^{-12}$  C.V<sup>-1</sup>.cm<sup>-1</sup>),  $q$  is the electronic charge ( $1.602 \times 10^{-19}$  C),  $N_A$  is the silicon acceptor dopant concentration (typically  $4.0 \times 10^{12}$  cm<sup>-3</sup> for X-ray detection), and  $V_T$  is the channel potential, given by:

$$V_T = V_g + \Phi_{cho} - V_{ss} \quad (2.46)$$

where  $\phi_{cho}$  is the inbuilt channel potential, typically between 10 V and 12 V for e2v devices (taken to be 11 V). The clock operation used with the CCD54 always holds one electrode high as shown in Figure 2.28, assuming on average one will be held at  $\sim 5$  V with the other at 0 V, each accounting for  $\sim 33\%$  of the pixel area, the  $V_{pot}$  will equal  $16 \text{ V} - V_{ss}$  (10 V for the CCD54). Based on these assumptions the theoretical depletion depth is found to be 44.0  $\mu\text{m}$ , some percentage of the pixel is taken up by the channel stop structure therefore the actual depth will be lower than calculated.

The photons have to travel through the gate structure, as illustrated in Figure 2.16, there is a small chance that a photon will interact within the SiO<sub>2</sub>, the Si electrode and the Si<sub>3</sub>N<sub>4</sub> layers illustrated in Figure 2.14 and not be detected. The sensitivity for a front side illuminated CCD can be estimated by [Janesick 2001]:

$$QE = R_{REF} e^{\frac{-x_{poly}}{l_{poly}}} e^{\frac{-x_{SiO_2}}{l_{SiO_2}}} e^{\frac{-x_{Si_3N_4}}{l_{Si_3N_4}}} \left( 1 - e^{\frac{-x_{Si}}{L_{Si}}} \right) \quad (2.47)$$

where  $R_{REF}$  is the transmission coefficient of silicon (assumed to be 100%),  $x_{poly}$  is the electrode thickness ( $\mu\text{m}$ ),  $x_{SiO_2}$  is the silicon dioxide thickness ( $\mu\text{m}$ ),  $x_{Si_3N_4}$  is the silicon nitride thickness ( $\mu\text{m}$ ),  $x_{Si}$  is the depletion depth ( $\mu\text{m}$ ),  $l_{poly}$ ,  $l_{SiO_2}$ ,  $l_{Si_3N_4}$  and  $l_{Si}$  are the respective attenuation lengths ( $\mu\text{m}$ ) assuming photons are incident at 90° to the surface of the device. The predicted QE curve for the CCD54 is shown in Figure 2.37, with a 0.835  $\mu\text{m}$  SiO<sub>2</sub> layer, a 0.085  $\mu\text{m}$  Si<sub>3</sub>N<sub>4</sub> layer, a 0.835  $\mu\text{m}$  polysilicon electrode and depletion depths of 12.0  $\mu\text{m}$  and 44.0  $\mu\text{m}$ . The sharp reduction in QE as a result of the oxygen and silicon absorption K-edges is clear, as marked in Figure 2.37. When making comparisons between the QE of different devices the value at 5,898 eV is used, corresponding to Mn-K $\alpha$  X-rays.

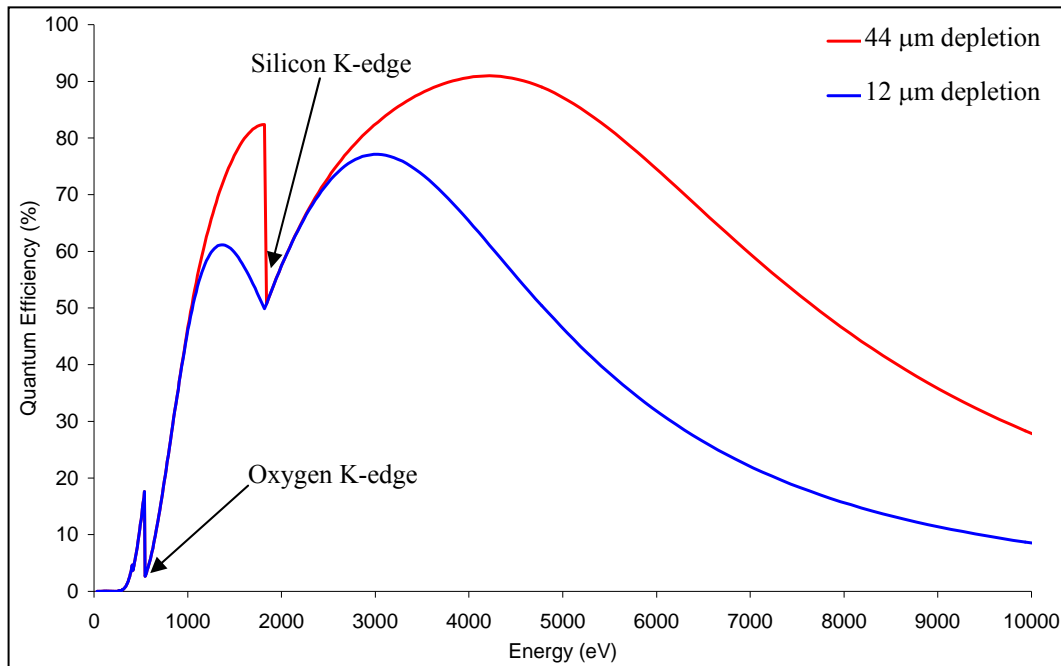


**Figure 2.37:** Quantum efficiency curve of the CCD54 with an active depth of 12  $\mu\text{m}$  and 44  $\mu\text{m}$

## 2.7 Other Semiconductor Detectors

This section describes four other semiconductor detectors available for X-ray detection, describing their basic operation, their advantages and disadvantages. The four detectors are the silicon PIN diode, the silicon lithium (Si(Li)) detector, the silicon drift detector (SDD) and the complementary metal oxide semiconductor (CMOS) active pixel sensor (APS). A brief comparison between the Si PIN, Si(Li), SDD and the CCD54 is performed in Section 7.5.

### 2.7.1 Silicon PIN Diode

The silicon PIN diode is created by taking a wafer of intrinsically pure silicon and then diffusing a p-type region on one side and an n-type region on the other. The intrinsic material reduces the overall device capacitance [Webster 1999] and forms a depletion region between the p-type and n-type silicon. The depletion region width increases with the application of a reverse bias,  $\sim 100$  V for X-ray photons. Charge collected within the Si PIN is transferred to a charge sensitive preamplifier where it undergoes charge to voltage conversion. The voltage signal is then passed on to a multi-channel analyser (MCA) for further amplification and analogue to digital conversion. The Si PIN diode can provide a high count rate, with a reasonable energy resolution (145 to 230 eV at Mn- $K\alpha$ ). The Mars Pathfinder Sojourner Rover used an AMP TEK XR-100CR Si PIN diode in its alpha particle X-Ray spectrometer (APXS) to analyse rock samples, an example spectrum is illustrated in Figure 2.38, with an energy resolution of 254 eV at Fe- $K\alpha$  (6,403 eV) [Rieder *et al.* 1997].

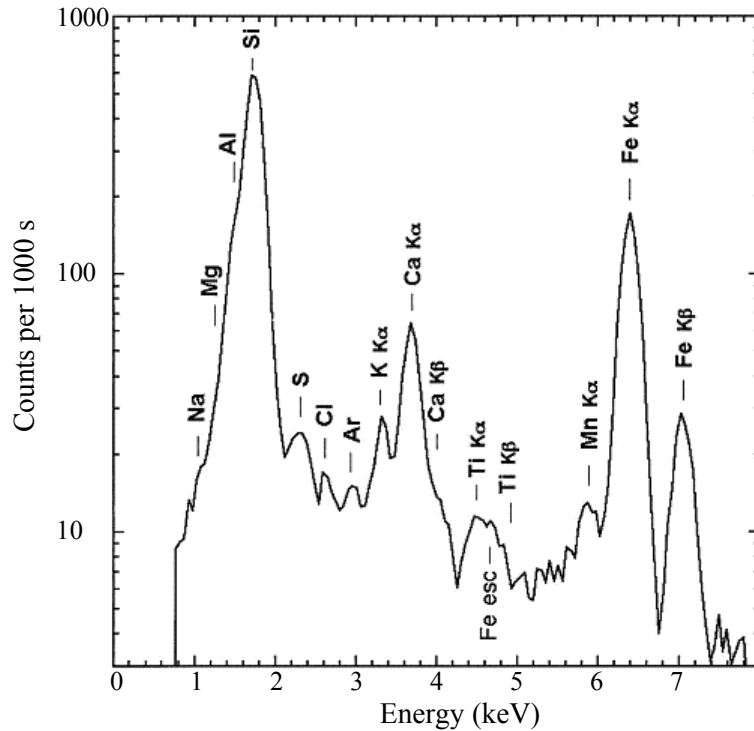


**Figure 2.38:** Spectrum collected by the APXS on the Sojourner Rover using a Si PIN diode, the spectrum is from rock A-3, Barnacle Bill [Rieder *et al.* 1997]

## 2.7.2 Silicon Lithium Detector

The Si(Li) detector is based on the same operation principles of the Si PIN diode, with a lithium intrinsic layer forming a PIN junction. The intrinsic region is formed using the process of lithium drifting first demonstrated in the 1950s and early 1960s [Pell 1960] using lithium ions infused into p-type silicon to form a depleted Si(Li) layer, an n-type layer, and a p-type layer, as illustrated in Figure 2.39. The resulting crystal can be ~10 mm thick [Beckhoff *et al.* 2006]. A potential of ~500 to 1000 V is required to create the depletion region capable of detecting X-rays of energies up to ~40 keV [Beckhoff *et al.* 2006]. The e2v Sirius Si(Li) has a ~4.5 mm depletion region. The large depletion region provides an excellent QE and very good energy resolution, the detector volume requires the crystal to be cooled, with cooling often provided using liquid nitrogen. The liquid nitrogen is held in a dewar, making the detector system bulky and not portable. Such a detector was used in the QE calibration described in Chapter 4.

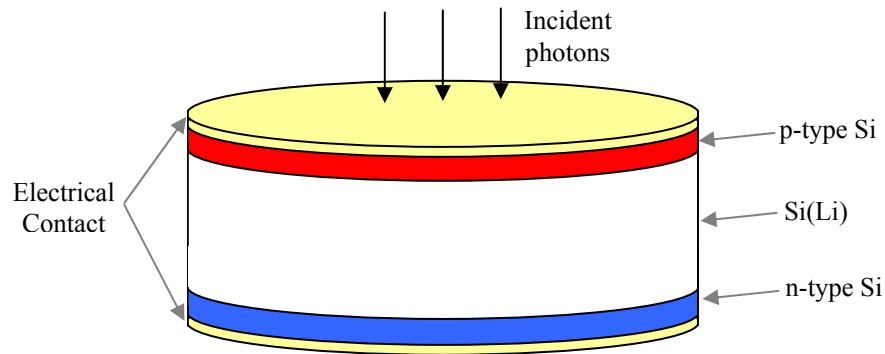


**Figure 2.39:** Silicon Lithium Detector

### 2.7.3 Silicon Drift Detector

In the early 1980s the silicon drift detector (SDD) was conceived by Gatti and Rehak, introducing the concept of lateral charge collection with respect to the electrodes [Gatti and Rehak 1984]. The reduction in surface area of the electrical contact to the n-type silicon anode reduces the capacitance; the capacitance is proportional to the size of the electrode and not the detector. Charge collection could now be performed using a much larger area than previously possible, with an excellent responsivity. The detector consists of p-type silicon rings, as illustrated in Figure 2.40, biased with a decreasing potential to ensure the rapid collection of charge deposited within the detector at the anode. The detector is depleted from both sides using the front concentric rings and the p-type silicon back of the device, providing a large volume for charge collection. The cooling required can be provided by a thermo electric cooler making the SDD a very versatile device for science use inside and outside of the laboratory.

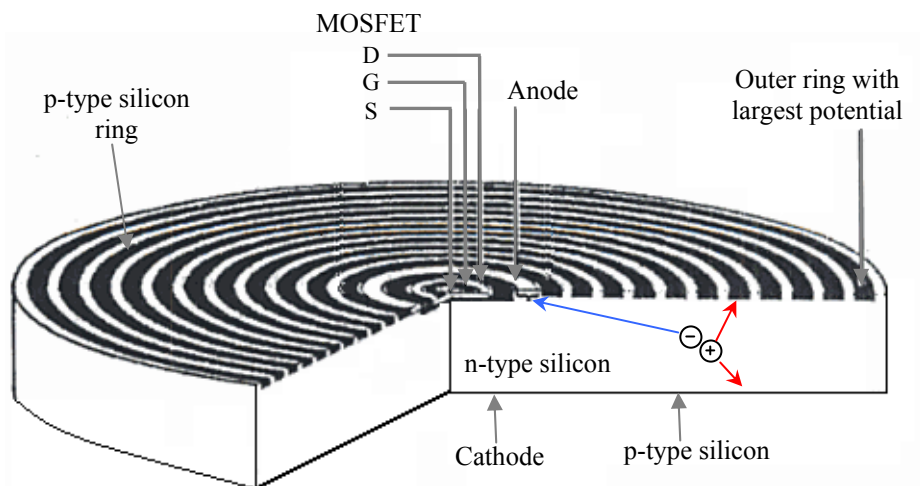


**Figure 2.40:** Schematic of a Silicon Drift Detector [adapted from Lechner *et al.* 2004]

### 2.7.4 CMOS APS

The Complementary metal-oxide-semiconductor (CMOS) active pixel sensor (APS) was developed at JPL in 1992 [Fossum 1998] the idea having first been conceived in 1968 [Noble 1968]. The APS devices were hailed as a considerable leap beyond CCDs, providing a small size, low cost and low powered alternative to the CCD. It is the read-out mechanism that is the greatest difference between the CCD, as a result of the charge to voltage conversion taking place within the pixel, as illustrated in Figure 2.41. Each pixel contains two transistors to perform the function provided by the output circuit illustrated in Figure 2.13, and an extra switch transistor to select which pixels should be read-out. The shift registers are connected to the read-out transistors and allow the pixels to be read-out to the column amplifiers, where the signal can be read-out as an analogue output or processed in an on-chip ADC to provide a digital output. It would be impractical to add this feature to a CCD as it would require extensive redevelopment of an already expensive production process. The problem of CTE is removed as each pixel is accessed directly. It is however replaced by an increased amount of reset and transistor noise due to the difference in signal amplification from pixel to pixel.

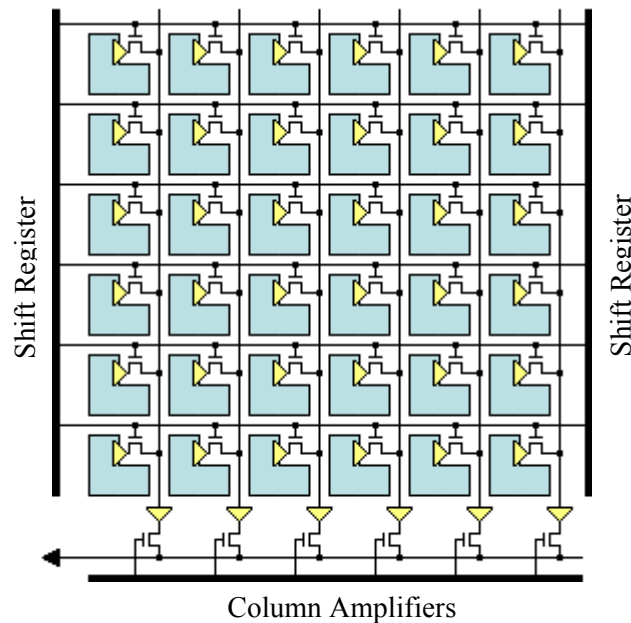


**Figure 2.41:** Schematic of a CMOS APS

## 2.8 Chapter Summary

This chapter has described some of the physics behind X-ray formation and detection within a number of different solid state detectors. The focus was on the CCD, in particular the SCD CCD54, describing its manufacture and the physics governing charge storage, transport and read-out. The principal components, structure and operation of the CCD and SCD are all described. The sources of noise and their effects on device performance and methods for minimising them have been

discussed, as has the measure of CCD performance in terms of the spatial and energy resolution and QE. The SCD architecture and operational mode were also described, these lead to a number of advantages over a conventional CCD:

- The **electrode design** allows fast read-out ( $\sim 100 \text{ kHz}\cdot\text{sample}^{-1}$ ) allowing for a **large charge collection area**, while minimising dark current generation. The SDD and Si PIN detector described in Chapter 7 with comparable energy resolution performance have  $\sim 70\%$  less charge collection area.
- The structure allows **continuous read-out** to be used, allowing the device to use IMO. **Suppressing the surface generated dark current**, and avoiding dark current generated during the integration period of a conventional CCD. It also allows the device to be **operated at a higher temperature** than a conventional CCD, typically operated at around  $-110 \text{ }^\circ\text{C}$ . A conventional CCD can be operated using continuous read-out.
- The avoidance of an image integration period allows the device to be used with a **higher incident X-ray flux** than conventional operation. During an integration period incident X-ray photons could obscure previously detected events saturating the detector.
- The **large channel stop pitch of  $25 \text{ }\mu\text{m}$**  allows the charge generated by an incident X-ray photon to be detected within one sample. A device with the same charge collection area and a channel stop pitch of  $12.5 \text{ }\mu\text{m}$  would take twice as long to read-out, requiring twice as many charge transfers increasing the susceptibility to CTI.
- The **simplified design** of the SCD only requires one set of clocks, reducing the complexity of drive electronics and **reducing the overall power consumption**.

The next Chapter describes the space radiation environment and the resulting effects on device performance.

## Chapter 3: The Space Environment and its Effects on CCDs

### 3.1 Introduction

It is important to understand how the performance of a CCD will change over the course of a space mission. The radiation exposure needs to be understood for the instrument's entire life, the exposure depending on the orbit, and mission duration. This understanding allows adequate shielding and appropriate technologies to be selected. There are two different classifications of radiation, 'non-ionising' which includes the electromagnetic spectrum and 'ionising'. Ionising radiation includes alpha particles, beta particles, and protons which cause direct ionisation and neutrons,  $\gamma$ -rays and X-rays which cause indirect ionisation. In space, the main source of damage from radiation is due to protons. It should also be noted that damage can occur due to dust, micrometeoroids and space debris.

### 3.2 The Space Radiation Environment

This section will cover what forms the space radiation environment, from the Earth's radiation belts to cosmic rays which may have travelled hundreds of light years before entering our solar system. The environment can be classified into two types, the 'trapped' environment and the 'non-trapped' or 'transiting' environment [Stassinopoulos and Raymond 1988]. The table below gives examples of some spacecraft orbits and highlights the main source of radiation exposure that will affect them. In the case of Chandrayaan-1 the main source of radiation damage is from solar protons during its two years at the Moon, with a smaller dose from its time spent within the Earth's radiation belts.

Orbit Type	Description	Main source	Other sources
Low Earth Orbit (LEO)	Altitude below 2,000 km	Trapped	
Sun Synchronous Orbit (SSO)	Altitude 700 to 800 km	Trapped	
Highly Elliptical Orbit (HEO)	Low altitude perigee and high altitude apogee	Trapped	Non-Trapped
Geocentric Earth Orbit (GEO)	Altitude 35,790 km	Non-Trapped	Trapped
L2	Transfer orbit to L2 at an altitude of 1.5 million km	Non-Trapped	Trapped
Lunar	Transfer orbit to the Moon	Non-Trapped	Trapped
Inter-Planetary	Transfer orbit, interplanetary travel, orbit at final destination	Non-Trapped	Trapped and Trapped at destination

**Table 3.1:** Typical orbits with a brief description and the main and secondary sources of radiation

The orbital paths are defined using parameters known as Keplerian elements, illustrated in Figure 3.1 which shows the orbital path of a spacecraft around the Earth. The apogee and perigee represent the furthest and closest approach of the orbiting body to the Earth respectively, described by the eccentricity, a constant defining the shape of the orbit (circular = 0), and the semi-major axis, a constant describing the orbit size. The inclination,  $I$ , is the angle between the orbital plane at the ascending node and the equatorial plane also called the line of nodes. The right ascension of the ascending node,  $\Omega$ , is the angle between the ascending node which defines the point where the spacecraft crosses from the southern to northern hemisphere and the direction of vernal equinox. The vernal equinox is a fixed point, being the location of the ascending node of the Sun's orbit which occurs on the first day of spring. The constellation of Aries provides the same angle of measurement. The argument of perigee,  $\omega$ , is the angle between the ascending node and the perigee. The true anomaly,  $\nu$ , is the angle from the perigee direction to the satellite direction.

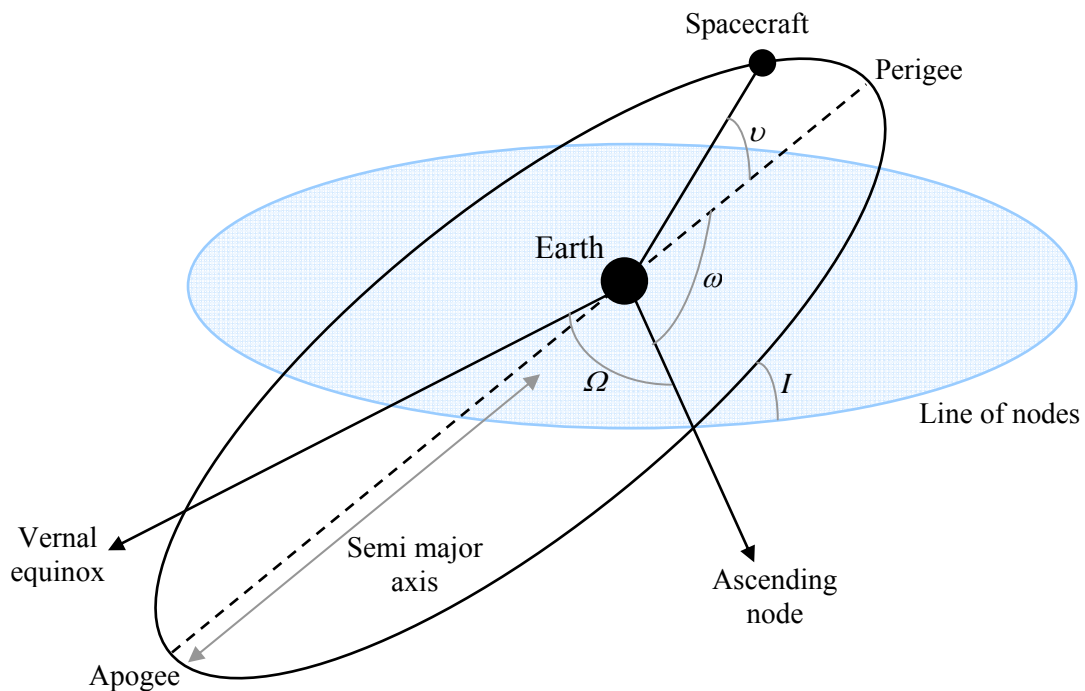


**Figure 3.1:** The Keplerian elements used to define the orbit of Chandrayaan-1 in SPENVIS

### 3.2.1 Trapped Radiation

The Earth's radiation belts were first detected in 1958 by Explorer 1 and also Sputnik 3. Known as the Van Allen belts, after James Van Allen who led the cosmic ray instrument team launched onboard Explorer 1 [Van Allen and Frank 1959]. The belts are formed by charge particles becoming trapped in the Earth's magnetosphere, as shown in Figure 3.2. The area where stable trapping occurs is dependent on the charge, energy and magnetic field strength. The particles are not static, each particle travelling along a magnetic field line in a spiral, described by the gyroradius, between the north and south poles while drifting around the Earth. Electrons drift east

and protons west, resulting in electrons and protons colliding with the atmosphere to produce the auroras observed at the north and south poles.

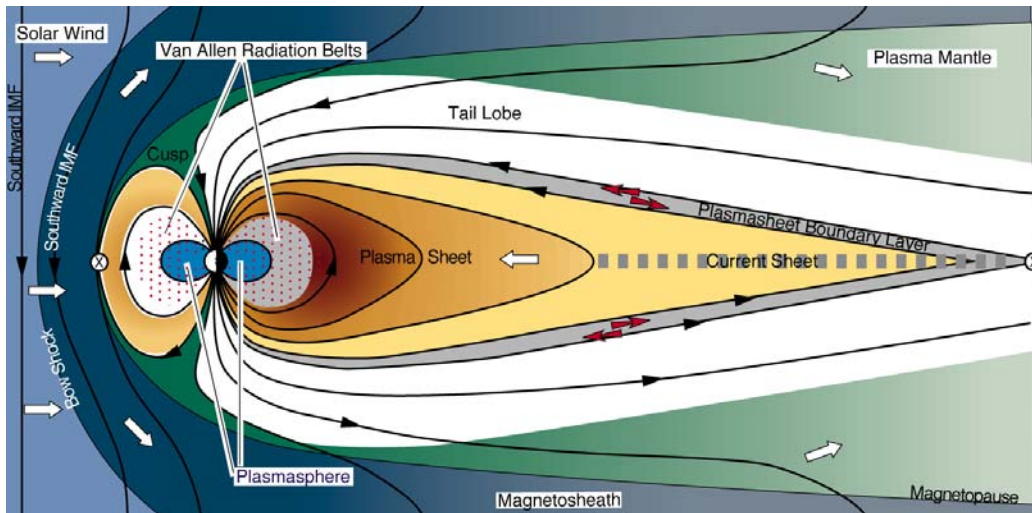


**Figure 3.2:** The Earth's Magnetosphere [Reiff 1999]

The interplanetary magnetic field lines also effect the movement of charged particles in space, the gyroradius (also known as the radius of gyration and the Larmor radius) for protons is given by [Chen 1984]:

$$r_g = \frac{m v}{q B} \quad (3.1)$$

where  $r_g$  is the gyroradius,  $m$  is the mass of the charge particle,  $v$  is the velocity perpendicular to the direction of the magnetic field,  $q$  is the charge and  $B$  is the magnetic field strength. The magnetic field strength near the earth ranges from 1 to 37 nT, with an average value of 6 nT [Space Research Interactive Data Source].

The belts contain areas that are dominated by protons and by electrons, with protons tending towards lower orbits. The proton belts may be modelled using the NASA AP-8 MAX proton maps [Sawyer and Vette 1976] shown in Figure 3.3, where 1 Earth radii is 6,378 km. The proton belt is located higher than an altitude of 500 km from the Earth's surface, with protons of energies greater than 10 MeV being confined below an altitude of around 20,000 km. Protons below 1 MeV can extend as far as GEO altitudes [Sawyer and Vette 1976]. The electron belts may be modelled with the NASA AE-8 MAX model [Vette 1991], the map is displayed in Figure 3.4. The belt is divided into an inner zone with electrons of energies up to around 5 MeV while the outer zone contains electrons of up to 7 MeV [Vette 1991]. The two zones are separated by a region of low intensity which is known as 'the slot'. Both maps are based on data collected from more than twenty satellites between 1958 and 1970.

The radiation environment in space is not stable, space storms can drain particles from the Van Allen belts, relocating them much closer to the Earth [Horne *et al.* 2005]. This effect was observed twice in October and November of 2003, resulting in the exposure of spacecraft to higher than expected levels of radiation [Horne *et al.* 2005]. This demonstrates why worst case scenario models should always be used when determining the radiation dose the spacecraft could be exposed to.

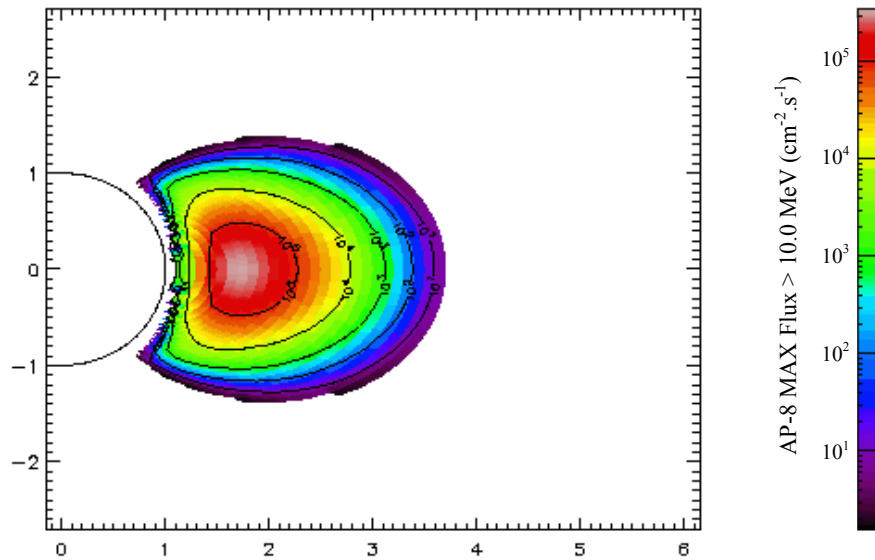


**Figure 3.3:** Trapped proton flux for protons >10 MeV, distance in Earth radii

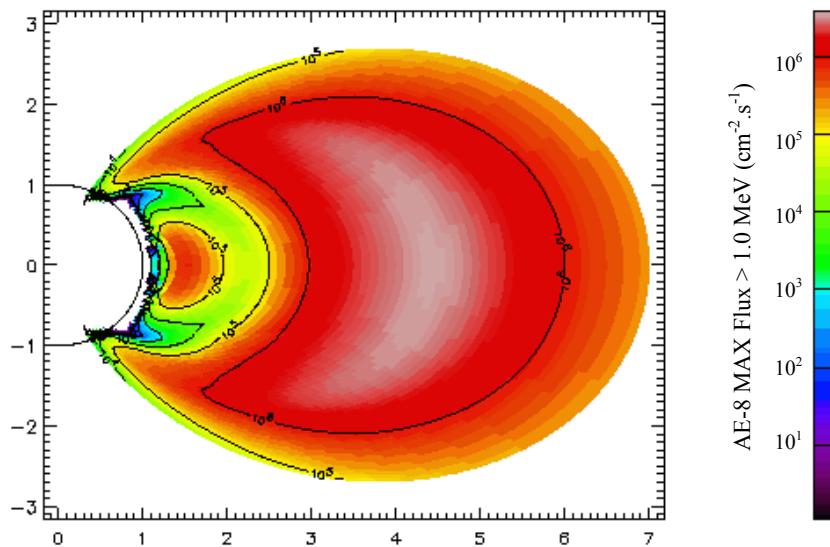


**Figure 3.4:** Trapped electron flux for electrons >1 MeV, distance in Earth radii

It is vital for any space based instrument that the spacecraft spend as little time as possible within the Earth's radiation belts and avoid regular exposure to the south Atlantic anomaly or the auroral horns, described in the next section. SMART-1 spent around 18 months within the Earth's radiation belts which led to the large decrease in performance upon its arrival at the Moon.

### 3.2.1.1 The South Atlantic Anomaly and the Auroral Horns

The Earth's magnetic dipole is tilted by around 11.5 degrees with respect to the rotational axis. The magnetic field is weaker towards the South Pole. This results in the radiation belts being closer to the Earth's surface, peaking in an area over the South Atlantic, known as the South Atlantic Anomaly (SAA). The SAA is highlighted in Figures 3.5 and 3.6 showing the AP-8 MAX flux map of trapped  $>10$  MeV protons, and the AE-8 MAX flux map of trapped  $>1$  MeV electrons at an altitude of 500 km respectively. An orbital path at a  $17^\circ$  inclination is also included in each Figure. The auroral horns are visible in Figure 3.6. It is advisable that sensitive equipment is shutdown while passing through these regions of high flux, and if possible they should be avoided in the case of both manned and un-manned missions to limit radiation exposure. It should be noted that the SAA is drifting west and north at a rate of  $0.28 \text{ deg.yr}^{-1}$  and  $0.08 \text{ deg.yr}^{-1}$  respectively [Badhwar 1997].

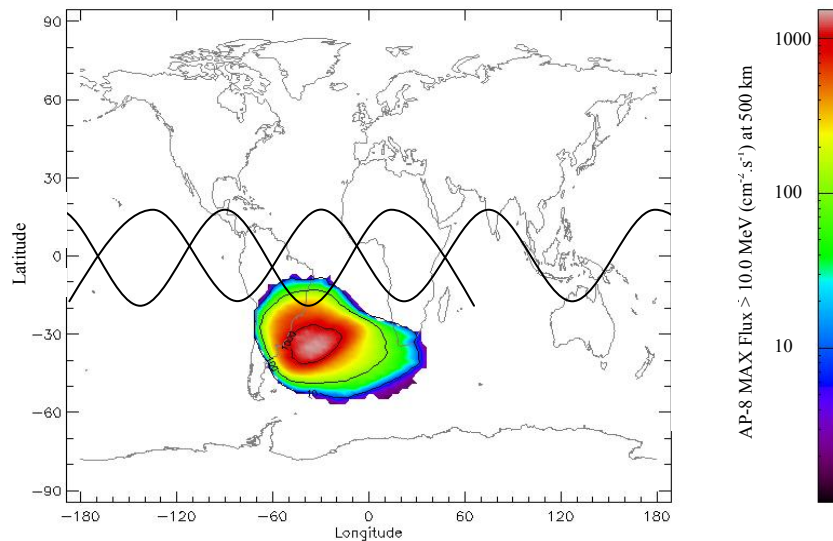


**Figure 3.5:** Trapped proton flux for protons  $>10$  MeV, at 500 km

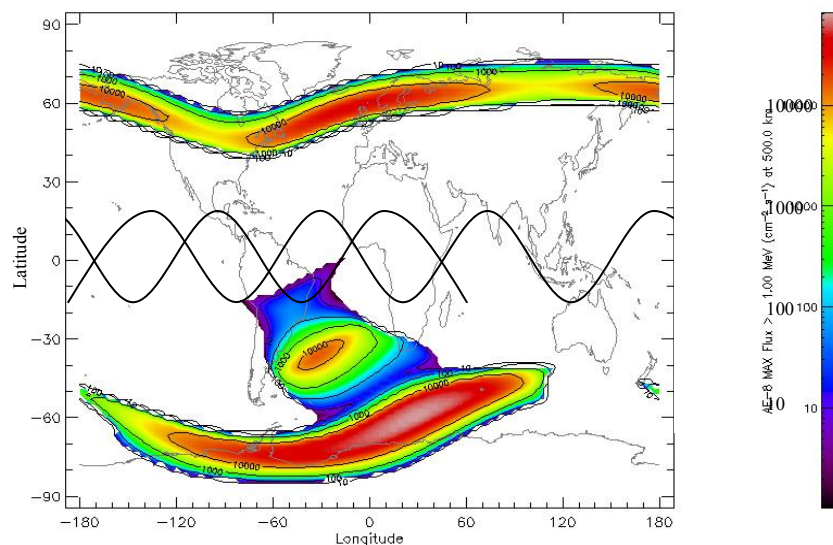


**Figure 3.6:** Trapped electron flux for electrons  $>1$  MeV, at 500 km

### 3.2.2 Non-Trapped

This section describes the sources of radiation that comprise the non-trapped environment, including galactic and solar cosmic rays, and solar proton events and flares.

#### 3.2.2.1 Cosmic Rays

Cosmic rays originate from two different sources, galactic and solar. Galactic cosmic rays consist of 85% protons, 14% alpha particles, and 1% nuclides with  $Z$  greater than 4. Heavy ions with  $Z$  greater than 26 are rare. The particle energies extend to  $10^{20}$  eV, while it is the particles in the energy range  $1\text{-}20\text{ GeV}\cdot\text{nucleon}^{-1}$  which have the most influence to instrumentation [Dyer 1998]. The reason for the lack of abundance of heavy ions is due to the large number of collisions that occur during a particle's journey through space. Current theory holds that galactic cosmic rays originate from stars and are then accelerated in the blast waves of supernova remnants in the expanding gas clouds and magnetic fields. However some cosmic rays have been detected with energies higher than can be achieved from supernova remnants, as of yet their source is unknown.

Solar cosmic rays are similar in composition to galactic cosmic rays, and originate from the solar wind ejected from the Sun's chromosphere and in solar events/flares. The solar wind consists of protons and electrons of a few MeV influencing a region of space known as the heliosphere which extends out past the orbit of Pluto. The Sun's magnetic field causes galactic cosmic rays to lose some of their energy. This effect is greater at times of high solar activity, resulting in the population of galactic particles peaking in solar minimum and the population of solar particles peaking at solar maximum. The Sun follows an approximate eleven year cycle which can be identified by sunspot activity, first observed by Johann Rudolf Wolf in 1848 [Schove 1983].

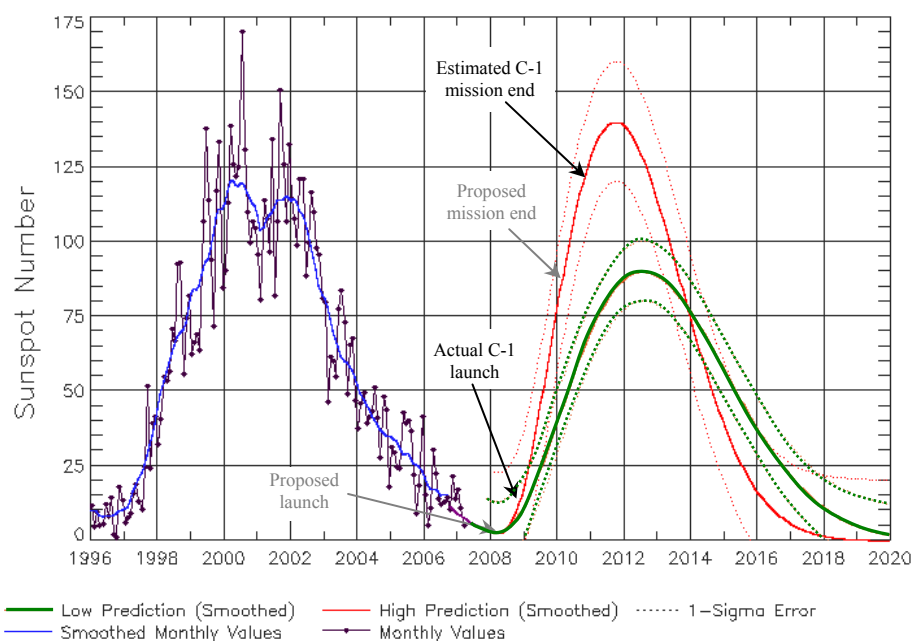


**Figure 3.7:** Solar cycle 23 from experimental data and the NOAA SWPC prediction for cycle 24

The solar cycle from 1996 to February 2008 is called cycle 23 and is shown in Figure 3.7, the data produced by the National Oceanic & Atmospheric Administration (NOAA) Space Weather Prediction Centre (SWPC). Cycle 24 starts in March 2008 and has been predicted to be 30% to 50% greater than the previous cycle with the solar max occurring in 2012 [Dikpati *et al.* 2006]. The predicted solar cycle 24 is also shown in Figure 3.7 with the latest launch and end of mission dates of Chandrayaan-1 highlighted. The prediction is produced by a panel consisting of members from NOAA, NASA and other international organisations.

### 3.2.2.2 Solar Flares and Solar Proton Events

During a solar flare the Sun ejects radiation across the entire electromagnetic spectrum with the highest concentration of flares around Sun spots causing their intensity to increase towards solar maximum. It is the X-rays within these flares that stimulate the surface of the Moon to cause X-ray fluorescence allowing the response to be detected by C1XS. The flares are classified by the peak X-ray flux in units of Watts per square metre ( $\text{W}\cdot\text{m}^{-2}$ ), and placed into categories A, B, C, M or X illustrated in Figure 3.8 which shows the flux recorded by the Geostationary Operational Environmental Satellites (GOES) 10 and 12. Figure 3.8 shows the GOES 10 and 12 data for early November 2003 which includes an X45 flare, the largest flare detected to date [Thomson *et al.* 2005]. Data is recorded in the energy range of 3.1 keV to 24.8 keV (0.5 to 4.0 Å) and 1.6 keV to 12.4 keV (1.0 to 8.0 Å). The Extreme-ultraviolet Imaging Telescope onboard SOHO captured the event as shown in Figure 3.9, the horizontal lines through the flare are as a result of charge spreading within the detector.

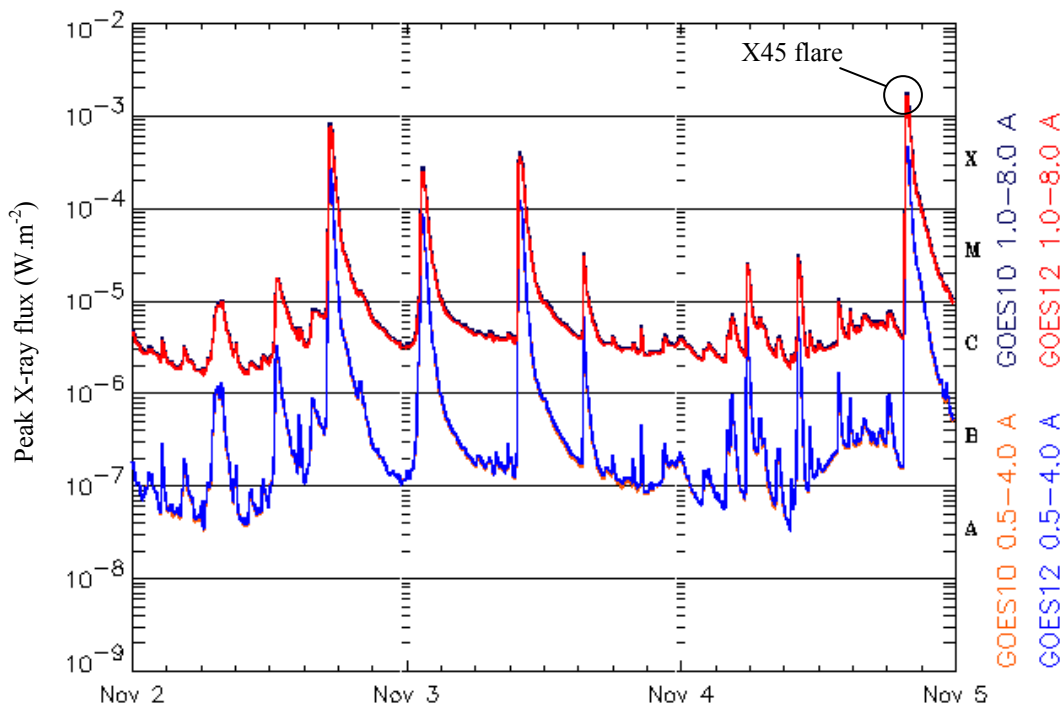


**Figure 3.8:** GOES 10 and 12 X-ray flux plots for November 2<sup>nd</sup> to 5<sup>th</sup> 2003

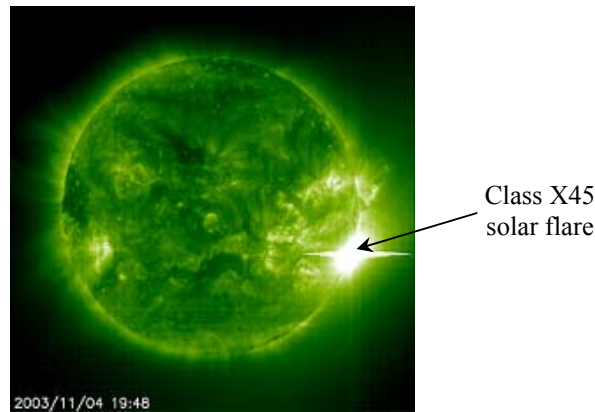


**Figure 3.9:** A false colour image of the X45 flare taken using the Extreme-ultraviolet Imaging Telescope onboard SOHO on the 4<sup>th</sup> of November 2003

The Sun also ejects protons, electrons, and a small number of heavy ions, the emission being often associated with solar flares but not always [Tribble 2003]. It is the protons that cause significant damage to CCDs. These ejections are called coronal mass ejections or solar proton events and can form the largest component of exposure to transiting radiation of a spacecraft. An event in 1972 dominated cycle 20 in terms of fluence and total dose. The occurrence of the 1972 solar proton event and other large events is shown in Figure 3.10 [Holmes-Siedle and Adams 2002] correlated with sunspot numbers. The size of an event can be approximated by the soft X-ray emission which precedes them, the charged particles follow the have to travel a greater distance as they spiral along the magnetic field lines. Until recently it was believed that a proton shower reached maximum intensity after two or more hours after the soft X-ray emissions [Beasley 2005]. However, in January 2005 a shower of protons peaked after only fifteen minutes, making this the most intense burst of solar protons in fifty years [Beasley 2005].

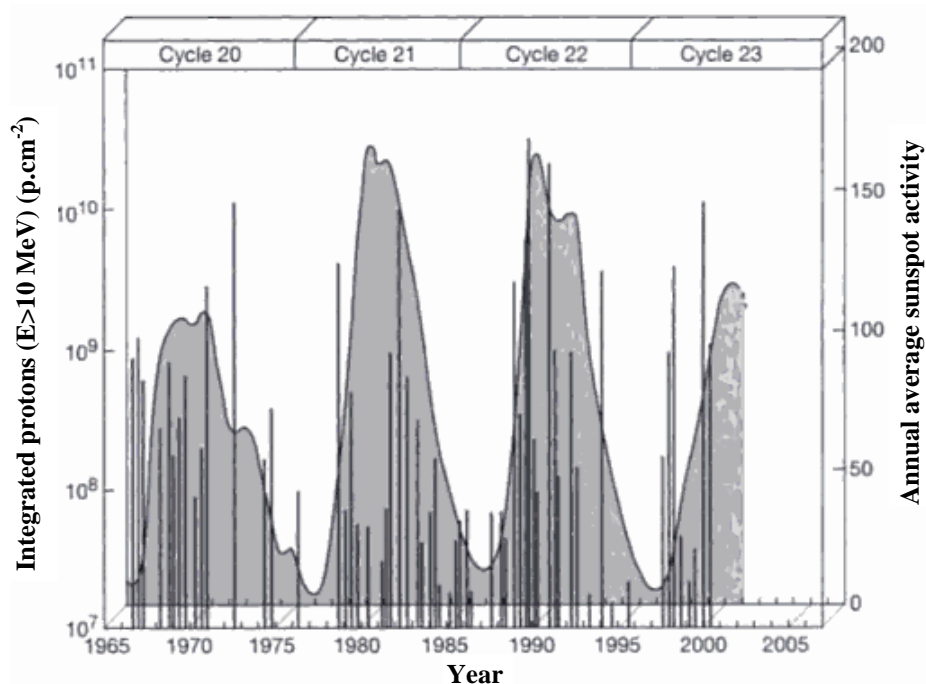


**Figure 3.10:** The occurrence of large solar proton events correlated with average sunspot levels

Solar events last for days, flooding the space environment with charged particles which bombard the Earth's magnetic field compressing the magnetosheath, shown in Figure 3.2. The compressed magnetic field and funnelling of protons along field lines towards the poles exposes spacecraft to solar protons that may otherwise have been shielded by the Earth's magnetic field. Interplanetary missions and those with highly elliptical, high altitude and highly inclined orbits are very susceptible to solar protons [Holmes-Siedle 2002].

Solar proton events may be modelled using the JPL solar energetic particle models, for example JPL 91. The problem of the sporadic nature of both the frequency and intensity of solar proton events is tackled using a confidence value, dependant on mission duration. The recommendations from JPL-91 are given in Table 3.2. A confidence level of 95% means that only 5% of missions identical to the one considered will have a larger fluence than that determined for the 95% confidence level [Feynman *et al.* 1993].

<i>Mission duration (years)</i>	<i>Confidence level (%)</i>
1	97
2	95
3	95
$\geq 4$	90

**Figure 3.2:** Recommended confidence levels for use with the JPL-91 solar proton model based on mission duration

### 3.3 Other Source of Radiation

This section describes other sources of radiation, including those from artificial sources and atmospheric and spacecraft secondaries.

#### 3.3.1 Artificial Sources

There are two artificial sources in space that can result in damage to space instrumentation, due to nuclear detonations and onboard nuclear power supplies. The use of a nuclear powered craft is required when solar power is unpractical, i.e. missions that will travel a great distance from the Sun and for high energy requirements such as RADAR. The nuclear test ban treaty of 1963 banned nuclear weapons testing in the atmosphere, outer space and under water. The ban for space was a direct result of the previous year's Starfish prime 1.5 Megaton detonation. The detonation created a large amount of MeV beta particles [Brown 1963] forming an artificial radiation belt around the Earth, leading to the failure of several spacecraft within a few months of the detonation, including Telstar 1.

### 3.3.2 Atmospheric and Spacecraft Secondaries

The creation of secondary charged particles can also occur inside spacecraft as a result of spacecraft and instrument structure and instrument shielding. This can become very significant for heavy structures where path lengths can reach values that are equivalent to the atmospheric Pfozter maximum [Dyer 1998]. As primary charged particles travel through the spacecraft structure, and the atmosphere, their number decreases whereas the number of secondaries increases, the Pfozter maximum represents the point of maximum dose. The effect of secondaries caused the CCDs on the Chandra X-ray observatory to experience high levels of low energy protons, the CCDs were placed at Pfozter maximum. Spacecraft secondaries can be modelled using particle transport particle codes such as Geant4 and SPENVIS to provide an idea of how damaging they could be to the onboard sensors.

## 3.4 Shielding

Shielding arises from two sources, the Earth's Magnetic field and physical shielding around the onboard CCDs. The magnetic field does not provide a spacecraft with uniform protection, and the protection it does provide is highly dependant on the orbit and the solar cycle as discussed in Section 3.2. Physical shielding comes in the form of specific radiation shields, usually aluminium or tantalum, and from spacecraft and instrument structure. The shielding around the CCD54s in C1XS consists of a 4 mm thick Al instrument box, and a 6 mm Ta block behind the detectors. It also benefits from the 3 mm Cu cold finger and the surrounding instrument and spacecraft structure. Figure 3.11 displays the range of protons as a function of energy in both Al and Ta. The C1XS proton fluence from trapped and solar protons is also shown to highlight the importance of removing the large number of low energy protons.

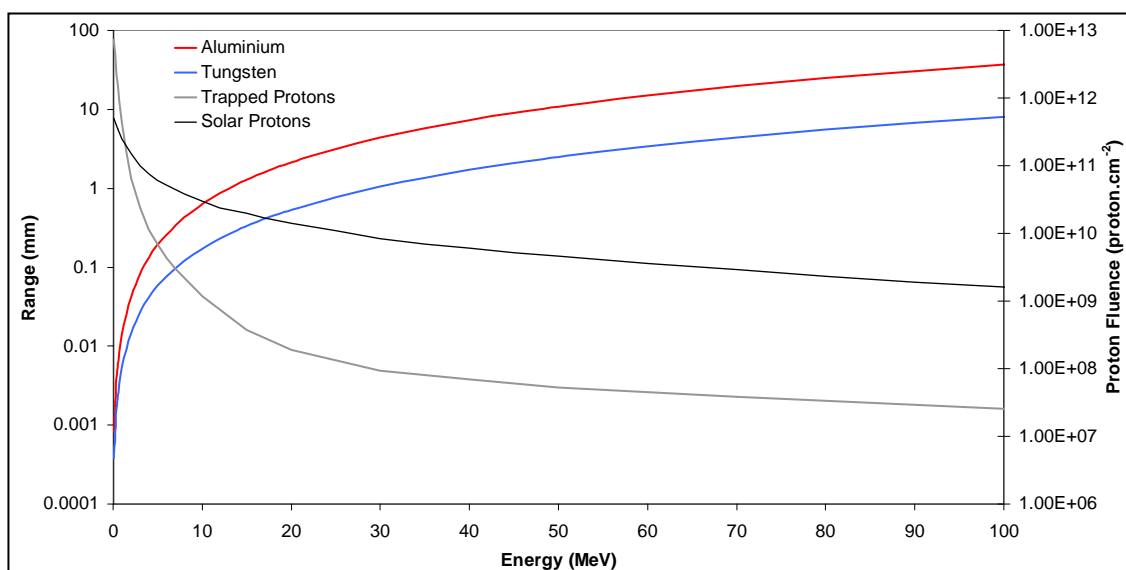


**Figure 3.11:** The range of protons in Al and Ta and the expected C1XS fluence of trapped and solar protons as a function of proton energy

### 3.5 Modelling the Space Radiation Environment

The dose of radiation experienced by a spacecraft will depend on its launch date, orbit, mission duration, and shielding. The need for a program to incorporate orbital, radiation and shielding models was filled in 1998 through the development of the SPace ENVironment Information System (SPENVIS) by ESA [Heynderickx *et al.* 2000]. The mission launch date is selected and orbital parameters entered in a number of mission segments. Based on these inputs the spacecraft's trajectory is plotted. The next stage is to model the exposed radiation environment, producing the proton fluence as a function of energy for both the trapped and solar proton contributions. Trapped protons are modelled using the AP-8 MAX model while solar protons are modelled using the JPL-91 model, producing the proton fluence observed in Figure 3.12.

The effect of different shielding thickness can then be modelled using the ionising and non-ionising dose models for simple geometries, the first options are SHIELDOSE [Seltzer 1980] and the updated version SHIELDOSE 2 [Seltzer 1994] which allow the radiation dose in rads versus Al shield thickness to be found as shown in Figure 3.11 for C1XS trapped and solar protons. The dose is a measure of the energy deposited per unit mass. The system international unit is the Gray (Gy) while the unit commonly used for CCD irradiation studies is the rad, where 1 rad is equal to 1 cGy. To experimentally test a device, the range of proton energies shown in Figure 3.12 would be hard to simulate. The Non-Ionising Energy Loss (NIEL) function is therefore used as a scaling factor to provide a single equivalent proton fluence. The fluence is the total number of protons that intersect a unit area ( $\text{protons.cm}^{-2}$ ), while flux is the number that intersect a unit area per unit time ( $\text{protons.cm}^{-2}.\text{s}^{-1}$ ).

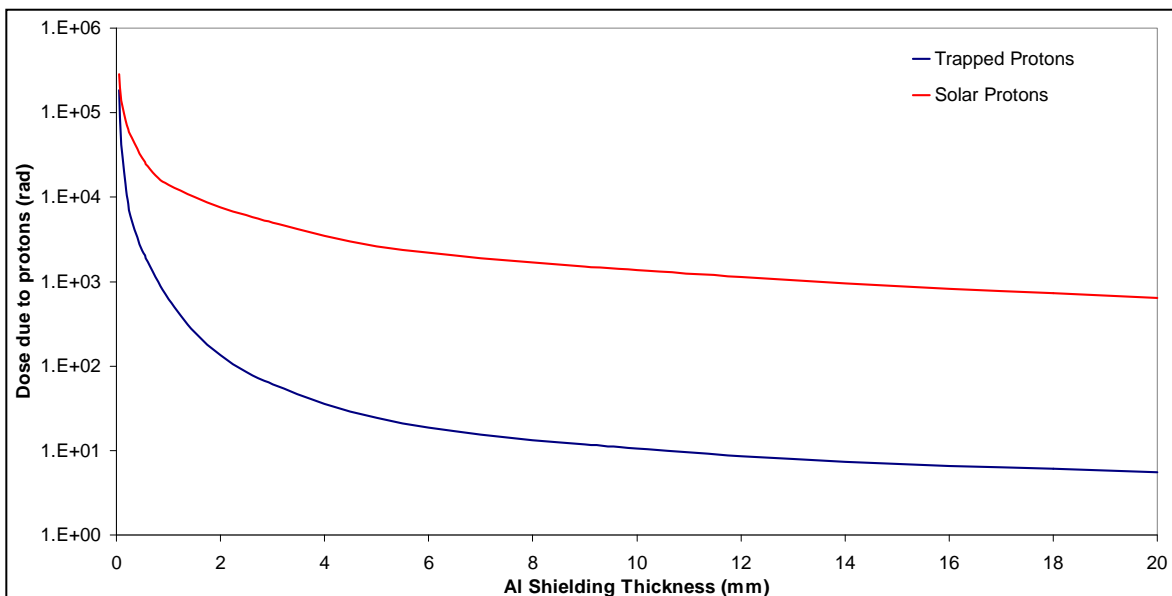


**Figure 3.12:** The dose of solar and trapped protons (rad) as a function of Al shielding thickness for C1XS as modelled using SPENVIS

### 3.5.1 Non-Ionising Energy Loss Function

When protons interact within an environment they transfer kinetic energy to the medium in which they are interacting, this is discussed further in Section 3.6. The amount of kinetic energy released in a medium (KERMA) by a proton that will cause displacement damage is given by the SPENVIS NIEL model as the displacement damage dose as a function of Al shielding thickness. The dose in silicon in units of  $\text{MeV.g(Si)}^{-1}$  can be converted to provide an equivalent proton damage fluence using the NIEL function in units of  $\text{MeV.cm}^2.\text{g}^{-1}$  shown in Figure 3.13. The 10 MeV equivalent proton fluence is the industry standard, as 10 MeV protons are achievable by most proton accelerator facilities, however, there are times when other proton beam energies have to be used. The NIEL function normalised to 10 MeV is used to compare the displacement damage caused by a proton energy of for example 45 MeV with that caused by the equivalent 10 MeV proton fluence.

The use of the NIEL function in silicon is described in detail by Burke (1986) and Van Lint (1987) and in CCDs by Srour *et al.* (2003). The NIEL function normalised to 10 MeV is shown in Figure 3.13 as a function of the proton energy  $E_p$ . The line can be approximated using:

$$10\text{ MeV NIEL Function} = \frac{8}{E_p^{0.9}} \quad (3.2)$$

where  $E_p$  is less than 13.5 MeV

$$10\text{ MeV NIEL Function} = \frac{1.6}{E_p^{0.28}} \quad (3.3)$$

where  $E_p$  is greater than 13.5 MeV.

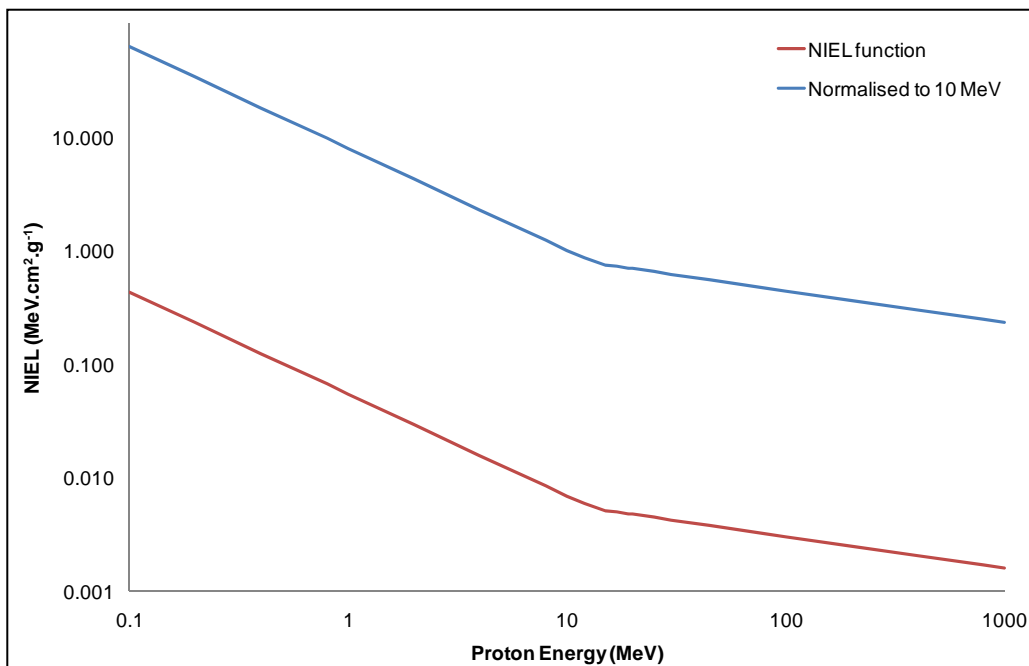


**Figure 3.13:** The NIEL function as a function of proton energy found using Equations 3.2 and 3.3

### 3.6 Radiation Damage Mechanisms

The three dominant radiation interactions are inelastic collisions with atomic electrons which produce ionisations and elastic and inelastic collisions with atomic nuclei which lead to displacement damage. The two damage mechanisms cause a variety of different defects, highlighted in Table 3.3 and in Figure 3.14 which shows the path of a charge particle through a CCD. The severity of each defect is dependent on the radiation type, energy, and its fluence. Protons form the main damage component for the Chandrayaan-1 mission due to their high concentration in the space environment.

<i>Damage Mechanism</i>	<i>Location</i>	<i>Resulting Defects</i>
Ionisation	SiO <sub>2</sub> below the polysilicon gates (gate dielectric)	Generation of a flat band voltage shift, shifting clock and output amplifier bias signals
Ionisation	Si-SiO <sub>2</sub> interface	Generation of traps at the surface, further increasing flatband voltage shift and surface generated dark current
Ionisation	Region of charge generation and collection	Transient effects
Displacement	Silicon where charge is generated, collected, transferred and measured	Decreased CTE Increase dark current generation Increased numbers of dark current spikes, dark current non-uniformity, and random telegraph signals

**Table 3.3:** Table showing the radiation damage mechanism and its location of interaction and the resulting defect

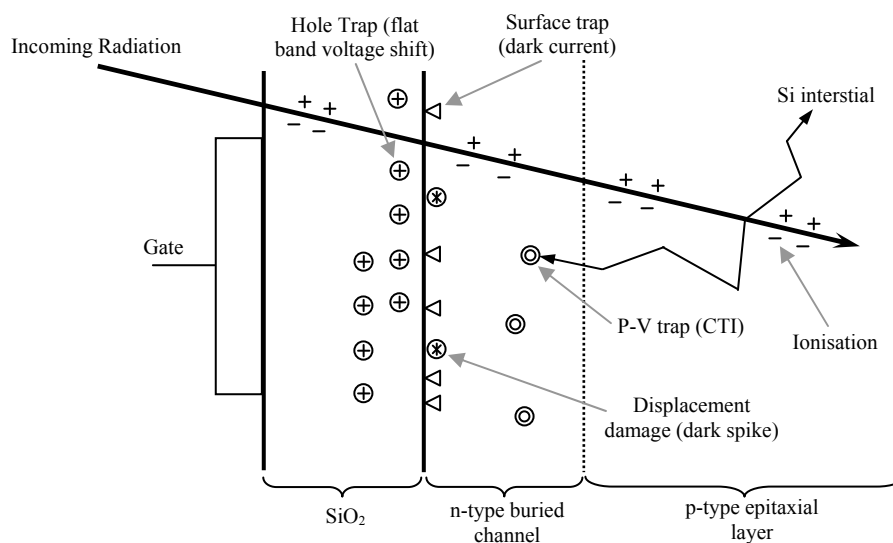


**Figure 3.14:** Cross section of a CCD showing the path of an incident charged particle, highlighting the areas affected by ionisation and displacement damage [Janesick 2001]

### 3.6.1 Ionisation Damage and its Effects

Ionisation occurs when an orbital electron is removed from an atom, as discussed in Section 2.6.1, via the photoelectric effect, Compton scattering, or pair production. Direct ionisation occurs with alphas, betas, and protons which are charged, while non-charged radiation, e.g. neutrons, X-rays and  $\gamma$ -rays, can cause indirect ionisation. The net result is the creation of a number of electron hole (e-h) pairs. This number is dependent on the energy required to create an e-h pair, which is independent of the type and energy of the incident ionising particle. The mean ionisation energy required to create an e-h pair is 3.65 eV for silicon and 18 eV for silicon-dioxide [Emery and Rabson 1965], the two materials of primary interest for silicon detectors.

As the incident particle travels through the device it will generate e-h pairs until it no longer possesses enough energy. The number of e-h pairs generated can be found using Equation 2.39. The rate of energy loss is described by the linear energy transfer (LET), this is the energy deposited per unit path length divided by the unit density ( $\text{MeV} \cdot \text{cm}^2 \cdot \text{g}^{-1}$ ). Figure 3.15 shows the LET for Si and  $\text{SiO}_2$ . At energies  $> 0.5$  MeV the Bethe formulae [Bethe 1932] is used, while at  $< 0.5$  MeV a fitting formula based on experimental data is used [ICRU 1993]. The Bethe formula is given by:

$$-\frac{dE}{dx} = \frac{4\pi}{m_e c^2} \frac{n z_e^2}{\beta^2} \left( \frac{e^2}{4\pi\epsilon_0} \right)^2 \left[ \ln \left( \frac{2m_e c^2 \beta^2}{I(1-\beta^2)} \right) - \beta^2 \right] \quad (3.4)$$

where  $m_e$  is the rest mass of an electron (kg),  $c$  is the speed of light ( $\text{m} \cdot \text{s}^{-1}$ ),  $z_e$  is the charge on the incident particle (C),  $\beta$  is  $v/c$  where  $v$  is the velocity of the incident particle,  $I$  is the mean excitation potential of the target (eV), and  $n$  is the electron density given by:

$$n = \frac{N_A Z \rho}{A} \quad (3.5)$$

where  $N_A$  is the Avogadro number,  $Z$  is the atomic number,  $\rho$  is the density ( $\text{g} \cdot \text{cm}^{-3}$ ) and  $A$  is the mass number of the target material. The number of e-h pairs generated per ion is dependent on the incident particle's LET given by:

$$n_{eh} = \frac{LET \ r \ \rho}{10^6 \ \omega} \quad (3.6)$$

where  $r$  is the range (cm), and  $\omega$  is the energy required to generate an e-h pair (eV).

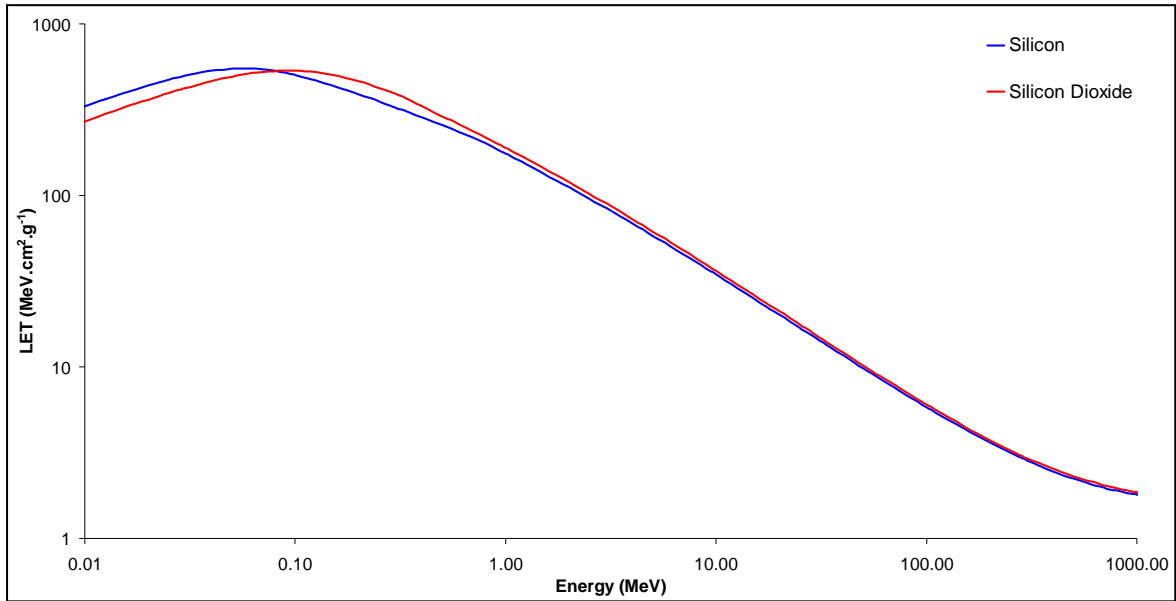


**Figure 3.15:** Linear energy transfer of Si and SiO<sub>2</sub> as a function of energy

It is clear from Figure 3.15 that lower energy protons will lose energy at a greater rate within a target material than higher energy protons. This is highlighted in the Bragg curve in Figure 3.16, which shows the LET with units of eV.μm<sup>-1</sup> as a function of material thickness. The area below the line, coloured in red, is the energy deposited into the target. The maximum energy deposited occurs at the Bragg Peak, this occurs shortly before the proton stops. The entrance dose is low so the depth at which the proton does come to a stop will experience the greatest dose. Figure 3.16 shows the resulting curve for a 300 keV proton as it travels through the front structure of the CCD54, which consists of a 0.75μm SiO<sub>2</sub> layer, 0.30μm polysilicon, 0.085μm Si<sub>3</sub>N<sub>4</sub>, 0.085μm SiO<sub>2</sub>, and the epitaxial silicon. The path of 15,000 protons is shown in Figure 3.17, modelled using SRIM.

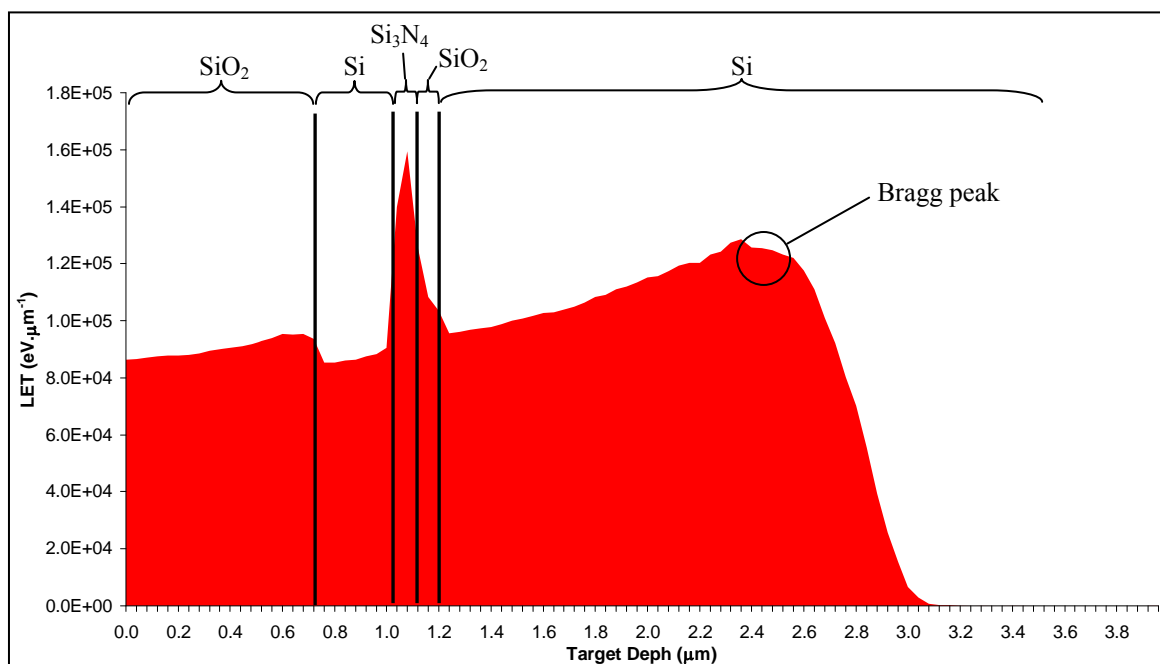


**Figure 3.16:** Ionising energy loss of a 300 keV proton as a function of depth into the CCD54

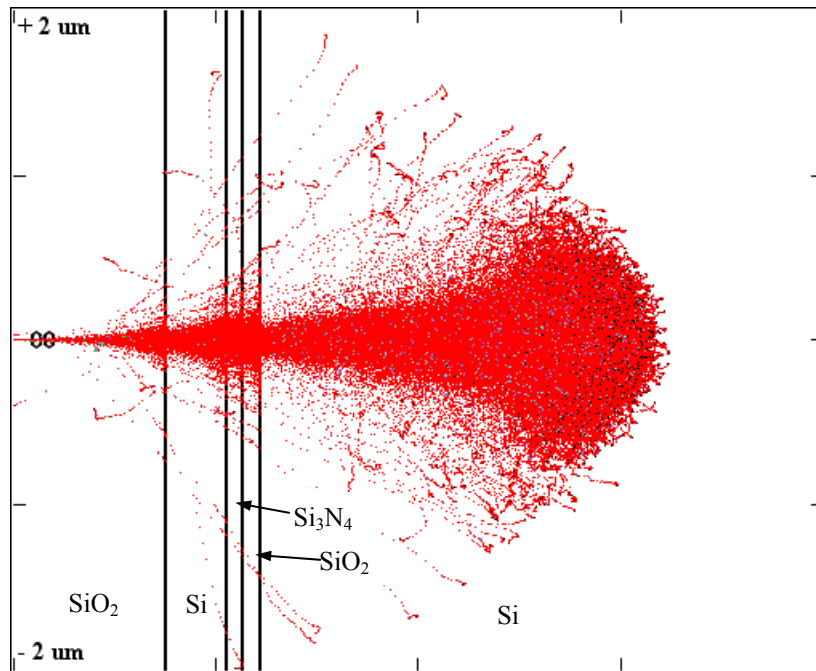


**Figure 3.17:** SRIM output showing 300 keV proton interactions within the CCD54

The increase in LET in the Si<sub>3</sub>N<sub>4</sub> and SiO<sub>2</sub> layers is as a result of ‘dose enhancement’, where the electrons generated by the incident proton are reflected when they travel from low to higher Z [Hsiao-Hua, Chen, and Vasilik 2001]. The effect also occurs during photon irradiations where both the photons and electrons are reflected; dose measurement is extremely complicated and requires Monte Carlo modelling [Hsiao-Hua, Chen, and Vasilik 2001]. The effect increases with increasing Z, and decreases with decreasing incident particle energy [Li *et al.* 1999]. Care must be taken, during instrument design, to avoid placing high Z materials around the detectors.

There is a chance that the e-h pairs generated during the ionisation will recombine. This must take place shortly after their generation otherwise they will become separated by diffusion or by field induced drift. The electrons generated within the charge collection and storage regions will be collected in the potential wells, and the holes removed, forming the transient noise discussed in Section 2.5.8. Pairs generated at the Si-SiO<sub>2</sub> interface that do not recombine diffuse through the lattice with the electrons removed quickly due to their considerably higher mobility. In SiO<sub>2</sub> electron mobility ranges from 20 to 40 cm<sup>2</sup>.V<sup>-1</sup>.s<sup>-1</sup>, while for holes it ranges from 10<sup>-4</sup> to 10<sup>-7</sup> cm<sup>2</sup>.V<sup>-1</sup>.s<sup>-1</sup> [Janesick 2001]. The holes become trapped at the Si-SiO<sub>2</sub> interface of the detector due to the high concentration of impurities, the deeper a hole is trapped within the lattice the longer it will be until it is released as greater energy is required. The increased positive charge results in an increase in the surface generated dark current, discussed in Section 2.5.1. Increased impact ionisation, also known as field enhanced emission, discussed in Section 2.5.4, and the creation of a flat-band voltage shift.

### 3.6.1.1 Flat-Band Voltage Shift

The positive charge generated in the gate dielectric, shown in Figure 3.14, increases the size of the electric field below the gate, as shown in Figure 3.18 [Roy *et al.* 1989]. In Figure 3.18 the solid lines represent pre-irradiated potential wells, while the dashed lines represent the potentials after irradiation. The resulting flat-band voltage shift  $\Delta V_{FB}$  of 10 V will not affect charge transfer as long as each gate is affected similarly, i.e. a uniform irradiation. However the potential well generated on the output node by  $V_{rd}$  may no longer be enough to efficiently transfer charge. In the example illustrated in Figure 3.18 no charge will be transferred into the read-out node. Over a mission the  $V_{rd}$  will have to be increased to ensure the charge handling capacity of the read-out node is maintained, increasing the device power requirement. Thinning the oxide layer reduces the number of trap sites [Shiono *et al.* 1983], while using a p-type buried channel and n-type bulk silicon would result in the holes being swept away from the Si-SiO<sub>2</sub> interface. The output node is not affected because there is no Si-SiO<sub>2</sub> interface above it to trap the holes.

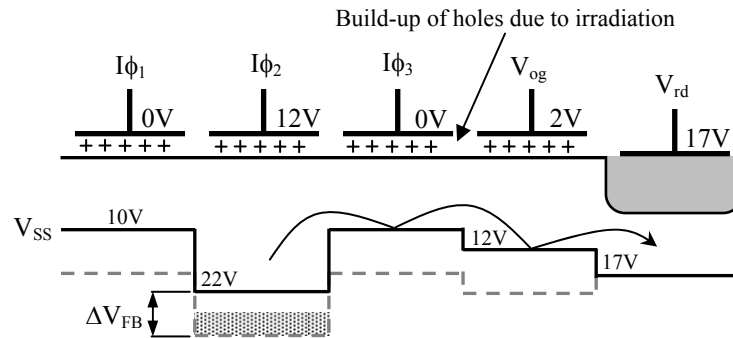


**Figure 3.18:** The result of a radiation induced flat-band voltage shift near the output gate with the potentials marked by solid lines pre-irradiation and dashed post-irradiation

### 3.6.2 Displacement Damage and its Effects

Displacement is caused when an energetic particle displaces an atomic nucleus from the lattice; this is referred to as a 'primary knock-on'. The resulting damage is dependent on a number of variables including, particle type and energy, time and thermal history after irradiation, and impurity levels in the target materials [Srouf *et al.* 2003]. The most abundant charged particle in space is the proton hence these form the main source of displacement damage to the CCD54s in C1XS. Displacement damage is also caused by electrons with energies above 150 keV and neutrons. Energetic electrons and protons cause isolated defects, while neutrons, ions, and highly energetic protons produce defect clusters. The particle must have energy greater than  $E_d$ , the displacement threshold, which for silicon is  $\sim 20$  eV.

An elastic collision is illustrated in Figure 3.19. The energetic incident particle undergoes coulombic interactions. Elastic coulombic scattering is called Rutherford scattering. The result is to

impart energy to atomic nuclei, resulting in its displacement from the lattice. The displaced atom can in-turn displace further atoms, so long as its energy is greater than  $2E_d$  [Kinchin 1955]. It is also possible for energetic particles to interact directly by a ‘hard sphere’ collision with the nucleus, resulting in knock-on atoms with energy 3-15 times  $E_d$  [Kinchin 1955]. These energetic displaced atoms will displace many other atoms forming a defect cluster.

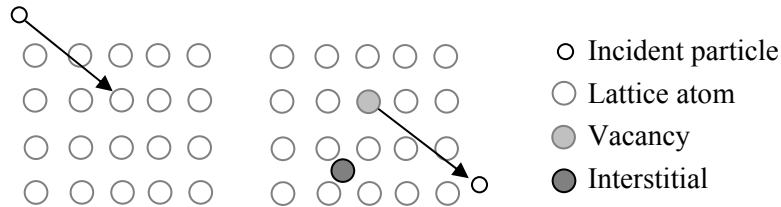


**Figure 3.19:** Interstitial and vacancy creation in the atomic lattice

Inelastic collisions occur when highly energetic protons ( $E_p > 10$  MeV) and neutrons interact with the nucleus leaving it in an excited state [Janesick 2001]. The nucleus is displaced and emits energetic nucleons, this process is referred to as spallation and leads to defect clusters. The result of these collisions is to produce a displacement cascade.

Elastic and inelastic collisions can both result in the displacement of atomic nuclei. Atoms in non-lattice positions are referred to as interstitials and a vacancy is the absence of an atom from the lattice as shown in Figure 3.19. Together the vacancies and interstitials are referred to as Frenkel pairs. The total number of displacements created per incident particle is related to the NIEL value ( $\text{MeV}\cdot\text{cm}^2\cdot\text{g}^{-1}$ ), the NIEL for a proton in silicon is illustrated in Figure 3.13, an approximation is given by [Burke 1986]:

$$n_{eh} = \frac{NIEL r \rho}{10^6 E_d} \quad (3.7)$$

although the NIEL value is lower than LET, when a displacement does occur the damage done has a greater affect on CCD performance.

Not all the atoms that are displaced will remain as interstitials [Messenger 1992]. If after the interaction the silicon interstitial has energy less than the lattice binding energy, which for silicon is 2.3 eV, it will drop into the vacancy created. This process is referred to as replacement collision. Figure 3.20 shows the results of a simulation in SRIM for the CCD54 structure. The total number of displacements, vacancies and replacement collisions are shown as a function of protons and depth into the CCD. In this case 7.4% of the vacancies are removed due to replacement collisions.

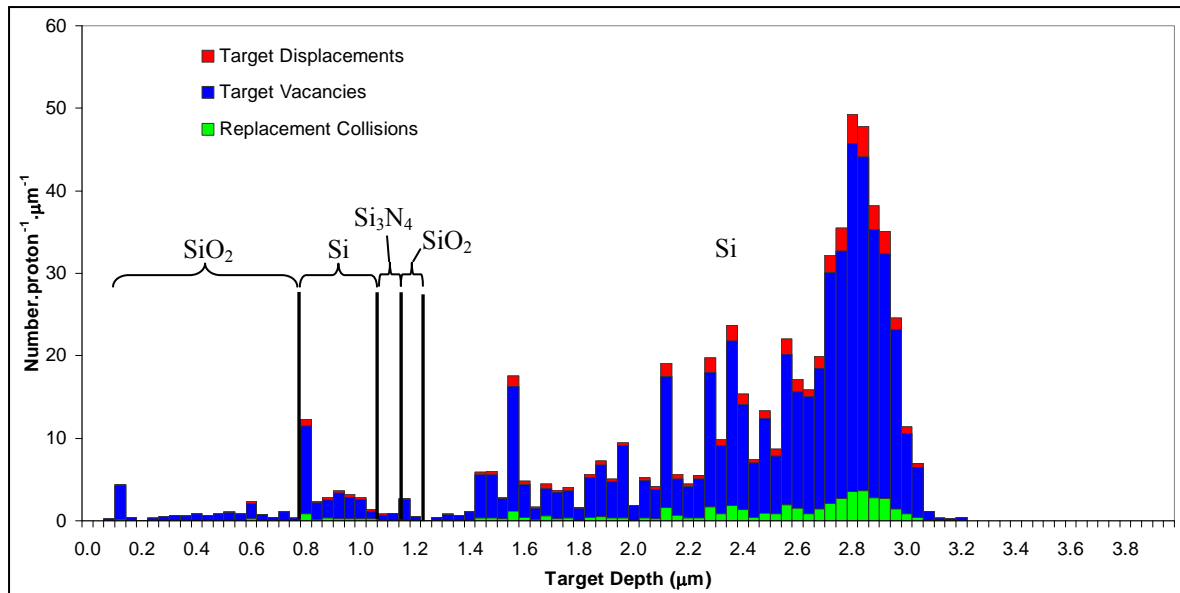


**Figure 3.20:** Displacement, vacancies and replacement collisions from 300 keV protons as a function of depth into the CCD54

If vacancies possess a thermal energy greater than 100 K they will drift through the lattice and combine with other defects to form stable defects, although on average 98% recombine with interstitials [Van Lint 1987]. The three main stable defects are the phosphorus-vacancy (E-centre), the oxygen-vacancy (A-centre) which are the result of impurity atoms in the lattice, and the divacancy (J-centre) consisting of two adjacent vacancies. The lattice defects create energy levels in the silicon band-gap as illustrated in Figure 3.21, which change the electrical properties of the material through several different processes, given below:

- **Generation:** The thermal generation of e-h pairs at a level near the middle of the band-gap (mid-gap), which causes an increase in the dark current within the depletion region of the device.
- **Recombination:** The defect centre captures electrons and holes, thus reducing the minority carrier lifetime. The rate is dependent on the recombination centre density, the free carrier concentration, the electron hole capture cross section and the energy level position [Srouf 2003]. This is the dominant mechanism for gain degradation in bipolar transistors.
- **Trapping:** The defect centre, typically at a shallow level, captures a carrier. If no recombination occurs the carrier is released after a time dependent upon the type of defect centre. This is the process responsible for loss of CTE in CCDs.
- **Compensation:** Results in a reduction in the majority carrier concentration due to the compensation of donors or acceptors by a defect centre.
- **Tunnelling:** The defect assists the carriers tunnelling through a potential barrier from the valence band to the conduction band. Resulting in increased current within the device. Also

referred to as trap-assisted tunnelling, it can only take place when the electric field strength is greater than  $10^6 \text{ V.cm}^{-1}$  [Rodina *et al.*2002]

- **Scattering:** The defects act as scattering centres, reducing carrier mobility with increased impurity concentration. At temperatures less than 300 K this effect dominates over lattice scattering, where electrons are scattered through collisions with vibrating atoms within the lattice [Srouf 2003].
- **Type Conversion:** Type conversion does not occur in the bulk silicon, it simply becomes compensated intrinsic, i.e. when the silicon is doped with equal densities of donors and acceptors [Li 1995].
- **Enhanced Thermal Generation:** This occurs in regions of high electric field. The Pool Frenkel effect, pure tunnelling and phonon assisted tunnelling are thought to be responsible for this process [Srouf and Hartmann 1989]. This process is also referred to as impact ionisation.

Generation and trapping form the main component of decreased performance in a CCD, resulting in increased dark current and a reduction of CTE respectively. Recombination and combination affect the number of available carriers and enhanced thermal generation will cause increased levels of impact ionisation.

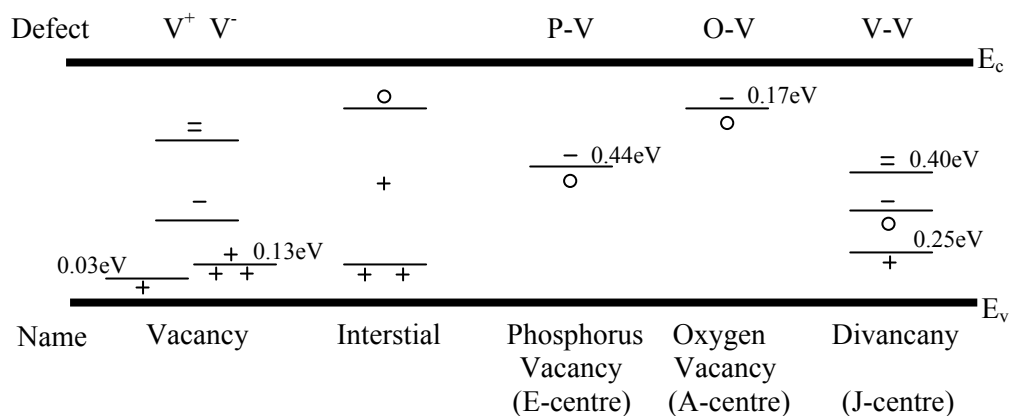


**Figure 3.21:** The energy levels created in the silicon band-gap as a result of the main stable defects are shown, with the energy level measured from the nearest band-edge [Grove 1967]

### 3.6.2.1 Increased Charge Transfer Inefficiency

The increase in CTI is as a result of increased trap sites formed as a result of displacement damage within the silicon band-gap which hold onto electrons as described in Section 2.5.7. The trap emission time constant is dependant on temperature and the trap type. Figure 3.22 covers the temperatures under which the CCD54 was operated in the experiments described in this thesis. The increase in CTI can be evaluated by characterising the change in the mean energy of an X-ray peak

with respect to the position across the CCD [Holland 1990], the gradient of the resulting slope being proportional to the CTI.

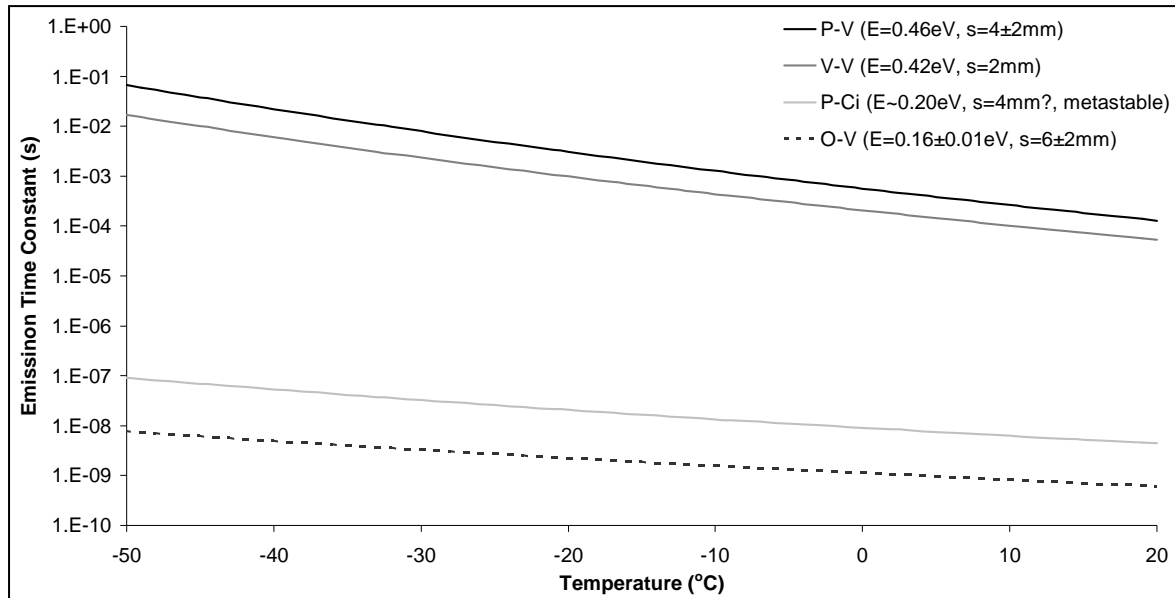


**Figure 3.22:** Trap emission time constant as a function of temperature for the E, A, and J-centres [adapted from Burt 2008]

There are a number of methods in which the increased CTI can be reduced:

- **Increased charge levels:** A larger charge packet will undergo a smaller percentage reduction as a result of trapping. Low energy X-rays will be more affected.
- **Faster pixel transfer:** Through increasing the clocking speed to faster than the trap time constant, less charge will become lost.
- **Low operation temperature:** As the temperature is lowered carriers become 'frozen' in trap sites [Holland *et al.* 1991] as shown in Figure 3.22.
- **Changes to channel structure:** The use of a narrow channel [Holland *et al.* 1991] or a supplementary buried channel [Bredthauer *et al.* 1991] where the charge is confined to a smaller volume. This reduces the number of trap sites a charge packet can encounter, however in the case of the supplementary channel at some level of charge the volume undergoes a sudden increase.
- **Annealing:** Trap sites can be annealed at high temperatures, the temperature required is trap site dependant [Holland *et al.* 1991]. The temperatures required to anneal the main defects are given in Table 3.4 [Kraner 1984 and MacEvoy, Hall, and Gill 1996].
- **Charge injection:** Structure to allow charge to be injected into a devices first row, or every 200 rows fills the trap sites [Holland *et al.* 1993 and Smith *et al.* 2004], both methods improve CTE however they add noise and the second method reduces the effective imaging area. 100% charge injection can also be used, where the injected charge is

measured before injection into each row and then subtracted before read-out, this removes the noise generated by the additional signal.

<i>Defect</i>	<i>Annealing temperature (°C)</i>
A-centre	300
E-centre	150
O-centre	350

**Table 3.4:** Required temperatures to anneal the three main defect centres in n-channel CCDs

### 3.7 Chapter Summary

This chapter has described the transient and non-transient components of the natural space radiation environment, with a brief mention of artificial sources. A method for simulating the expected radiation exposure using SPENVIS which can be used to recommend operational and design requirements has been defined, based on the spacecrafts orbital parameters and time schedule. The physical processes involved in both ionisation and displacement damage have been discussed, highlighting the sensitive areas of the CCD and the resulting damage effects and some methods of minimising the performance loss. The next Chapter describes the first set of experimental results including the CCD54 characterisation and X-ray event analysis work.

## Chapter 4: Optimisation and Flight Device Screening

### 4.1 Introduction

This chapter discusses the characterisation process conducted using the CCD54, split into three sections detailing the optimisation of timings and voltages discussed in Chapter 2, the characterisation of 56 devices available for flight selection, and a QE analysis. The work was conducted to investigate device performance, to identify trends in device behaviour and identify the suitability and make recommendations for using the CCD54 to perform high quality X-ray fluorescence analysis. The three sections detail the experimental arrangement and procedures followed by the results, discussion and final conclusions.

The CCD54 devices tested were held on ceramic modules, shown in the photograph in Figure 1.5 and a schematic in Figure 4.1 showing the device numbering system used. Each device comprises an active area of approximately  $1.07 \text{ cm}^2$  covered with electrodes in a herringbone structure as described in Section 2.4. The charge detection circuit is based on that used in the CCD30 and CCD47, manufactured by e2v technologies plc., with an output amplifier responsivity of  $2.5 \mu\text{V}\cdot\text{electron}^{-1}$ , pixel saturation at approximately 800 thousand electrons and a read noise of around 3 electrons r.m.s., at a clock frequency of 50 kHz. The read noise increases to  $\sim 7$  to 8 electrons r.m.s. at 1 MHz [Pool 1997].

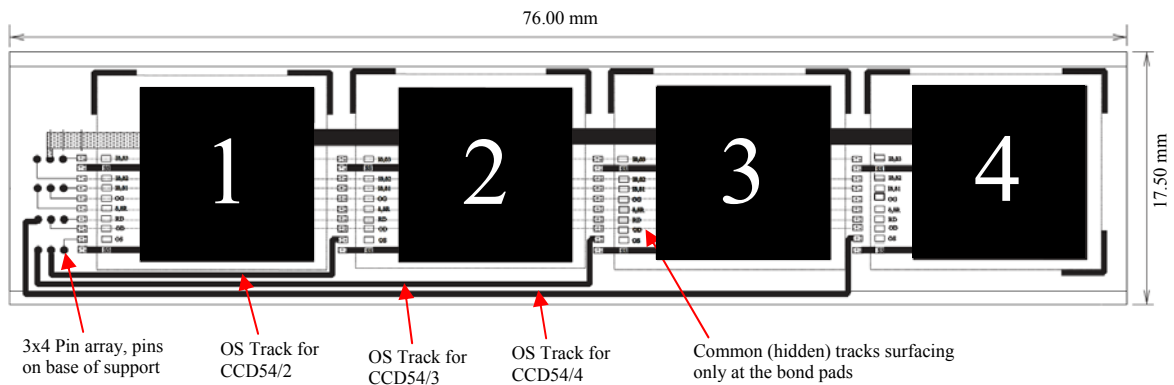


**Figure 4.1:** Schematic of a C1XS module showing the device number scheme [adapted from Hotston 2000]

### 4.2 Voltage and Clock Optimisation

The voltage and clock optimisation study was conducted to produce a set of values that would be used throughout all further device testing, to provide the best achievable operating conditions and provide consistency over the testing involved in this thesis. Stable operation would also be identified as in the unlikely event of voltage fluctuations over the duration of the C1XS operational

lifetime the performance of the CCD54 should not be greatly affected, i.e. a slight change in operational voltages should not affect the QE or the measured energy resolution which would introduce additional errors in the scientific data. The starting voltages given in Table 4.1 were those used by Holland and Hutchinson 1998. The clock optimisation would allow the most efficient device operating frequency and CDS timings to be selected to provide the optimal energy resolution and noise performance, and also provide good QE.

<i>Clock/Bias</i>	<i>Voltage (V)</i>
Image	8.0
Reset	10.0
V <sub>od</sub>	30.0
V <sub>rd</sub>	17.0
V <sub>og</sub>	3.0
V <sub>ss</sub>	10.0

**Table 4.1:** CD54 initial operating voltages

#### 4.2.1 Experimental Arrangement

The CCD54 module used was housed inside the vacuum test facility shown in Figure 4.2. A Pfeiffer vacuum pump was used to evacuate the air in the chamber, with testing occurring at a pressure of  $< 10^{-4}$  mbar. The system was operated under vacuum to ensure that water vapour not condense on the detector during cooling and to mitigate the attenuation of X-rays by air within the chamber. The module was clamped to an aluminium cold finger resting on a two stage thermo electric cooler (TEC), attached to the copper heat exchanger shown the schematic in Figure 4.3. The TEC had a maximum current rating of 3.5 A, which allowed the device to be cooled to around  $-40.0$  °C. Heat produced by the TEC was removed using water cooling through the copper heat exchanger. Temperature control was provided by an ILX Lightwave controller (model number LDT-5525) to a stability of  $\pm 0.2$  °C. The temperature was measured using a  $1,000 \Omega$  platinum resistance thermometer (PRT) attached to the module ceramic next to device number 2 (it is assumed the device silicon is in good thermal contact with the ceramic). An  $^{55}\text{Fe}$  source was held in front of the CCD54 to illuminate it with Mn- $K\alpha$  X-rays, providing a known signal of 1,600  $e^-$  per event. When handling a radioactive source, exposure time should be limited. Regular radiation level monitoring was provided using a Mini 900 42B radiation scintillation monitor. The drive voltages and timings were provided by an XCAM Ltd. USBREM2 drive box (voltages were measured using a digital voltage meter to an accuracy of  $\pm 0.1$  V), and controlled using USBREM3 software. All data collection and processing was conducted using this software. Error analysis was

based on the error on the weighted mean of the noise peak and X-ray peak locations, from which the energy resolution and dark current and calibration values were calculated.

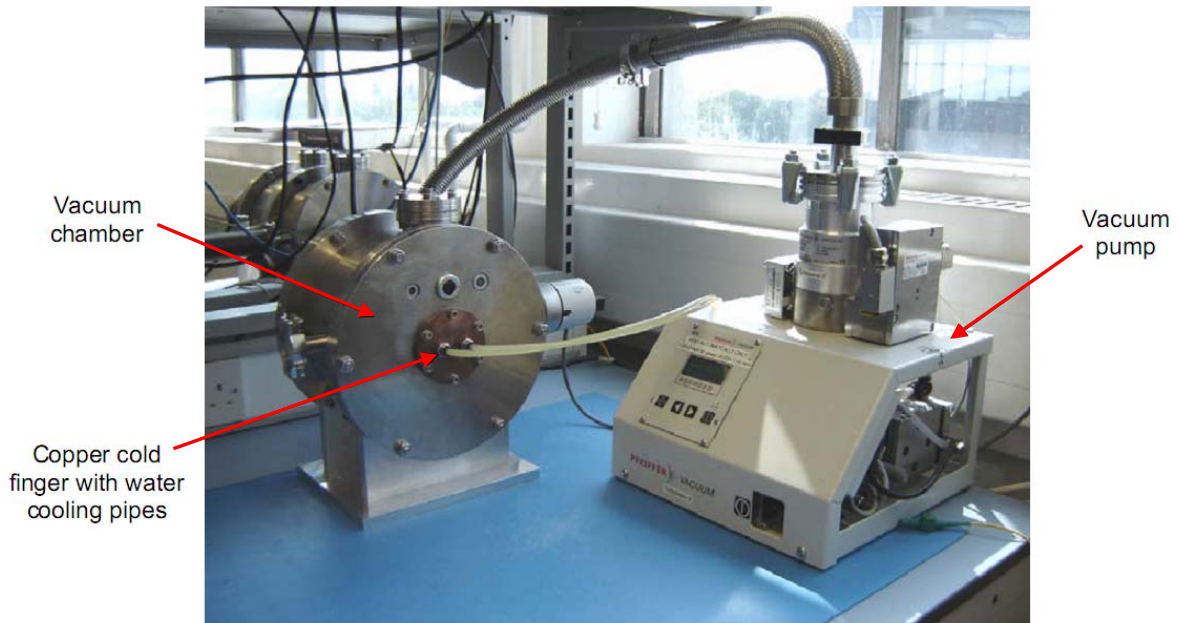


**Figure 4.2:** A photograph of the SCD test facility while using an  $^{55}\text{Fe}$  source

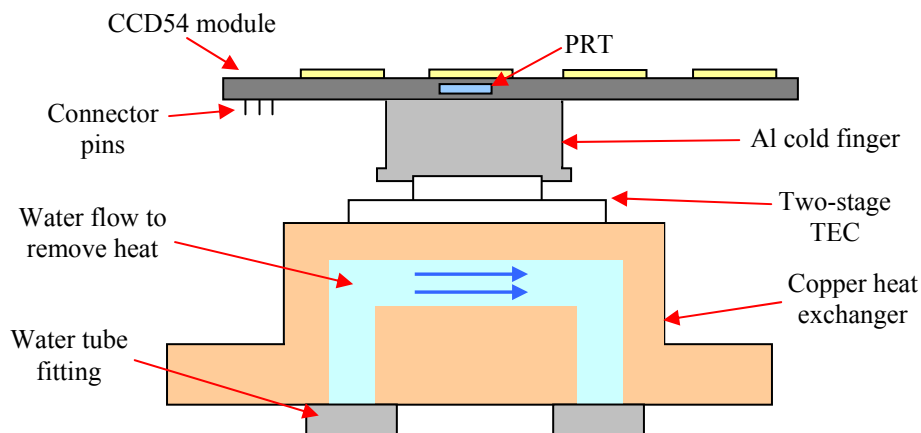


**Figure 4.3:** A schematic of the CCD54 mounting within the vacuum chamber

#### 4.2.2 Experimental Procedure

Once the air was evacuated from the chamber the module was cooled slowly at a rate of  $\sim 1.0$  °C per minute so that device two reached  $-20.0$  °C. A settling time of 1 hour was allowed for the temperature to stabilise,  $\sim 30$  minutes was found to be sufficient. The operational parameters, other than the specific variable being tested, were fixed at the values given in Table 4.1 and Table 4.2 which provide the initial timing values based on quick optimisation tests performed when the CCD54 modules were received. The resulting clock waveform is illustrated in Figure 2.28. Three

runs were conducted for each data point, where a run consisted of 2,000 read-outs of the CCD54, with a region of interest selected to provide 1,980 read-outs for analysis. The temperature was allowed 60 s to settle after each voltage change. The steps used for each voltage and timing are given in Table 4.3.

<i>Parameter</i>	<i>Time (<math>\mu\text{s}</math>)</i>
Int + delay	2.11
Int - delay	0.53
Int time	3.51
Clock pulse width delay	4.53

**Table 4.2:** CCD54 clock timings from initial optimisation study

<i>Parameter</i>	<i>Voltage (V) or Time (<math>\mu\text{s}</math>) tested</i>
Image Clock	5.5 to 13.0 V in 0.5 V steps
Reset Clock	2.5 to 10.5 V in 0.5 V steps
Reset Drain	14.0 to 19.0 V in 0.2 V steps
Output Drain	23.0 to 29.0 in 0.2 V steps
Substrate Voltage	7.0 to 12.0 V in 0.2 V steps
Clock settling	0.24 to 3.00 $\mu\text{s}$ in $\sim 0.23$ $\mu\text{s}$ steps
Reset settling	0.24, 0.53, 1.02, 1.51 and 2.01 $\mu\text{s}$
Int time	1.48 to 5.02 $\mu\text{s}$ in $\sim 0.30$ $\mu\text{s}$ steps
Clock pulse width delay	1.02 to 4.52 $\mu\text{s}$ in $\sim 0.23$ $\mu\text{s}$ steps

**Table 4.3:** Voltages and timings used during testing

The sequence used to control voltages and timings was called ‘sequence 1’, designed to read-out the whole of the device area, resetting the charge packet for each subsequent sample where the device is read-out continually with no integration period. The image produced using sequence 1 which reads out 575 samples in Figure 4.4 is similar to that produced by a standard CCD, however each row corresponds to a single read-out of the CCD54. The X-ray spectrum from the  $^{55}\text{Fe}$  source is shown in Figure 4.5, showing the noise peak, the Mn-K $\alpha$  and Mn-K $\beta$  X-rays peaks and the Mn-K $\alpha$  escape peak. Data analysis was conducted using only isolated events, resulting in the spectrum shown in Figure 4.5. Isolated event selection was provided by the USBREM3 software, removing unwanted events based on their and the surrounding pixel ADC values. The USBREM software is designed for use with a standard 2D CCD read-out, removing events based on vertical selection and not just horizontal selection required for the 1D SCD read-out. The process of event selection is discussed in Section 2.46, and in detail in Section 4.4 including the discussion of event analysis code designed specifically for the SCD.

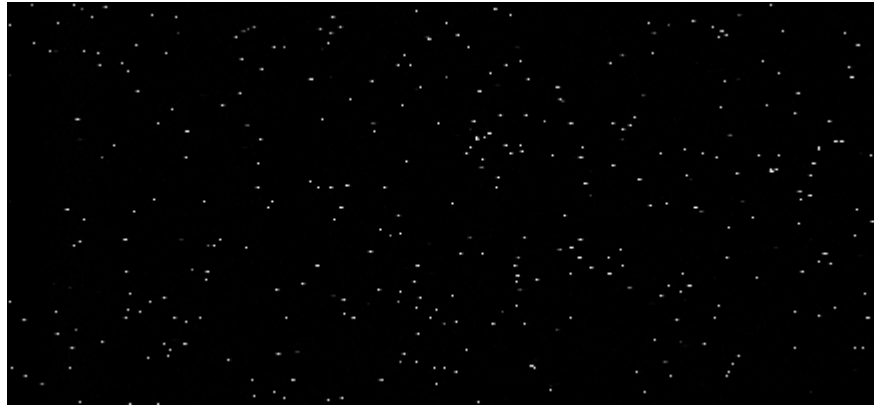


**Figure 4.4:** A 2D pseudo image resulting from 200 read-outs recorded using sequence 1

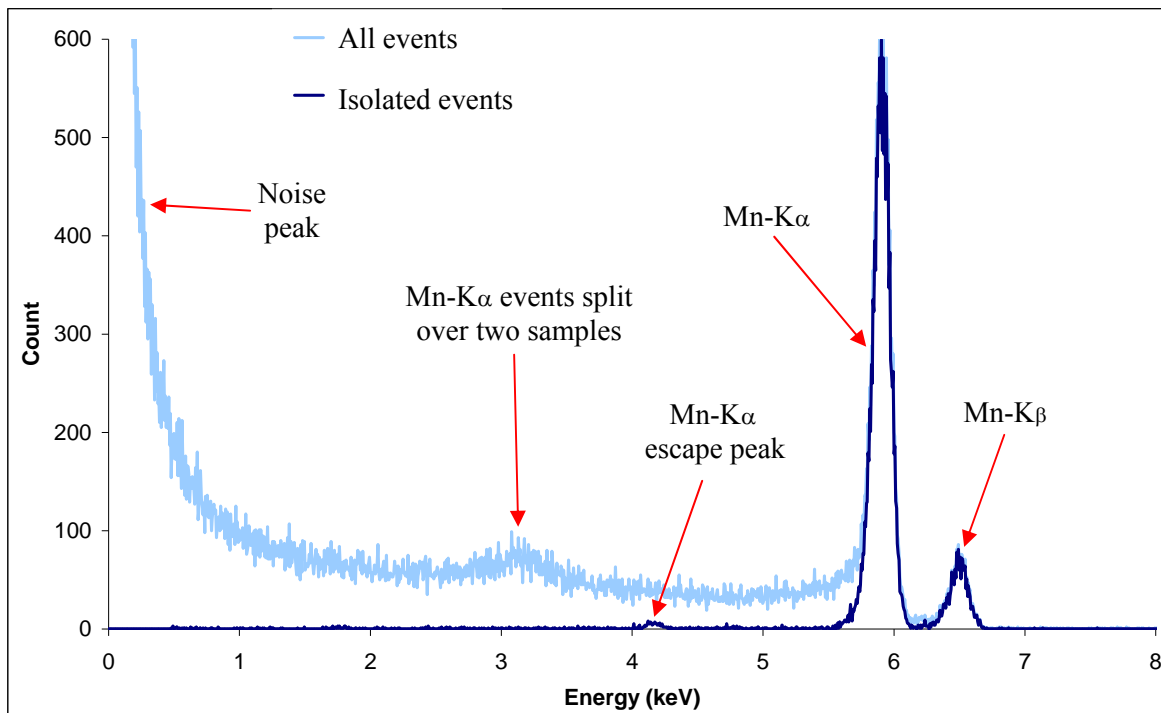


**Figure 4.5:** Spectrum recorded using the  $^{55}\text{Fe}$  source using all and isolated events with the CCD54 held at  $-20.0^\circ\text{C}$

### 4.2.3 I-Clock

The image clock was varied from 4.0 to 13.0 V in 0.5 V steps. At 4.0 V the potential well generated was not deep enough to transport X-ray generated charge packets. As the voltage was increased to 5.0 V, the X-ray events were smeared across multiple read-out samples, the potential not being sufficient to provide efficient charge transfer as described in Section 2.4. Only above 5.5 V was the potential sufficient to provide a resolvable energy spectrum. The read-outs shown in Figure 4.6 show the improvement in charge transfer and the reduction in charge smearing as the I-clock was increased from 4.5 to 5.5 V.

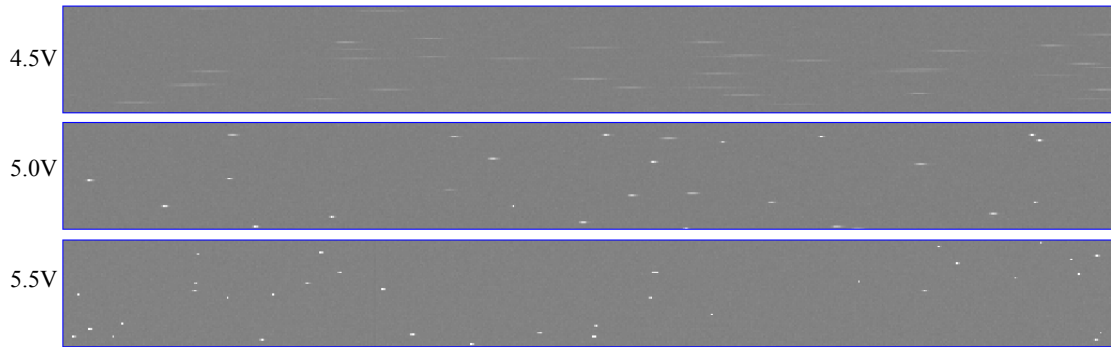


**Figure 4.6:** 100 read-outs of the CCD54 showing the resulting 575 samples taken using an I-clock of 4.5 V, 5.0 V and 5.5 V

The change in the measured energy resolution at Mn-K $\alpha$  and total noise as a function of I-clock voltage are shown in Figure 4.7. The measured energy resolution quickly improves as the charge packets start to be effectively transported, remaining at  $\sim 169$  eV as the voltage is further increased from 6.5 V. The noise level increases from 10 to 12 electrons r.m.s. as a result of increased clock induced charge with increasing clock voltage, as previously discussed in Section 2.5. The counts in the Mn-K $\alpha$  X-ray peak and calibration in eV per ADC channel number are shown in Figure 4.8. The calibration remains at around 30 eV per ADC channel, while the number of counts increases rapidly from  $\sim 250$  at 5.5 V to  $\sim 410$  at 10.5 V, and then slowly increasing to  $\sim 420$  at 13.0 V.

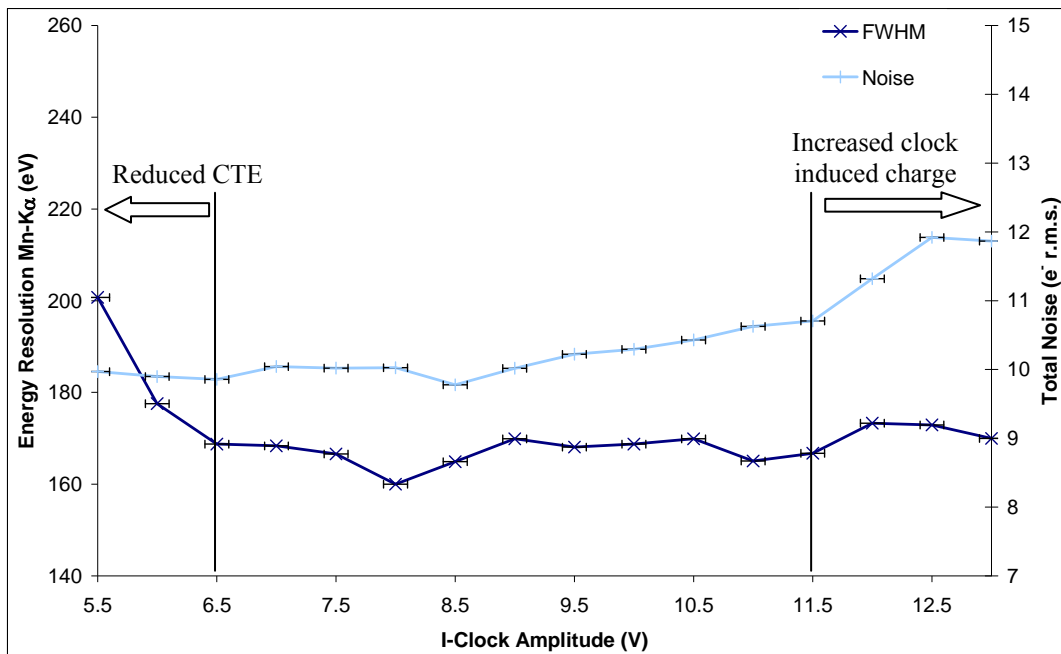


**Figure 4.7:** FWHM and total noise as a function of I-clock voltage

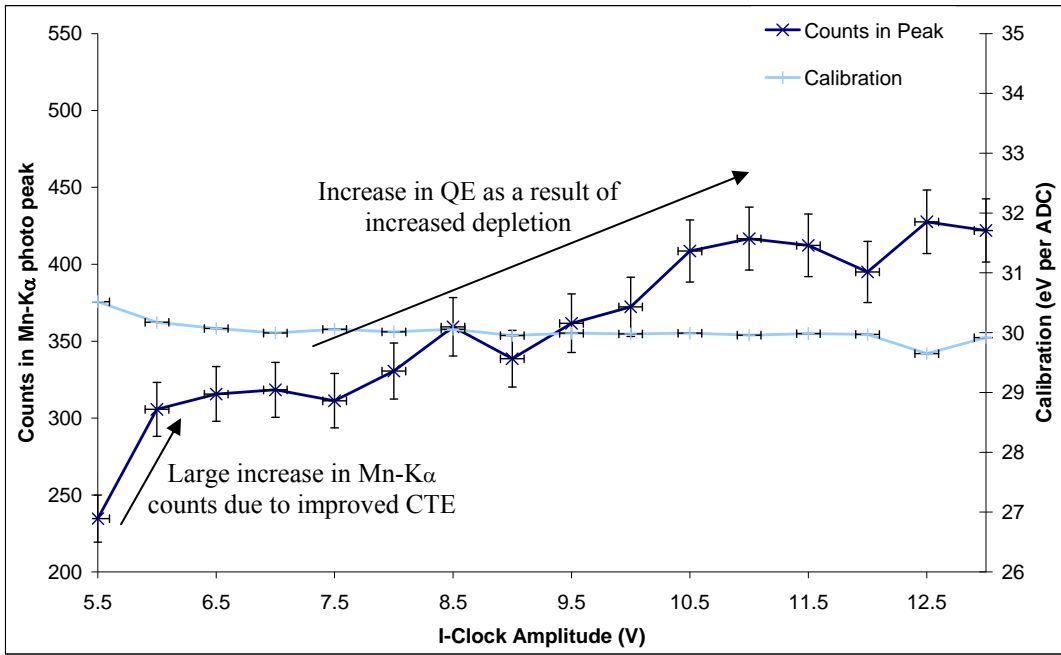


**Figure 4.8:** Counts in the peak and eV per ADC as a function of I-clock voltage

The ratio of isolated to total events and the total number of events is given in Figure 4.9. The total number of Mn-K $\alpha$  events identified remained at  $\sim 774$  within the error as shown in Figure 4.9, while the number of events identified as an isolated event increased linearly with clock voltage. The deeper potential well increases the percentage of X-ray generated charge that is collected within one sample, and improves the transport, of charge collected, across the device resulting in an increase in the number of events detected as isolated events.

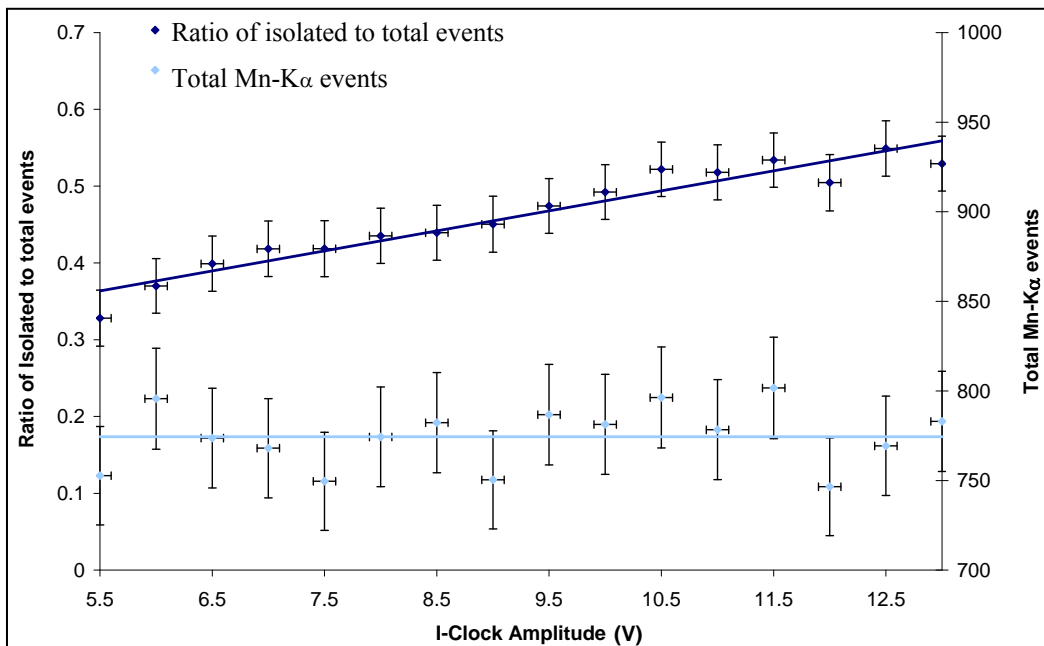


**Figure 4.9:** Ratio of split and isolated events and the total events as a function of I-clock voltage

The change in dark current was measured using the change in the noise peak location with the I-clock at 5.5 V as the reference. The increase in dark current, generated through clock induced charge, is shown in Figure 4.10. Although there is an increase in the dark current generated by having a higher clock voltage, the number of events identified as isolated events increased rapidly; the calibration and measured energy resolution were not greatly affected. Between 5.5 and 10.5 V there is an increase of  $\sim 32 \text{ counts.V}^{-1}$ , while between 10.5 V and 13.0 V there is only an increase of  $\sim 4 \text{ counts.V}^{-1}$ . Over the same voltage range the increase in dark current was  $132 \text{ e}^{-}.\text{sample}^{-1}.\text{V}^{-1}$  and  $89 \text{ e}^{-}.\text{sample}^{-1}.\text{V}^{-1}$  respectively. The increase in charge collection outweighs the increase in dark current. An image clock voltage of 10.0 V was selected for laboratory testing to provide a balance of energy resolution and QE with a non-performance limiting increase in dark current. In situations with a controllable or high ( $<M$ -class solar flare) X-ray flux the I-clock could be reduced to 7.0 V to provide improved energy resolution with a slight decrease in QE. The decrease in the gradient as the image clock approaches 13.0 V suggests that the  $v_s$  is approaching  $v_{sat}$ , as illustrated in Figure 2.23.

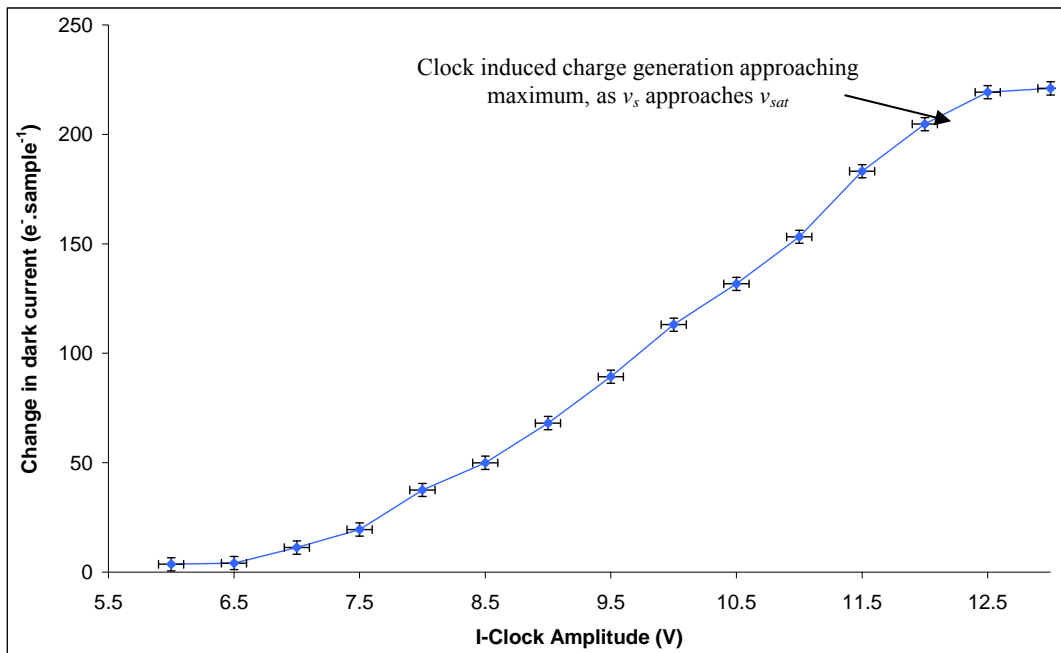


**Figure 4.10:** Relative change in dark current as a function of I-clock voltage

#### 4.2.4 Reset Drain Voltage $V_{rd}$

The reset drain voltage,  $V_{rd}$ , must obey the rule:

$$V_{rd} > V_{og} + \phi_{cho} + V_{sig} + 1$$

where  $V_{sig}$  is the signal voltage, to ensure efficient charge transfer to the output node, illustrated in Figure 3.18. With a  $V_{sig}$  of  $\sim 0.04 \text{ V}$  from a Mn- $K\alpha$  X-ray event, found using the responsivity of the CCD54 with a gain of 11, a  $V_{og}$  of 3 V and taking  $\phi_{cho}$  to be 11 V,  $V_{rd}$  should be greater than 15.0 V. To confirm this  $V_{rd}$  was increased from 14.5 V to 19.0 V in steps of 0.2 V (the voltage step

increase of the XCAM software is not always linear). As  $V_{rd}$  was increased from 14.5 to 15.5 V the noise decreased and the measured energy resolution at Mn-K $\alpha$  increased rapidly as shown in Figure 4.11. This is as a result of less charge spreading into other samples during read-out because the potential well generated by  $V_{rd} < 15.5$  V is not sufficient to efficiently transfer charge. The poor charge transfer is clear in Figure 4.12 from the large improvement in the gain (described by the calibration) between 14.5 and 15.5 V. Between 15.0 and 15.5V,  $V_{rd}$  is sufficient to transfer all the charge produced by the Mn-K $\alpha$  X-rays in agreement with the recommended value. Suggesting that the  $\phi_{cho}$  of the CCD54 tested was between 11.0 and 11.5 V.

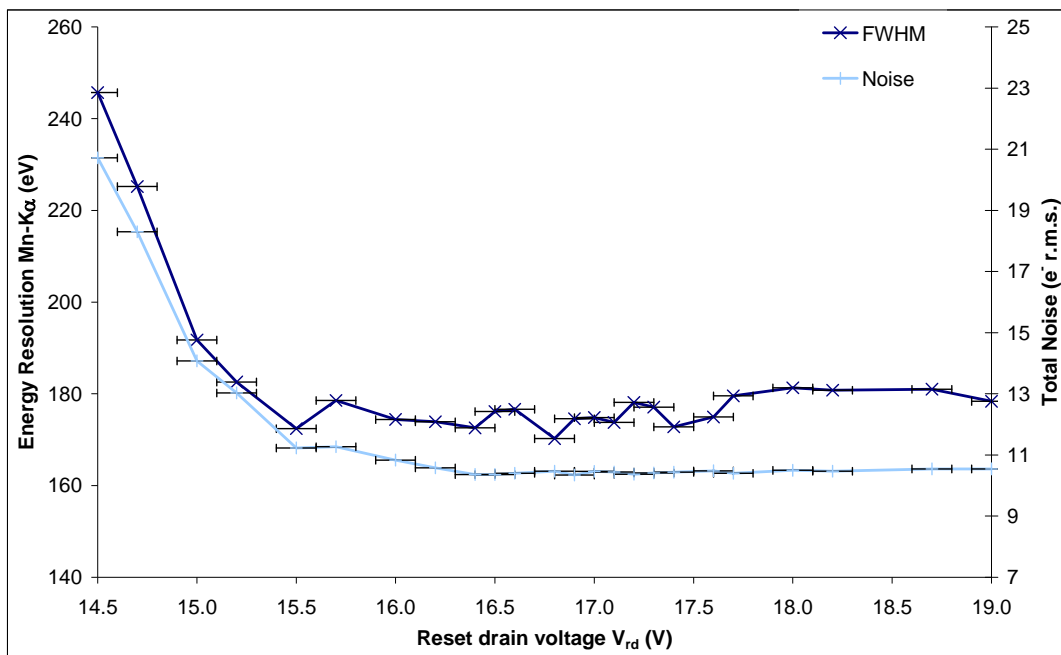


**Figure 4.11:** FWHM and noise as a function of  $V_{rd}$

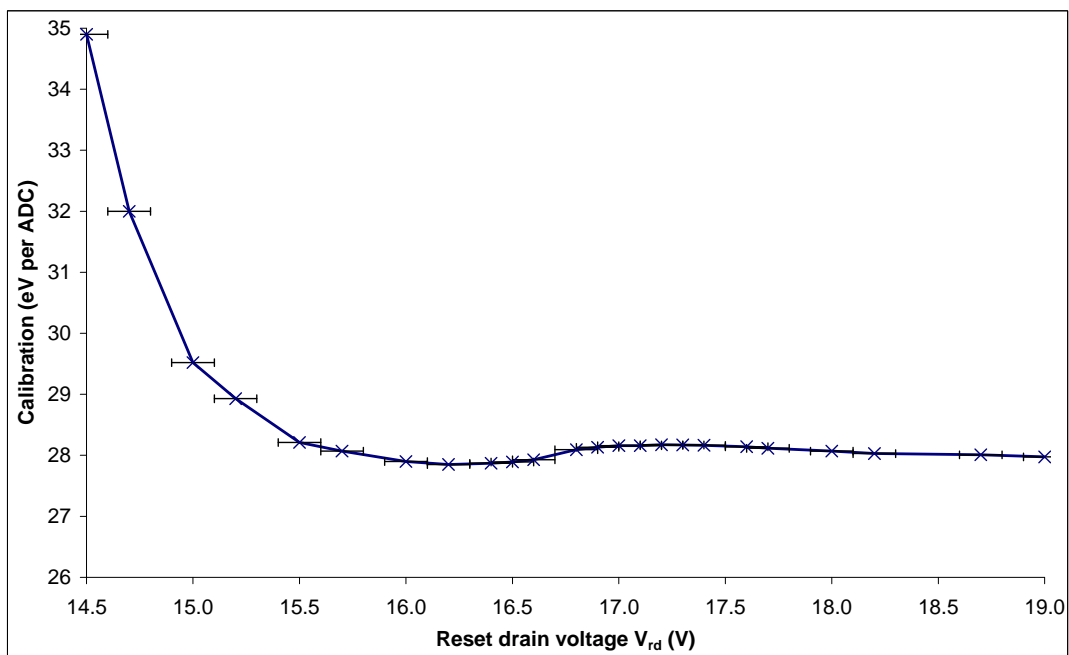


**Figure 4.12:** eV per ADC as a function of  $V_{rd}$

A voltage of 17.0 V was selected for optimum operation, to provide efficient charge transfer for higher energy X-rays in agreement with the initial voltage.

#### 4.2.5 Reset Clock

The reset clock,  $\phi_R$ , must obey the rule:

$$\phi_R + \phi_{cho} > V_{rd}$$

to ensure that the reset transistor is switched on, i.e. at least 6.0 V. The reset clock was varied from 2.5 to 11.0 V in steps of 0.5 V. Below 3.5 V the reset clock voltage was not sufficient to effectively trigger the reset FET, as shown by the large amount of noise and poor energy resolution below 3.5 V in Figure 4.11. As the voltage is increased beyond 3.5 to 11.0 V the noise increased by  $\sim 1$  electron r.m.s., while the measured energy resolution at Mn-K $\alpha$  decreased by  $\sim 30$  eV. The number of counts remained within error. The dip in noise at 5.5 and 6.5 V lead to more detailed testing over the range of 5.0 to 7.0 V in steps of 0.1 V, the change in dark current over this range is shown in Figure 4.12, with the peak location at 5.0 V used as the reference. The relative change in dark current dipped by  $-225 \text{ e}^- \cdot \text{sample}^{-1}$  at  $\sim 6.1$  V, near the recommended operating voltage of 6.0 V. A reset clock voltage of 6.1V was selected for operation, efficiently triggering the reset FET while providing the lowest amount of charge feed through and therefore the optimal operating conditions.

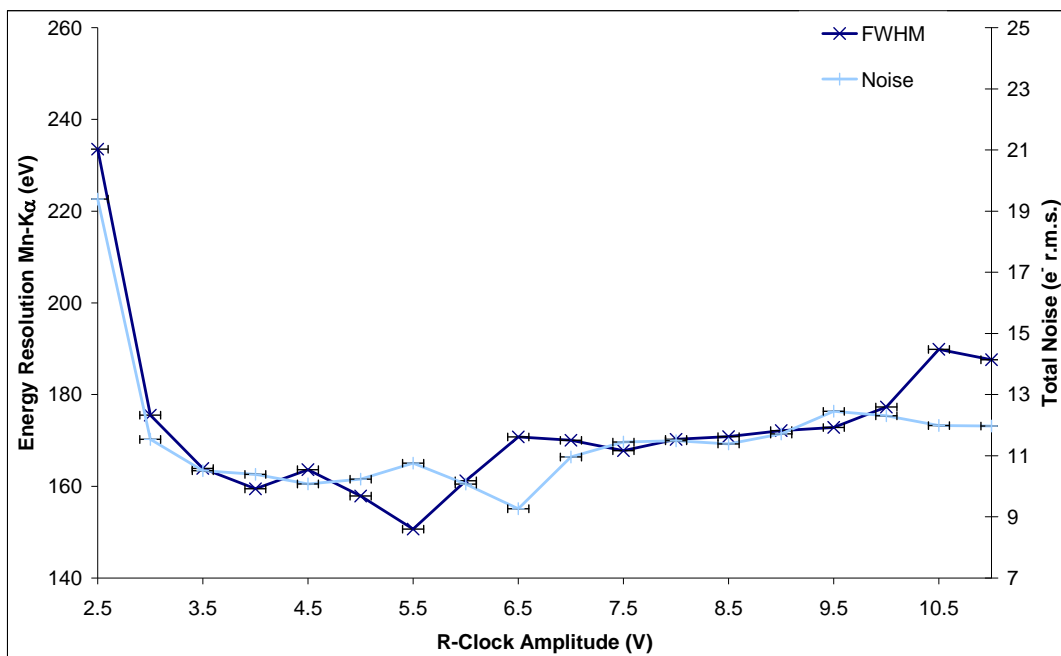


**Figure 4.13:** FWHM and total noise as a function of Reset-clock voltage

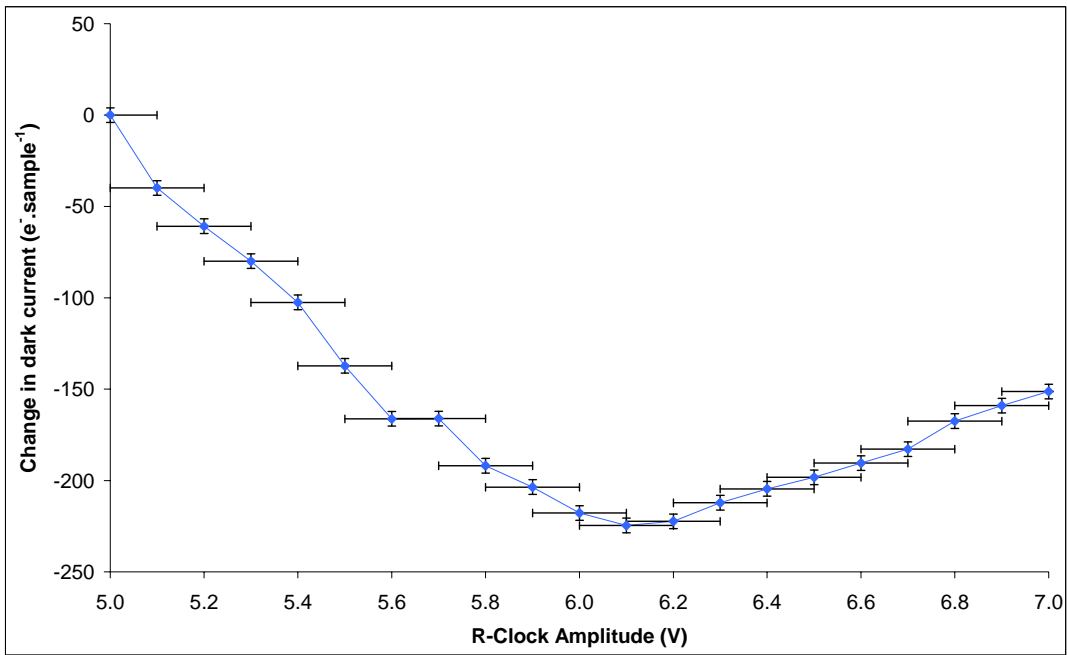


**Figure 4.14:** Relative change in dark current as a function of Reset-clock voltage

#### 4.2.6 Output Drain Voltage $V_{od}$

The output drain,  $V_{od}$ , should be:

$$V_{od} = V_{rd} + \phi_{cho} (\pm 1 \text{ V})$$

to ensure stable operation, i.e. 28.0 V. The output drain voltage was increased from 23.0 to 29.0 V in steps of 0.2 V. With  $V_{od}$  less than 25.0 V the Mn-K $\beta$  peak is un-resolvable (i.e. it is merged with the Mn-K $\alpha$  peak). This is the cause of the large amount of noise below 25.0 V, shown in Figure 4.15, as many X-ray split events form part of the noise peak and the merger of the Mn-K $\alpha$  and Mn-K $\beta$  peaks offsets the calibration (i.e. the peak location of the Mn-K $\alpha$  used in the calibration is shifted). The noise then increased slowly due to increased hot electron generation as discussed in Section 2.5.4, levelling at  $\sim$ 28.0 V. The measured energy resolution at Mn-K $\alpha$  improves after 25.0 V as it no longer includes the Mn-K $\beta$  events, hence the decrease in counts shown in Figure 4.16. The increase in gain is clearly observed in Figure 4.16, still increasing up to the maximum output voltage of 29.0 V. It was decided that 29.0 V would be used to provide the highest gain possible, within  $\pm 1$  V of the recommended  $V_{od}$ .

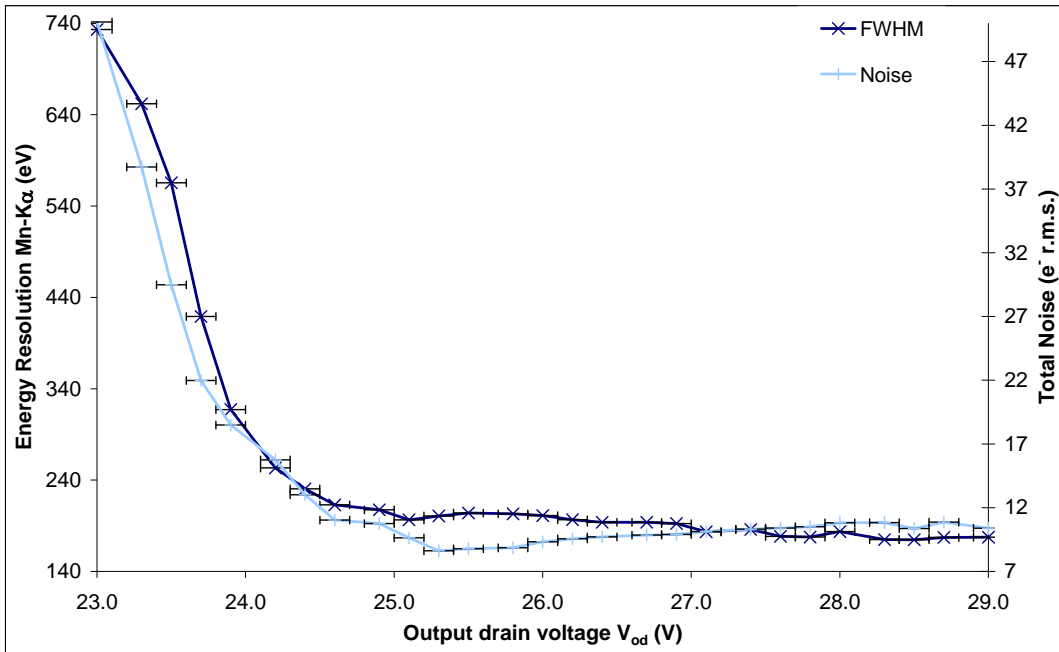


**Figure 4.15:** FWHM and noise as a function of  $V_{od}$

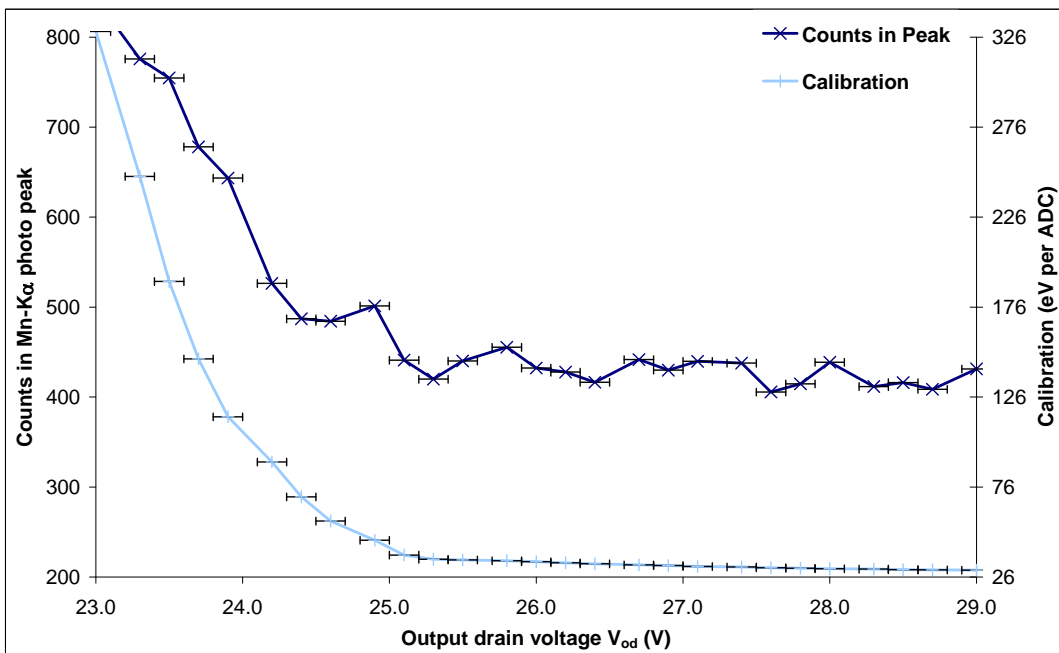


**Figure 4.16:** Counts in the peak and eV per ADC as a function of  $V_{od}$

#### 4.2.7 Substrate Voltage $V_{ss}$

The substrate voltage,  $V_{ss}$ , should be greater than the substrate to substrate pinning potential,  $V_{ssp}$ , to ensure the silicon surface is pinned.  $V_{ssp}$  is the voltage required to pin the silicon surface and is typically in the range of 7.5 to 9.5 V. The substrate voltage was increased from 7.0 to 11.5 V in steps of 0.2 V (the voltage step increase of the XCAM software is not always linear). The effect of inverting/pinning the surface, discussed in Section 2.5, is shown by the decrease in noise as the

surface dark current is suppressed, the surface becoming fully inverted at  $\sim 8.3$  V as shown in Figure 4.17. The measured energy resolution at Mn-K $\alpha$  is also improved with the suppression of surface generated dark current.

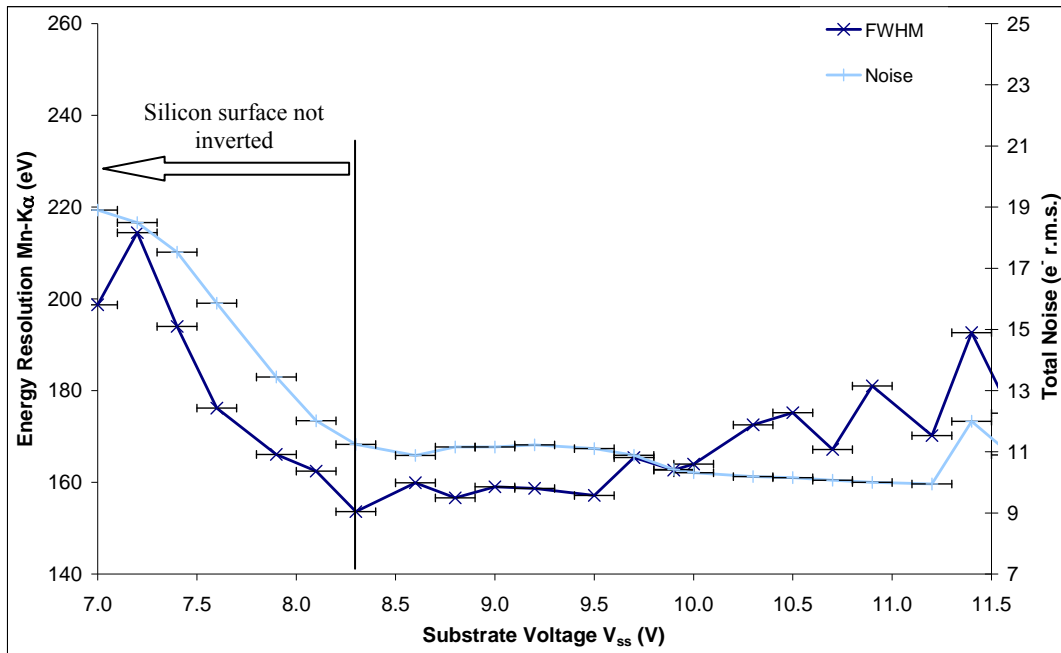


**Figure 4.17:** FWHM and noise as a function of  $V_{ss}$

The change in dark current as the substrate voltage is increased is shown in Figure 4.18, with the peak location at 7.0 V used as the reference. The optimal dark current performance occurs at  $\sim 8.5$  V, the dark current then rises to form a peak around 10.0 V. The dark current then decreases further, however, the resulting gain began to decrease as the potential difference between  $V_{og} + V_{ss}$  and  $V_{rd}$  decreases, reducing the CTE. The resultant decrease in gain causes the Mn-K $\alpha$  peak to start to merge with the Mn-K $\beta$  peak, causing the decrease in measured energy resolution above 10.0 V. It was decided that 10.0 V would be used, allowing the SCD to be operated on the stable peak, 8.5V could be more suitable for performance, however, any voltage fluctuations could cause performance instability with the device only just inverted and to account for radiation induced surface generated dark current which would require  $V_{ss}$  to be increased. To reduce C1XS power consumption a minimum  $V_{ss}$  of 9.0 V was recommended.

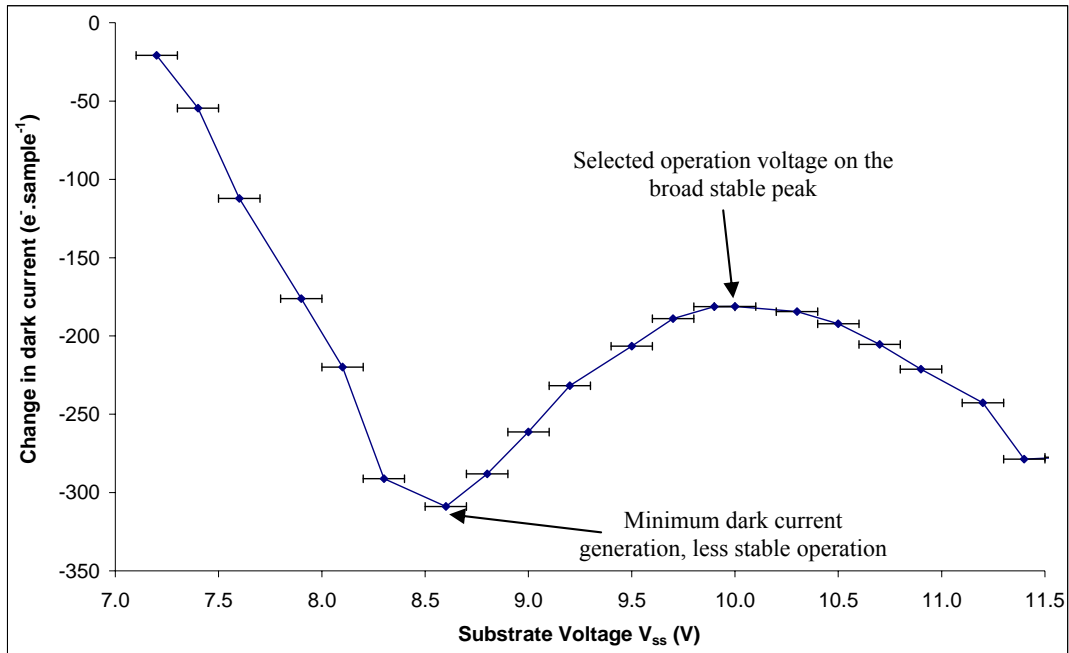


**Figure 4.18:** Decrease in dark current as a function of  $V_{ss}$

#### 4.2.8 Integration Time and Delays

Increasing the integration time over which the reset reference level and the pixel charge level are measured improves the accuracy of the CDS method described in Section 2.5.9, improving the measured energy resolution and noise performance as shown in Figure 4.19. The number of X-ray events detected within a single read-out increases linearly with increased read-out time, as shown in Figure 4.20. To avoid the risk of detecting increased pile up and increased dark current (dark current generation does not change) the read-out time should be as low as possible. The Int time should be selected to allow fast read-out while minimising the noise. Higher values allow more charge to be sampled, resulting in the observed change in calibration in Figure 4.20 and the improved noise performance due to the CDS process.

An integration time of  $4.53 \mu\text{s}$  was selected to provide the optimal energy resolution and noise performance, while also providing a high count rate and an effective amount of gain, while not leading to an excessively long read-out time. The two delays, clock and reset settling, were set to ensure that the effects of capacitive coupling are removed and that the signal had stabilised before the integration began, both by using the output trace in Figure 2.28 and by testing the energy resolution and noise performance.

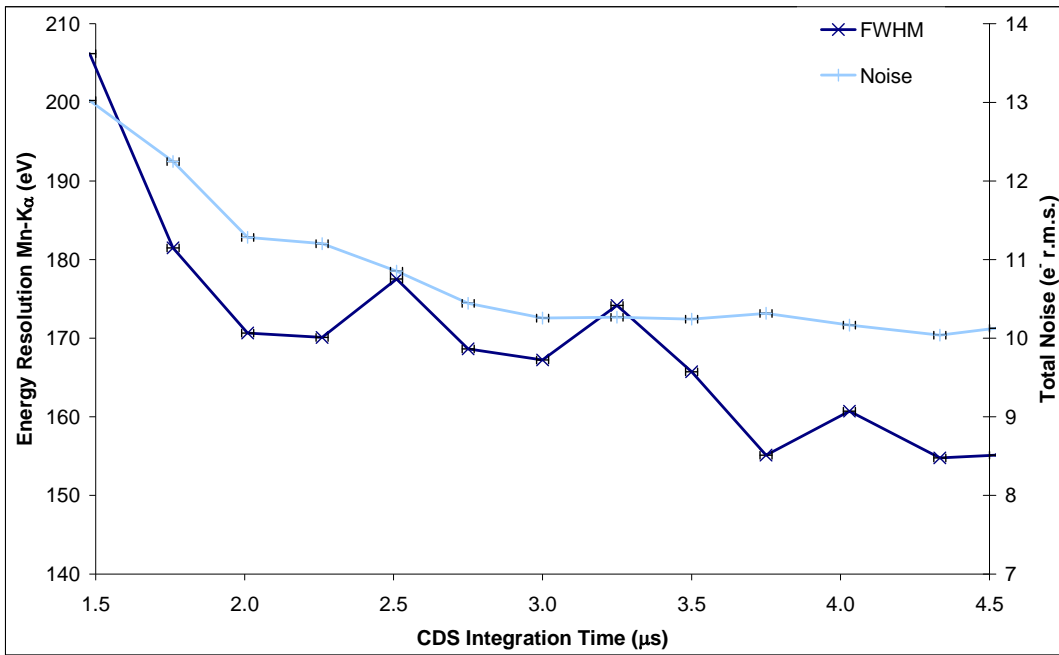


**Figure 4.19:** FWHM and noise as a function of integration time

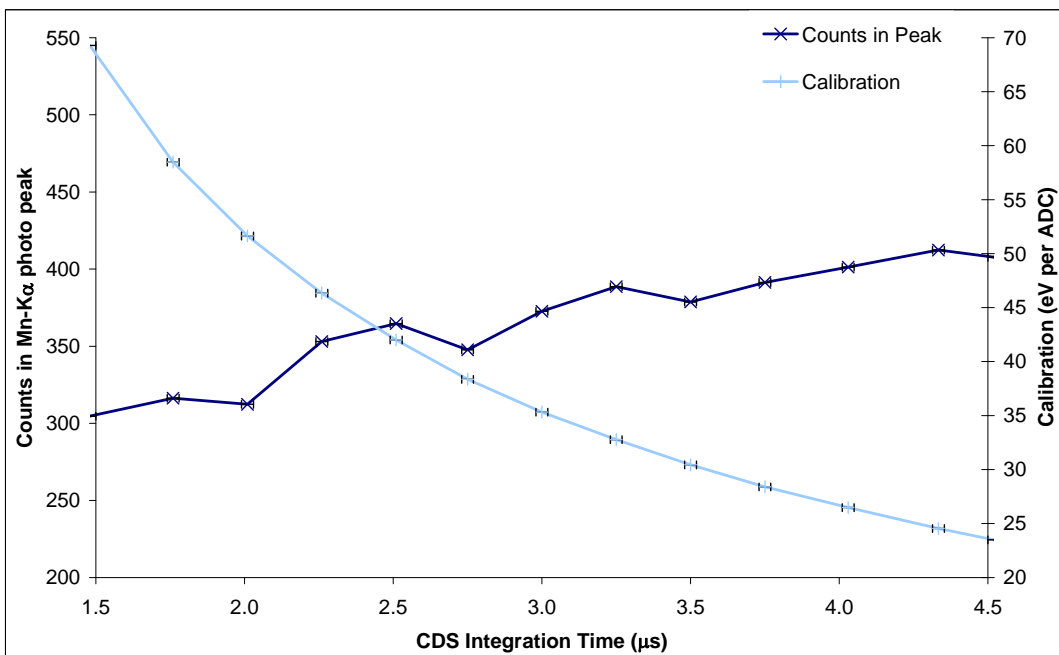


**Figure 4.20:** Counts in the peak and eV per ADC as a function of integration time

#### 4.2.9 Conclusion

The voltages and timings were selected to provide optimal laboratory testing conditions and to provide stable operating conditions with a relatively quick read-out (one read-out takes 0.0126 s). It was predicted that the overall gain at this stage of testing would not be sufficient to effectively resolve the magnesium, aluminium and silicon  $K\alpha$  X-ray peaks should the device be subject to radiation damage. A resistor in the pre-amplifier circuit was replaced with one of half the resistance

to improve the gain from 24 eV per ADC channel to 12 eV per ADC channel. The recommended operation voltages and timings are given in Tables 4.4 and 4.5 respectively following the study described above.

<i>Clock/Bias</i>	<i>Voltage (V)</i>
Image	10.0
Reset	6.1
$V_{od}$	29.0
$V_{rd}$	17.0
$V_{og}$	3.0
$V_{ss}$	10.0

**Table 4.4:** Voltages recommended for use with the CCD54

<i>Parameter</i>	<i>Time (<math>\mu s</math>)</i>
Clock settling	2.11
Reset settling	0.53
Int time	3.51
Clock pulse width delay	4.53

**Table 4.5:** Clock timings recommended for use with the CCD54

### 4.3 Pre-Flight Device Characterisation

There were fourteen CCD54 modules available for flight selection, a total of fifty six devices. The aim of the work presented in this section was to test all the modules and make a recommendation for six of them to be used in C1XS. It was important that the selected devices perform well as a group, therefore both devices of poor and above average performance would not make a good flight device. A point scheme was setup to allow selection of the most suitable modules to be made.

#### 4.3.1 Experimental Arrangement

The CCD54 module being tested was housed inside a camera head, shown in Figure 4.21. The camera head was designed to limit unwanted X-ray scatter from inside the vacuum chamber. The vacuum test facility and equipment used is the same as described in Section 4.2 with the addition of an Oxford instruments XTF5011/75 TH X-ray tube (tungsten filament) and an octagonal target holder on a rotary feed through, with the CCD54 module now mounted on a shapal (aluminium nitride ceramic) cold finger. A copper and aluminium target were attached to the target holder at 45° to the incident X-ray beam. The rotary target holder allows multiple targets to be fluoresced without the need to warm up the CCD54 and bring the chamber up to atmospheric pressure.

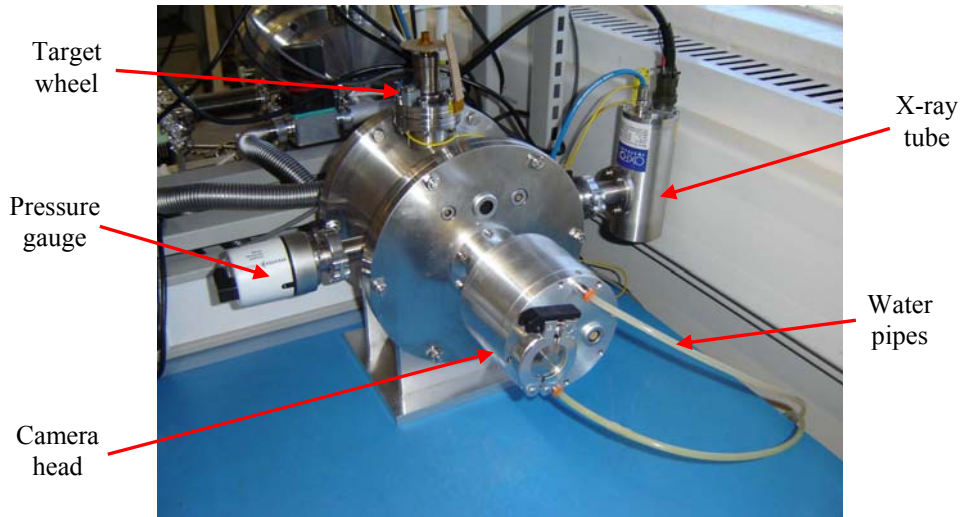


**Figure 4.21:** A photograph of the SCD Test facility while using an X-ray tube

### 4.3.2 Experimental Procedure

Data were taken using sequence 1 at  $-10.0$ ,  $-20.0$ ,  $-30.0$  and  $-40.0$  °C. The reason for taking readings at  $-40.0$  °C was due to the possibility of a C1XS lunar operating temperature below  $-30$  °C to as low as  $-70.0$  °C for a small part of the mission. Three runs were conducted at each temperature for both the aluminium and copper target, where a run consisted of 2000 read-outs of the CCD54 with analysis performed on 1980 of these read-outs (due to the ROI selection in the USBREM3 software). The temperature was allowed 30 minutes to settle after reaching each target temperature to ensure the temperature was stable to within  $\pm 0.2$  °C.

Data were also taken at  $+20.0$  °C, and the temperatures given above, using ‘sequence 2’. This sequence was used to integrate the charge, providing a programmable delay between successive line read-outs, effectively an image integration period programmable in units of ms between 1 and 15 ms. Data were acquired using 10 ms. An image produced using sequence 2 is displayed in Figure 4.22. The characteristic triangular profile shown in Figure 4.23 is a result of the device structure, where the magnitude of the dark current relates to the area of the electrode under which it was integrated. Any bright defects in the device are clearly visible using sequence 2 as shown in Figure 2.23. Using sequence 1 at  $20.0$  °C these bright defects are undetectable due to the removal of the image integration period. The tails shown to the right of the bright defects are as a result of charge being left behind after a transfer, i.e. poor CTE due to trapping.

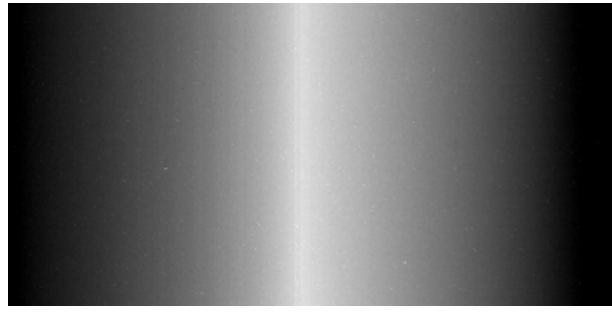


**Figure 4.22:** A pseudo image of 150 linear SCD read-outs recorded using sequence 2

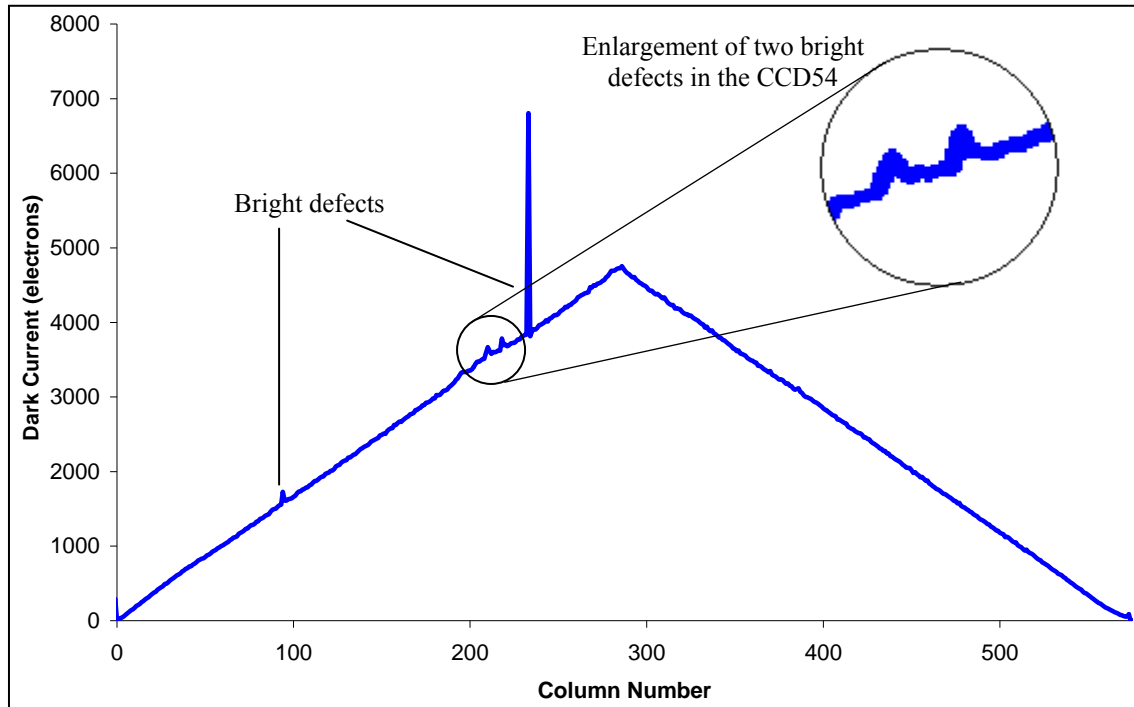


**Figure 4.23:** The characteristic triangular dark current profile of an SCD with a 10 ms integration

The testing conducted for each device was divided into cosmetic quality, functionality, and performance:

**Cosmetic quality:** Visual inspection of the devices reporting ‘particulate matter’ and bond wire condition.

**Functionality:** Sequence 2 was used to test for correct operation, to record the dark current profile, and to observe any bright/dark defects.

**Performance:** The energy calibration was performed using the Cu-K $\alpha$  X-rays, followed by the measurement of the energy resolution of the Cu-K $\alpha$  and Al-K $\alpha$  X-ray peaks, and the noise, using sequence 1. Energy linearity was also investigated using the position of the Cu-L $\alpha$  X-ray peak. Gain was also recorded.

The measured energy resolution of devices across a module was found to vary, with devices 2 and 3 providing the best performance. Only device 2 and half of device 3 are physically held on the cold finger, experiencing a slightly lower operating temperature than devices 1 and 4. A PRT was mounted onto the module ceramic opposite each device, with a fifth PRT mounted on the cold finger. One temperature controller was connected to the PRT mounted onto the cold finger and set to temperatures between 20.0 °C and -40.0 °C in 5.0 °C steps. A time of 1 hour was allowed for the temperature to settle after each temperature change (30 minutes had been demonstrated to be sufficient). This allowed the temperature across the module to be mapped, and the generation of an equation to find the device temperature based on just the temperature of device 4.

The temperature profile of the module at cold finger temperatures of 0.0 °C, -20.0 °C and -40.0 °C is shown in Figure 4.24, ~90% and ~70% of device 2 and 3 are held over the cold finger respectively. The heat generated within the module is as a result of the static and dynamic power dissipation of the clocks and biases provided to the module. The profile shown in Figure 4.24 with device 1 the warmest and device 2 the coolest is as a result of device 1 being next to the connector pins, device 2 and 3 being partially held over the cold finger and device 4 held away from the cold finger. The cooling to device 1 and 4 is limited as a result of distance from the cold finger and the location of the connector pins.

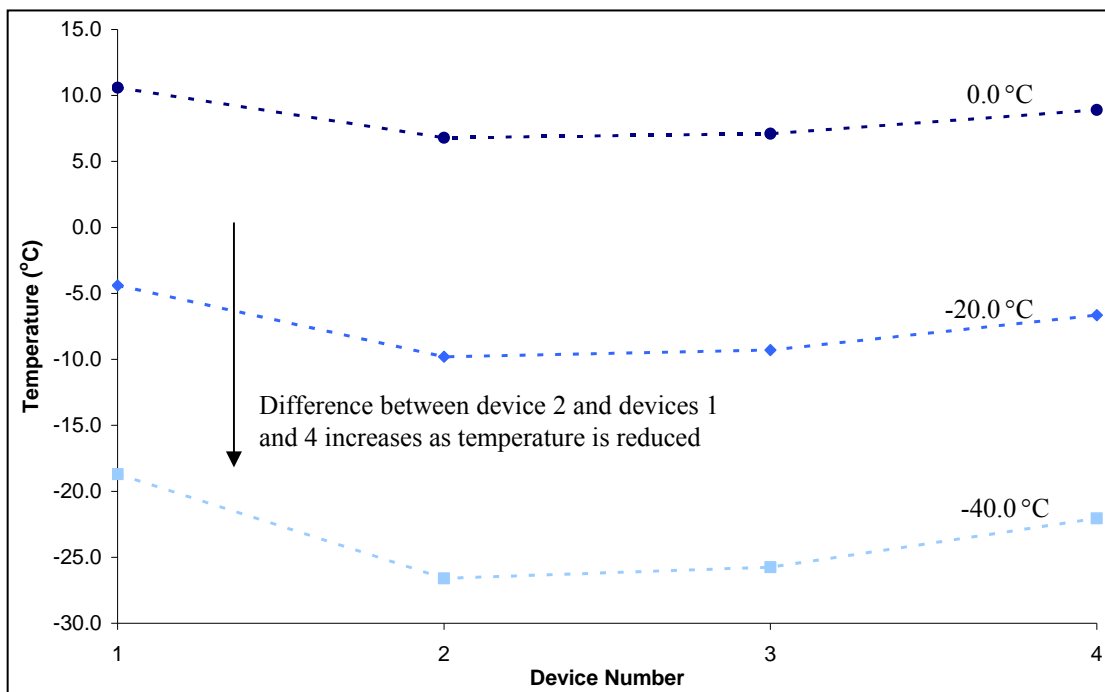


**Figure 4.24:** Temperature profile across the CCD54 module at different cold finger temperatures

### 4.3.3 Summary of Results

The first factor to be highlighted was the importance of uniform cooling of the entire CCD54 module. Only device 2 and half of device 3 are physically held on the cold finger and these were found to provide the best performance due to their slightly lower operating temperature. The spread in energy resolution of the Cu-K $\alpha$  X-ray peak from each device of the ten best modules as a function of temperature is shown in Figure 4.25. The reduced performance of devices 1 and 4 is clear in Figure 4.25 at -10.0 °C and -20.0 °C (cold finger temperature) as a result of the warmer operating temperature. Rapidly improving as the devices were cooled further to -40.0 °C and device position on the cold finger is no longer relevant to performance, i.e. device temperature is below  $\sim$  -20 °C where the dark current is suppressed.

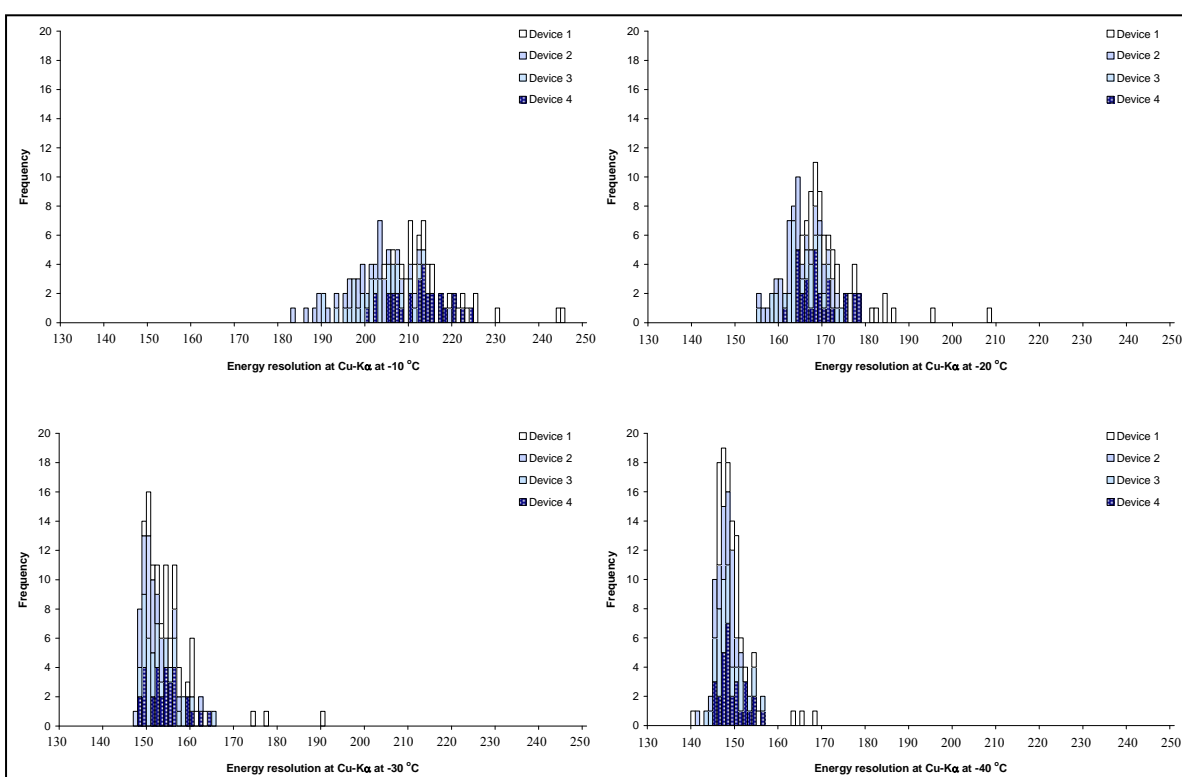


**Figure 4.25:** The FWHM of the Cu-K $\alpha$  X-ray peak from the ten best modules as a function of temperature

The initial assessment was based on the dark current profile, measured energy resolution and noise performance. Module 4 failed, as the devices produced no read-out. The secondary assessment was based on the number of bright defects. As already discussed, the bright defects were not detectable using sequence 1. Module 5 had a number of bright defects yet still performed well. A points scheme was setup where devices received a negative score equal to half the number of bright defects, a positive score for being within one standard deviation of the average energy resolution and noise of all 52 devices, and for having a low dark current profile. Using this scheme, six

modules were characterised as flight quality, four as flight spare, three reject, and one fail. The average energy resolution, noise, and standard deviation from the ten modules suitable for flight at each temperature are given in Table 4.6 for Cu-K $\alpha$  and 4.7 for Al-K $\alpha$  X-rays.

<i>Temp</i> (°C)	<i>Device</i>	<i>Average</i>		<i>St Dev</i>	
		<i>FWHM</i> (eV)	<i>Noise</i> (e <sup>-</sup> r.m.s.)	<i>FWHM</i>	<i>Noise</i>
-10	1	234.6	18.2	10.1	1.6
	2	199.6	15.2	8.2	1.0
	3	201.3	15.4	5.9	0.6
	4	211.3	16.7	5.9	0.7
-20	1	173.9	11.3	9.5	1.3
	2	163.9	9.5	4.8	0.6
	3	164.4	9.6	4.5	0.6
	4	168.6	10.2	5.9	0.5
-30	1	157.3	7.9	8.6	1.2
	2	150.7	6.8	3.1	0.3
	3	152.2	7.0	4.0	0.6
	4	153.5	7.1	4.0	0.4
-40	1	149.7	6.5	5.8	1.1
	2	147.0	5.8	2.2	0.3
	3	147.5	6.0	3.2	0.7
	4	148.5	5.9	2.7	0.3

**Table 4.6:** Averaged Cu-K $\alpha$  energy resolution and noise

<i>Temp</i> (°C)	<i>Device</i>	<i>Average</i>		<i>St Dev</i>	
		<i>FWHM</i> (eV)	<i>Noise</i> (e <sup>-</sup> r.m.s.)	<i>FWHM</i>	<i>Noise</i>
-10	1	183.8	17.7	14.6	1.3
	2	159.0	14.7	9.1	0.9
	3	159.8	14.8	7.5	0.6
	4	170.2	16.3	8.2	0.7
-20	1	117.1	10.6	9.4	0.8
	2	103.9	9.0	6.1	0.7
	3	105.1	9.0	4.0	0.5
	4	111.5	9.8	8.2	0.5
-30	1	91.8	7.1	6.9	0.6
	2	85.7	6.3	4.1	0.4
	3	87.4	6.3	4.0	0.4
	4	89.3	6.6	4.9	0.4
-40	1	82.1	5.7	4.3	0.4
	2	77.8	5.4	2.9	0.3
	3	78.8	5.6	4.1	0.4
	4	80.3	5.5	3.9	0.3

**Table 4.7:** Averaged Al-K $\alpha$  energy resolution and noise

The noise results measured using both photo peaks are in good agreement, demonstrating excellent linearity, from the measuring using 400 e<sup>-</sup> generated by Al-K $\alpha$  X-rays and 2,200 e<sup>-</sup> generated by Cu-K $\alpha$  X-rays.

The gain was found to be similar for each device, and the difference in the location in eV of the Cu-L $\alpha$  peak was found to be consistent, with all but two modules within  $\pm 1$  ADC channel. The measured difference between the Cu-L $\alpha$  line at 928 eV and the measured peak location are shown in Figure 4.26 for a number of modules. The calibration was 6.5 eV per ADC channel. This information coupled with the points scheme allows the identification of modules 2, 5, 6, 8, 9, 10, 11, 12, and 13 as being the ones most suitable for selection. Module 1 was not suitable due to the failure of device 2 to provide isolated events (only tested down to -30.0 °C), modules 3 and 7 showed poor performance across all devices, and module 4 was non-functional. Module 7 was found to have a very high dark current, and was retested a second time (7a). The problem was still present and could not be corrected using different voltages. Module 14 was an unlikely candidate due to the poor performance of device 1, although with the exception of the data taken at -10.0 °C, the performance was similar to the other modules.

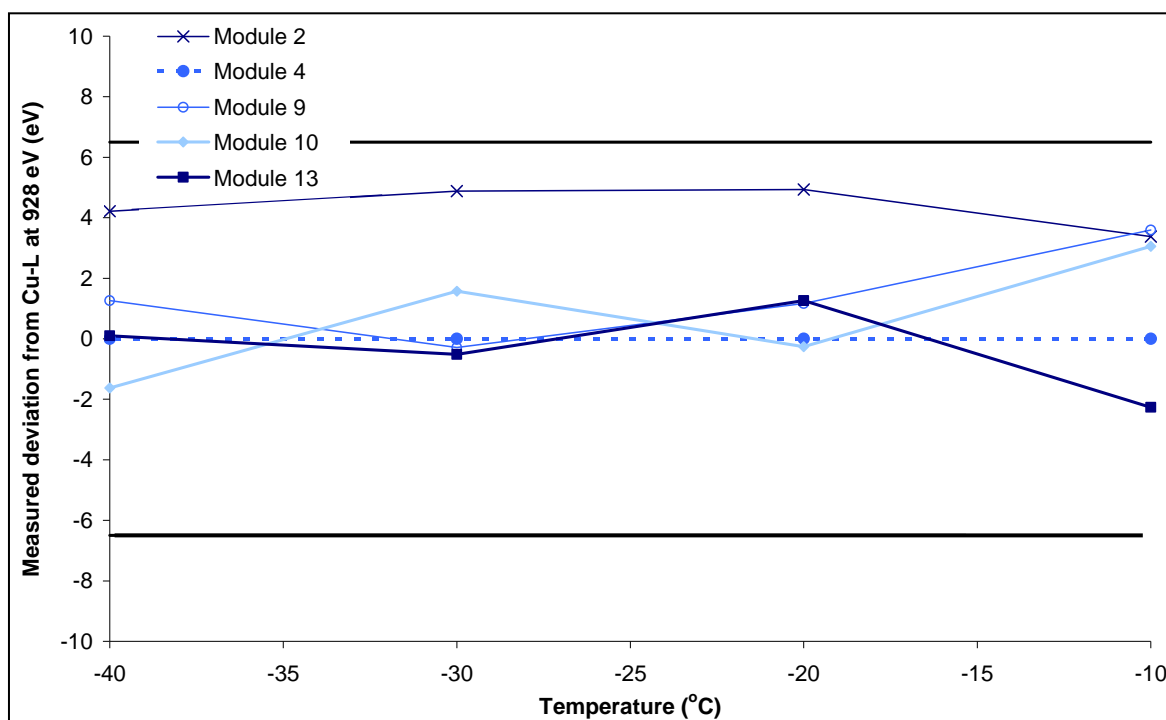


**Figure 4.26:** Module comparison of measured deviation in Cu-L energy vs. temperature, the lines mark  $\pm 1$  ADC channel ( $\pm 6.5$  eV)

Devices found to have a low dark current profile, found using sequence 2 at 20.0 °C, demonstrated a higher level of performance than devices which exhibited a higher dark current profile, as would

be expected from Equation 2.44. It was found that the gradient of the triangular dark current profile could be used to predict the device performance, with the assumption that devices have similar CTE performance. An extrapolation was produced where the gradient at 20.0 °C could be entered to obtain a prediction of the energy resolution for different  $K\alpha$  X-ray energies, to within ~2% of the experimental results. The extrapolation was based on the experimental data acquired during the characterisation work, and some additional tests using different elemental targets. Figure 4.27 shows the theoretical results for device 1 of module 11 and the experimental data points for Al- $K\alpha$  and Cu- $K\alpha$ . This allows for device performance to be assessed and predicted at room temperature, without the need to cool the device or use X-rays.

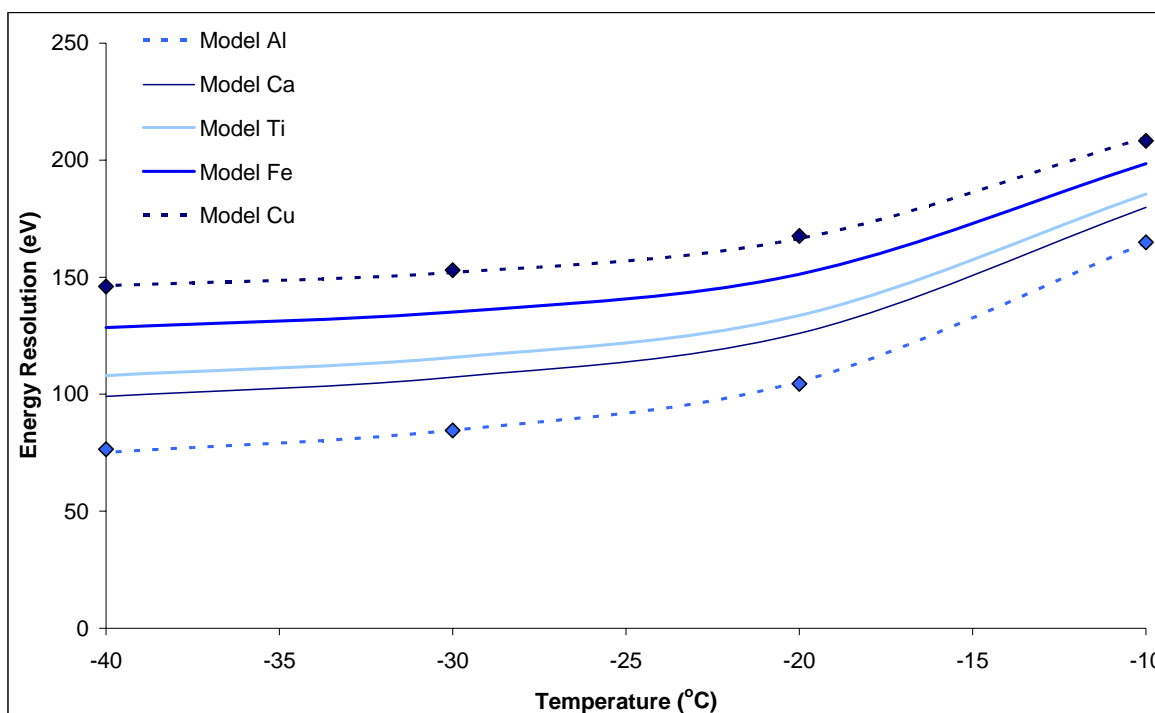


**Figure 4.27:** Theoretical FWHM as a function of temperature compared with experimental data from a copper and aluminium target

#### 4.3.4 Conclusion

The points scheme resulted in Table 4.8, recommending modules 2, 5, 8, 10, 12 and 13 to be used in C1XS, the flight quality modules were selected at RAL to be used. Module 2 failed during later testing and was replaced with module 6. Module 7 exhibited high dark current and was retested as module 7a, clamped tighter onto the cold finger for improved thermal contact. Module 11 offered the highest energy resolution out of all those tested, however for device selection similar performance was preferential. As mentioned early it was preferable to have devices with similar performance, for ease of analysing the large amounts of data that C1XS will produce.

<i>Choice</i>	<i>Mod</i>	<i>Score from sequence 2</i>	<i>Score from performance</i>	<i>Total Score</i>	<i>Rating</i>
1st	<b>12</b>	3	63	66	Flight quality
2nd	<b>13</b>	4	59	63	Flight quality
3rd	<b>5</b>	6	56	62	Flight quality
4th	<b>8</b>	5	55	60	Flight quality
5th	<b>10</b>	0	59	59	Flight quality
6th	<b>2</b>	7	47	54	Flight quality
7th	<b>6</b>	-2	48	46	Flight spare
8th	<b>9</b>	1	44	45	Flight spare
9th	<b>14</b>	-3	38	35	Flight spare
10th	<b>11</b>	6	27	33	Flight spare
11th	<b>1</b>	3	1	4	Reject
12th	<b>7a</b>	0	1	1	Reject
12th	<b>7</b>	-2	0	-2	Reject
13th	<b>3</b>	-4	1	-4	Reject
14th	<b>4</b>	-10	-40	-50	Fail

**Table 4.8:** Module selection table

#### 4.4 X-ray Detection

Previous event analysis had been conducted using tools available in the XCAM software. A set of code was written to take the data acquired using the XCAM software and process it in MATLAB. This would allow events split over multiple samples to be combined and for the threshold used to select isolated events to be varied. The XCAM software creates a 16 bit (values of 0 to 65535) image array (.img file) with ADC values relating to the charge deposited. The MATLAB code was designed to;

- Count the number of isolated events, and split events that cover two to seven samples in a given read-out,
- Allow control over the pixel amplitude threshold controlling isolated event identification,
- Combine split events to form isolated events, identify pile up events,
- Measure the energy resolution (FWHM) of selected photo peaks, with the option to select isolated event or combined events,
- Measure the noise in  $e^-$  r.m.s.,

resulting in a set of code that could quickly analyse acquired data and import selected components into a spreadsheet for further analysis.

The first stage of the code was to define common values, such as a region of interest, the number of files to scan, the number of X-ray peaks and their energies, and the level of analysis to perform on

each peak. The resulting data array was then placed into a 16 bit histogram to allow the noise peak to be selected and a Gaussian fitting routine ( $\text{Chi}^2$  distribution) used to measure its standard deviation. The threshold used to identify isolated events is given by:

$$\text{Threshold} = N_{loc} + \lambda_m \sigma_n \quad (4.1)$$

where  $N_{loc}$  is the ADC value location of the Gaussian fitted noise peak,  $\lambda_m$  is a given value, referred to as the multiplier and used to vary the threshold of event selection, and  $\sigma_n$  is the standard deviation of the noise peak to account for changes in dark current non-uniformity. The XCAM software uses a multiplier of five and this was selected as a starting point. To allow events covering seven pixels to be identified an extra six columns of pixels with ADC values equal to  $N_{loc}$  are inserted at the start and end of a given read-out. The code then scans each row to identify event types identifying when samples are above and below threshold. An event greater than threshold with samples either side less than threshold would be identified as an isolated event. A smaller threshold would result in a less events being identified as isolated. The minimum value for the threshold is  $N_{loc}$ . Figure 4.28 shows example spectra taken using a CCD54 held at around  $-20.0\text{ }^\circ\text{C}$  with fluoresced X-rays from an aluminium, calcium, and copper target at different levels of threshold. The  $\sigma_n$  equalled 24.1, therefore the  $5\sigma_n$  and  $0.5\sigma_n$  additions are equivalent to ADC values of 120.5 and 12.1.

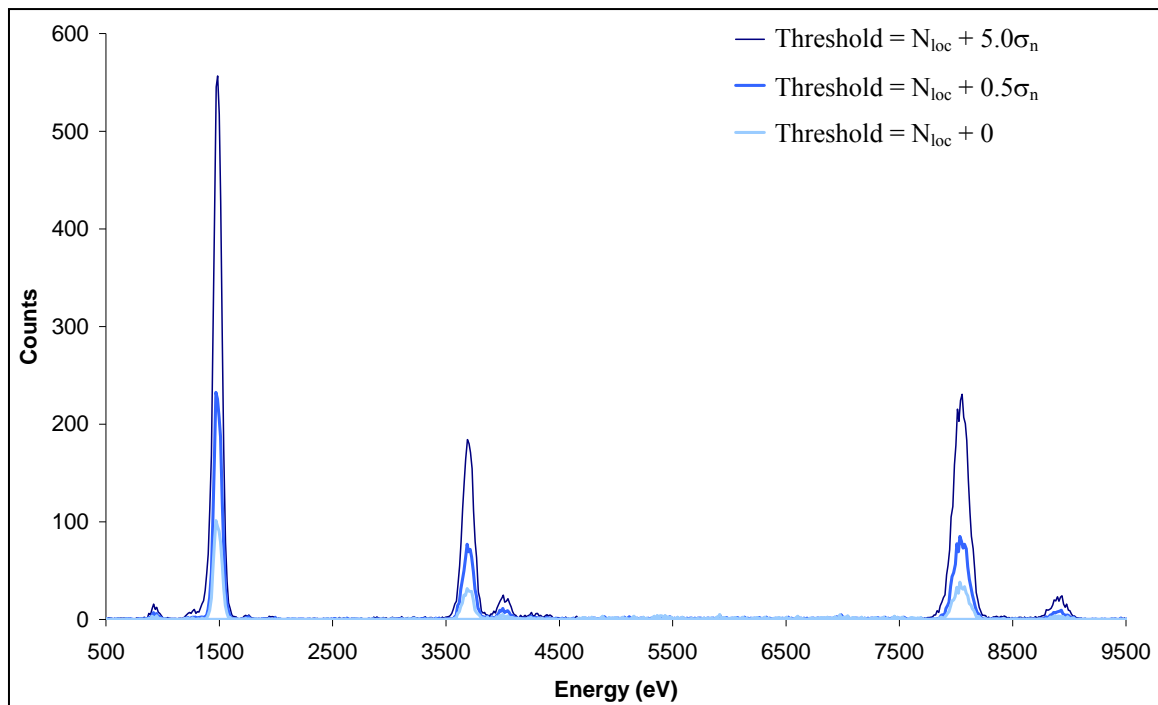


**Figure 4.28:** Spectra produced from an Al, Ca, and Cu target using different levels of threshold

A suitable threshold to use during analysis was selected by comparing spectra taken over the energy range of 1 to 9 keV at temperatures from  $13.0\text{ }^\circ\text{C}$  to  $-40.0\text{ }^\circ\text{C}$ . The selection was based on

the measured energy resolution and counts of the Al-K $\alpha$ , Ca-K $\alpha$  and Cu-K $\alpha$  X-ray peaks. Decreasing the threshold had the greatest effect at higher temperatures due to the increased dark current non-uniformity, as shown in Figure 4.29 which shows the measured energy resolution of the Cu-K $\alpha$  X-ray peak at different  $\lambda_m$  and the predicted energy resolution based on the quadrature summation of the X-ray Fano-limited statistics plus the measured noise.

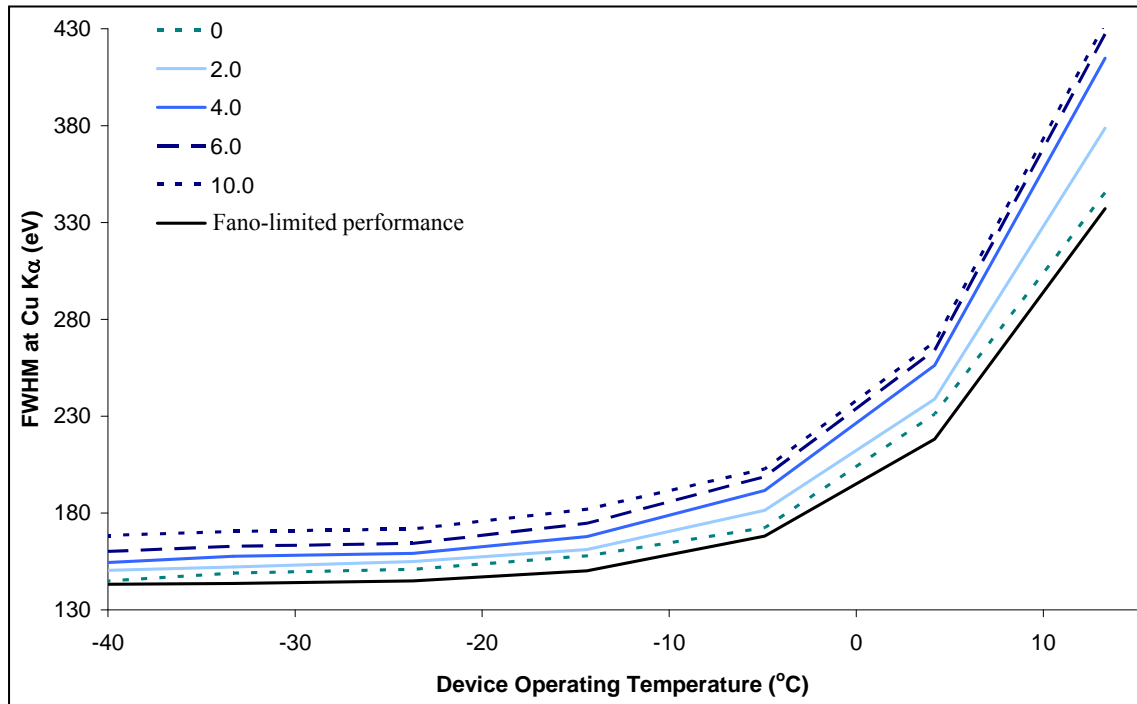


**Figure 4.29:** Measured energy resolution of isolated Cu-K $\alpha$  events found using different threshold multipliers as a function of temperature

$\lambda_m = 0$  provides the closest approximation to Fano-limited statistics as all events which have lost some portion of charge to a neighbouring sample, occurred adjacent to another X-ray event, or are not in an area of mean dark current have been removed. A value of  $\lambda_m = 2$  was selected, as it provided a good measured energy resolution at higher temperatures while not greatly impacting on the number of isolated events recorded for the purpose of good statistics. After events have been classified an image array is created, for isolated events and different levels of combined events, to be used in the next stage of processing

The Gaussian fitting routine is then used on selected X-ray peaks, to find the peak location and its standard deviation. The calibration is given in eV per ADC, based on the highest energy peak location and the  $N_{loc}$ , typically 0.860 eV per ADC. The total noise,  $n_s$ , in electrons r.m.s. is given by:

$$n_s = \frac{\sigma_n \times Cal}{\omega} \quad (4.2)$$

The energy resolution is measured using Equation 2.43, where  $\sigma_x$  has been converted from an ADC value to eV. This process can be applied to each image array created producing an array containing energy resolution, event numbers, and measured and fitted spectra.

Using a histogram of 16 bit values resulted in large output files and a longer processing time than desired. To solve the problem the ADC values in the array imported from the .img files were divided by 16, reducing the size of saved arrays and increasing the process speed while not significantly affecting the results. Unless otherwise stated when using the MATLAB code to analyse the results this method was used.

## 4.5 Quantum Efficiency Analysis

The QE of a device is the fraction of incident photons that provide useful signal at a given energy, discussed in Section 2.6.2. To understand what the detectors are observing it is essential to understand the QE of a device. This allows the correct elemental abundances to be found from experimental data which is essential for C1XS to achieve its mission goals. The QE is dependent on the device operating voltages. The QE test detailed in this section will be required to be completed using the C1XS drive electronics to ensure the correct calibration is used.

### 4.5.1 Experimental Arrangement

The standard vacuum chamber used in the previous experiments was extended to allow for collimation and translation of the fluoresced X-rays, as shown in the schematic in Figure 4.30 [Murray *et al.* 2008]. The same type of X-ray tube is used as discussed in Section 4.3, with the target resting in a target holder. A liquid nitrogen cooled lithium drifted silicon crystal Si(Li) detector was used as a reference detector as it possesses a high QE in the energy range of 5 keV to 20 keV as shown in Figure 4.34. The Si(Li) detector is depleted to  $\sim 4.5$  mm with an active area of  $30 \text{ mm}^2$ , driven with a e2v Titan pulse processor and read out using a Canberra Eagle 4k MCA with the spectra analysed using Genie 2000 software. The rear part of the camera head described in Section 4.3.1 was removed and placed on the face of the flange on the front of the chamber, designed to line up device 2 with the collimator. The Si(Li) detector was adjusted to hold both detector surfaces at the same distance from the target to ensure both detectors receive the same X-ray flux.

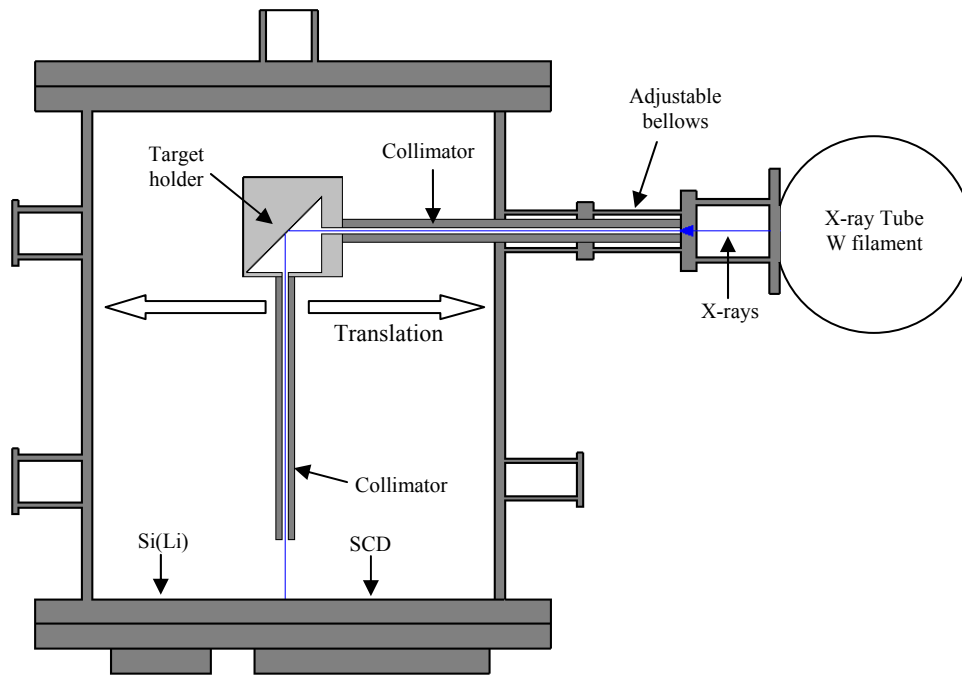


**Figure 4.30:** A schematic of the QE test facility for use with the SCD

#### 4.5.2 Experimental Procedure

The X-rays were collimated towards an aluminium target holder placed at 45° to the incident X-ray beam. The targets given in Table 4.9 were selected to provide a number of data points over the C1XS energy range. To limit unwanted X-ray scatter, the fluoresced X-rays are collimated towards the detector. Gafchromic film (HD-810) was used to confirm that the X-ray photons leaving the collimator would all interact within the detector's surface area, a blue dot indicating the location of the beam. The film has a chemical layer which reacts as energy is deposited. The increase in optical density of the film is proportional to the dose, with the film becoming blue as energy is deposited. The target and X-ray tube can be moved backwards and forwards with the aid of a set of bellows to quickly illuminate the Si(Li) reference detector and then device 2, held at -40.0 °C, of module 17. The same target position ensures the same area is illuminated by X-rays generated by the X-ray tube, and quick repeatability limits the effect of small fluctuations within the incident X-ray beam.

<i>Target</i>	<i>Target Type</i>	<i>Elements</i>			
1	Copper Sulphate	Al	S		Cu
2	Calcium	Ca			
3	NaCl on Steel		Cl		Fe
4	Etna Basalt			Ca	Fe
5	Slate	Si	K	Ti	Fe
6	Mg	Mg			
7	Silicon on Steel	Si			Fe

**Table 4.9:** Target materials selected for use during QE testing

The stability of the X-ray beam was tested by recording the count rate of Cu-K $\alpha$  X-rays over a period of 90 minutes after the X-ray tube had been powered up. Data were recorded using an integration period of 20 s with readings taken every minute. The count rate variation is illustrated in Figure 4.31. Trend lines highlight the improvement to beam stability over time. The instability is as a result of temperature fluctuations in the X-ray tube's tungsten anode. The number of counts in the Cu-K $\alpha$  X-ray peak over a period of 30 minutes for the Si(Li) detector and then the CCD54 were recorded, the bellows moved between each acquisition to ensure repeatability. Data were recorded using an integration period of 30 s with readings taken every minute. Figure 4.32 shows the number of counts detected by the Si(Li) and CCD54 detectors. The difference in counts is due to the different QE of the detectors. The standard deviation of each detector over the 30 minute period was found to be within ~3.5%.

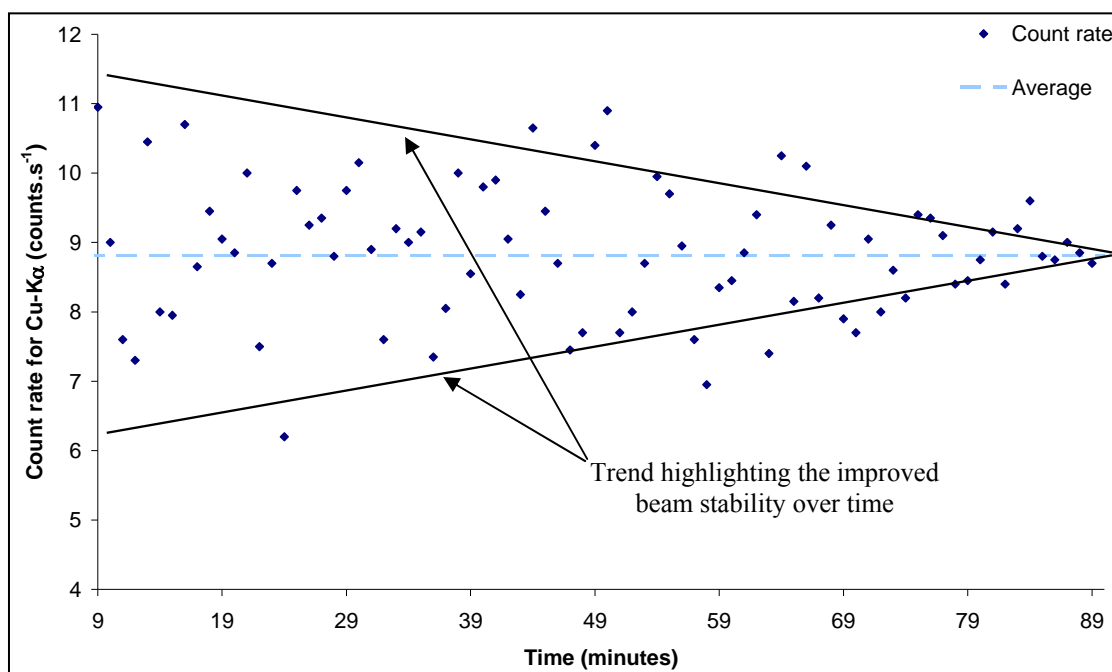


**Figure 4.31:** Count rate of Cu-K $\alpha$  X-rays as a function of time over 90 minutes after powering up the X-ray tube

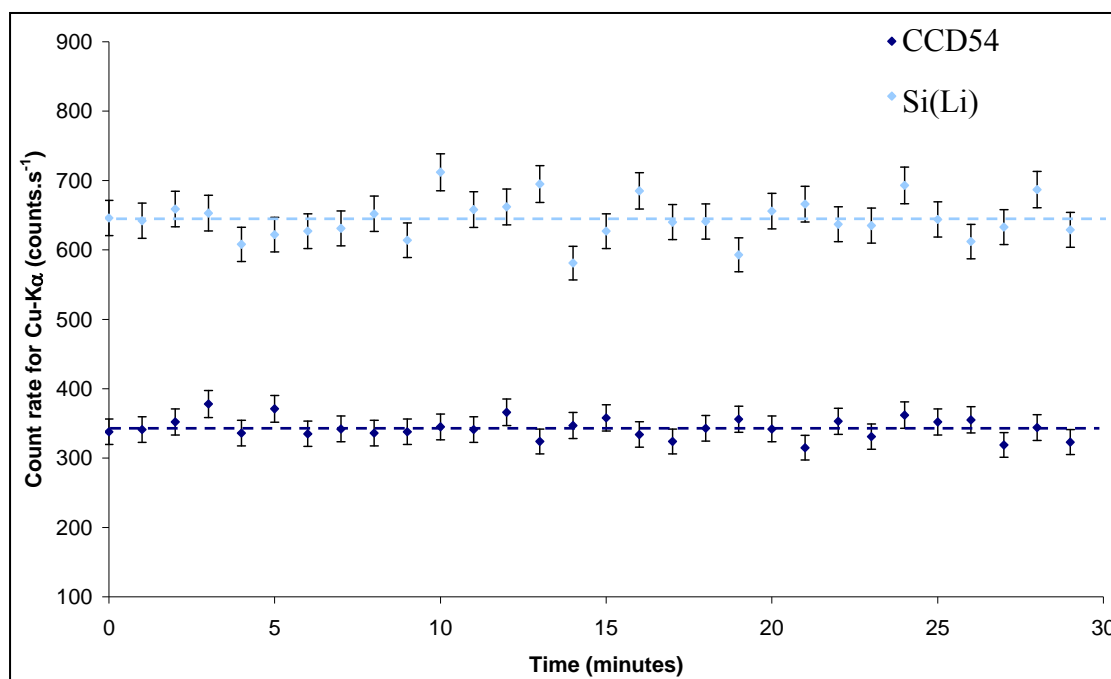


**Figure 4.32:** Counts in the Cu-K $\alpha$  X-ray peak as a function of time using the Si(Li) detector and the CCD54

To collect the data required to find the QE of the CCD54, X-rays were recorded on the Si(Li) detector for 60 s. The target and X-ray tube were then moved to illuminate the CCD54 for 60 s. This process was repeated ten times for each target. The number of counts in the X-ray peak from the Si(Li) detector was found using the Genie 2000 software, the peaks were manually identified and the software's Gaussian fitting routine provides the number of counts within the photo peak. The acceptable error on the counts was set to be 4.5%, where the minimum counts in the photo peak is 500.

### 4.5.3 Experimental Results

The MATLAB code was used to analyse the QE based on using only isolated events and then combining split events over two to seven samples as shown in Figure 4.33. There is a large improvement in QE once events over two samples are included. There was however a corresponding decrease in the X-ray peak energy resolution as the read noise increases due to the inclusion of events spread over multiple samples, Table 4.10 gives the measured energy resolution of Si-K $\alpha$ , Ca-K $\alpha$ , Fe-K $\alpha$ , and Cu-K $\alpha$  X-ray peaks found using different event combinations. If the signal to noise level is high with the photo peaks clearly defined above the noise it would be advisable to only use isolated events, and possibly use a lower threshold to achieve the best possible measured energy resolution. A low signal to noise or higher energy X-rays benefit from event combination as shown in Figure 4.33 by the large increase in QE with event combination at

higher energies. X-ray events below 3,691 eV show little QE improvement after three sample split events were combined while events above 3,691 eV continue to benefit, with up to five sample split events being combined.

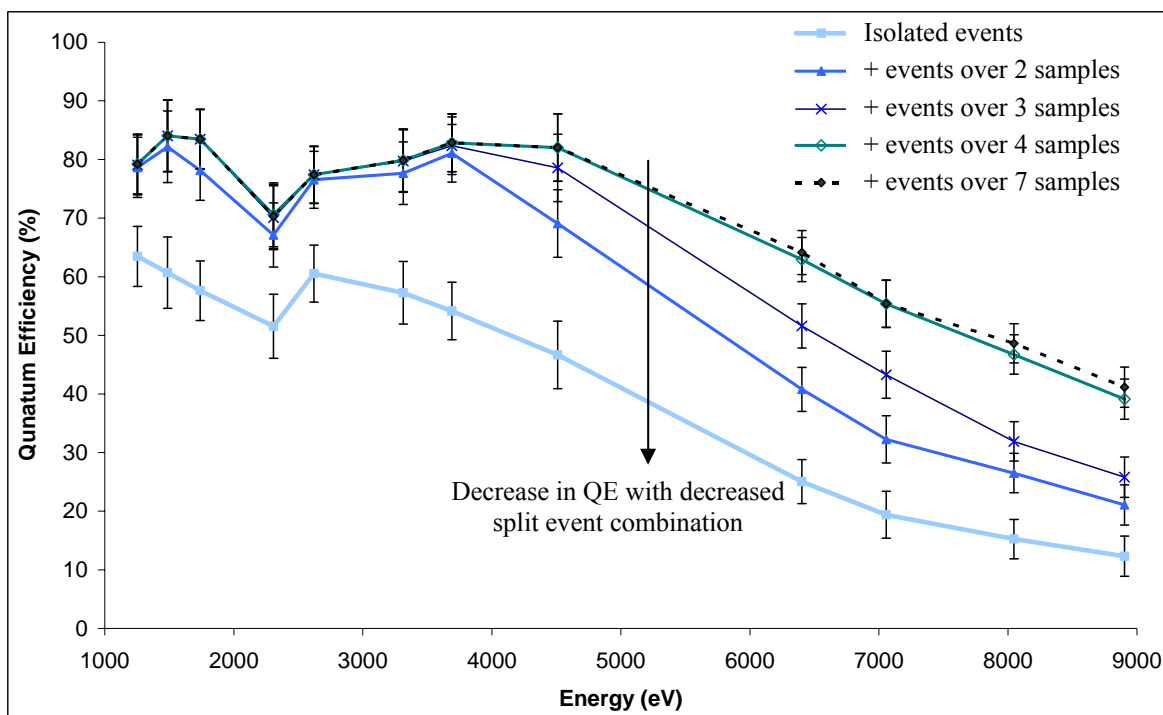


**Figure 4.33:** Quantum efficiency of the CCD54 using different levels of event processing

Element	Energy (eV)	Isolated events	Measured energy resolution (eV)					
			Size of events combined					
			2	3	4	5	6	7
Si	1740	81.6	87	93	94	94	94	94
Ca	3691	108.4	111	114	114	114	114	114
Fe	6403	135.0	140	146	152	157	158	158
Cu	8047	150	155	164	171	177	178	178

**Table 4.10:** Measured energy resolution as a function of combined event size

A fitting routine was used to compare the experimental data, found by combining split events over seven samples, to Equation 2.47 describing the QE of the device. The fitting was based on the difference between the experimental and theoretical data. Found by varying the depletion depth, then based on the difference in calculated and measured QE a score was provided, the highest score was selected. The depletion depth of the CCD54 was calculated to be 42  $\mu\text{m}$ , the line calculated using a depletion depth of 42  $\mu\text{m}$ , found using Equation 2.47, is shown in Figure 4.34. A line with an active depth of 12  $\mu\text{m}$  was fitted to data using only isolated events, showing an effective improvement of 30  $\mu\text{m}$  in depletion depth by combining split events. The spectral data from the

Si(Li) detector and the CCD54 is also included in Figure 4.34 showing the similar energy resolution performance of the CCD54 compared to the Si(Li) detector, even after combing split events. The error on the CCD54 data points is as a result of the 3.5% beam instability and the number of counts in each X-ray peak.

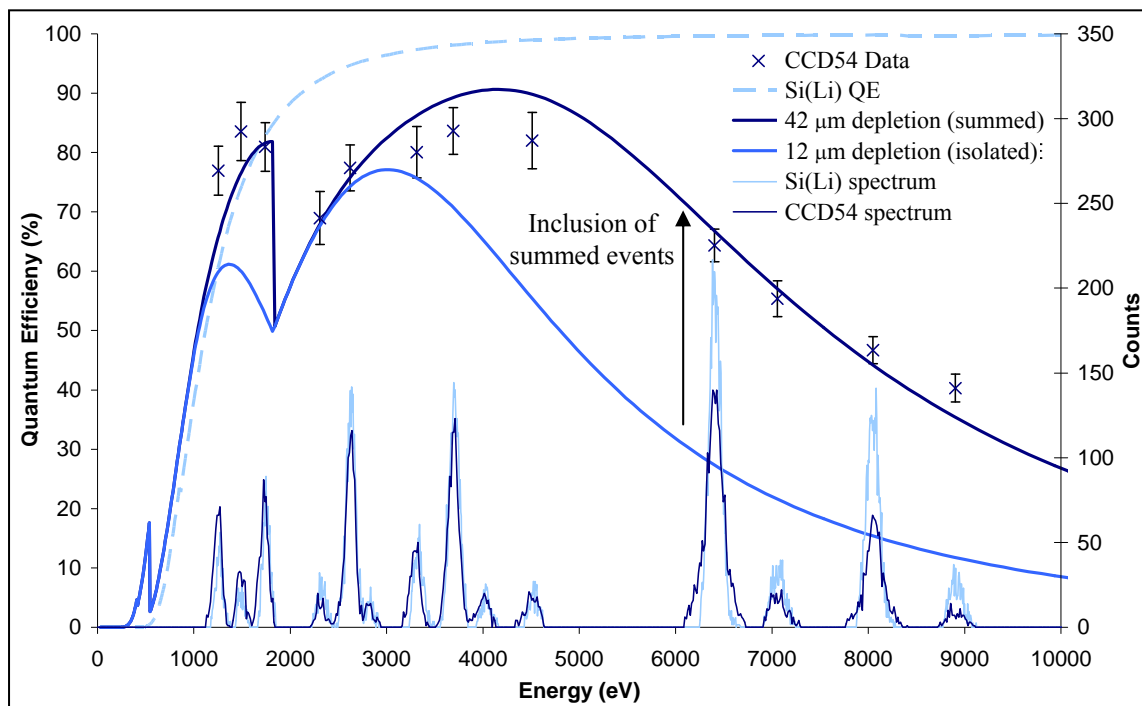


**Figure 4.34:** Measured quantum efficiency of the CCD54 and Si(Li) detector as a function of X-ray photon energy and the results from using Equation 2.47 to find the active depth. The spectra from the CCD54 and Si(Li) detector is also shown

It should be noted that the CCD54s used in C1XS used an aluminium and carbon filter to remove the optical background, with 200 nm of each mounted on the top and bottom of the collimator stack, two layers were used to reduce the risk of pin hole defects [Howe *et al.* 2009]. The effect on the QE is illustrated in Figure 4.35, showing the reduced QE at low energies, below 5 keV. The Al K-edge results in a reduction of 26% in the QE at Si-K $\alpha$  (1,740 eV). However, compared to the increased photon shot noise and non-uniformity from optical light exposure the decrease in QE has a negligible effect on instrument performance.

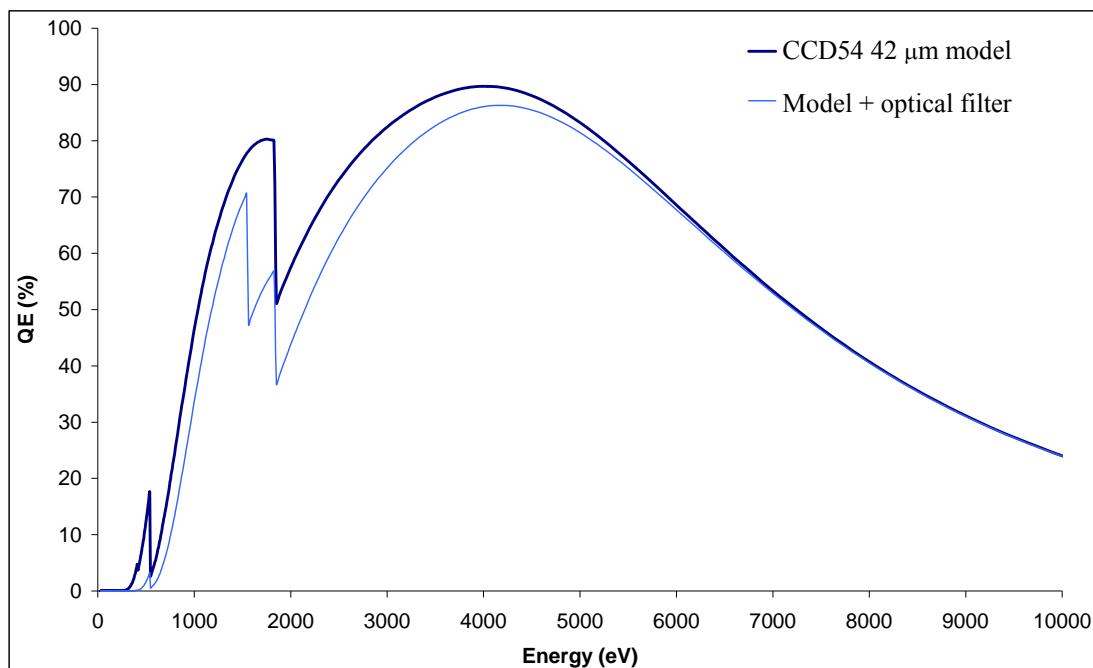


**Figure 4.35:** Modelled CCD54 QE with and without the 400 nm of C and Al optical filter

#### 4.5.4 Conclusion

It has been shown that for a high QE it is essential to combine split events over at least four samples, but at a cost to the energy resolution. As would be expected, X-ray events with a high energy are more likely to form split events due to charge diffusion when collected within the bulk silicon. High energy X-rays are also more susceptible to poor CTE as the charge is spread over a large volume as it is transferred through the silicon. The effects of CTE on charge transfer before and after proton irradiation are discussed in Chapter 6. The QE is typically quoted at the Mn-K $\alpha$  peak (at 5,898 eV). The Mn-K $\alpha$  QE of the CCD54 was found to be 74%. When only considering isolated events the calculated QE of the device is reduced to 41%, this could be improved by increasing the electrode pitch from 25  $\mu\text{m}$  so more charge is collected within one sample.

## 4.6 Chapter Summary

This chapter has presented work carried out to assess the performance of a number of CCD54 devices which were available to be used on the C1XS instrument. Optimal operating voltages and CDS timings were obtained, then fourteen modules, a total of fifty six devices, were characterised over the nominal temperature range at which C1XS will operate, to make a recommendation of six modules most suitable for use in C1XS and four modules as flight spares. A QE analysis of device 2 of module 17, a device with similar performance to those recommended as flight quality, was also carried out. The QE was found to be 74%, with a depletion depth of 42  $\mu\text{m}$ , comparing well

with the theoretical value of 44  $\mu\text{m}$  given in Section 2.5. Improved charge collection within one sample could be achieved by increasing the electrode pitch. The next chapter describes the first proton irradiation of module 15 and module 16. The aim of this study was to assess the effects on device performance of the worse case 50% and 100% end of life proton fluence that C1XS could experience during two years operation.

## Chapter 5: CCD54 Proton Radiation Damage Assessment

### 5.1 Introduction

This chapter presents an investigation into the effects of proton damage on the CCD54 devices for use in C1XS. The proton fluence was modelled using SPENVIS, discussed in Section 3.5. Two CCD54 modules were irradiated using the Accelerateur Groningen-ORsay (AGOR) cyclotron at the Kernfysisch Versneller Instituut (KVI) in Holland to 50% and 100% of the expected end of mission proton fluence. This work was carried out in support of the C1XS instrument development with the aim of demonstrating the ability of the CCD54 to resolve Mg, Al, and Si X-ray peaks which are required for C1XS to complete its scientific goals, defined in Section 1.2, following radiation damage. The affect of proton damage on the device performance was investigated by looking at the energy resolution and noise after irradiation along with the sensitivity of the charge collection area and the central transfer channels of the device.

### 5.2 Chandrayaan-1 Radiation Environment

The orbit parameters were adapted from Narendranath 2006, with the mission launch date set to be the 29<sup>th</sup> of February 2008, based on the mission schedule at the time. The Earth-Moon transfer orbit would take around seven days, and the spacecraft would then spend two years in a 100 km polar orbit around the Moon. The mission was divided into four orbital segments, shown in Table 5.1, the first three describing the transfer orbits while the fourth holds the spacecraft at the Moon. Lunar orbit data was taken from Williams 2006. The Keplerian elements used are illustrated in Figure 3.1.

<i>Parameter</i>	<i>Segment 1</i>	<i>Segment 2</i>	<i>Segment 3</i>	<i>Segment 4</i>
Apogee:	23307.14 km	78672.05 km	374892.76 km	399132.56 km
Perigee:	247.14 km	247.12 km	238.36 km	356925.44 km
Inclination:	17.85°	17.85°	17.84°	17.84°
R. A. Ascending Node:	353.10°	352.72°	352.42°	352.42°
Argument of Perigee:	179.00°	179.44°	179.95°	179.95°
True Anomaly:	12.53°	68.72°	69.22°	69.22°
Segment length:	0.56 days	2.24 days	3.74 days	730.00 days

**Table 5.1:** Orbit parameters based on a launch date of 28<sup>th</sup> February 2008

The AP-8 trapped proton model and the JPL-91 solar proton model, set to a confidence of 95%, were used to calculate the fluence levels, as shown in Figure 5.1. A confidence level of 95% is appropriate for a mission duration of two years, as described in Section 3.2. The two years at the

Moon included 1.38 years spent at solar maximum. A second SPENVIS run was included with a later launch date to include 2 years at solar maximum to observe the results of a delay to the launch date.

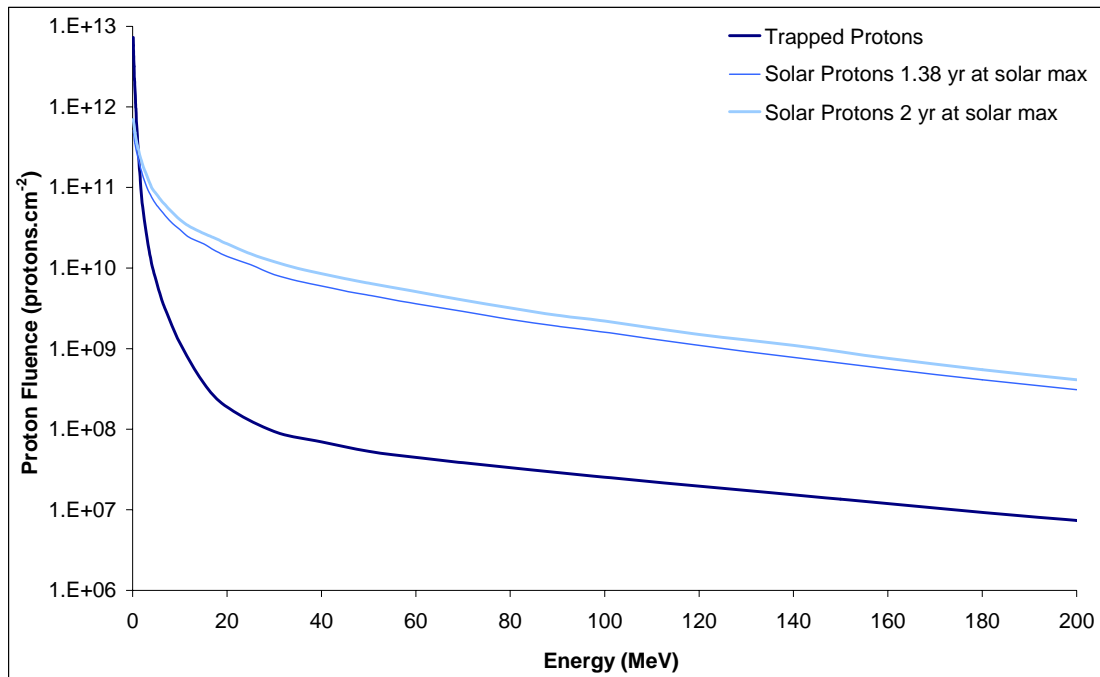


**Figure 5.1:** Proton fluence as a function of energy

It is clear from Figure 5.1 that solar protons will form the dominant damage component over the lifetime of the CCD54 devices. The total proton fluence accumulated during the transfer orbit segments was found to be  $7.3 \times 10^{12}$  protons.cm<sup>-2</sup> from 0.1 MeV to 400 MeV, higher than the  $5.9 \times 10^{12}$  protons.cm<sup>-2</sup> found by Narendranath 2006. The difference is as a result of the modification to the parameters and times to produce a continuous orbital path. The proton fluence between 0.1 MeV and 200 MeV was found to be  $5.1 \times 10^{11}$  protons.cm<sup>-2</sup> and  $7.0 \times 10^{11}$  protons.cm<sup>-2</sup> for a time at solar maximum of 1.38 years and 2 years respectively. The 2 years at solar maximum are comparable with the results of  $6.1 \times 10^{11}$  protons.cm<sup>-2</sup> and  $6.3 \times 10^{11}$  protons.cm<sup>-2</sup> found by Narendranath 2006 and Sørensen 2005 respectively. The reason for the ~10% difference with the fluence values is the launch dates used in the other models. Sørensen states that the fluence accounting for launch time with respect to the solar cycle would give around two thirds of the value found, which would give  $\sim 4.1 \times 10^{11}$  protons.cm<sup>-2</sup>. This value is lower than that found using a launch date of 29<sup>th</sup> February 2008, the data with the mission experiencing 1.38 years at solar maximum was used as the basis for the shielding study.

The next stage in using SPENVIS is to convert the energy to a dose in silicon in MeV.g(Si)<sup>-1</sup> and model the effect of different amounts of Al shielding on reducing the dose, converting to a 10 MeV equivalent proton fluence as described in Section 3.5. Shielding thicknesses of 0.05 mm to 50 mm

were used, the results shown in Figure 5.2. The proton flux as a function of shielding was also found, shown in Figure 5.3, clearly showing the large flux of trapped protons during the transfer orbit. This large flux in the proton belts resulted in the CCD54 devices in the D-CIXS instrument suffering extensive radiation damage over the 18 months it took to reach the Moon.

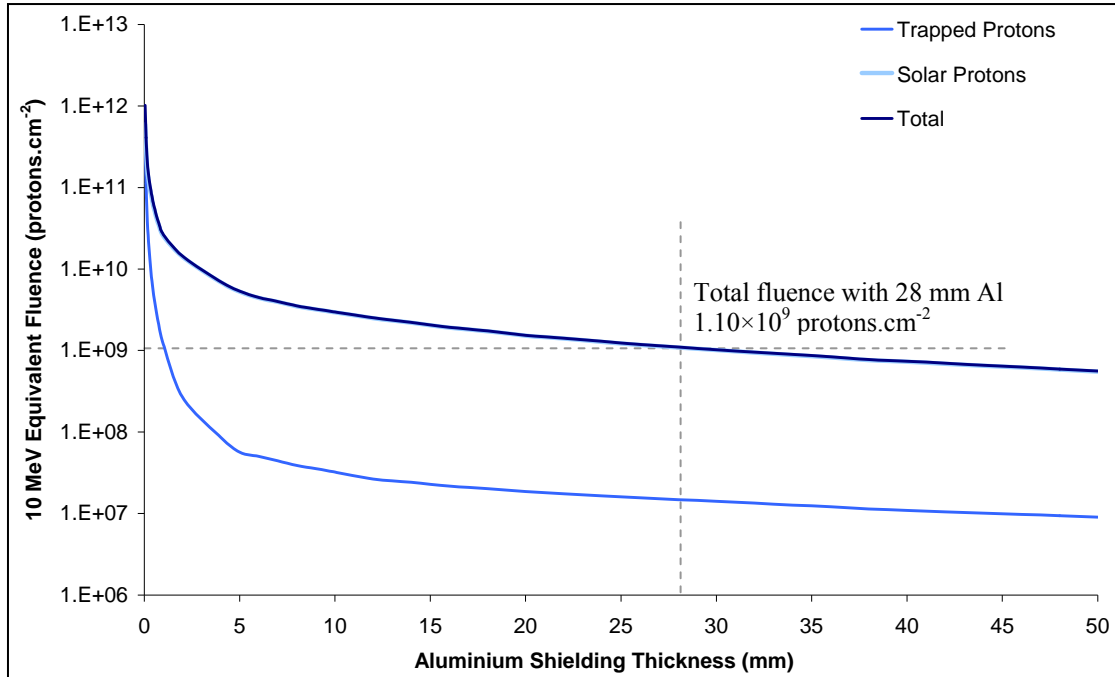


Figure 5.2: 10 MeV proton fluence as a function of shielding thickness

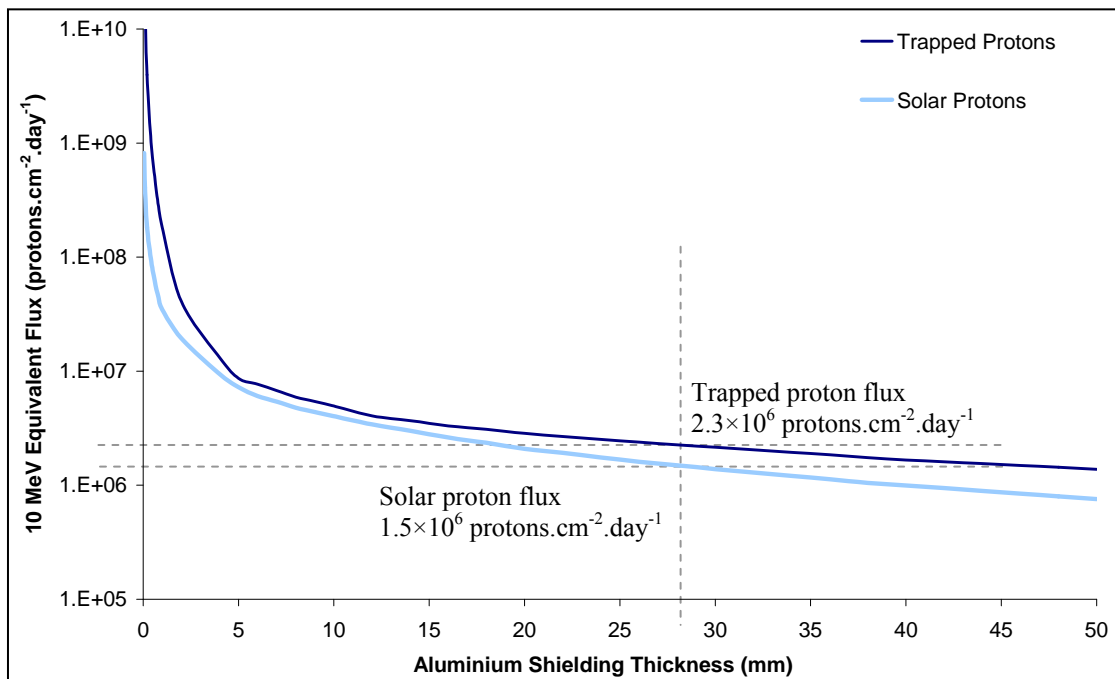


Figure 5.3: 10 MeV proton flux as a function of shielding thickness

A recommendation of using at least 3 mm of Al and 6 mm of Ta was made, providing a conservative estimate of 28 mm of Al shielding (where 6 mm of Ta is equivalent to ~25 mm of Al).

Based on this shielding thickness the 10 MeV equivalent proton fluence at the end of the two mission would be  $1.10 \times 10^9$  protons.cm<sup>-2</sup>, composed of  $1.09 \times 10^9$  protons.cm<sup>-2</sup> solar protons and  $0.01 \times 10^9$  protons.cm<sup>-2</sup> trapped protons. The flux rates for trapped and solar protons were found to be  $2.3 \times 10^6$  protons.cm<sup>-2</sup>.day<sup>-1</sup> and  $1.5 \times 10^6$  protons.cm<sup>-2</sup>.day<sup>-1</sup> respectively. Trapped protons have a 50% higher flux rate than solar protons, meaning that time spent within the radiation belts should be as low as possible. The 3 mm Cu cold finger and spacecraft structure were not included in shielding calculations. The aim was to provide worse case proton fluence based on the recommended shielding providing a conservative estimate of device performance, hence not accounting for the Cu cold finger. Spacecraft structure would be hard to simulate to any accuracy without a detailed model, which would provide nothing to the aim of the study.

The proton fluence would be further reduced by the spacecraft's 100 km altitude orbit around the Moon. The gyration radius was found, using Equation 3.1, over a range of proton energies between 1 and 37 nT. A 1 keV protons gyroradius was found to be ~900 km at 5 nT comparable with results given by Dolginov *et al.* 1962. As the gyration radius of low energy protons is much greater than the 100 km spacecraft orbit it is unlikely that these protons will enter the front  $2\pi$  of the detector, the contribution to proton fluence would be negligible. It has recently been suggested that the terrestrial magnetosphere will provide additional shielding as the Moon spends around 25% of its orbit within the terrestrial magnetosphere [Winglee 2007]. Further shielding will be provided when Chandrayaan-1 flies over the dark side of the Moon, dependant on the orbit, although this is not accounted for.

The  $2\pi$  behind the detector will be shielded by 3 mm Al and 6 mm Ta and the front  $2\pi$  100% shielded by the Moon, therefore the 10 MeV equivalent proton fluence at end of life has been estimated to be  $5.5 \times 10^8$  protons.cm<sup>-2</sup>. An irradiation was planned to irradiate three devices from modules 15 and 16 to 50% and 100% of this end of life proton fluence. The estimates are conservative due to the missing 3 mm of Cu, spacecraft structure, and additional lunar/terrestrial shielding mentioned above.

The importance of shielding to remove the large flux of low energy protons, illustrated in Figure 5.1, was demonstrated in the XRF detector onboard the Japanese KAGUYA (SELENE) mission, which used CCDs. The detectors had no front  $2\pi$  shielding. During the 2.4 orbits within Earths radiation belts the large flux of low energy protons (0.8 to 1.0 MeV) were attenuated by the Be window over the detector to ~300 keV, which, as shown in Figure 3.17, will deposit large amounts on energy within the buried channel. The proton damage resulted in a massive decrease in CTE, with an estimated 0.3 MeV fluence of  $\sim 3.0 \times 10^8$  protons.cm<sup>-2</sup> [Okada 2009]. The 10 MeV equivalent proton fluence was calculated using NIEL to be  $7.1 \times 10^9$  protons.cm<sup>-2</sup>, around  $\times 700$

greater than the predicted trapped fluence for C1XS and around  $\times 12$  greater than the C1XS end of life proton fluence!

### 5.3 Experimental Arrangement

The same experimental arrangement as that described in Section 4.2 was used with the  $\text{Fe}^{55}$  source to expose the device to Mn- $K\alpha$  X-rays. The XTF5011/75-TH X-ray tube was used to fluoresce an aluminium target and a magnesium, aluminium, silicon combination target. During the initial functionality assessment, the PRT was mounted on the cold finger. During characterisation and all post-irradiation testing it was mounted next to the device being tested to provide the temperature of the silicon (it is assumed the device silicon is in good thermal contact with the ceramic package).

### 5.4 Experimental Procedure

This section describes the experimental procedure used during the functionality and pre-irradiation testing, the proton irradiation, and the post-irradiation testing.

#### 5.4.1 Cosmetic Quality Pre-Irradiation Testing

The cosmetic quality and functionality of each device was assessed using sequence 2 with the PRT reading 20.0 °C. Device 1 of module 15 was found to be non-functional. Device 2 of module 15 and device 1 and 3 of module 16 were characterised using sequence 1 to provide three lots of 1980 read-outs with the  $\text{Fe}^{55}$  source at 0.0, -10.0, and -20.0 °C, recording the energy resolution at Mn- $K\alpha$  and the noise performance.

#### 5.4.2 CCD54 Proton Irradiation

An aluminium shield was designed to fit onto the radiation jig produced at RAL. Initially the shield was designed to fully irradiate device 1, however at the time of the study no other modules were available so device 1 was left as a control, as shown in Figure 5.4. The shield allowed one half of the charge collection area of device 2 to be shielded while irradiating the central transport channel and the charge collection area of device 3 to make a comparison of damage to the charge collection area and the central transport channels. The back half of device 4 was irradiated to observe the increase in dark current as a result of radiation damage. The aluminium shield thickness was selected to be 15 mm which is enough to stop 60 MeV protons, the beam energy used was 45 MeV. Aluminium was selected as the resulting activation that occurs during irradiation produces short lived isotopes so the shielding can be handled safely a few minutes after the irradiation. The

shielding jig and the shield are shown in Figure 5.5. During the irradiation the gap in the shield over device 1 was covered using additional 15 mm thick aluminium shielding.

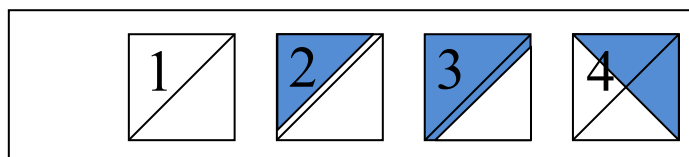


**Figure 5.4:** CCD54 module highlighting the areas to be irradiated in blue

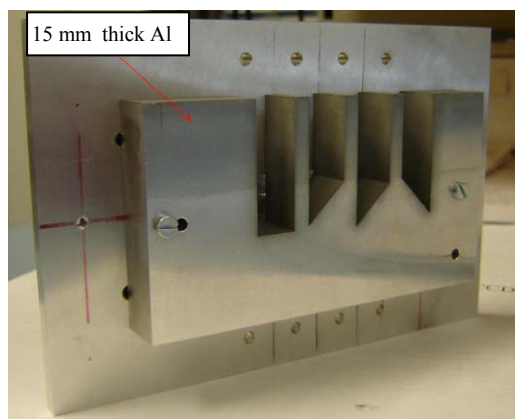


**Figure 5.5:** Proton irradiation jig and the aluminium shield

The irradiation was performed at KVI. The beam energy was measured to be 45 MeV at the detector. The irradiation parameters are given in Table 5.2. The reason for the slightly lower 10 MeV equivalent fluence compared with the targeted fluence levels is as a result of a mistake made converting the 10 MeV equivalent fluence to a 45 MeV fluence. The beam uniformity was measured using a LANEX (Kodak) scintillating screen, and found to be  $\pm 10\%$  in dose over an area 60-70 mm<sup>2</sup> by KVI staff, adequately covering the three devices being irradiated.

<i>SCD Module</i>	<i>45 MeV Fluence (proton.cm<sup>-2</sup>)</i>	<i>10 MeV Equivalent Fluence (proton.cm<sup>-2</sup>)</i>	<i>Irradiation Time (s)</i>
15	$3.9 \times 10^8$	$2.1 \times 10^8$	100
16	$7.8 \times 10^8$	$4.3 \times 10^8$	100

**Table 5.2:** Irradiation parameters

### 5.4.3 Post-Irradiation Laboratory Procedure

The cosmetic quality and functionality of each device was assessed using sequence 2 with an image integration period of 10 ms, and with the device held between 20.0 and -30.0 °C in 10.0 °C steps. The devices were then characterised using sequence 1 to provide three lots of 1980 read-outs with the Fe<sup>55</sup> source, with the CCD54 held between 10.0 and -40.0 °C in steps of 10.0 °C, recording the energy resolution at Mn-K $\alpha$  and the noise performance. The characterisation using the X-ray tube

and the Al target was performed at 0.0 °C, and between -10.0 and -40.0 °C in steps of 5.0 °C, recording the energy resolution at Al-K $\alpha$  and the total read-out noise. Data were recorded for X-rays collected in the irradiated section and those collected in the shielded section of each CCD54. A 2 mm thick piece of lead was used to shield areas of the device being tested from X-rays. Unfortunately module 15 suffered a catastrophic failure, the ceramic shattered, during cooling before testing device 2 using Al-K $\alpha$  X-rays so only Mn-K $\alpha$  data are presented for this module. The module was intact at room temperature when clamped onto the cold finger and failed at  $\sim$  -12 °C, it is possible that during cooling as the screws contracted they caused increased stress on the module ceramic causing it to fail. In future testing the screws were not tightened as much.

On chip sample binning tests were performed using device 3 of module 16 held between 0.0 and -40.0 °C in steps of 5.0 °C. The binning increased from 1 to 10 samples, effectively increasing the sample area from 25 to 250  $\mu\text{m}$ . The dark current increase and spatial resolution decrease due to the larger sample size, however the read-out time is decreased leading to a decrease in dark current. Initially the increased readout rate will outweigh the increased dark current.sample<sup>-1</sup>. However, as the sample size is further increased the advantage is lost. It should be noted that the dark current generation rate does not change, it is the area in which dark current is collected that is increased. These tests were performed to demonstrate the possible benefits of using devices with a larger sample size, and to observe the effect of sample binning on the measured energy resolution. The energy resolution, noise, change in dark current, and percentage of isolated events were recorded. The code described in Section 4.4 was used to identify split and isolated events.

The current on the X-ray tube was varied between 0.05 mA and 0.35 mA in 0.05 mA steps, fluorescing the Al target with device 3 of module 16 held at -30.0 °C, using sequence 1 to provide three lots of 1180 read-outs. These tests were performed to assess the CCD54's performance with increasing X-ray fluence. Increased X-ray flux will lead to increased shot noise but will reduce the CTI as there is more charge available to fill traps. The energy resolution, noise, and counts in the Al-K $\alpha$  X-ray peak were recorded.

## 5.5 Increase in Dark Current

The inclusion of an image integration period when using sequence 2 allows the radiation induced increase in dark current to be clearly identified, as shown in Figure 5.6. The dark current generation rate does not change; the integration time allows more to be collected. The modest increase as a result of  $4.3 \times 10^8$  protons.cm<sup>-2</sup> is shown by the bulge at the centre of the triangular read-out profile and the steeper gradient on the right hand side the dark current increasing proportionally with sample area. The advantage of cooling is clear by the reduction in ADC value from +20.0 to

+10.0 °C ± 0.2 °C. The small difference on the left hand side is as result the error on the measured temperature, reduced at +10.0 as a result of the decreased dark current generation rate.

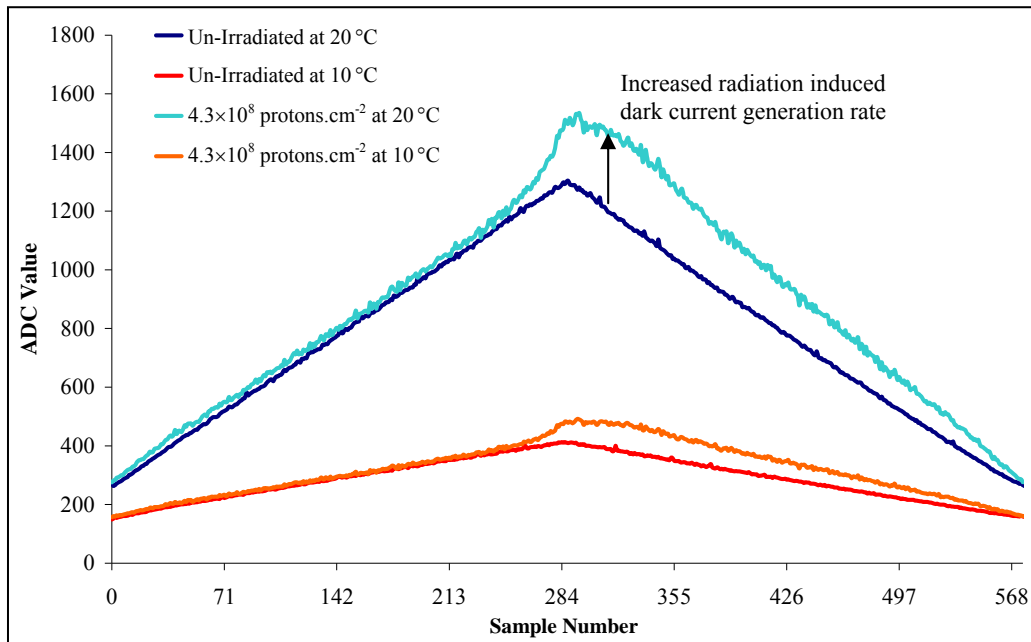


**Figure 5.6:** The characteristic triangular dark current profile recorded using device 4 of module 16 at +20.0 °C and +10.0 °C

### 5.6 CCD54 Performance Degradation

The energy resolution is clearly reduced as a result of the proton irradiation as shown in Figure 5.7 and Figure 5.8 which show the energy resolution of the Al-K $\alpha$  and Mn-K $\alpha$  X-ray peaks respectively as a function of temperature pre-irradiation and post-irradiation. Figure 5.9 shows the total read-out noise. The target mission resolution of 250 eV at Mn-K $\alpha$  is marked on Figure 5.8. The energy resolution and noise at -20.0 °C, the recommended minimum operating temperature, are summarised in Table 5.3.

<i>10 MeV Proton Fluence (proton.cm<sup>-2</sup>)</i>	<i>Read-out Noise (e<sup>-</sup> r.m.s.)</i>	<i>FWHM Al-K<math>\alpha</math> (eV)</i>	<i>FWHM Mn-K<math>\alpha</math> (eV)</i>
0	8.4	118.5	134.4
2.1	15.0	*	225.9
4.3	19.4	220.8	259.8

\* data not collected due to non-functional device

**Table 5.3:** CCD54 noise and energy resolution at Al-K $\alpha$  and Mn-K $\alpha$  X-ray peaks, with data collected at -20.0 °C pre- and post-proton irradiation

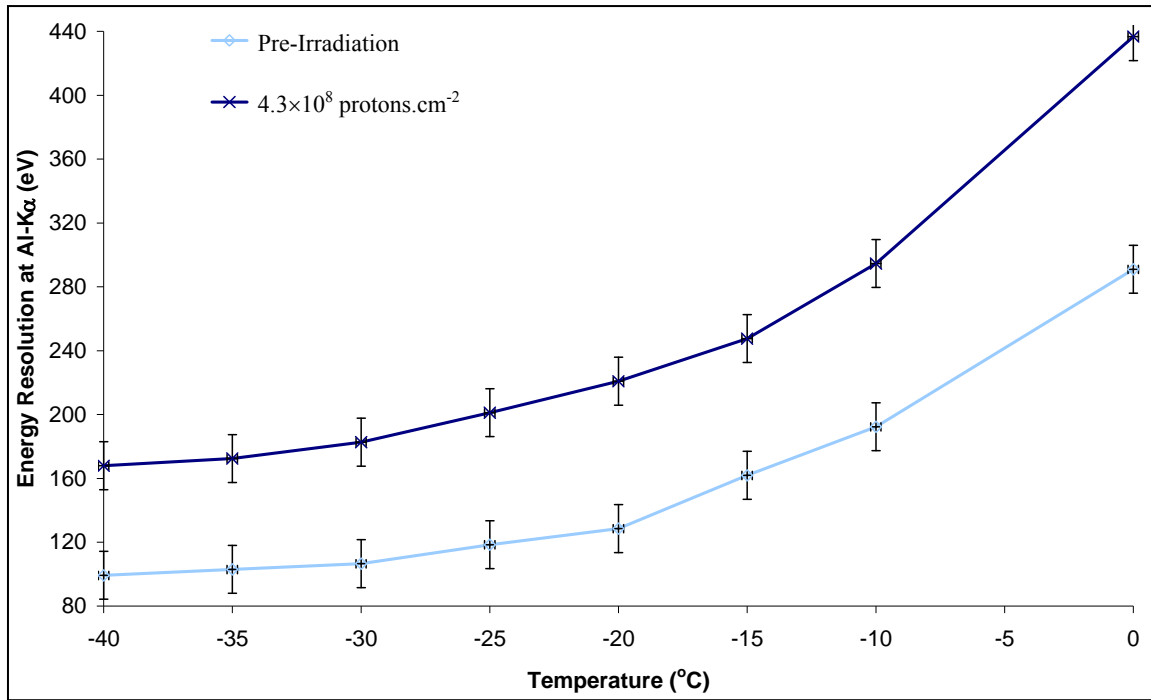


**Figure 5.7:** FWHM of Al-K $\alpha$  X-rays pre- and post-irradiation as a function of temperature

The decrease in performance appears to be linear with proton fluence, and the energy resolution, post-irradiation, will still allow good quality scientific data to be collected throughout the two year mission in orbit around the Moon when operated below -20 °C. The decrease in energy resolution would cause the merger of the Mg-K $\alpha$ , Al-K $\alpha$  and Si-K $\alpha$  photo peaks, meaning that a higher gain will be required to ensure the individual photo peaks can be identified. The performance is degraded by increased dark current generation and CTI. The dark current uniformity after the irradiation was within 5 $\sigma$  of the background level using sequence 1. The error on the energy resolution has been taken to be half the value of the calibration, as the calibration relates to the number of data points available for analysis. Module 15 was measured to have a larger calibration. The deviation from the expected energy resolution, based on the performance of the other devices, at 2.1x10<sup>8</sup> protons.cm<sup>-2</sup> is within the error.

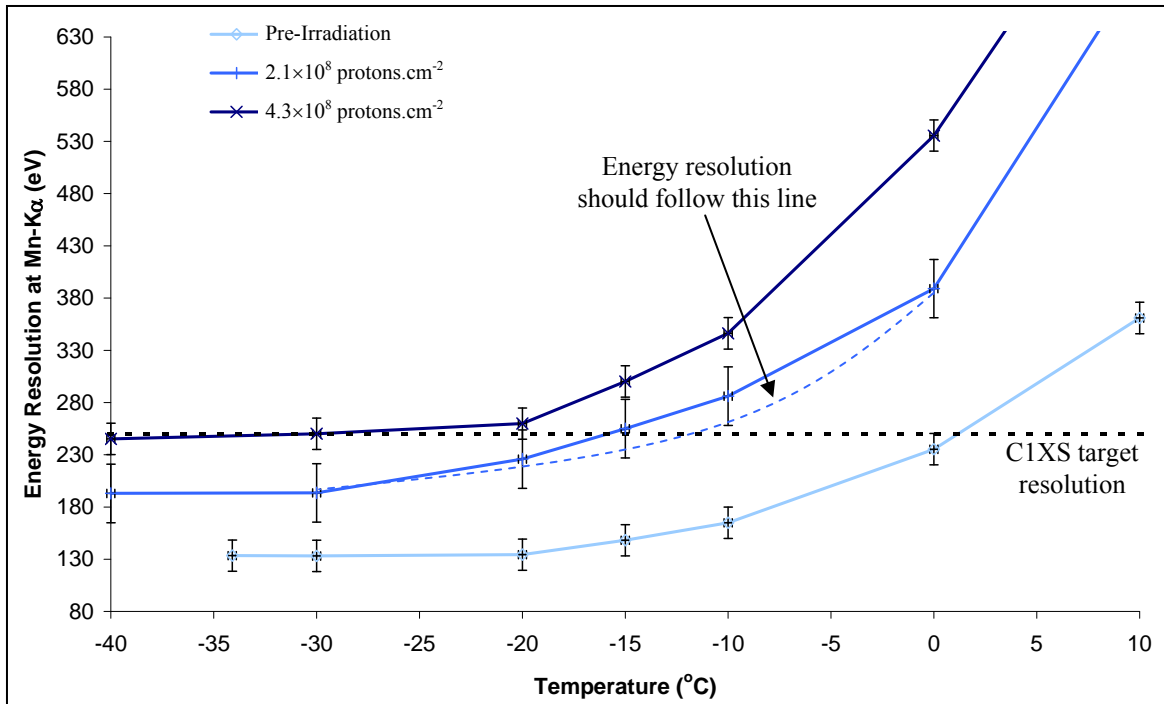


**Figure 5.8:** FWHM of Mn-K $\alpha$  X-rays pre- and post-irradiation as a function of temperature

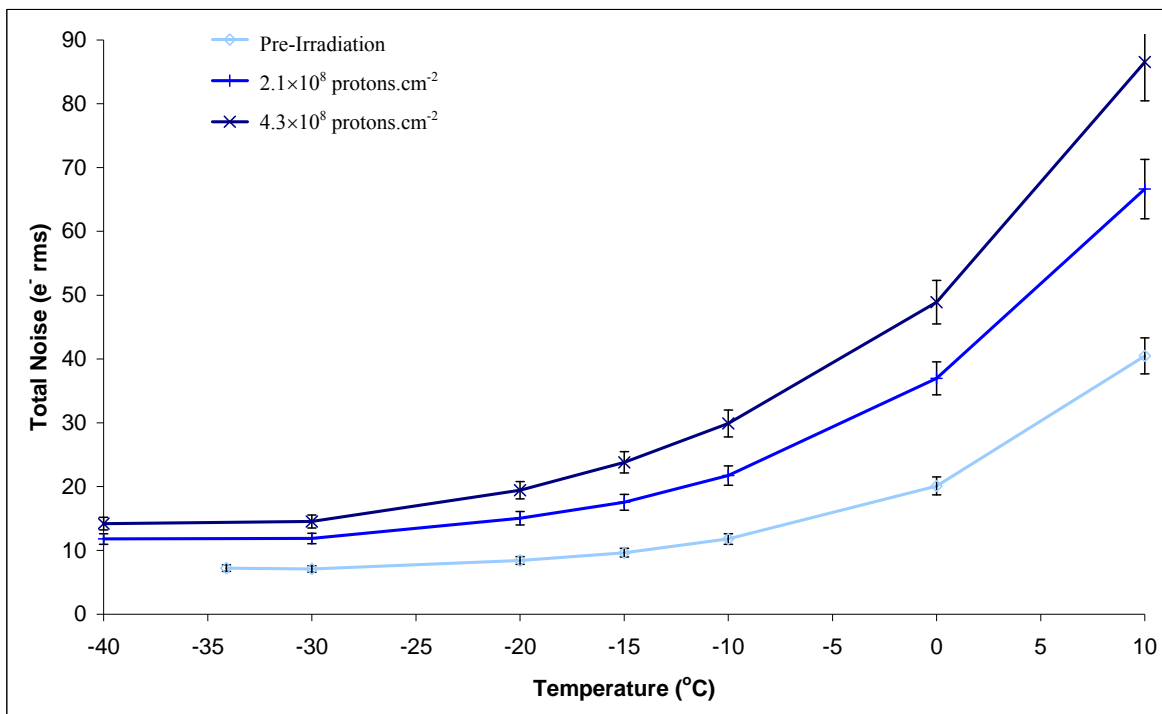


**Figure 5.9:** Noise pre- and post-irradiation as a function of temperature

### 5.7 Damage to the Charge Collection Area and Central Transport Channels

The measured energy resolution of Al-K $\alpha$  X-ray events collected in the irradiated and non-irradiated sections of devices 2 and 3 of module 16 are shown in Figure 5.10. Device 2 did not suffer any radiation damage to the central transport channels, as would be expected the noise

shown in Figure 5.11 increased only slightly, < 5 % over the whole temperature range. The energy resolution of X-ray events from the un-irradiated side was also decreased by ~5 % as a result of the increased dark current from the irradiated section of the device. Due to the read-out mechanism of the CCD54 where the charge collected from both sections is combined before the read-out node, as described in Section 2.4, the additional radiation induced dark current affects the performance of the un-irradiated side. The energy resolution of the X-ray events from the irradiated side was decreased by ~17 % over the whole temperature range, as a result of both increased dark current and increased CTI, demonstrating that increased CTI is the dominant source of performance loss for the CCD54. The effect of increased CTI on the recorded spectra is shown in Figure 5.12 with the increased tail to the left of the X-ray peak as a result of charge lost during transfers. The number of counts in the peak pre-irradiation and post-irradiation was within the measured error, based on the square root of the counts in the peak.

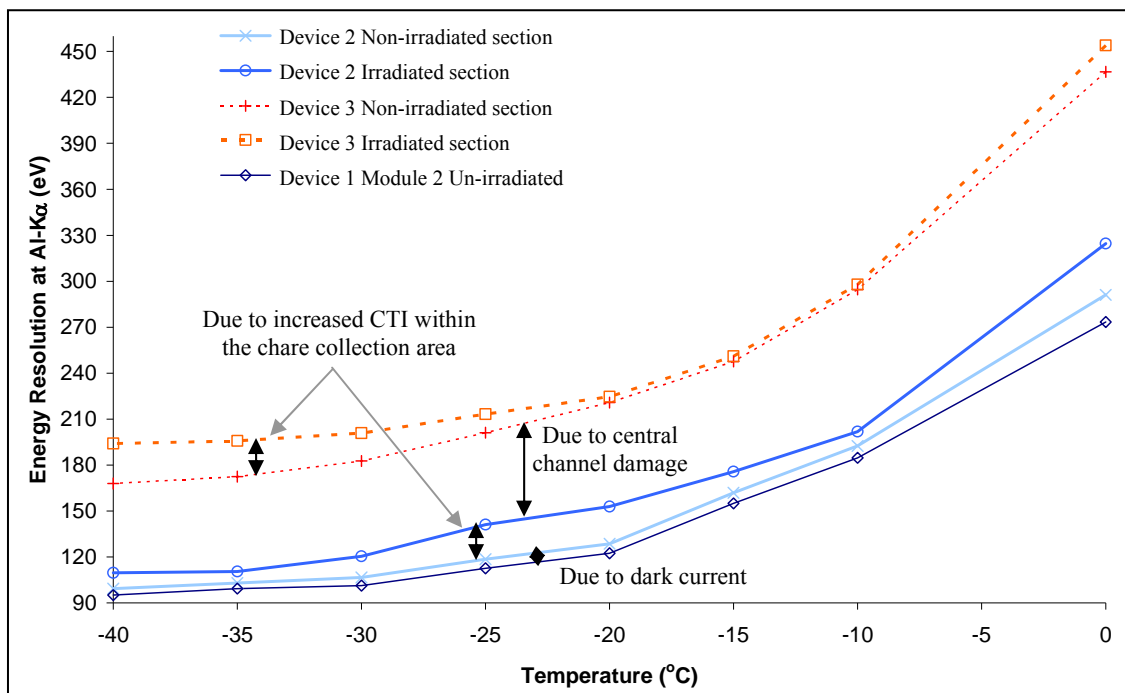


**Figure 5.10:** FWHM of Al-K $\alpha$  X-rays pre-irradiation and post  $4.3 \times 10^8$  protons.cm $^{-2}$  of device 2 and 3 as a function of temperature

The radiation damage to the central transport channels has a large affect on the device performance as shown in Figure 5.10. The total noise increased by ~70 % over the whole temperature range, while the energy resolution from X-ray events decreased by ~70 % between 0.0 and -20.0 °C. The measured energy resolution of X-ray events detected within the non-irradiated charge collection area of device 3 continues to benefit from further cooling below -20.0 °C, more than events detected within the irradiated section as a result of the CTI within the charge collection limiting the performance. The difference as a result of damage to the charge collection area to that with no damage to the collection area is 11 %, comparable with the 12 % difference in device 2.

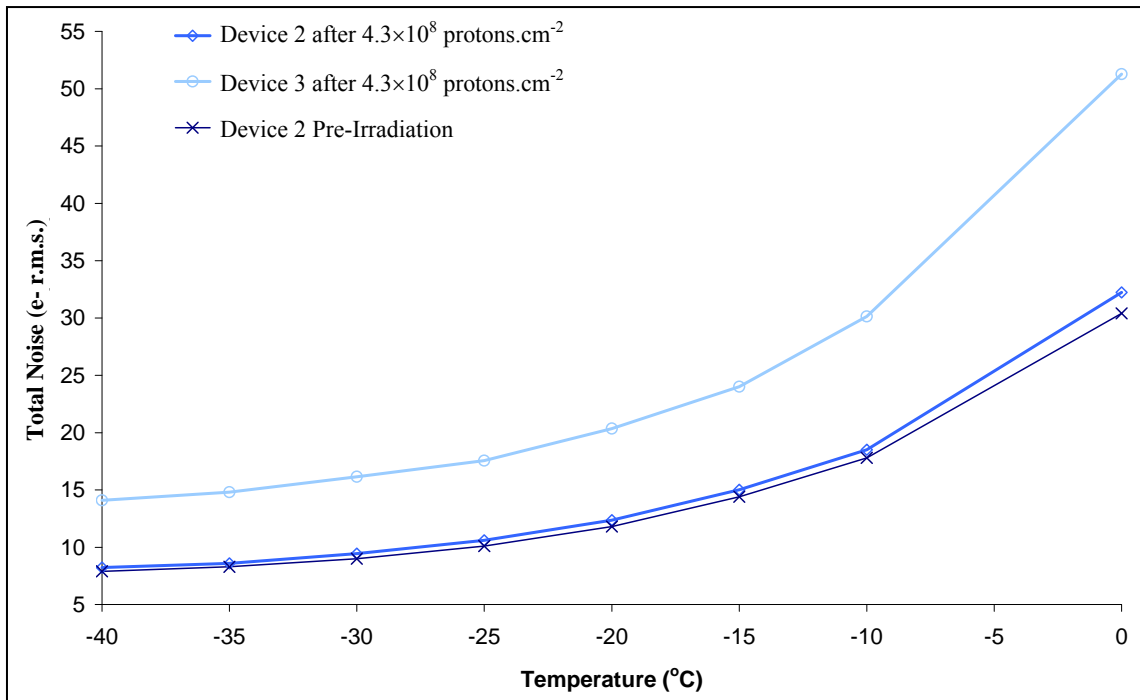


**Figure 5.11:** Total Noise pre-irradiation and post  $4.3 \times 10^8$  protons.cm<sup>-2</sup> of device 2 and 3 as a function of temperature

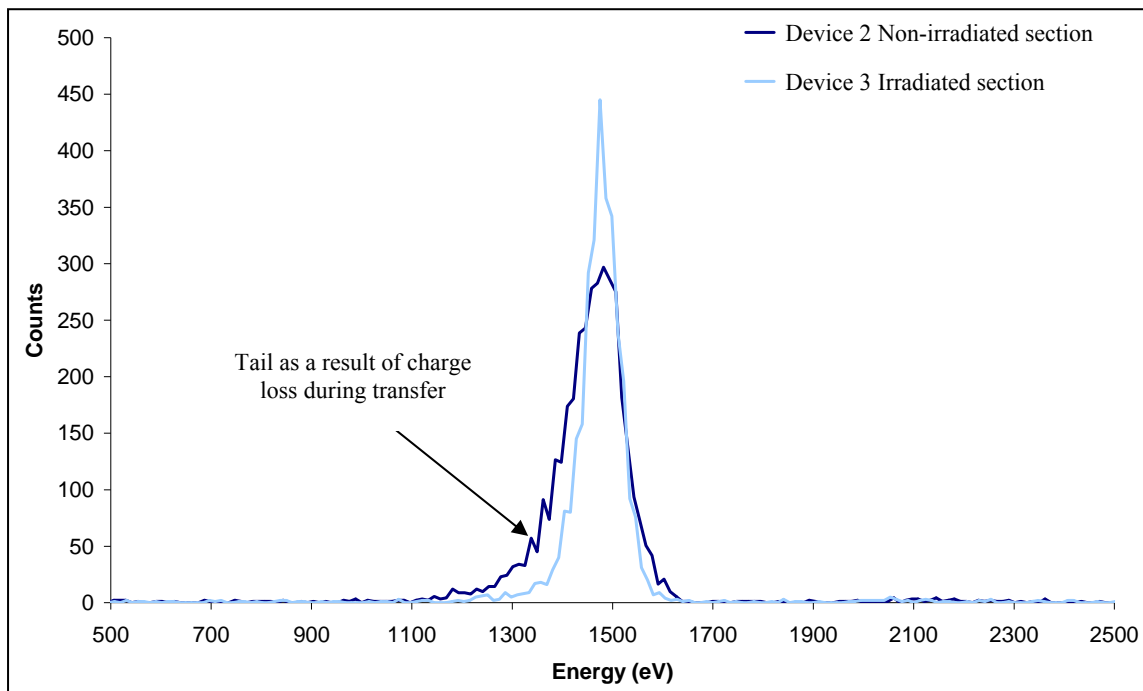


**Figure 5.12:** Spectra of Al-K $\alpha$  X-rays post  $4.3 \times 10^8$  protons.cm<sup>-2</sup> taken using the non-irradiated section of device 2 and irradiated section of device 3 at -25 °C

### 5.8 Increased On Chip Sample Binning

The lower dark current at lower temperature leads to an improvement in performance below -30.0 °C, at which temperature the dark current can be minimised. Testing was performed using

X-ray events detected on the irradiated side of device 3 of module 16. The energy resolution was improved from 205 eV at a sample bin value of 1, to 198 eV at a bin value of 2, as shown in Figure 5.13. The change in dark current is shown in Figure 5.14 showing the clear decrease due to the faster read-out. The advantage of faster readout over increased sample area is lost at a bin value of 5 at -30.0 °C while at -40.0 °C it will not be lost until a bin value of ~11. This suggests that at below -30.0 °C the energy resolution of a radiation damaged device will be improved using on chip binning.

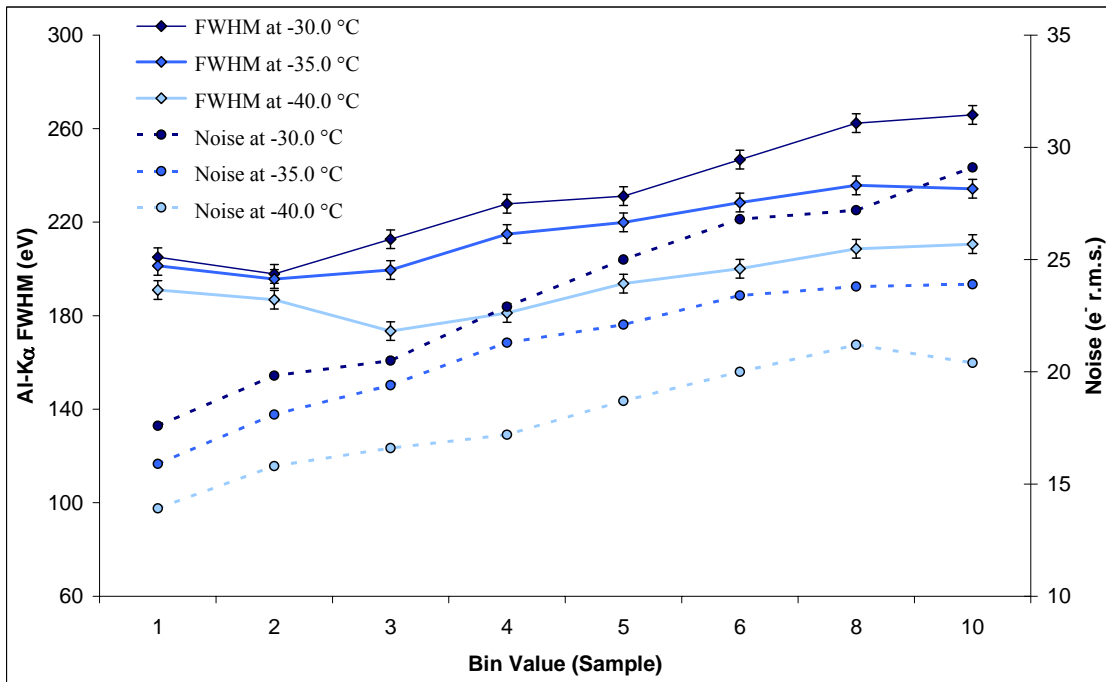


Figure 5.13: Energy resolution of Al-K $\alpha$  X-rays and total noise as a function of sample binning

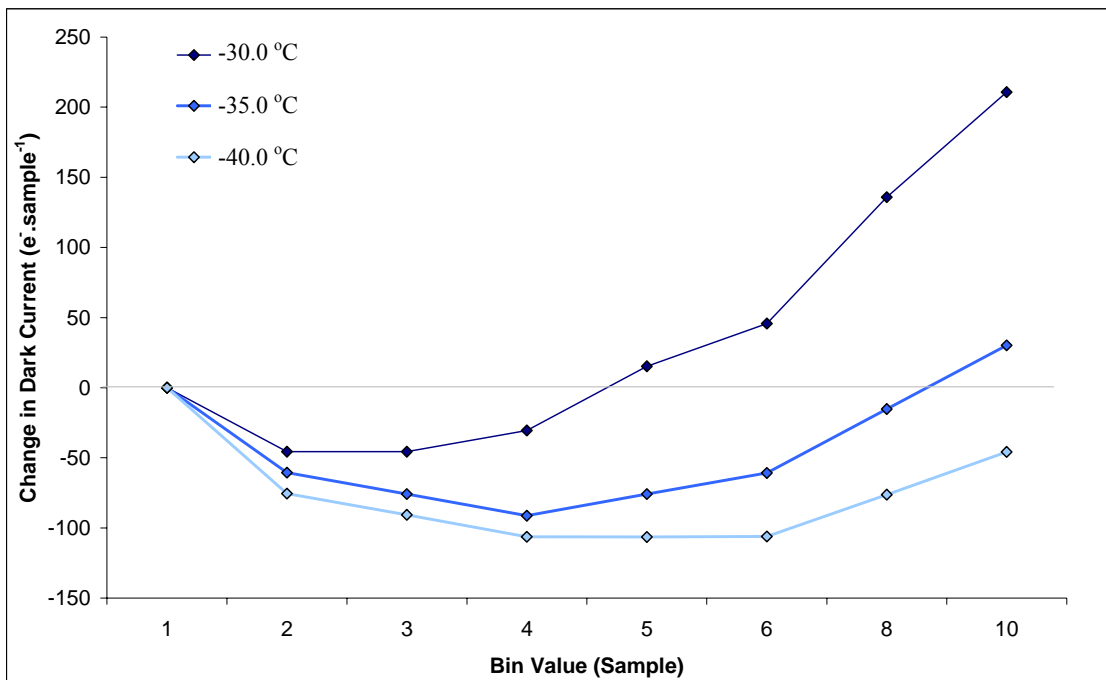
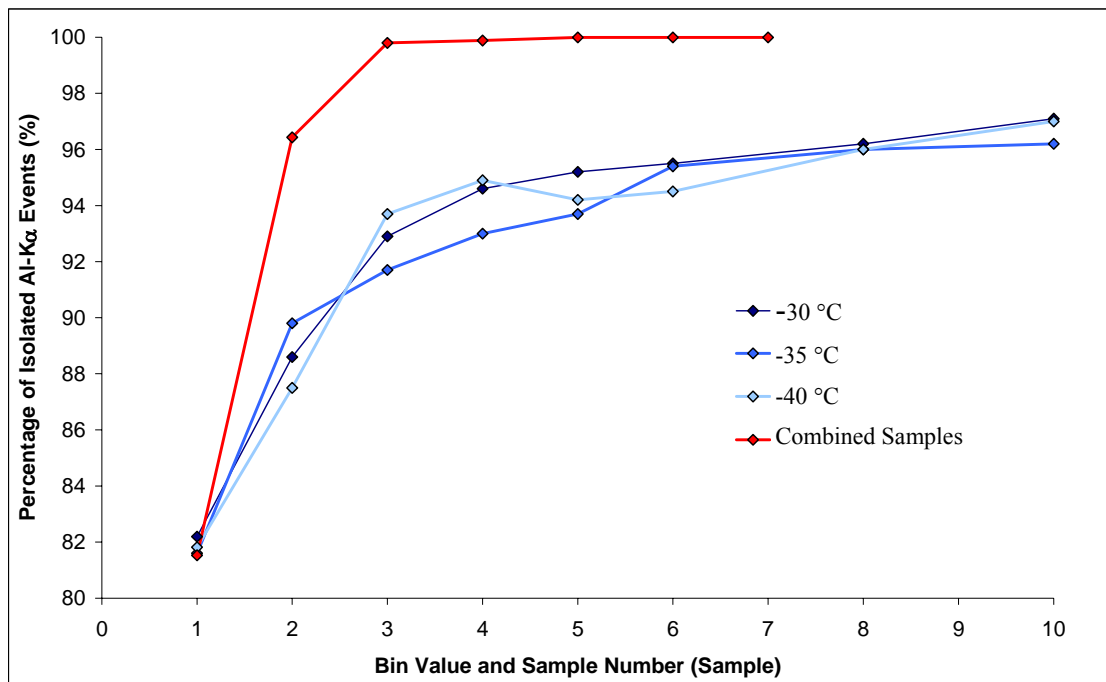


Figure 5.14: Change in dark current as a function of sample binning

The reason for the decreasing energy resolution is as a result of the decreased spatial resolution which can lead to the inclusion of charge collected within the sample originating from another X-ray event. A large sample will have a higher dark current non-uniformity which results in the increasing noise shown in Figure 5.14. The percentage of Al-K $\alpha$  events identified as isolated events is shown in Figure 5.15. The percentage of isolated events increases from ~82% at a bin value of 1 to ~97% at a bin value of ten as a result of the charge being collected within one sample. There is little improvement above a bin value of 4, corresponding to a sample size of 100  $\mu\text{m}$ , and the trend is not temperature dependant.



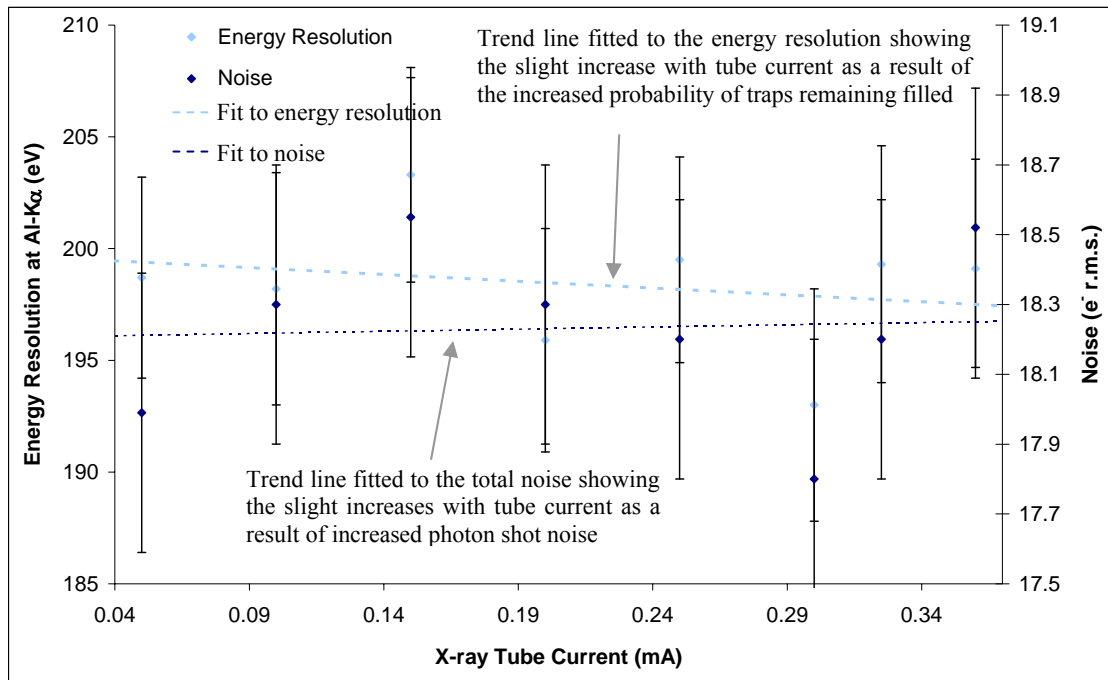
**Figure 5.15:** The percentage of Al-K $\alpha$  events identified as isolated as a function of sample binning

Figure 5.15 also shows the effect of combining multiple samples, found during the QE study discussed in Section 4.4. Event processing provides a greater improvement to the number of events identified as isolated, as it looks at each event irrespective of where in the sample it was detected. Although binning increases the sample area it is still possible for an event to interact on a sample border, being detected in both samples, and not identified as an isolated event. Combining events does not improve the measured energy resolution or increase the read-out rate.

## 5.9 Effect of Increased X-ray Flux

There are small trends to suggest a slight increase in energy resolution and total noise as a function of tube current, illustrated by the trend lines in Figure 5.16, however, they are within the calculated error. The error on the weighted mean, the X-ray and noise peak locations, was used to calculate the error on the measured energy resolution and noise. The dominant trap site for increased CTI in

n-channel devices is the E-centre. At  $-30.0\text{ }^{\circ}\text{C}$  the E-centre emission time, discussed in Section 3.6, is  $7.91 \times 10^{-3}\text{ s}$ . The time required to complete one clock triplet is  $2.19 \times 10^{-5}\text{ s}$ , therefore after  $\sim 361$  of the 575 clock triplets required to read-out the CCD54 the traps filled with charge deposited by an X-ray will be released. The number of events detected per read-out ranged from 1.5 to 9.8 between 0.05 and 0.36 mA. To ensure the traps had emptied, the events per read-out would be required to be less than 0.5 events per read-out (one read-out with one X-ray event, and the next with no X-ray event). During testing each read-out could benefit from charge deposited during a previous read-out, the device continues to be clocked when data is not collected, with the probability increasing with increasing X-ray flux. The slight increase in energy resolution with increasing flux is as a result of the increased probability of traps remaining filled. The CCD54 showed no signs of saturation with the number of Al-K $\alpha$  X-ray events detected increasing from  $130\text{ events.cm}^{-2}.\text{s}^{-1}$  to  $900\text{ events.cm}^{-2}.\text{s}^{-1}$ , the Al-K $\alpha$  count rate increasing linearly with the increasing tube current as shown in Figure 5.17. The increase in noise is as a result of increased photon shot noise.



**Figure 5.16:** FWHM and noise as a function of tube current

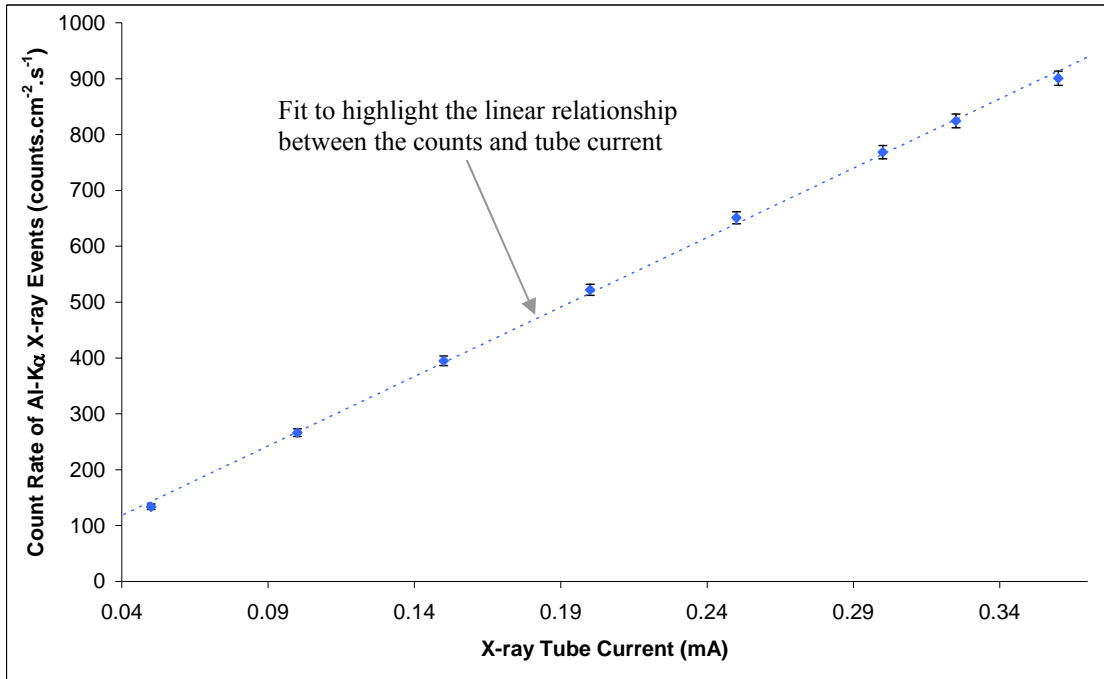


**Figure 5.17:** Al-K $\alpha$  events as a function of tube current

The maximum count rate of the CCD54, when readout at  $\sim 100$  kHz, is  $28,000$  events.cm $^{-2}$ .s $^{-1}$ , the instrument limit is  $5,100$  events.cm $^{-2}$ .s $^{-1}$  (Howe *et al.* 2009). The maximum expected count rate for the C1XS instrument, based on GOES X10 conditions, is  $840$  counts.cm $^{-2}$ .s $^{-1}$  (Howe *et al.* 2009), hence the selected range of X-ray tube current. The event rate will be lower for the majority of mission operation, dependant on solar activity, the SCD provides excellent performance at these count rates due to its method of operation and large surface area.

## 5.10 Energy Resolution Model of Experimental Data

To allow for the energy resolution at Al-K $\alpha$  and Mn-K $\alpha$  to be found over a range of temperatures and proton fluences a polynomial fit was applied to the experimental data. Based on these fits a simple computational model was created which allows the temperature and proton fluence received to be entered providing the energy resolution at Al-K $\alpha$  and Mn-K $\alpha$ . To counter failure of the fit at lower temperatures a limiting factor was included, if the energy resolution changed by less than  $1$  eV over  $2.0$  °C the energy resolution would remain unchanged. The results from the model are shown in Figure 5.18 and 5.19 for the energy resolution of Al-K $\alpha$  and Mn-K $\alpha$  X-rays as a function of temperature at different proton fluence levels, including 100% of end of mission fluence at  $5.5 \times 10^8$  proton.cm $^{-2}$ . The model was created to provide a simple and quick method of demonstrating the effect increased mission time or a delayed launch would have on C1XS performance. The inclusion of fluence levels of  $3.0 \times 10^8$  protons.cm $^{-2}$  and  $7.5 \times 10^8$  protons.cm $^{-2}$  will be discussed in Chapter 6 where this model is validated against additional experimental data sets.

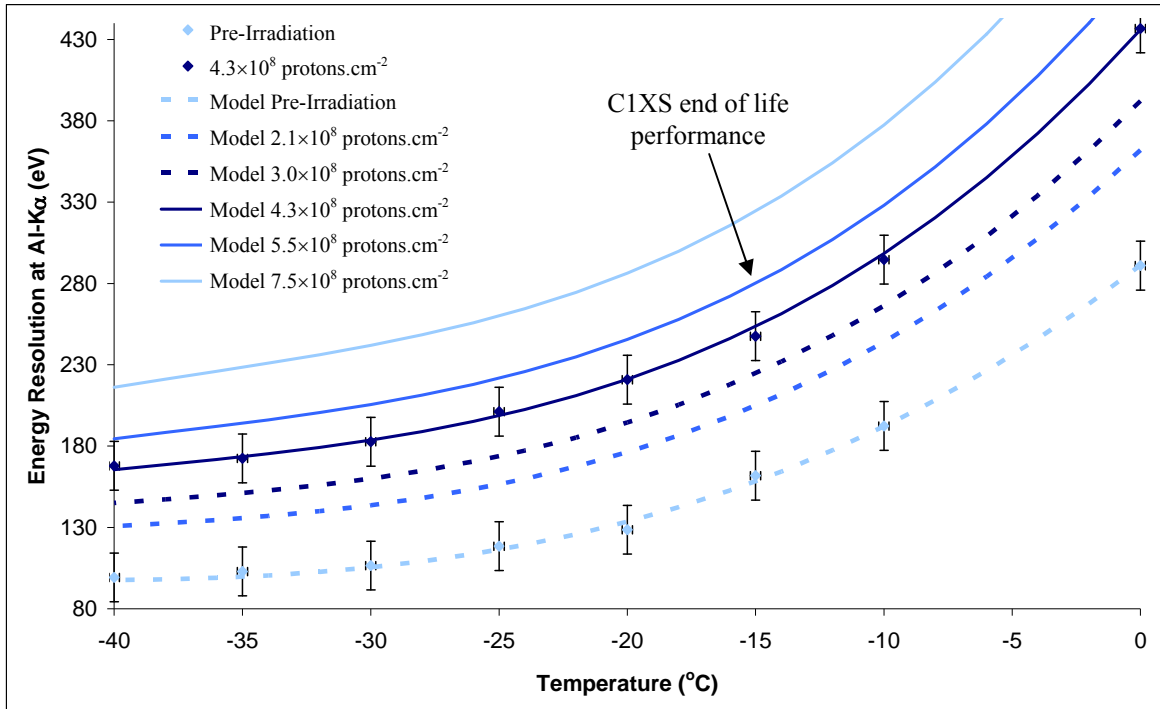


**Figure 5.18:** Modelled and experimental energy resolution at Al-K $\alpha$  as a function of temperature

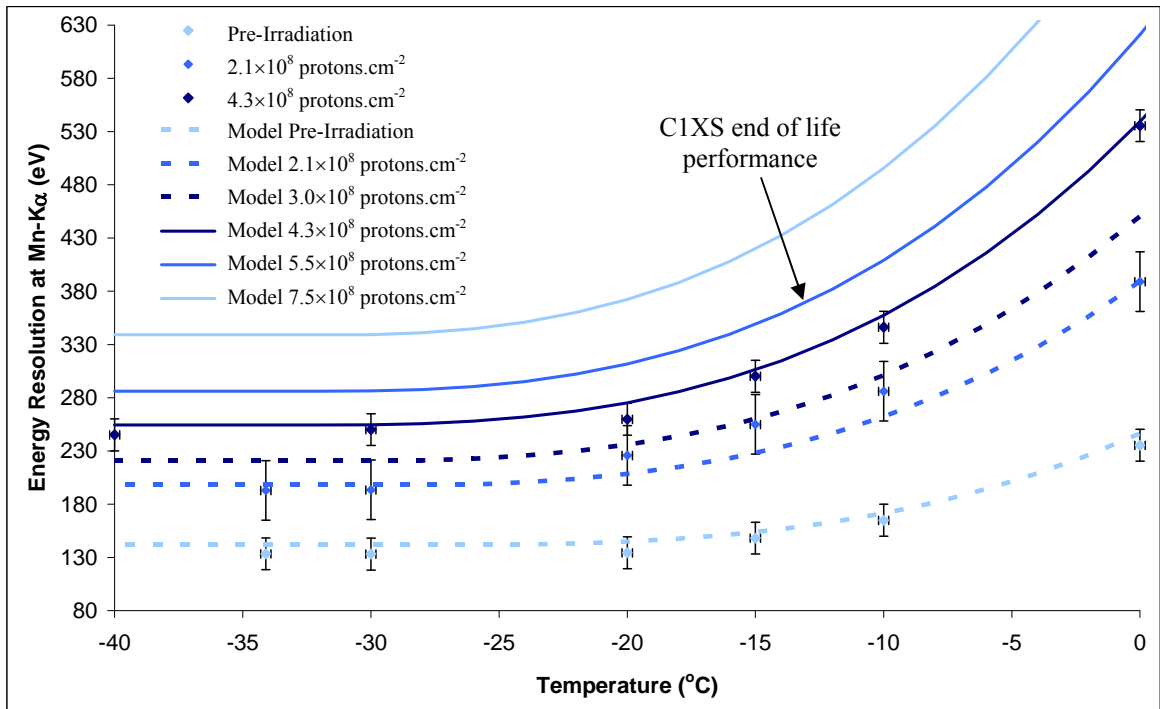


**Figure 5.19:** Modelled and experimental energy resolution at Mn-K $\alpha$  as a function of temperature

### 5.11 C1XS Review and Recommendations

A combination target using Mg, Al, and Si was created to demonstrate the ability of a CCD54 irradiated to near 100% of the end of life fluence to resolve the three peaks. The ability to define the Mg, Al, and Si X-ray events is essential for the success of the C1XS instrument. The resulting

spectrum showing pre- and post-irradiation spectra, taken at -15.0, -20.0, -30.0 and -40.0 °C are shown in Figure 5.20, 5.21, 5.22, and 5.23 respectively, clearly demonstrating the benefit of further cooling to device performance. At -15.0 °C the performance post-irradiation is comparable to D-CIXS performance, shown in Figure 1.2, where the three X-ray peaks are irresolvable. Cooling a further 5 °C, to -20.0 °C, allows the three separate peaks to be defined. Further cooling will only improve the energy resolution, desirable for improved instrument performance at the later stages of the mission, cooling to -40.0 °C provides performance similar to that attained pre-irradiation at -20.0 °C. Figure 5.21 alone demonstrates that the CCD54 modules are capable of providing high quality scientific data over the entire mission duration.

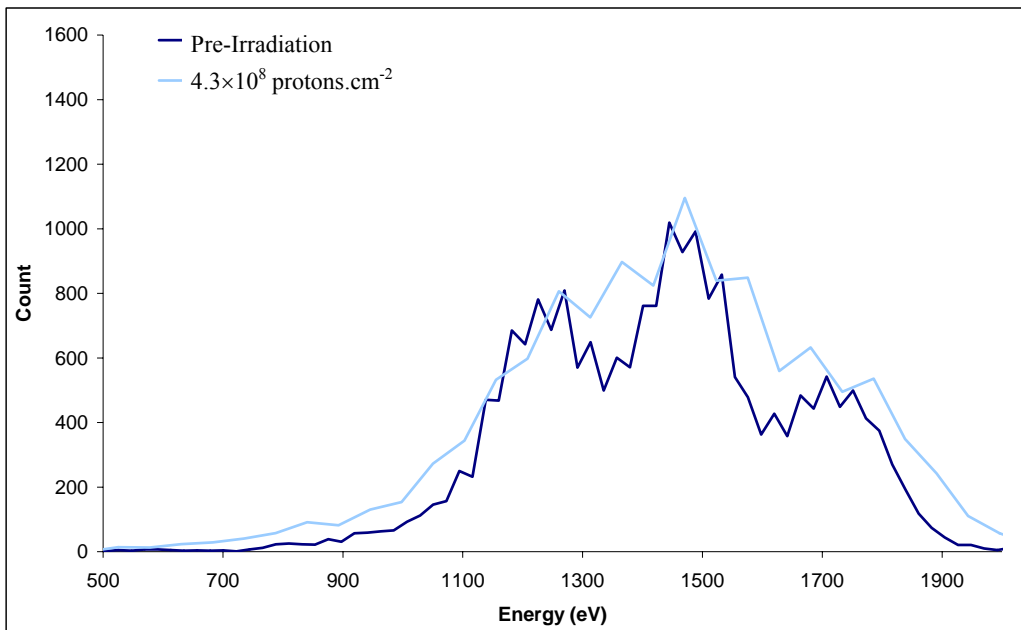


**Figure 5.20:** X-ray spectra produced using an Mg, Al and Si target at -15.0 °C

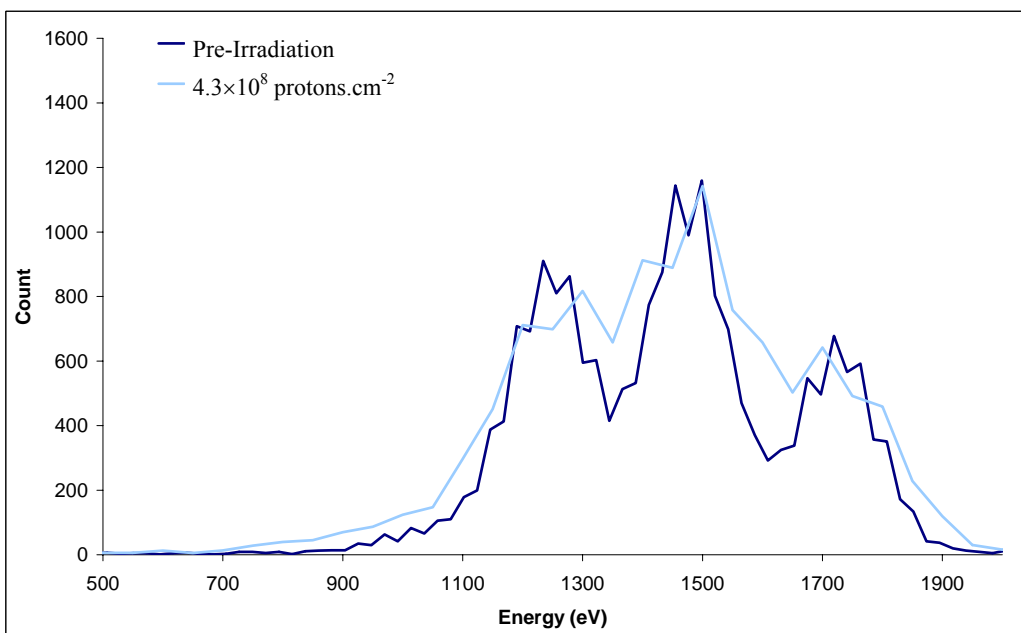


**Figure 5.21:** X-ray spectra produced using an Mg, Al and Si target between -20.0 °C

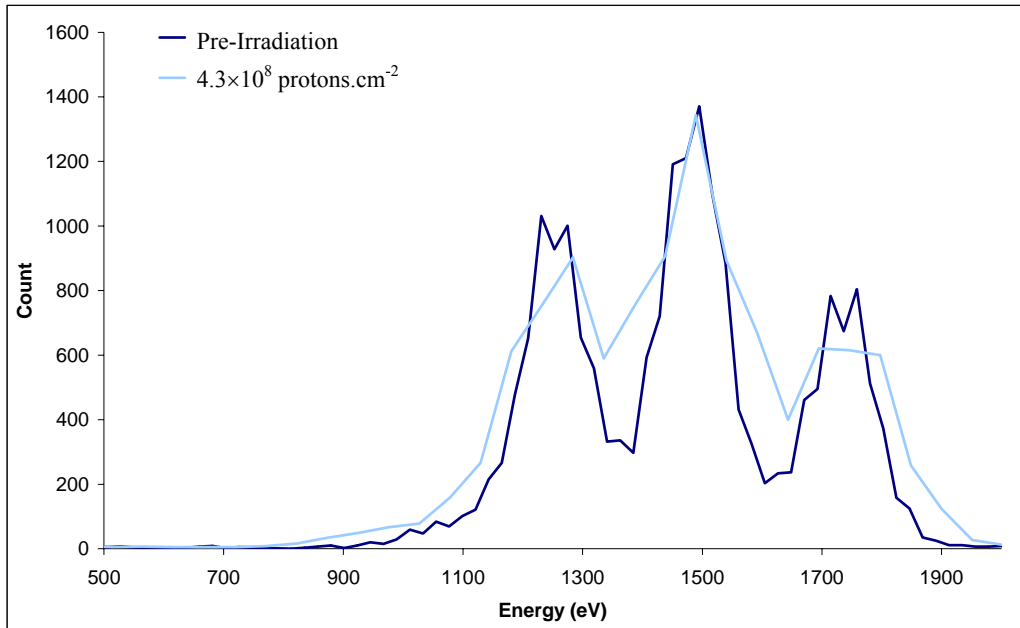


**Figure 5.22:** X-ray spectra produced using an Mg, Al and Si target between -30.0 °C

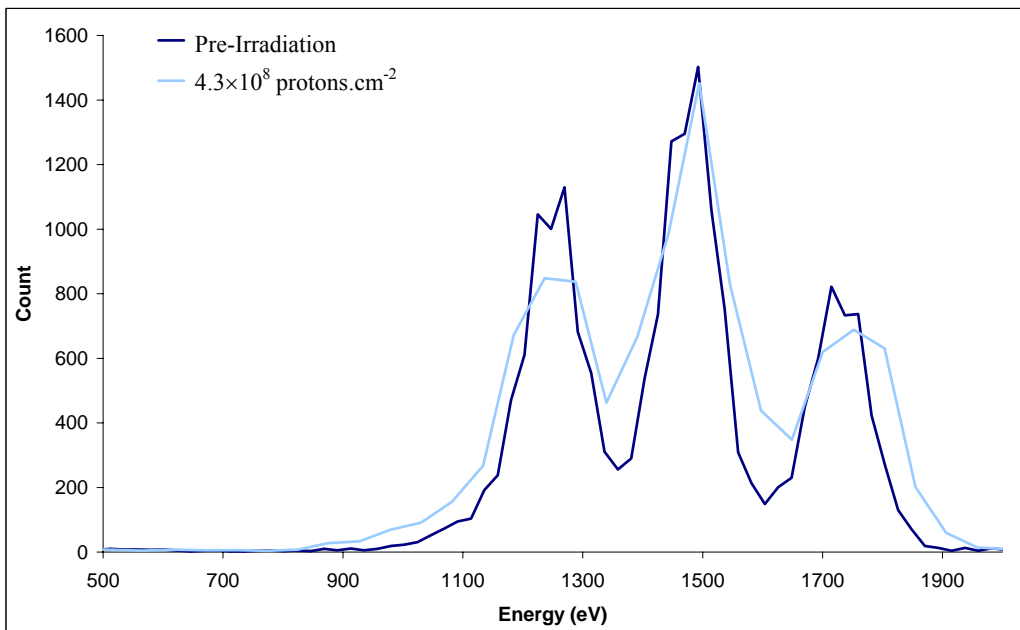


**Figure 5.23:** X-ray spectra produced using an Mg, Al and Si target between -40.0 °C

Using the computational model data shown in Figures 5.18 and 5.19 it can be seen that the CCD54 devices will no longer meet the scientific requirement of 250 eV at Mn-K $\alpha$  at -20.0 °C after  $3.5 \times 10^8$  protons.cm $^{-2}$ , around 60% through the mission. The energy resolution at different stages through the mission is shown in Table 5.4, with experimental and modelled values at -20.0 °C and -30.0 °C. The energy resolution at 78% and 38% of the total worst case end of mission fluence was compared to the results taken using the calibration Fe $^{55}$  source on the arrival of D-CIXS at the Moon, shown in Figure 5.24. The effect of reduced proton fluence is clear, showing the

improvement through the use of increased shielding and a shorter duration within the Earth's proton belts that will be the case with C1XS.

Mission Time	Proton Fluence (protons.cm <sup>-2</sup> )	FWHM at -20.0 °C		FWHM at -30.0 °C	
		Al-Kα (eV)	Mn-Kα (eV)	Al-Kα (eV)	Mn-Kα (eV)
0%	0	133.6	145.0	105.5	142.1
25%	1.38	161.7	186.8	130.6	177.4
38%	2.10	176.4	208.6	143.7	198.4
50%	2.75	189.6	228.3	155.5	213.6
78%	4.30	221.1	275.3	183.7	254.6
100%	5.50	245.6	311.7	205.6	286.4

**Table 5.4:** CCD54 energy resolution of Al-Kα and Mn-Kα at -20.0 °C and -30.0 °C over the two year mission at the Moon

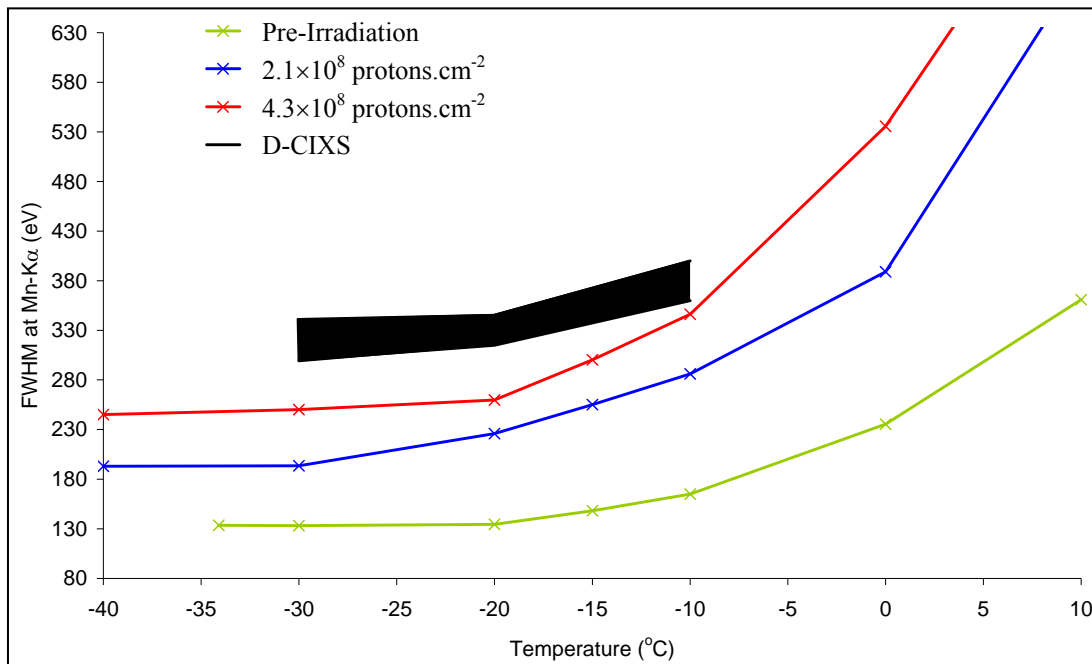


**Figure 5.24:** FWHM of Mn-Kα at different proton fluence levels compared with D-CIXS calibration data on arrival at the Moon as a function of temperature

Following the radiation study described in this chapter the minimum operational temperature for C1XS was recommended to be no less than -20.0 °C, with the possibility of temperature control to ensure stability and allow for further cooling if required. The shielding should be no less than what was used as a basis for the simulations, 3mm Al and 6mm Ta, and if mass is available should be increased. The experiments also demonstrated the importance of increasing the gain to improve read-out noise performance and allow Mg, Al, and Si X-ray events to be identified throughout the mission, even at low count rates. After these tests the SCD headboard used was modified,

increasing the resistance of the feedback resistor to provide an additional  $\times 6$  gain, improving the calibration from  $\sim 40$  eV per ADC to  $\sim 7$  eV per ADC for the work presented in the rest of this thesis.

## 5.12 Chapter Summary

This chapter has presented work carried out to assess the performance of the CCD54 after proton irradiation to ensure high quality scientific data collection over the two years C1XS will spend at the Moon, with the aim of making recommendations to improve device performance. The end of life worst case 10 MeV proton fluence was found using SPENVIS to be  $5.5 \times 10^8$  protons.cm<sup>-2</sup>, and three devices from two SCD modules were irradiated to fluence levels of  $2.1 \times 10^8$  protons.cm<sup>-2</sup> and  $4.3 \times 10^8$  protons.cm<sup>-2</sup> respectively at KVI in Holland.

The irradiation of the back half of device 4 showed a slight increase in the dark current and non-uniformity which was removed with cooling. The tests with sequence 2 showed that there was some improvement in dark current performance down to  $-30.0$  °C, the dark current generation being suppressed by freezing charge within traps. The read-out noise levels below  $-30.0$  °C, shown in Figure 5.9, and the performance improvement provided by on-chip binning below  $-30.0$  °C, shown in Figure 5.13, also demonstrate the effective suppression of dark current. Decreased spatial resolution, resulting in multiple X-ray events in one sample, is the limiting factor for increasing the on-chip bin value. Combining split events, using event processing, greatly improved the identification of events as isolated as shown in Figure 5.15. There is however, a small decrease in the measured energy resolution, for example the energy resolution at Al-K $\alpha$  decreased by 2 eV, when combining events split over two samples, the isolated energy resolution at Al-K $\alpha$  was 82 eV. Event processing does not offer a faster readout-rate. The use of sample binning should be considered for C1XS, and increased sample area would benefit future SCD development.

The total energy resolution at Al-K $\alpha$  decreased by  $\sim 17\%$  after the proton irradiation of the charge collection area, 5% as a result of increased dark current and 12% as a result of increased CTI. The increased dark current affects the entire read-out from the device, whereas the increase in CTI only affected the read-out from the irradiated side of the CCD54, demonstrating that increased CTI is the dominant source of performance loss for the CCD54. Radiation damage to the central transport channels was found to account for 80% of lost performance, as a result of every charge packet travelling through some length of the central transport channel, while each charge packet only travels through one transport channel within a given charge collection region. The trap density is higher within the central transport channels as they are larger. A reduction in volume or the

inclusion of a supplementary buried channel could help to improve the performance by reducing the silicon volume involved in charge transport as discussed in Section 3.6.

After making these recommendations the location of C1XS onboard Chandrayaan-1 was changed. The C1XS operational temperature was then predicted to be less than  $-17\text{ }^{\circ}\text{C}$  for  $\sim 90\%$  of the mission reaching as low as  $-70\text{ }^{\circ}\text{C}$  [Howe 2007]. The thermal isolation between the C1XS drive electronics and the CCD54 devices was improved to ensure adequate cooling, with a dedicated cooling system for the CCD54s being provided by Chandrayaan-1 [Howe *et al.* 2009]. The shielding around the detectors was increased to a 4 mm thick aluminium electronics box and 6 mm of tantalum behind the CCD54 modules, with the window reduced to 7 mm of Al due to the short amount of time spent within the radiation belts. The amplification provided by the electronics was increased to greatly improve upon the performance provided by D-CIXS, resulting in a read-out noise of 6-7 electrons r.m.s. [Kellet *et al.* 2008]. These changes necessitated a second proton radiation study, described in the next chapter.

## Chapter 6: Radiation Damage Study and Analysis Methods

### 6.1 Introduction

This chapter discusses the second irradiation of two CCD54 devices, the 10 MeV equivalent proton fluence delivered to each device based on an updated C1XS end of life dose. The change in the total end of life dose was as a result of the mission being launched six months later in October, with an increased Earth-Moon transfer time of seventeen days, compared with the previous seven days. The targeted average operating temperature was  $-20.0\text{ }^{\circ}\text{C}$  with a maximum operating temperature of  $-5\text{ }^{\circ}\text{C}$ , above this temperature C1XS enters ‘resting mode’. SPENVIS was again used to model the increased proton fluence, focussing on the transfer orbit, and to investigate the option of adding an additional 1 cm of Ta to the forward shielding. The October launch date resulted in the mission being launched further into solar cycle 24, which under worse case conditions would lead to a large increase in the received proton fluence as shown in Figure 3.6 and Figure 5.1.

Two devices from one module were irradiated to 10 MeV equivalent proton fluences of  $3.0\times 10^8$  protons. $\text{cm}^{-2}$  and  $7.5\times 10^8$  protons. $\text{cm}^{-2}$  using the MC40 cyclotron at the University of Birmingham in the UK. The effect of increased noise and dark current, X-ray detection including energy calibration and linearity effects, X-ray spectroscopic degradation and the identification of when increased CTI becomes the main component of decreased energy resolution are discussed, with the creation of a computational model to predict performance based on temperature and proton fluence. A sample of lunar regolith simulant and a combination magnesium, aluminium, and silicon target were used to clearly demonstrate the effect of increased proton fluence on spectra and the ability of C1XS to achieve its scientific goals.

#### 6.1.1 Chandrayaan-1 Radiation Environment October 2008 Launch

The updated orbit parameters were provided by ISRO [Shyama 2008] with the launch date set to the 22<sup>nd</sup> of October 2008, with the Earth-Moon transfer taking 16.8 days. The shielding used in the new SPENVIS calculations is given in Table 6.1. The attitude of the spacecraft during this transfer was unknown therefore the shielding was divided into areas covering the front and rear  $2\pi$  surrounding the detectors. The same settings and assumptions made in the previous SPENVIS runs were used to find the predicted end of life fluence. These provided a total end of life fluence of  $8.8\times 10^8$  protons. $\text{cm}^{-2}$ . The main source of the increase, compared with the calculations in Chapter 5, was as a result of the longer transfer time spent within the Earth’s proton belts, the inclusion of solar protons within the transfer due to increased solar activity and the use of front and rear face shielding contributions instead of a sphere of 3 mm aluminium and 6 mm tantalum. The value used

in previous reports [Gow *et al.* 2008 and Smith *et al.* 2008] used the original seven day transfer orbit calculations which gave a 10 MeV equivalent proton fluence of  $0.25 \times 10^8$  protons.cm<sup>-2</sup> for the transfer orbit, and a total end of life fluence of  $7.5 \times 10^8$  protons.cm<sup>-2</sup>.

	<i>Face</i>	<i>Shielding</i>	<i>10 MeV Proton Fluence (p.cm<sup>-2</sup>)</i>		
			<i>Trapped</i>	<i>Solar</i>	<i>Total</i>
<i>Transfer Orbit</i>	Front 2π -- A	7mm Al	0.41E+08	0.67E+08	1.08E+08
	Front 2π -- B	7mm Al + 1mm Ta	0.27E+08	0.48E+08	0.75E+08
	Rear 2π	4mm Al + 6mm Ta	0.15E+08	0.23E+08	0.38E+08
			Total from Transfer A =		1.46E+08
			Total from Transfer B =		1.13E+08
<i>Lunar Orbit</i>	Front 2π	The Moon	0	0	0
	Rear 2π	4mm Al + 6mm Ta	0	7.35E+08	7.35E+08
			Total from Lunar =		7.35E+08
			<b>Total =</b>		<b>8.81E+08</b>

**Table 6.1:** 4π shielding used during the transfer and lunar orbit, and the resulting predicted 10 MeV equivalent proton fluence for trapped and solar protons

The inclusion of a 1 mm thick piece of Ta to the front 2π shielding would only reduce the fluence by  $0.33 \times 10^8$  protons.cm<sup>-2</sup>. Using the model described in Chapter 5 this would lead to an improvement in performance of ~13 eV at Mn-K<sub>α</sub> at -20 °C. As a result of the small improvement in energy resolution it was decided not to attach the Ta sheet, due to the complexity of the work involved to incorporate it into the instrument. At the time of this comparison the instrument was already at ISRO awaiting attachment to the spacecraft. The predicted decrease in energy resolution, at Mn-K<sub>α</sub>, as a result of the change in launch date and accounting for front and rear shielding was around 44 eV at -20 °C.

The number of sunspots recorded since the creation of the model for cycle 24, illustrated in Figure 3.6, was lower than predicted as shown in Figure 6.1. SPENVIS was run at solar maximum, with the predicted solar maximum flux used for the entire mission duration. The actual solar proton fluence received during the transfer orbit and during the initial time spent at the Moon will be lower than shown in Table 6.1. This lower proton and X-ray flux at mission start will lead to a decreased damage rate and lower fluoresced X-ray detection rate. This could allow the mission lifetime of C1XS to be extended, increasing the detail that will be generated by the larger solar flares towards solar maximum. The revised 100% end of life fluence used in this second radiation study should also be considered worse case.

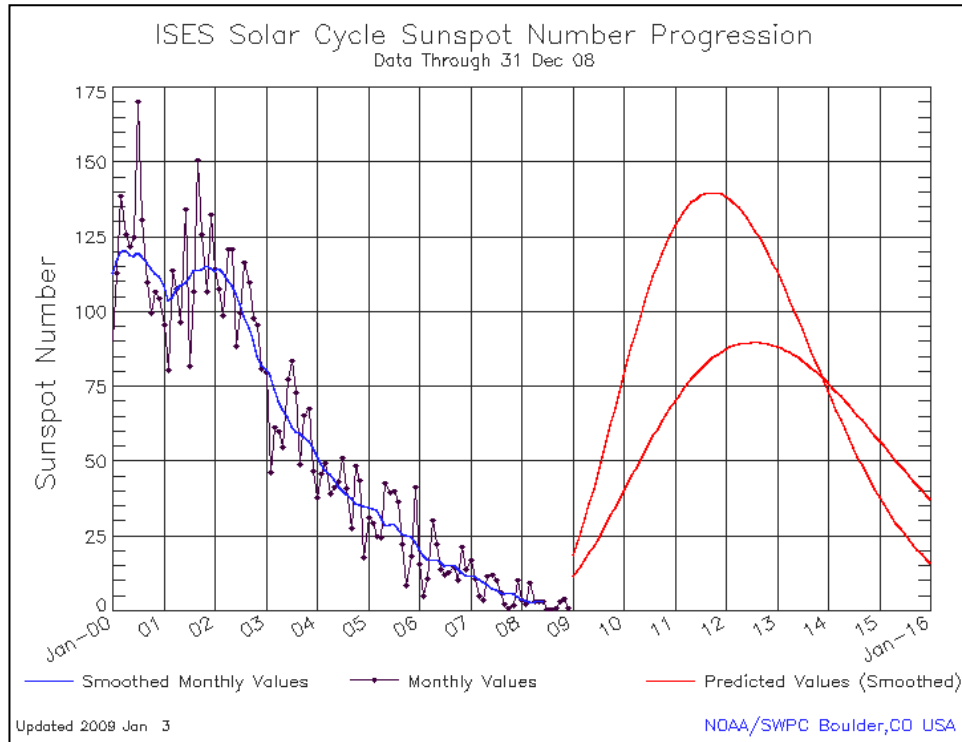


**Figure 6.1:** Solar cycle 23 and the start of cycle 24 from experimental data and the NOAA SWPC prediction for cycle 24 (image courtesy of NOAA/SWPC)

## 6.2 Experimental Arrangement and Procedure

This section describes the experimental arrangement, the test procedure used during the pre-irradiation, the proton irradiation and the dosimetry, and post-irradiation characterisation of two CCD54 devices from module 17.

### 6.2.1 Laboratory Experimental Arrangement

The experimental arrangement described in Section 4.3 was used to hold CCD54 module 17, with the addition of a modified target wheel and a collimator, as shown in Figure 6.2. The target wheel was modified to hold the targets surface at the same distance from the detector and X-ray tube, to within an error of  $\pm 0.5$  mm, in preparation of testing performed in Chapter 7 which required the geometry to be known. All data analysis was conducted using the MATLAB software described in Chapter 4. The target wheel was aligned using a laser to provide improved repeatability by allowing the angle of incidence to be controlled to an accuracy of  $\pm 1$  degree. The laser was attached to the chamber inside the beam input tube on the right side and aligned centrally using a target held on the input tube on the left side, illustrated in Figure 4.21 with the pressure gauge connected. The target wheel was then placed inside the chamber and rotated with the light reflecting onto a ruler held across the mid point of the chamber to identify the point at which an

incident angle of 45 degrees was achieved. The control handle which had been designed to show the angle of incidence and the currently exposed target was then attached to the external part of the target wheel.

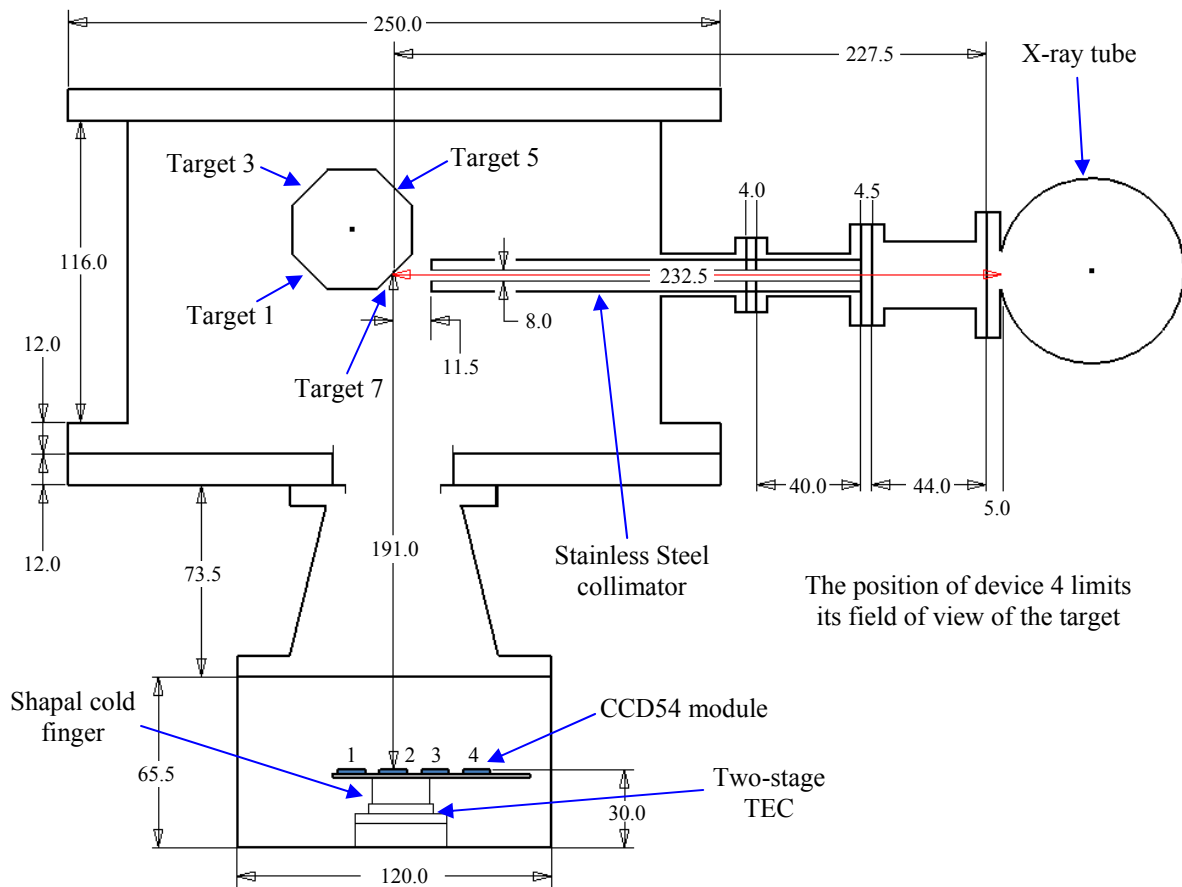


**Figure 6.2:** Schematic of the CCD54 test equipment, showing the numbered target surfaces, device location on the SCD module and the collimator, with measurements in mm

The collimator ended 11.5 mm from the front surface of targets held on the target wheel as shown in Figure 6.2, to limit un-wanted X-ray fluorescence from within the chamber. Dosimetric film, HD-810, was used to ensure that X-rays from the tube would be focussed on the target. The film is sensitive to charged particles, with the change in optical density proportional to the received dose. A piece of film was placed onto points one, three, five and seven of the target wheel, the X-ray tube power supply was increased to 25 kV and 0.5 mA and operated for three hours with the beam focussed at target 7. The dose deposited onto the film at target 7 was clear, and there was no discernable change in the films held on the other targets. Indicating no unwanted XRF from the other targets held within the chamber.

In an attempt to improve the thermal contact between the cold finger and the module ceramic a piece of aluminium foil was placed between them. Experimental work conducted during Chapter 4 demonstrated that 30 minutes, after reaching the target temperature, was sufficient for the module

temperature to stabilise to within  $\pm 0.2$  °C, with a cooling rate of  $\sim 2$  °C.min<sup>-1</sup>. During the testing the temperature of device 4 was monitored to ensure it remained within  $\pm 0.2$  °C of the temperature recorded at the start of testing. Using the modules temperature dependence, discussed in Section 4.3.2, the temperature of device 1, 2, and 3 was calculated.

Targets were selected to provide X-rays over the energy range of 1.25 keV to 8.05 keV. The four selected are shown in Table 6.2. Target one would allow the investigation of the three main points of interest for C1XS the magnesium, aluminium, and silicon X-ray lines, while target three would provide three clearly separated energies at 1.49 keV, 3.69 keV and 8.05 keV covering the target energy range of the CCD54. Target five was a pellet of lunar regolith simulant JSC-1, provided by I. Crawford from Birkbeck College UCL, to provide an example of a possible lunar spectra, with target seven being a piece of Rhodonite to provide manganese X-rays to make comparisons with the previous irradiation study. Due to its low fluorescent yield, around 0.4% from Equation 2.5, it was unlikely that oxygen, large quantities present in the rock samples  $\sim 45\%$  of the lunar regolith simulant, would be observed in the resulting spectra, unless the integration time was increased.

<i>Target</i>	<i>Material</i>	<i>Detected Elements</i>
1	Mg, Al, Si	Mg, Al, Si
3	Al, Ca, Cu	Al, Ca, Cu
5	Lunar Regolith Simulant	Na, Mg, Al, Si, P, K, Ca, Mn, Ti, Fe
7	Rhodonite	Si, Ca, Mn

**Table 6.2:** X-ray fluorescence targets

### 6.2.2 Laboratory Test Procedure

Data was acquired using three sets of 4765 read-outs for each device and target using sequence 1, and 600 read-outs using sequence 2 with a delay of 10 ms. The cold finger temperature was varied between 20.0 °C and -50.0 °C in steps of 10.0 °C (all  $\pm 0.2$  °C), with a settle time of 30 minutes from the time the temperature controller reached the target temperature, providing a full range of possible operating temperatures. The X-ray tube potential was set to 15 kV with a tube current of 0.15 mA. Previous testing had shown the resulting beam to be stable to within 3%. The number of rows was equivalent to a live time of 60 seconds with an average of four events per read-out ( $\sim 300$  events.cm<sup>-2</sup>.s<sup>-1</sup>). This was selected to limit the affect on trap filling by having a high X-ray flux, which would artificially improve the device CTE. To observe the effects of displacement damage on the operating voltages they were varied over the same ranges described in Chapter 4, with the cold finger held at -20.0 °C and -40.0 °C (both  $\pm 0.2$  °C) using target 3. The tube current was varied to observe the effect of increased X-ray flux post-irradiation and the tube potential was varied to

simulate the energy provided by different solar flares with the cold finger held at  $-20.0\text{ }^{\circ}\text{C} \pm 0.2\text{ }^{\circ}\text{C}$  to provide near mission average operating temperature using target 3. The results from varying the tube potential are discussed in Chapter 7, the effect of increased X-ray flux is discussed in Section 5.9. Device 1 failed during the last stage of testing prior to the irradiation. The device was operating normally, however when testing resumed it was no longer functional.

A clock sequence program was written to back clock the CDC54, called sequence 3, to allow the system noise component to be decoupled from the dark current component. The system noise includes noise from the drive electronics and clock induced charge. The shot noise can be found by removing the incident X-rays. The system noise was measured to be  $4.5\text{ e}^-$  r.m.s. Dark current generation is minimised below  $-30.0\text{ }^{\circ}\text{C}$ , cooling the device to  $-40.0\text{ }^{\circ}\text{C}$  the shot noise component was found to be  $0.4\text{ e}^-$  r.m.s. Therefore  $4.9\text{ e}^-$  r.m.s. forms the limit of the device performance achieved only after the dark current component has been minimised.

### 6.2.3 The Accelerator Facility and Dosimetry

A 10 mm thick aluminium shield was constructed that would allow the whole active area of devices 1, 3 or 4 to be irradiated, shown in Figure 6.4. Additional aluminium shields would cover the devices not to be irradiated, with device 2 held as a control. At the time of the second irradiation the revised end of life 10 MeV equivalent proton fluence was predicted to be  $7.5 \times 10^8\text{ protons.cm}^{-2}$  so two proton fluences were selected,  $3.0 \times 10^8\text{ protons.cm}^{-2}$  and  $7.5 \times 10^8\text{ protons.cm}^{-2}$  to be delivered to device 4 and 3 respectively, as shown in the irradiation summary in Table 6.3. Device 3 was selected to receive the higher fluence as it could be cooled slightly more than device 4, allowing the resulting increase in dark current to be minimised.

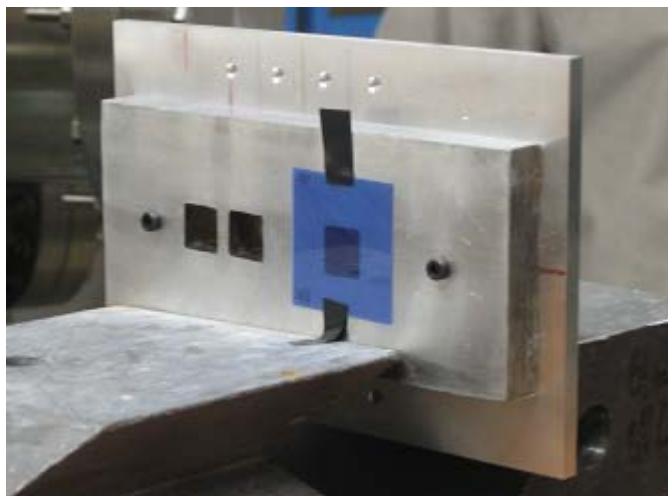


**Figure 6.4:** Aluminium shield used with the MC40 cyclotron, showing irradiated HD-810 film

Dosimetry was provided using Gafchromic HD-810 film. The film was calibrated in the Brunel University Cobalt-60 cell using a Farmer ionisation chamber, comparing the dose received by the detector to the change in optical density of the film over a range of exposure times. The film is  $\sim 100 \mu\text{m}$  thick consisting of a  $0.75 \mu\text{m}$  surface layer, a  $6.6 \mu\text{m}$  active layer and a layer of  $\sim 97 \mu\text{m}$  transparent polyester. Charge deposited within the active layer causes a change in the optical density of the film as the active layer forms a blue coloured polymer, the response is enhanced using red light. This effect is shown in Figure 6.4 which formed part of the five pre-irradiation beam calibration and uniformity tests and in Figure 6.5 which shows the reference film and a piece held over the beam exit. The film was scanned using an Epson V750 Pro scanner immediately after the irradiation as previous testing demonstrated that the optical density continued to increase with time [Glaser and Ravotti 2006]. The program ImageJ was used to find the mean ADC value for the red part of the spectrum. The dose expressed in krad,  $D$ , is then given by:

$$D = 23.1 \times OD = 23.1 \times \log_{10} \left( \frac{\phi_{ref}}{\phi_{Irrad}} \right) \quad (6.1)$$

where 23.1 is the calibration factor (film dependant),  $OD$  is the optical density,  $\phi_{ref}$  and  $\phi_{Irrad}$  are the reference and irradiated mean peak intensity found using ImageJ. The 10 MeV equivalent proton fluence expressed in protons. $\text{cm}^{-2}$ ,  $\Phi$ , is given by:

$$\Phi = \frac{D \times K}{(dE/dx)_m} \quad (6.2)$$

where  $K = 2.356 \times 10^9$  is a scale factor, and  $(dE/dx)_m$  is the minimum ionising energy loss rate in silicon of  $1.6 \text{ MeV} \cdot \text{cm}^2 \cdot \text{g}(\text{Si})^{-1}$ .

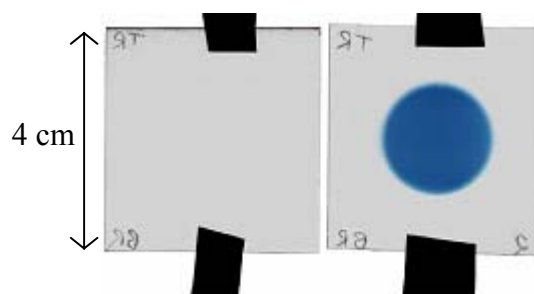


**Figure 6.5:** HD-810 Dosimetric film, showing an un-irradiated sample on the left and one held over the beam exit during an irradiation on the right

The accelerator facility used was the University of Birmingham MC40 cyclotron shown in Figure 6.6. The cyclotron can provide protons with energies between 12 and 38 MeV, achieving stable beams at the pA and nA range up to  $30 \mu\text{A}$ , with a beam diameter of 1 to 10 mm. A  $30 \mu\text{m}$  Havar window is mounted in the flange on the beam exit, separating the cyclotron vacuum system held at a pressure of  $\sim 10^{-5}$  mbar from the open air.



**Figure 6.6:** The University of Birmingham's MC40 cyclotron

#### 6.2.4 Irradiation of the CCD54 Module

The irradiation took place with the CCD54s unbiased held in air using 15 MeV protons, with the front surface of the CCD54 to be irradiated placed at a distance where the protons had attenuated to 10 MeV, as shown in Figure 6.7. A laser was used to align the module holder with the beam exit. A 100  $\mu\text{m}$  Tungsten scattering foil was used to provide a larger beam size, stable to within  $\pm 10\%$  (the CCD54 requires a minimum beam diameter of at least 15 mm), and a piece of HD-810 was placed over devices 3 and 4 when they were irradiated. The distance required in air, for attenuation to 10 MeV at the surface of the CCD, was found using the stopping powers of the materials through which the protons travelled, providing a required air gap of 66.7 cm of air, measured to  $\pm 0.5$  cm, the error corresponding to  $\pm 20$  keV, well within acceptable error.

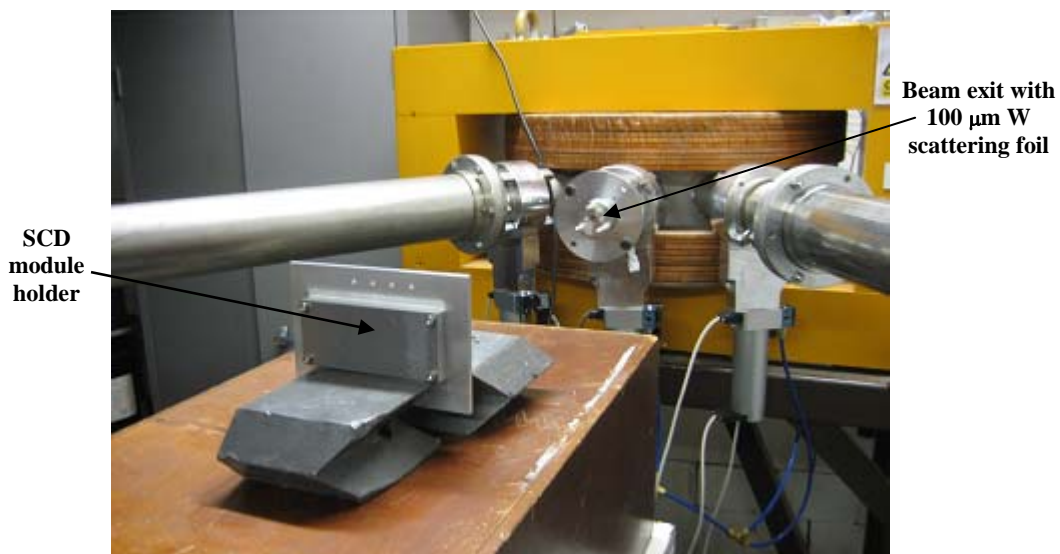


**Figure 6.7:** SCD mounted in line with the proton beam

The 10 MeV proton fluence found using the two pieces of film held over devices 3 and 4, as shown in Figure 6.8 marking the acceptable  $\pm 10\%$  error. The results were found by taking the average ADC value across the film to produce data points in  $\sim 0.1$  mm steps. The total 10 MeV fluence delivered was  $7.54 \times 10^8$  protons. $\text{cm}^{-2}$  and  $3.03 \times 10^8$  protons. $\text{cm}^{-2}$  to devices 3 and 4 respectively, as shown in the radiation summary in Table 6.3. These values correspond to 86% and 34% of the revised worse case end of life proton fluence for C1XS. The levels were selected prior to the change in transfer orbit, when  $7.5 \times 10^8$  protons. $\text{cm}^{-2}$  was the end of life proton fluence.

<i>Parameter</i>	<i>Value</i>
No. SCDs	2
Irradiation area	Whole device
Beam energy at SCD	10 MeV
<b>10 MeV Fluence</b>	<b><math>3.0 \times 10^8</math>, and <math>7.5 \times 10^8</math> protons.<math>\text{cm}^{-2}</math></b>
Beam Flux	$8.4 \times 10^5$ protons. $\text{cm}^{-2}.\text{s}^{-1}$
Beam uniformity	10%

**Table 6.3:** Proton irradiation characteristics

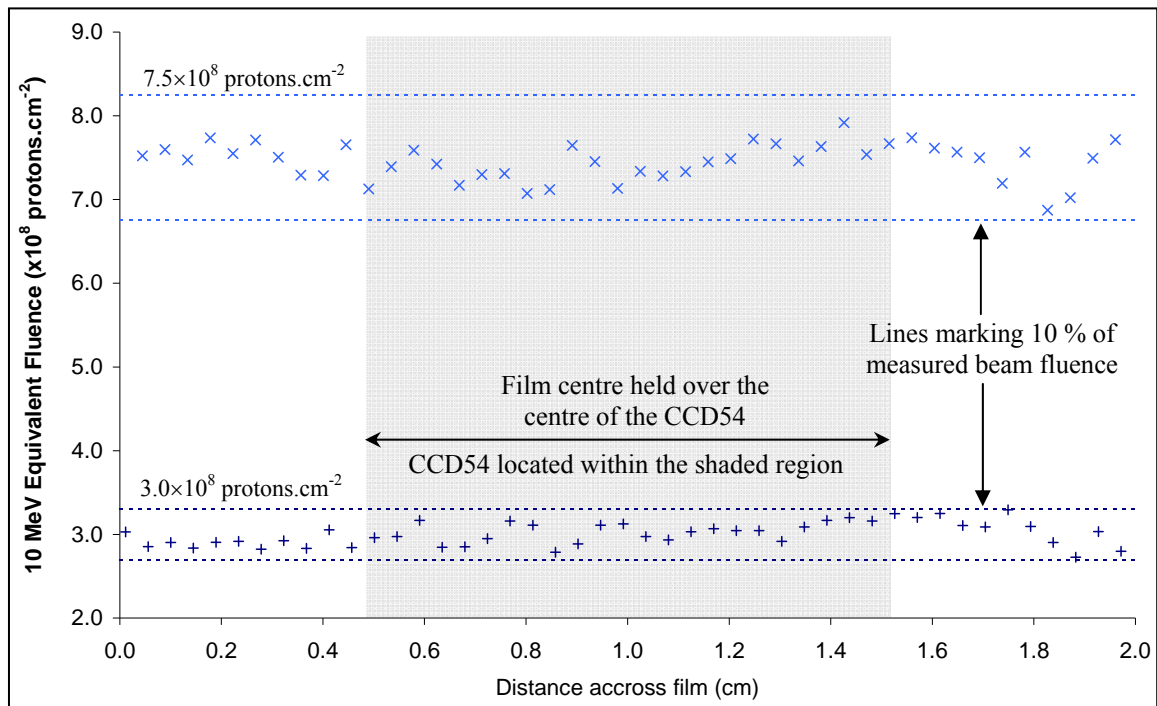


**Figure 6.8:** Measured proton beam fluence as a function of distance across the target area

To provide confirmation that the beam energy was around 10 MeV a piece of film was held, edge on to the incident proton beam, within a polythene block to identify the Bragg peak. The dark blue line, marking the Bragg peak, was clearly visible after an irradiation and measured to be  $1.1 \pm 0.2$  mm, the error arises from positioning the film within the polythene block and measuring the peak location in ImageJ. The Bragg peak, for polythene, was found using SRIM to be at 1.2 mm for 10 MeV protons. The measured peak corresponds to an energy of  $\sim 9.7$  MeV,  $\pm 10\%$ .

### 6.3 Noise

The noise calibration was found using the Cu-K $\alpha$  X-ray peak from target 3, as shown in Figure 6.9 which gives the read-out noise value pre- and post-irradiation as a function of temperature and the combined system and shot noise of 4.9 e<sup>-</sup> r.m.s. measured using sequence 3. Post-irradiation there is a clear increase in noise due to radiation induced dark current within the silicon. The increase is strongly affected by operating above -20.0 °C. At near -40.0 °C the total noise is closely approaching system limited performance. The values given in Table 6.4 show the noise values at -20.0 °C, found using a polynomial fit to the data, and the predicted energy resolution at Al, Ca, Mn and Cu-K $\alpha$  pre- and post-irradiation based on the quadrature summation of the X-ray Fano-limited statistics plus the measured noise, described by Equation 2.44. These predicted energy resolutions would only be true if no other damage mechanisms occurred that would impact the measured energy resolution, for example increased CTI.

10 MeV Fluence (protons.cm <sup>-2</sup> )	Noise (e <sup>-</sup> r.m.s.)	Predicted FWHM (eV)			
		Al-K $\alpha$	Ca-K $\alpha$	Mn-K $\alpha$	Cu-K $\alpha$
0.0	6.3	80.2	107.5	129.2	147.3
3.0	10.5	107.8	129.4	147.9	164.0
7.5	15.0	142.0	159.0	174.4	188.2

**Table 6.4:** Predicted energy resolution of Al, Ca, Mn, and Cu-K $\alpha$  events at -20 °C

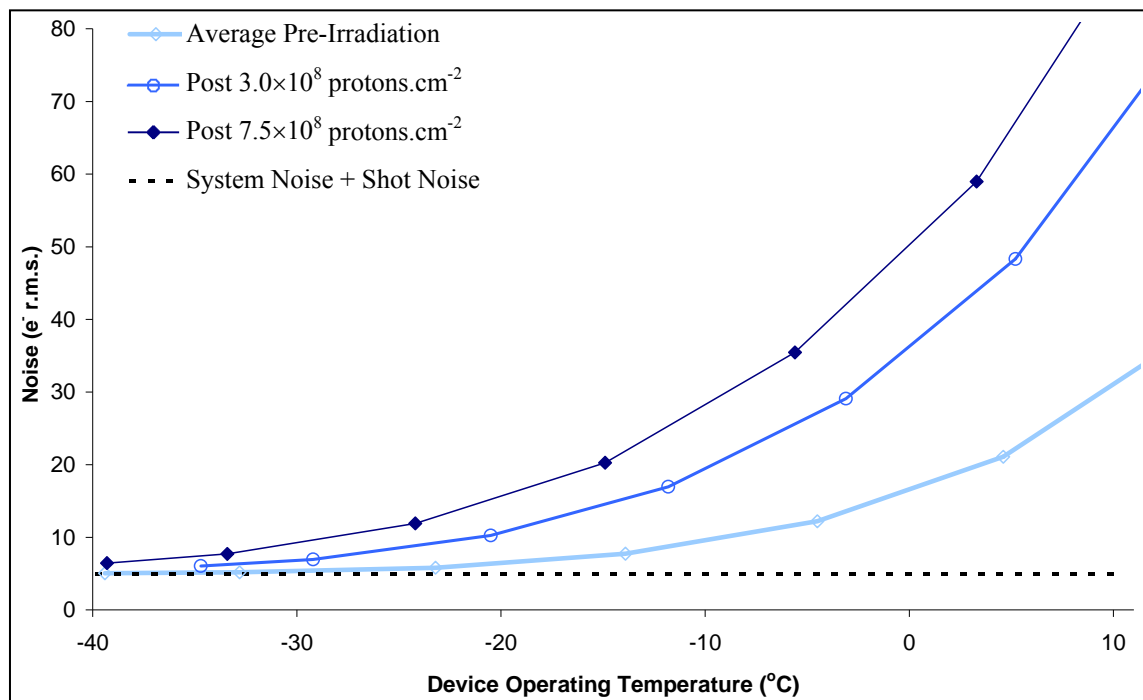


**Figure 6.9:** Measured noise as a function of temperature for devices 2, 3 and 4

## 6.4 Dark Current

The dark current was estimated and compared using two different methods, found to be comparable to within  $\pm 2\%$ . The two methods were to measure the shift in the noise peak location with the peak location at around  $-40.0^\circ\text{C}$  as the reference, and to subtract the square of the system noise and from the total measured noise. The later method was used to produce the results in this section. The increase in dark current after irradiation, shown in Figure 6.10 is linear with increasing proton fluence.

The main component of the increased dark current should be as a result of thermally generated electrons within the bulk silicon and not at the Si-SiO<sub>2</sub> interface, as a result maintaining the inversion at the surface using continuous clocking. To confirm this, device 3 held at  $-15.0^\circ\text{C}$  was taken out of inversion by reducing the substrate voltage,  $V_{ss} \pm 0.05\text{ V}$ . There is a clear increase in dark current generation as the CCD54 is taken out of inversion, shown in Figure 6.11, which is attributed to increased surface generated dark current caused by ionisation damage. The post-irradiation dark current was then normalised to the pre-irradiation value with  $V_{ss}$  held at  $10.0\text{ V}$ , to clearly show the increase in surface generated dark current when not operating in inverted mode. The voltage required to minimise the surface generated dark current increased from  $\sim 8.5\text{ V}$  to  $\sim 9.0\text{ V}$ , the operational range of  $V_{ss}$  should be in the range of  $9.0$  to  $10.0\text{ V}$ , the lower limit recommendation made to avoid increased impact ionisation and power consumption while not reducing the performance over the mission.

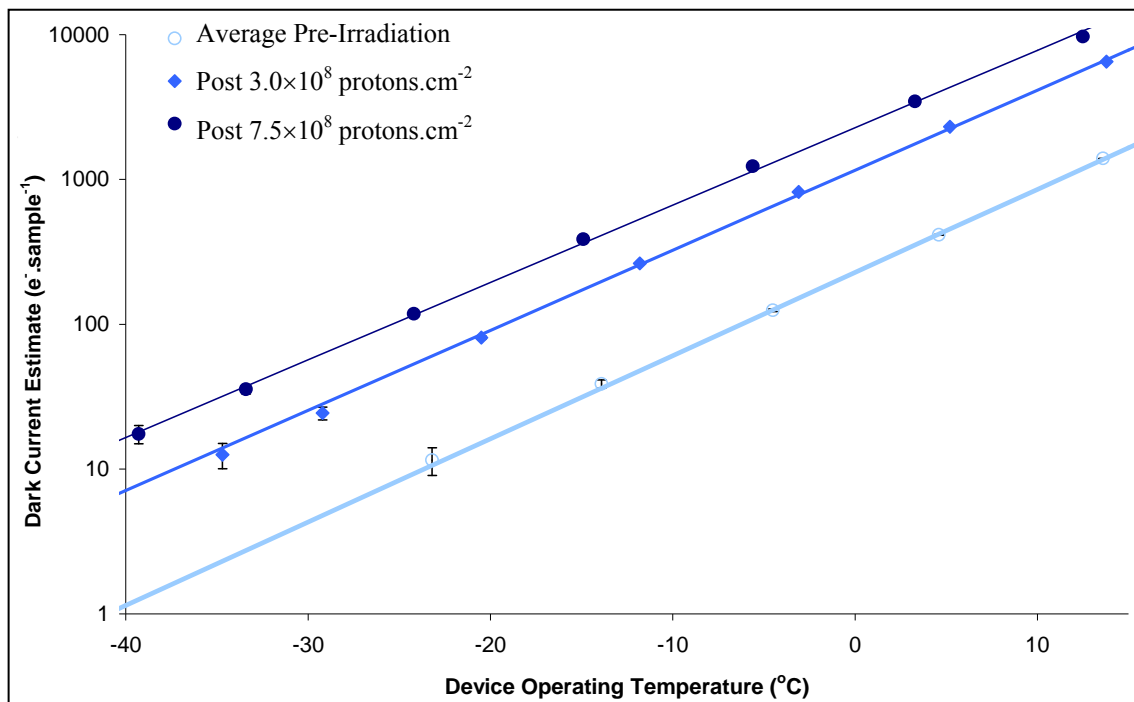


**Figure 6.10:** Estimated dark current as a function of temperature found using the square of the system noise subtracted from the square of the measured noise

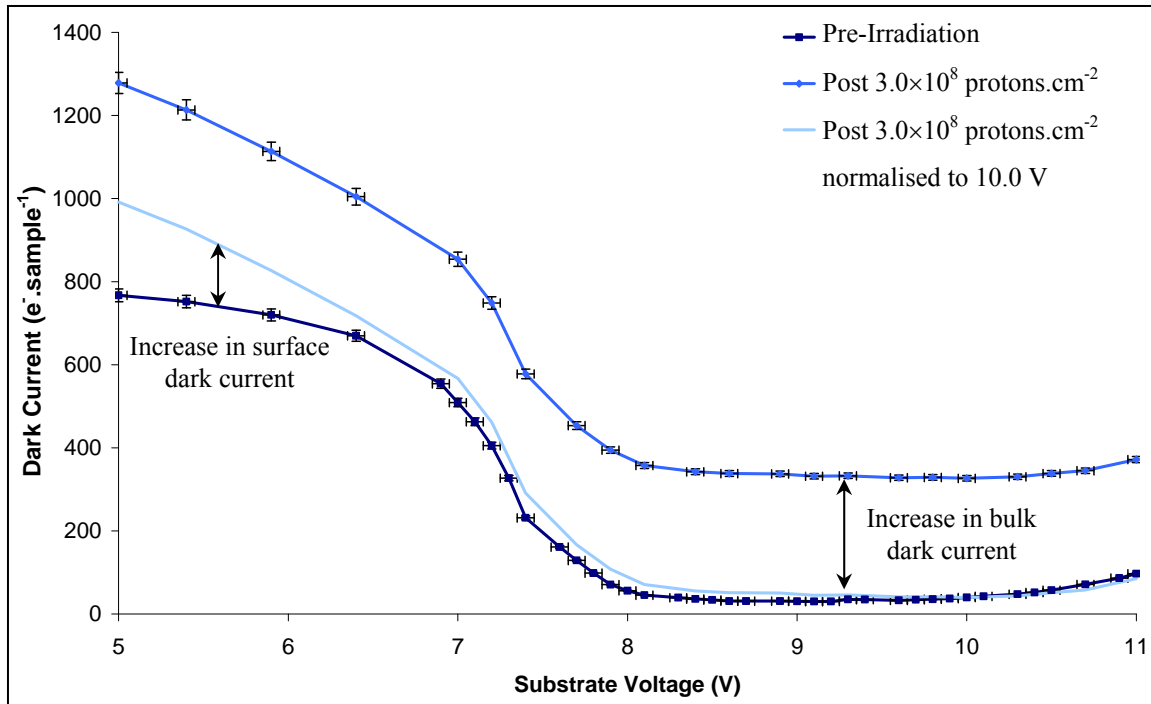


**Figure 6.11:** Estimated dark current as a function of substrate voltage, device 3 held at  $-15.0\text{ }^{\circ}\text{C}$  pre- and post-irradiation with  $7.5 \times 10^8\text{ protons.cm}^{-2}$

To identify the dominant trap sites pre- and post-irradiation the dark current was plotted as a function of  $1/T$  in an Arrhenius plot [Connors 1990], as shown in Figure 6.12. The exponential term is then given by:

$$\frac{(E_g - E_t)}{k} \quad (6.3)$$

taken from Equation 2.30, where  $k = 8.62 \times 10^{-5}\text{ eV.K}^{-1}$ . The dominant trap levels are 0.32 eV pre-irradiation, 0.39 eV after  $3.0 \times 10^8\text{ protons.cm}^{-2}$  and 0.44 eV after  $7.5 \times 10^8\text{ protons.cm}^{-2}$ . This compares very well with previously measured trap levels of un-irradiated CCDs of 0.30 eV from an unknown defect [Holland 1993], then as the number of E-centre defects increases the trap level tends towards 0.44 eV which compares very well with other reported levels for the E-centre, 0.42 eV [Holland 1993] and 0.44 eV [Janesick 2001].

The density of 0.32 eV traps was calculated using Equation 2.28, assuming that the density of E-centre traps pre-irradiation and surface contribution were negligible, to be  $3.5 \times 10^{12}\text{ cm}^{-3}$ . The 0.32 eV trap density was then estimated, based on the increase with proton fluence found by Holland 1991, at  $3.0 \times 10^8\text{ protons.cm}^{-2}$  and  $7.5 \times 10^8\text{ protons.cm}^{-2}$ . The density of E-centre traps was then calculated, assuming the E-centre trap is responsible for the remaining dark current generated. The trap densities are given in Table 6.6.

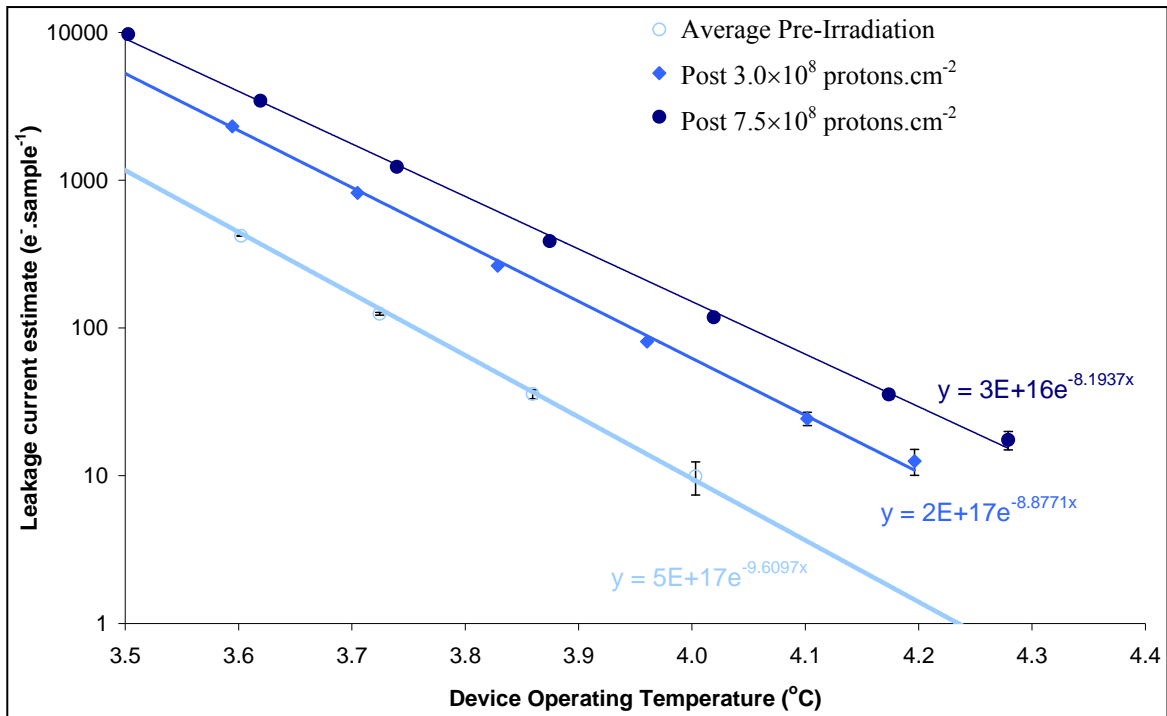


**Figure 6.12:** Arrhenius plot of dark current as a function of  $1000/T$  for pre-irradiated and devices 3 and 4 irradiated to  $3.0$  and  $7.5 \times 10^8$  protons. $\text{cm}^{-2}$  respectively

Trap Name	Energy Level (eV)	Un-Irradiated $N_B$ ( $\text{cm}^{-3}$ )	$3.0 \times 10^8$ protons. $\text{cm}^{-2}$ $N_B$ ( $\text{cm}^{-3}$ )	$7.5 \times 10^8$ protons. $\text{cm}^{-2}$ $N_B$ ( $\text{cm}^{-3}$ )
Unknown	0.32	3.5E+12	5.3E+12	7.9E+12
E-centre	0.44	-	1.6E+11	3.1E+11

**Table 6.6:** Calculated bulk trap densities found using Equation 2.28

The calculated trap densities, in Table 6.6, are orders of magnitude higher than found by Holland 1993. Using the measured dark current to calculate trap densities is not very accurate due to the assumptions made to produce Equation 2.15 and the problems involved with multiple traps at different energy levels. Extensive modelling of CTE has been performed to calculate the trap density, which is very sensitive to the trap energy level and cross section, of the E-centre [Robbins, Roy, and Watts 1991, and Robbins 1992], Divacancy [Hardy *et al.* 1998], A-centre [Holland 1993] and the Unknown at 0.3 eV [Holland 1993]. Using 1D and 2D CTE models to calculate the trap energy levels and densities is more accurate than using the measured dark current, due to the removal of Equation 2.15. Using the trap cross sections and the trap density as a function of 10 MeV equivalent proton fluence found by these studies the increase in dark current, at 20.0 °C, after irradiation was calculated. The results and the calculated trap densities are shown in Table 6.7, the calculated dark current does not account for all of the measured dark current. The remainder originates from traps at mid-band traps ( $\sim 0.56$  eV) which are much more effective at generating dark current, as discussed in Section 2.5.

Fluence ( $p.cm^{-2}$ )	<i>E</i> -centre $N_B$ ( $cm^{-3}$ )	Divacancy $N_B$ ( $cm^{-3}$ )	<i>A</i> -centre $N_B$ ( $cm^{-3}$ )	Unknown $N_B$ ( $cm^{-3}$ )	Dark Current Contribution	Remaining Dark Current
$3.0 \times 10^8$	$6.0 \times 10^9$	$9.3 \times 10^8$	$1.2 \times 10^{10}$	$1.2 \times 10^9$	43 pA.cm <sup>-2</sup>	254 pA.cm <sup>-2</sup>
$7.5 \times 10^8$	$1.5 \times 10^{10}$	$2.3 \times 10^9$	$3.0 \times 10^{10}$	$3.0 \times 10^9$	107 pA.cm <sup>-2</sup>	495 pA.cm <sup>-2</sup>

**Table 6.7:** Calculated bulk trap densities and their contribution to the post irradiation increase in dark current at 20.0 °C, and the remaining dark current attributed to trap sites at mid-band

## 6.5 X-ray Detection

This section describes the results of radiation damage to event selection, energy calibration, and the effect on device linearity.

### 6.5.1 Threshold of Event Selection

The study conducted on the threshold of event selection, using Equation 4.1, was repeated for an irradiated device. The measured energy resolution above -10.0 °C is greatly affected by  $\lambda_m$  as shown in Figure 6.13 which gives the measured energy resolution of Cu-K $\alpha$  found using device 3 post-irradiation to  $7.5 \times 10^8$  protons.cm<sup>-2</sup>. To remove the thresholding effect from data used to identify the dominant source of decreased energy resolution,  $\lambda_m$  was reduced until no further change in energy resolution was measured while still providing an error of 4.5% on the number of counts. A value of 0.1 was selected.

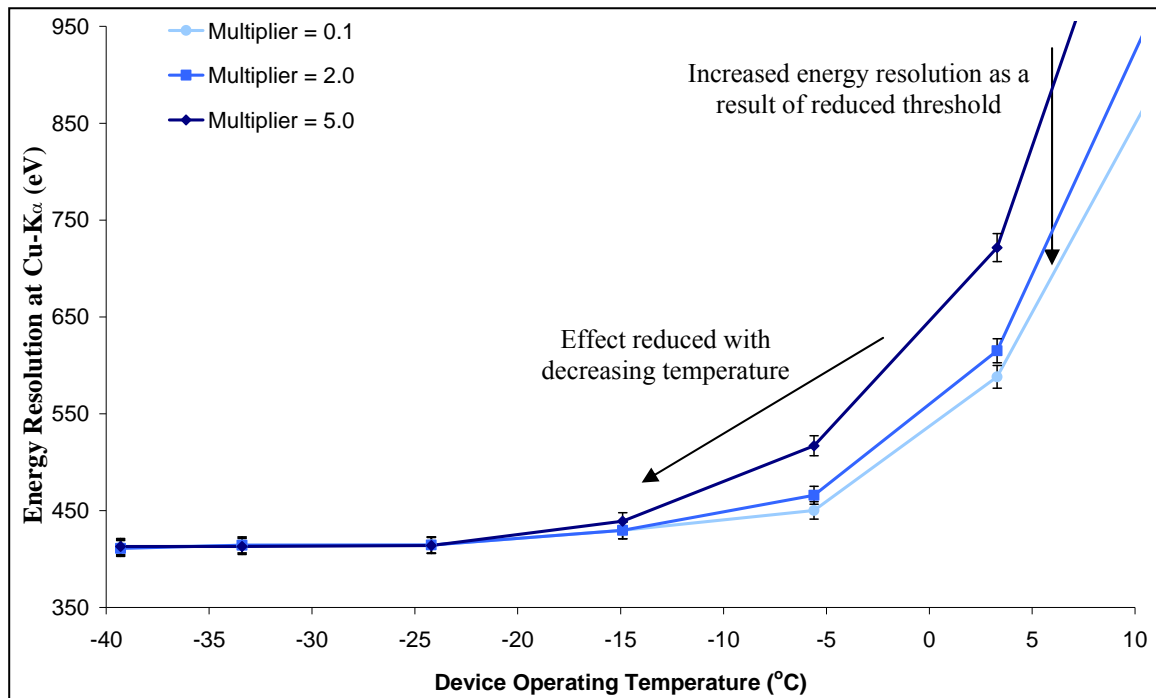


**Figure 6.13:** Measured energy resolution of Cu-K $\alpha$  as a function of  $\lambda_m$  for device 3

The typical frequency of event size,  $\pm 1\%$ , was recorded as a function of proton fluence as shown in Table 6.6 for  $\lambda_m = 2.0$ , used for all MATLAB testing unless stated otherwise. As expected, higher energy X-rays are more likely to spread over more pixels, with only 43% of Cu-K $\alpha$  events being recorded as isolated events. The small change in event frequency is as a result of the increased generation of electrons in traps, bright defects, causing an increase in the dark current non-uniformity. The time to complete one three phase transfer is of the order  $10^{-5}$  seconds, the trap time constant of the E and A centres, given in Figure 3.22, are orders of magnitude greater. Trapped electrons will not be recombined by event processing as the electrons will be released hundreds of transfers later. Therefore it is unlikely that electron recombination will affect the frequency of isolated events, unless the trap time constant is of a similar order to the transfer time.

Event size (samples)	Typical Frequency %								
	Al-K $\alpha$ (1487 eV)			Ca-K $\alpha$ (3691 eV)			Cu-K $\alpha$ (8047 eV)		
	Pre	$3.0 \times 10^8$	$7.5 \times 10^8$	Pre	$3.0 \times 10^8$	$7.5 \times 10^8$	Pre	$3.0 \times 10^8$	$7.5 \times 10^8$
1	68%	68%	68%	63%	62%	62%	43%	42%	41%
2	28%	27%	27%	30%	31%	31%	37%	35%	34%
3	3%	4%	4%	4%	4%	4%	8%	8%	9%
4	1%	1%	1%	2%	2%	2%	7%	7%	8%
5	0%	0%	0%	1%	1%	1%	4%	6%	6%
6	0%	0%	0%	0%	0%	0%	1%	2%	2%
7	0%	0%	0%	0%	0%	0%	0%	0%	0%

**Table 6.6:** Typical event size frequencies for Al, Ca, Cu-K $\alpha$  events,  $\lambda_m = 2$

### 6.5.2 Energy Calibration

The energy calibration was performed using the Cu-K $\alpha$  X-ray peak, as each device has a slightly different calibration the results were all normalised to those of device 3. The pre-irradiation energy calibration in eV per ADC channel decreases with decreasing temperature as shown in Figure 6.14, as a result of the trap time constant increasing, essentially freezing the electrons within the traps reducing the probability that charge generated by X-ray events will be captured. The increase in energy calibration with respect to proton fluence, shown in Figure 6.14, is as a result of increased re-combination within trap sites formed by displacement damage within the bulk silicon and by ionisation damage at the surface, essentially reducing the carrier lifetime. Over the temperature range detailed the increase is approximately linear. An equation to find the change in energy calibration is given by:

$$Cal = 0.011T_{SCD} + 6.44 \times 10^{-10} \Phi + 14.3 \quad (6.4)$$

where  $T_{SCD}$  is the temperature of the CCD54 in °C and  $\Phi$  is the 10 MeV equivalent proton fluence (protons.cm<sup>-2</sup>). The identification of the energy calibration at different temperatures and fluence levels removes the requirement to pre-calibrate the device with a known X-ray source as only the location of the noise peak is required. The energy calibration is affected by the 16-bit ADC read-out, the gain of  $\times 5$  applied by the drive electronics and the gain of  $\times 11$  on the headboard. The 16-bit calibration of the CCD54 at -20.0 °C operated using the voltages in Table 4.2 with no additional gain would be 48.4 eV per ADC, from Equation 6.4 accounting for the division of 16 described in Section 4.4. The difference in calibration to that in Chapter 5 is due to a new headboard, designed at XCAM, specifically for use with the CCD54 as part of the C1XS radiation damage study.

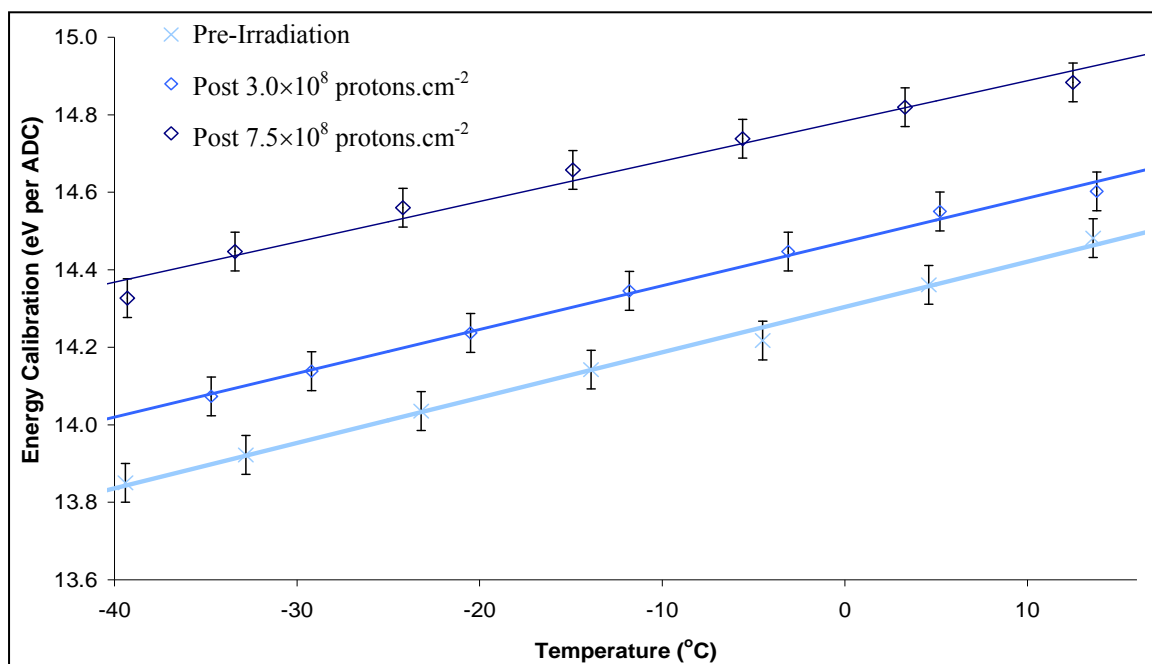


**Figure 6.14:** Calibration found using Cu-K $\alpha$  events as a function of temperature

### 6.5.3 Linearity Testing

It is essential that over the two year C1XS mission X-ray peaks are identifiable. With increasing proton fluence, the energy resolution decreases, making peak locations even more important in the identification of different X-ray lines. The Cu-L $\alpha$  peak was used in Chapter 4 to measure the pre-irradiation linearity. Similar results were found using the Al, Ca, and Fe-K $\alpha$  peaks as shown in Table 6.8 which shows the difference in measured peak location and the accepted value, all within error prior to the irradiation. The error was taken to be the energy calibration,  $\sim \pm 14$  eV. Table 6.8 shows that as the proton fluence increases so does the difference in measured peak location from the accepted value for lower energy X-rays. After  $7.5 \times 10^8$  protons.cm<sup>-2</sup> the Al-K $\alpha$  and Cu-L $\alpha$  peak centroids had shifted by  $\sim 4$  ADC channels.

<i>Element</i>	<i>Energy (eV)</i>	<i>Peak Divergence (eV)</i>		
		<i>0</i>	<i><math>3.0 \times 10^8</math></i>	<i><math>7.5 \times 10^8</math></i>
Al	1,487	6	21	53
Ca	3,691	6	18	34
Fe	6,403	6	13	19

**Table 6.7:** The divergence in the peak centroid, calibration found using Cu-K $\alpha$  events

The increased non-linearity at lower energies could be as a result of the recombination of electrons at the surface. At lower currents, the flow of minority carriers is greater near the surface causing recombination to remove electrons more effectively, referred to as the ‘surface gain factor’, and increased by irradiation [Holmes-Siedle 2002]. A reduction in CTE will contribute to peak shift, however the smaller charge clouds from low energy X-rays are less likely to encounter traps.

## 6.6 X-ray Spectroscopy Degradation

The measured energy resolution of the Mn-K $\alpha$  X-ray peak after a 10 MeV equivalent proton fluence of  $3.03 \times 10^8$  protons.cm $^{-2}$  and  $7.54 \times 10^8$  protons.cm $^{-2}$ , corresponding to 34% and 86% of the end of life fluence respectively, is shown in Figure 6.15. The decrease in energy resolution as a result of radiation damage is clear, where after  $\sim 7$  months the 250 eV resolution requirement will no longer be met within the operational temperature range. It should be re-iterated that the fluence values provided by SPENVIS are worse case. The proton fluence experienced during the transfer to the Moon will likely be lower than predicted here. It will be vital to ascertain the proton fluence experienced during the transfer, or a measure of the decrease in resolution, to adapt the prediction of performance while in orbit around the Moon. The Mn-K $\alpha$  energy resolution at -20.0 °C taken from Figure 6.15 was found to be 264 eV and 407 eV for the CCD54 irradiated to  $3.03 \times 10^8$  protons.cm $^{-2}$  and  $7.54 \times 10^8$  protons.cm $^{-2}$  respectively,  $\sim \times 2$  greater than predicted in Table 6.4, as a result of radiation induced CTI.

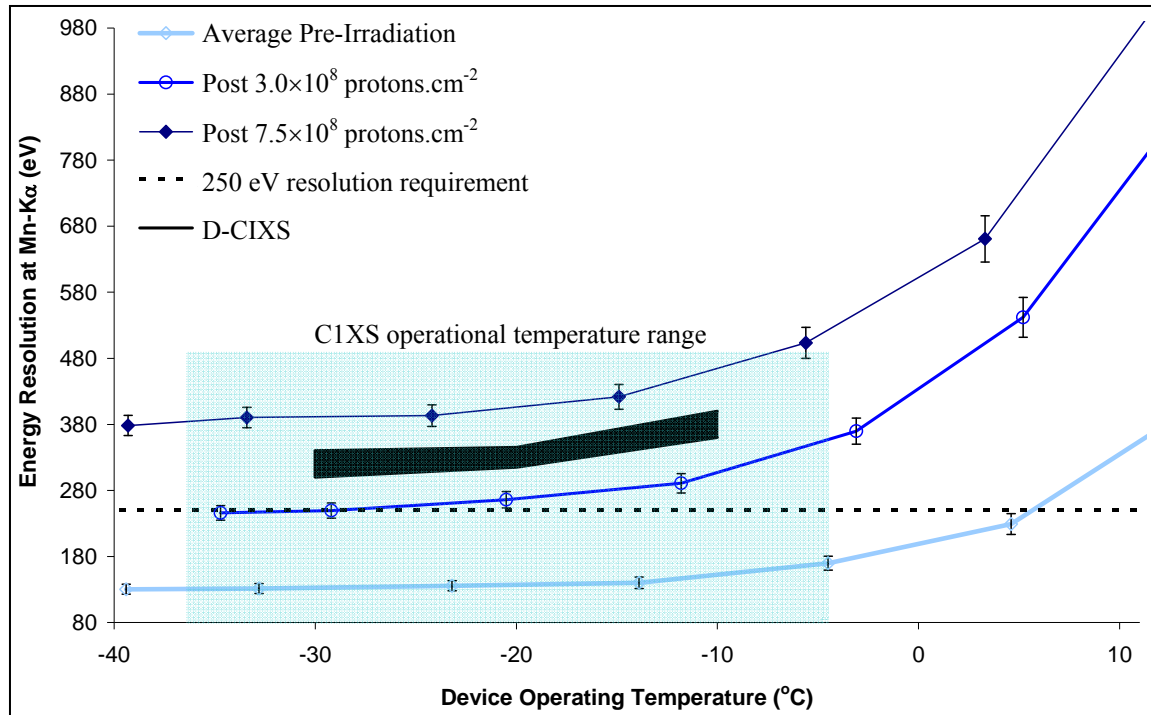


**Figure 6.15** Measured energy resolution of Mn-K $\alpha$  events as a function of temperature

### 6.6.1 The Dominant Source of Performance Loss

The initial proton irradiation study discussed in Chapter 5 demonstrated that increased CTI formed the main component of energy resolution loss. This section compares the measured energy resolution with the predicted energy resolution, described by Equation 2.44, at different X-ray energies to identify when CTI becomes the dominant source of performance loss. The measured and predicted energy resolution as a function of temperature of Al-K $\alpha$ , Ca-K $\alpha$ , and Cu-K $\alpha$  X-rays are given in Figures 6.16, 6.17 and 6.18 respectively.

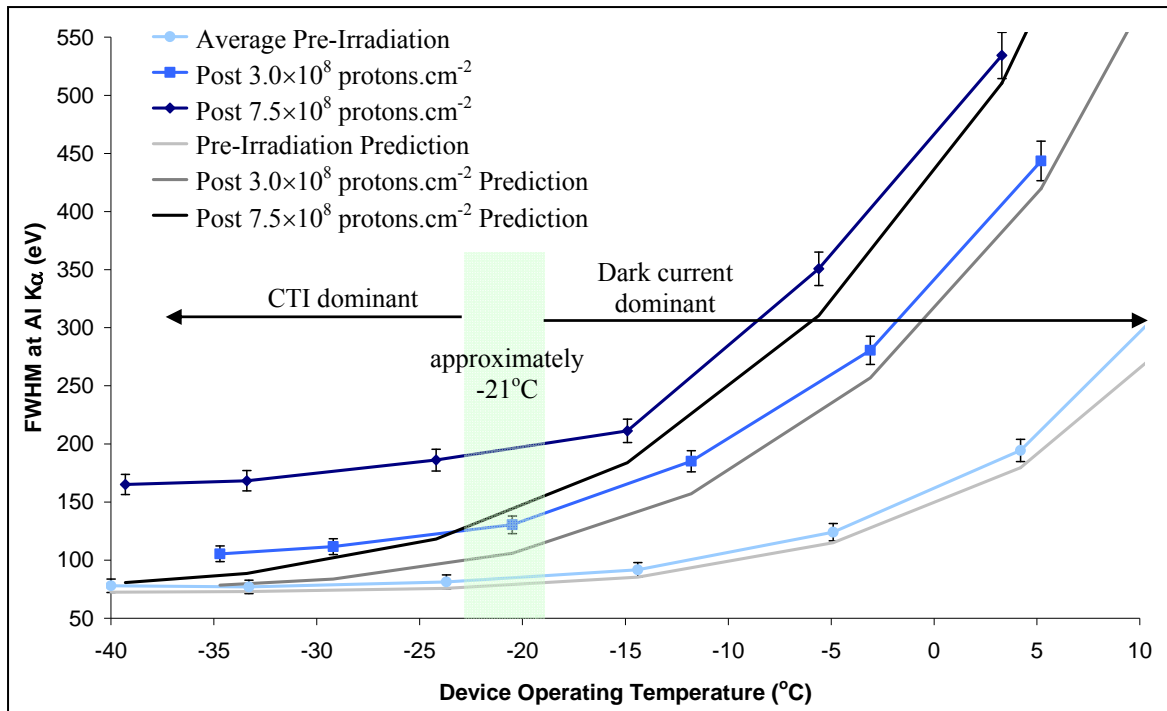


**Figure 6.16:** Measured energy resolution of Al-K $\alpha$  events pre- and post-irradiation as a function of temperature, and the predicted value based on Fano-limited statistics plus the measured read noise

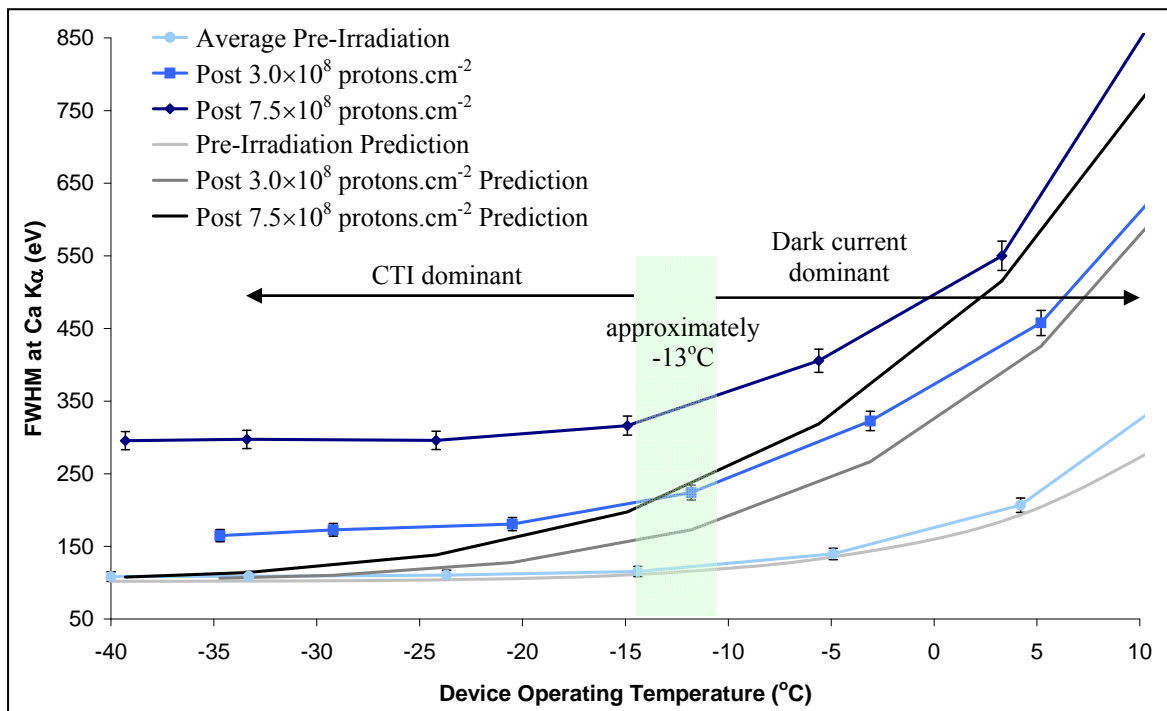


**Figure 6.17:** Measured energy resolution of Ca-K $\alpha$  events pre- and post-irradiation as a function of temperature, and the predicted value based on Fano-limited statistics plus the measured read noise

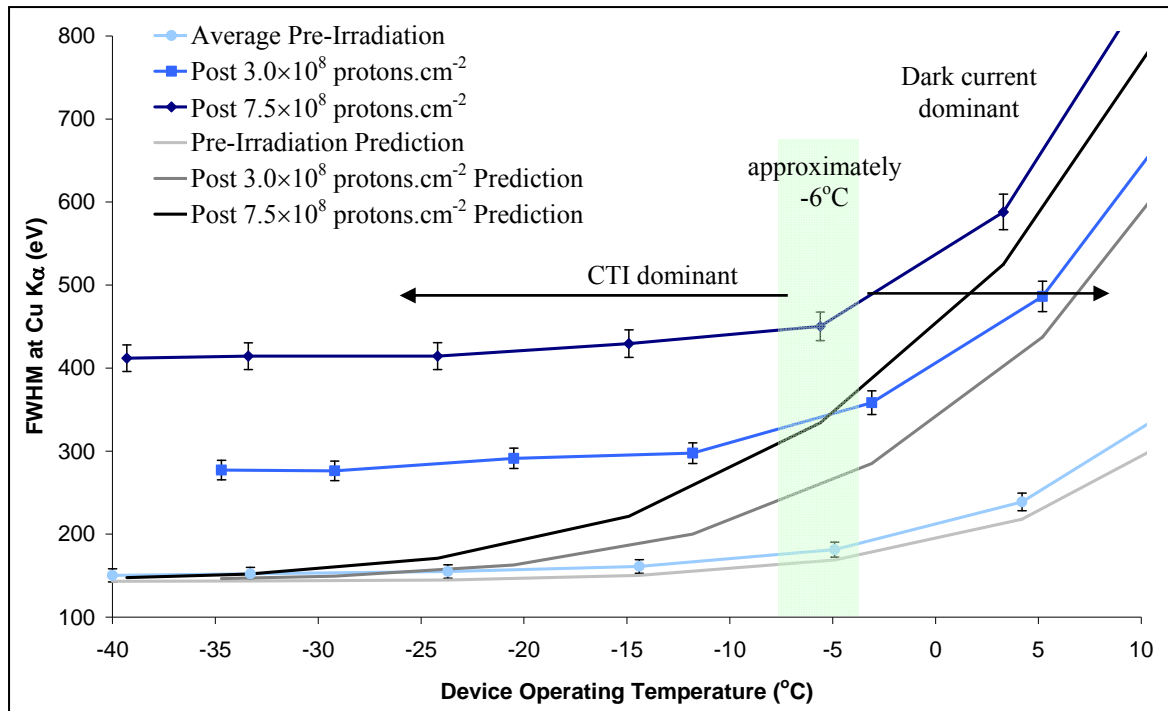


**Figure 6.19:** Measured energy resolution of Cu-K $\alpha$  events pre- and post-irradiation as a function of temperature, and the predicted value based on Fano-limited statistics plus the measured read noise

The increase in dark current forms the dominant source of decreased energy resolution at higher temperatures. The dark current decreases quickly as the operational temperature is reduced, becoming negligible at operating temperatures below -30 °C as shown in Figure 6.10. The point at which CTI becomes dominant is dependant on the incident X-ray energy. The approximate temperature was determined first visually and then comparing data fits to find -21 °C, -13 °C and -6 °C for 1,487 eV, 3,691 eV and 8,047 eV respectively. A line of best fit was applied to the data using MATLAB, the decrease in energy resolution as a function of increased dark current and increased CTI was found using the pre-irradiation values as a baseline. The point where the decrease in performance as a result of dark current and increased CTI is comparable was identified to provide the approximate temperature at which CTI becomes dominant. The fitted data and experimental data from the Al-K $\alpha$  and Ca-K $\alpha$  post  $7.5 \times 10^8$  protons.cm $^{-2}$  is illustrated in Figure 6.19. The point where CTI becomes dominant is highlighted. The mean temperature from the data taken at  $3.0 \times 10^8$  protons.cm $^{-2}$  and  $7.5 \times 10^8$  protons.cm $^{-2}$  was used to give the approximate temperature of CTI dominance.

The temperature dependence is as a result of the probability of encountering trap sites being proportional to the volume of the charge packet, and also that multi-pixel events are more degraded than single pixel events by increased CTI. Although only isolated events were used in the analysis due to the read-out mechanism of the SCD it is possible that an event detected as a multi-pixel

event is read-out as an isolated event, described in Section 2.6. This will only have a small effect on the device performance as the largest amount of resolution loss is as a result of CTI within the central transfer channel.

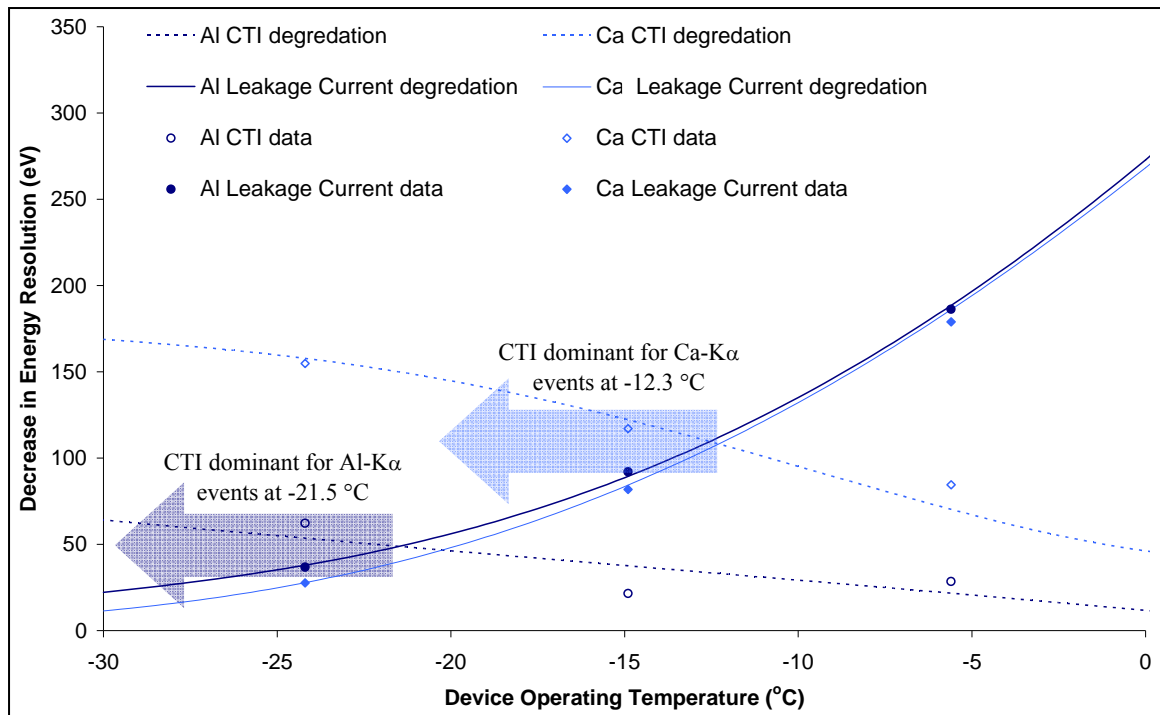


**Figure 6.19:** Decrease in energy resolution resulting from increased CTI and dark current as a function of temperature after  $7.5 \times 10^8$  protons.cm<sup>-2</sup> for Al-K $\alpha$  and Ca-K $\alpha$  X-ray events showing the point at which CTI becomes dominant

Over the C1XS operational temperature range the increase in CTI is the dominant source of performance loss. The measurement of low energy X-rays, Mg, Al, and Si will continue to benefit from further cooling, however as the energy increases the benefit of further cooling is reduced. The energy resolution of Ca-K $\alpha$  and Cu-K $\alpha$  becomes CTI limited at around -25 °C. Unlike a conventional CCD the location of the X-ray interaction is not defined, as a result an analysis technique similar to that described by Townsley *et al.* 2002 could not be used to perform CTI correction. To improve the radiation tolerance of a SCD the charge transfer should be improved, for example by increasing the element size, using a 2-phase clocking operation [Stevanov *et al.* 2000], and including a supplementary buried channel [Janesick 2001]. The clocking operation could be modified to increase the clock overlaps, or possibly have a larger area held under maximum potential during transfer. It was demonstrated that using a p-type buried channel, doped with boron, that the radiation tolerance to CTI is improved [Spratt *et al.* 1997]. Further testing has demonstrated an improvement of between  $\times 3$  and  $\times 10$  at various operating temperatures, for example Srouf 2000, Bebek *et al.* 2002, De Monte *et al.* 2008, and Gow *et al.* 2009.

### 6.6.2 Comparison with Previous Irradiation and Predictions

To allow a comparison with the model described in Section 5.10 the data were analysed using the XCAM Ltd. software, which uses a threshold multiplier of 5, i.e. isolated events are selected using a threshold of  $5\sigma_n$ , where  $\sigma_n$  is the standard deviation of the noise peak as described in Section 4.4. The measured values compare well to the predicted values, as shown in Figure 6.20. The simple model is capable of predicting the energy resolution as a function of energy, temperature and fluence, to within error below  $-10\text{ }^\circ\text{C}$  and within a few eV above, however, it does not account for a change in the threshold multiplier. The threshold multiplier of 2 produced similar results to those found using the C1XS drive electronics, another reason for its selection. The relationship between energy resolution and proton fluence is given in Figure 6.21, and shows the energy resolution of Mn-K $\alpha$  X-ray events at  $-20\text{ }^\circ\text{C}$  found using a threshold multiplier of 2, and a linear fit to highlight the trend. The energy resolution as a function of fluence is given by:

$$\text{Mn energy resolution} = 36.05\Phi + 144 \quad (6.5)$$

where at  $-20\text{ }^\circ\text{C}$  the 250 eV requirement will no longer be met after  $\sim 2.94 \times 10^8\text{ protons.cm}^{-2}$ .

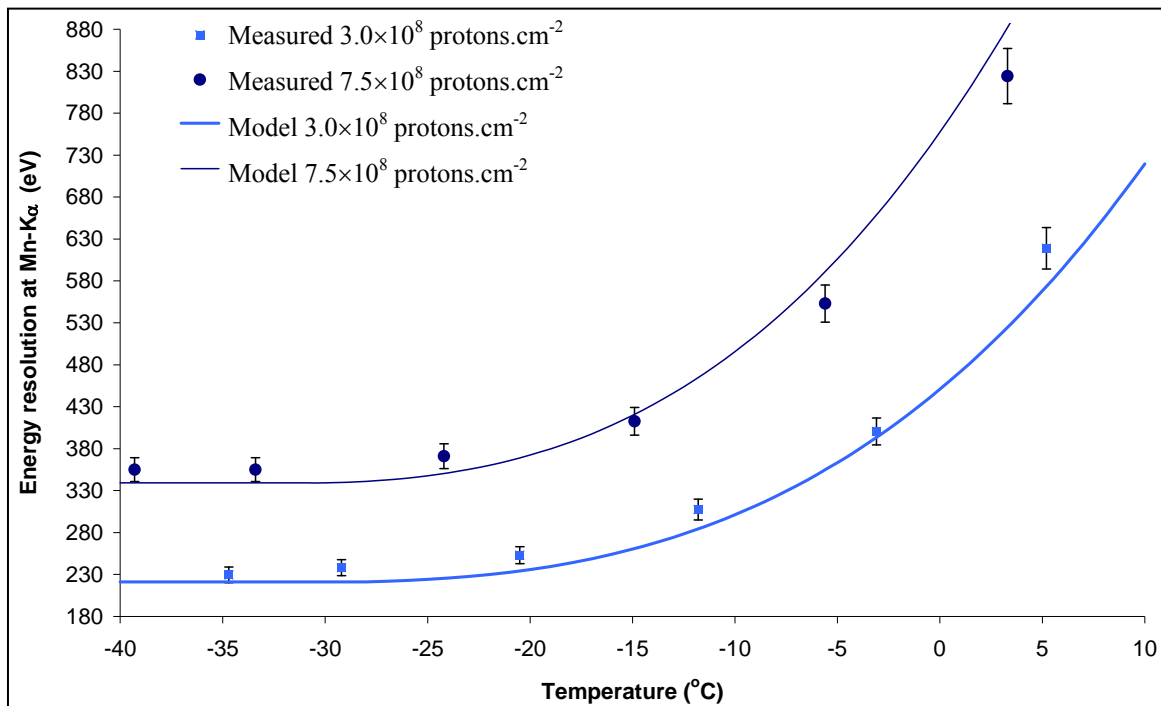


**Figure 6.20:** Comparison of the measured energy resolution found using the XCAM software and the initial model for 10 MeV equivalent proton fluences of  $3.0 \times 10^8$  and  $7.5 \times 10^8\text{ protons.cm}^{-2}$

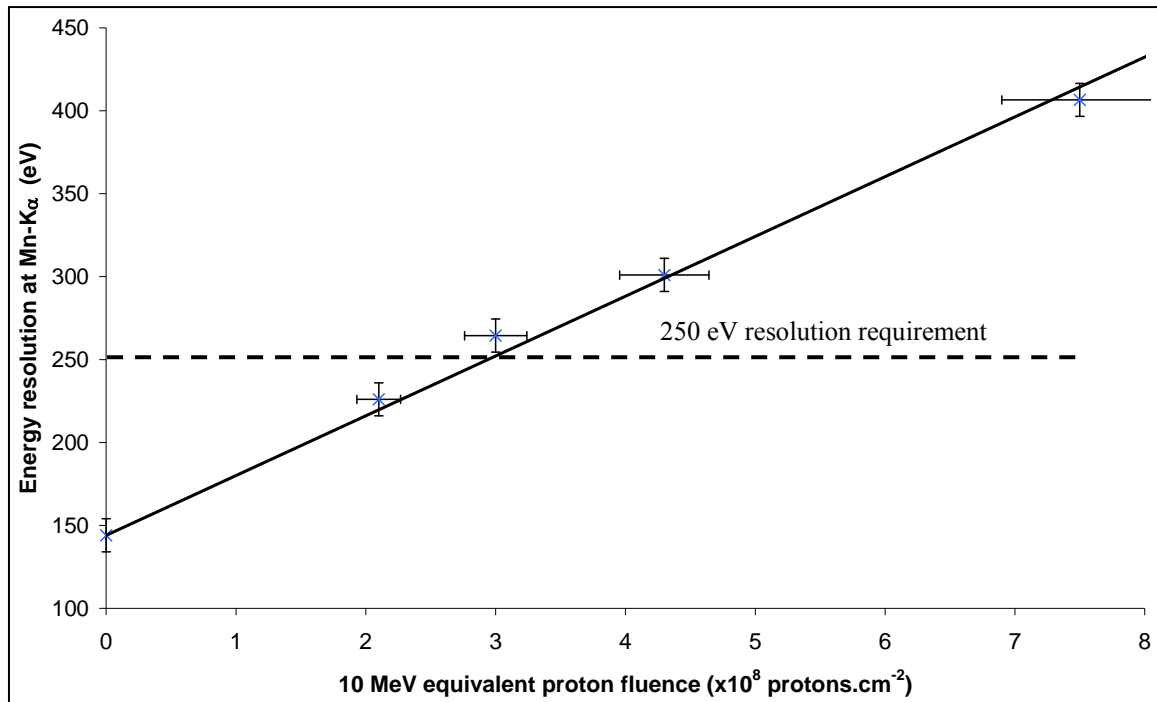


**Figure 6.21:** The measured Mn-K $\alpha$  event resolution at  $-20.0$  °C found using a multiplier of 2 as a function of the 10 MeV equivalent proton fluence delivered to the CCD54

### 6.6.3 Lunar Regolith Simulant and Mg, Al, Si Spectra

The lunar regolith simulant was fluoresced at each temperature pre- and post-irradiation. The spectra recorded at operating temperatures near  $-20$  °C are given in Figure 6.22. Pre-irradiation the X-ray peaks are clearly defined. The decreased energy resolution as a result of radiation damage is clear by the peak broadening and decrease in peak height in subsequent data sets. As a result, some peaks will become obscured, while low intensity peaks could be lost completely, as in the case of the K-K $\alpha$  peak. The decrease in Ca-K $\alpha$  resolution will obscure its K $\beta$  and the K-K $\alpha$  peak. After  $7.5 \times 10^8$  protons.cm $^{-2}$  the K-K $\alpha$  peak can no longer be identified. The tails to the left of the peaks are as a result of those charge packets that have undergone the most transfers. The most important peaks are still clearly identifiable after  $3.0 \times 10^8$  protons.cm $^{-2}$ , as highlighted in Figure 6.23, which shows spectra at around  $-20$  °C from the Mg, Al, Si target. At  $7.5 \times 10^8$  protons.cm $^{-2}$  the peaks can still be identified. However, the number of counts in the X-ray peak will also include counts from the neighbouring peaks. Elemental abundance information would no longer be attainable, without event processing. The contribution to the counts within the peak centroid will be negligible, therefore, based on a Gaussian fit to peak using the peak height and predicted energy resolution, based on the received proton fluence, it will be possible to use the counts under the fitted Gaussian to continue to provide elemental abundance information throughout the mission, with increased error.

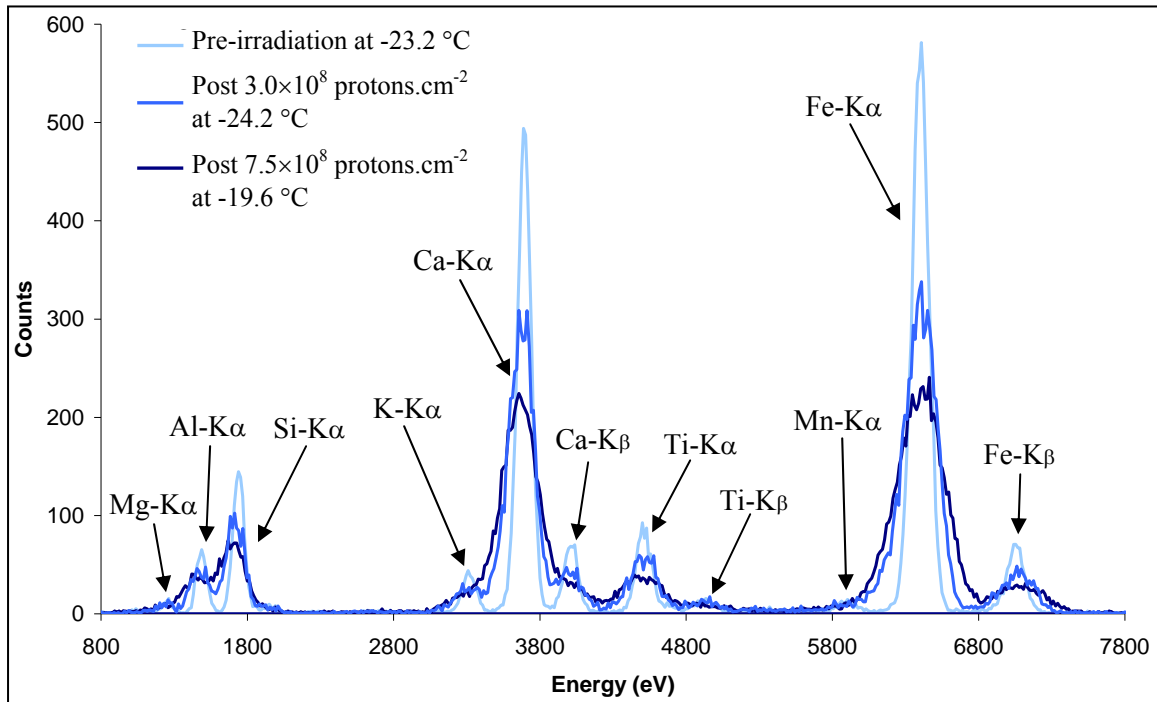


**Figure 6.22:** Lunar regolith simulant spectra at around -20 °C pre- and post-irradiation

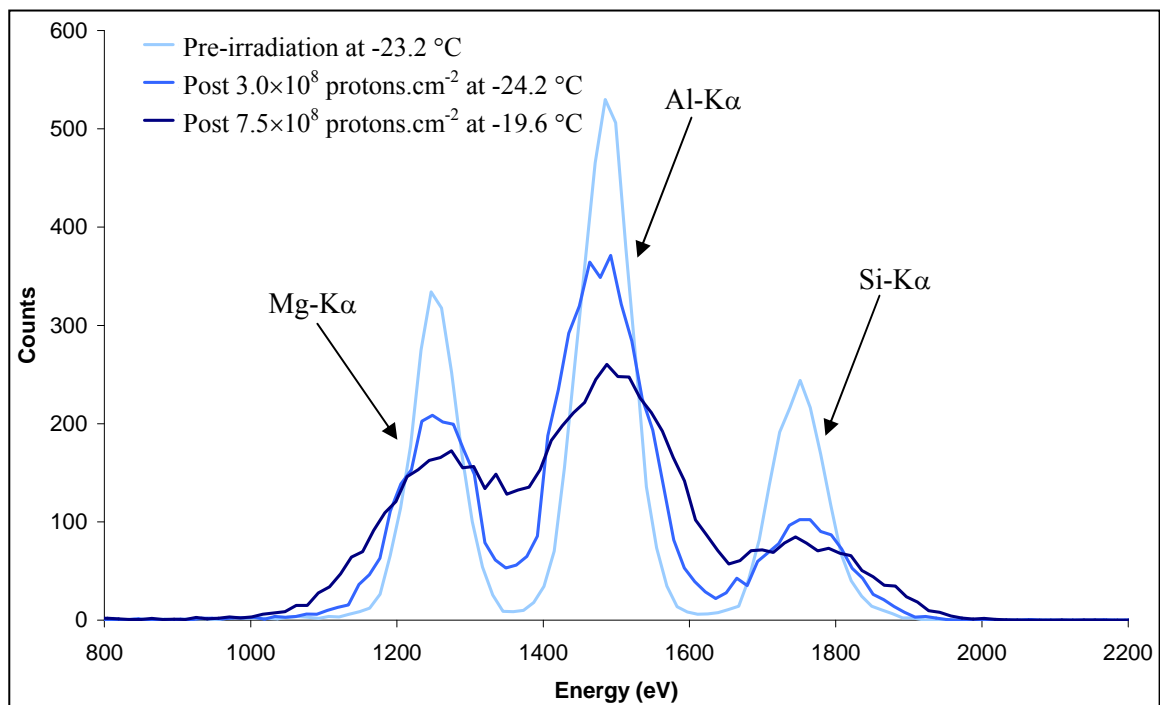


**Figure 6.23:** Mg, Al and Si target spectra at around -20 °C pre- and post-irradiation

## 6.7 Radiation Damage Model

The radiation model discussed in Chapter 5 was expanded to output an energy resolution and spectrum as a function of energy, temperature, proton fluence, and number of counts in the peak.

Although this models the energy resolution it was decided to model the CTI effects through the use of a CTI damage factor,  $CTI_{\phi}$ . The modelled energy resolution is given by:

$$Energy\ resolution = 2.35\omega\sqrt{n_T^2 + F_{Si}\frac{E_{\gamma}}{\omega} + CTI_{\phi}} \quad (6.6)$$

Standard CTI modelling techniques, measuring the charge lost by X-ray events across the CCD imaging area as a function of transfers, can not be employed as there is no positional information available, the read-out is in one dimension and the device is clocked continually.

$CTI_{\phi}$  is dependant on the energy, temperature, and the 10 MeV equivalent proton fluence. A weighted fitting routine was used to select a suitable value based on the experimental data. Temperatures within the C1XS operational range carried more weight. A piece of MATLAB code was written to provide a fit, based on Equation 6.6, allowing the energy resolution to be found as shown in Figure 6.24 which gives the modelled and experimental energy resolution after  $3.0 \times 10^8$  protons.cm<sup>-2</sup>. The values could then be used to create predicted spectra, as shown in Figure 6.25 which shows the modelled version of the Lunar Regolith simulant spectra shown in Figure 6.22. The model compares well with the experimental results. The CTI damage factor was removed from Equation 6.6 to highlight the importance of improved radiation tolerance to CTI, the Lunar Regolith simulant spectra shown in Figure 6.26 has suffered no radiation induced increase in CTI.

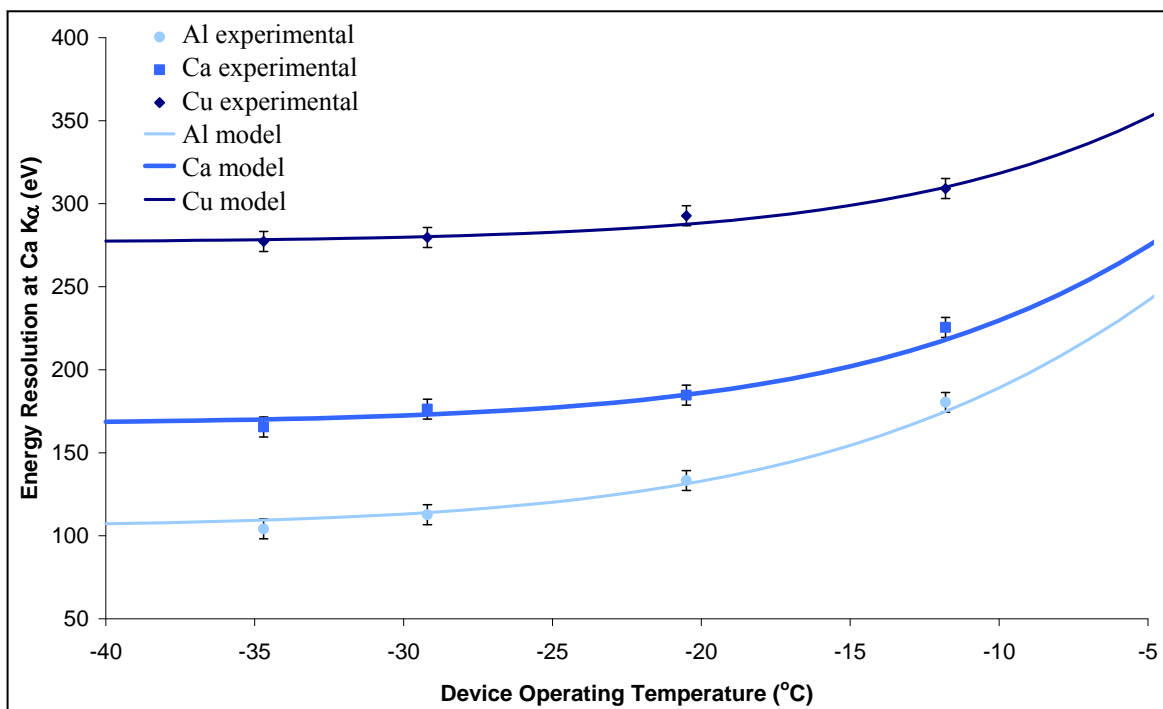


**Figure 6.24:** Comparison of experimental data with a model based on the quadrature summation of the X-ray Fano-limited statistics the measured read noise and CTI damage factor

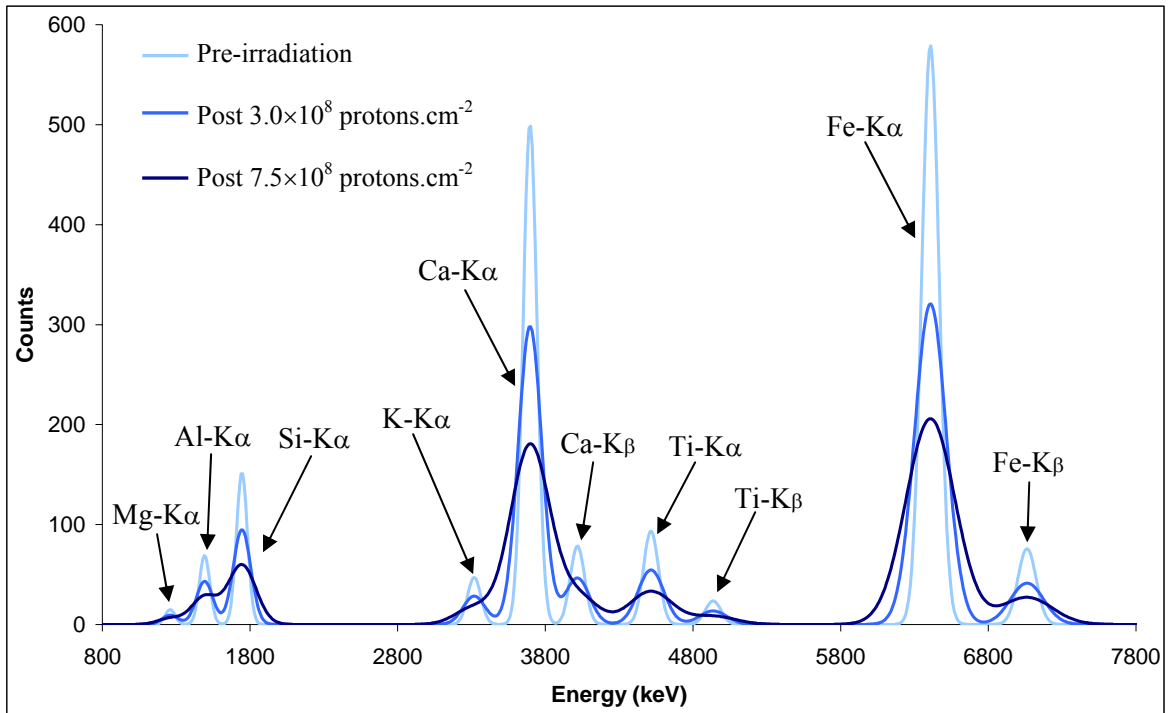


**Figure 6.25:** Model of Lunar Regolith Simulant spectra at  $-20^{\circ}\text{C}$  pre- and post-irradiation

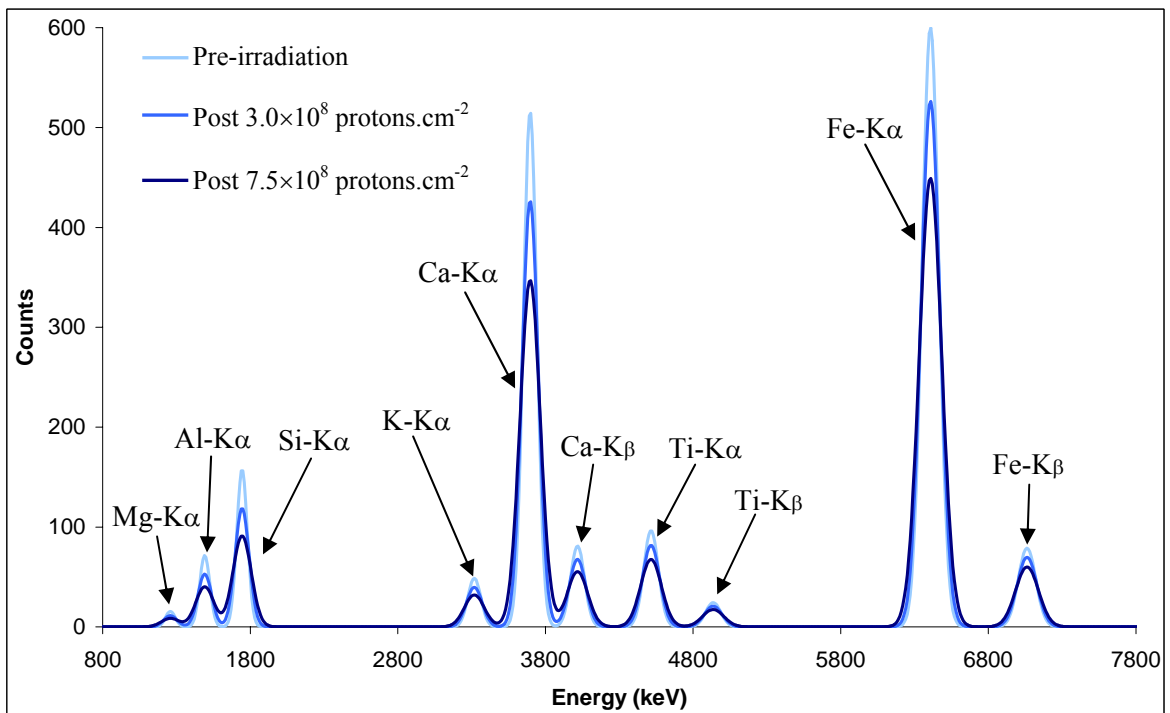


**Figure 6.26:** Model of Lunar Regolith Simulant spectra at  $-20^{\circ}\text{C}$  pre- and post-irradiation, not including the CTI damage factor

## 6.8 Chapter Summary

This chapter has presented work carried out to assess the impact of a delayed Chandrayaan-1 launch date, looking at the noise, dark current, X-ray detection, spectroscopic degradation, and a model of the radiation induced CTI effects. The delay to the launch date results in an increased proton flux as a result of launching further into cycle 24. The frequency and flux of solar flares will also increase and will improve data collection; therefore the delay will have no net negative impact on the performance of C1XS. As shown in Figure 6.1 the sunspot activity during launch is far lower than that predicted using SPENVIS reducing the damage caused to the SCDs on transfer to the Moon. The total proton fluence received will more likely be  $0.56 \times 10^8$  protons.cm<sup>-2</sup>, found using solar minimum tables, compared to  $1.46 \times 10^8$  protons.cm<sup>-2</sup> found using solar maximum tables in SPENVIS. The worse case end of life proton fluence was calculated to be  $8.8 \times 10^8$  protons.cm<sup>-2</sup>, however the actual proton fluence should be lower. If the SPENVIS predictions were to become fact the instrument would no longer be able to meet its 250 eV resolution requirement at 5,898 eV, at -20 °C, around seven months into the two year mission timeline.

## Chapter 7: XRF Modelling, C1XS Initial Results, and a XRF Detector Comparison

### 7.1 Introduction

This chapter discusses the work carried out to assist the C1XS science team in the development of the Swinyard XRF modelling code, presents the initial C1XS data provided by the C1XS science teams, and reports on a brief comparison of SCD performance compared with other XRF detectors demonstrating the excellent performance of the SCD CCD54.

The XRF modelling code is required to analyse the C1XS flight data in conjunction with the XSM data to provide elemental abundance information. The aim was to provide the code with incident and fluoresced X-ray spectra, using targets with different surface properties, to be used in the codes development and validation. The initial stage was to characterise the input X-ray spectrum from the X-ray tube using the Si(Li) detector discussed in Chapter 4, then to use target materials with different surface properties to generate a large set of data obtained using different integration times. The results of this work will be analysed as part of Shoshanna Wielder's PhD thesis and will not be discussed in detail in this chapter. The effects of changing the tube voltage and tube current were investigated as part of the pre- and post-irradiation testing and forms a brief investigation into the problems faced in planetary XRF. The initial results from the modelling code are presented.

The successful launch of Chandrayaan-1 and the first results from C1XS are also included, demonstrating the excellent performance of the instrument.

#### 7.1.1 Rocks, the History Books of the Universe

The analysis of chondrites, meteorites formed from the building blocks of the solar system, provide an insight into solar system creation and the history of our own planet as discussed in Chapter 1. One possible answer to the question of what killed the dinosaurs was provided through the study of rocks. In 1980 a layer of the rare metal iridium and other elements not often found within the Earth's crust was identified all over the world at the Cretaceous-Tertiary (K-T) boundary, a point dated at  $65.5 \pm 0.3$  million years ago. It was theorised that the layer was the remnants of a dust cloud resulting from the impact of a 10 km diameter meteorite [Alvarez 1980]. The isotropic abundance of iridium at the K-T boundary is similar to that found in chondrites. The crater, named Chicxulub, was not located until 1990 by Glen Penfield in the Yucatán region of Mexico.

An interesting example of the use of XRF is in the analysis of the stones used in construction of Stonehenge, identifying where the stones originated from their elemental composition. The study of rocks through the Earth's distant past can become very complicated, due to the rock cycle where rocks are weathered, eroded, transported, deposited in sedimentary layers, compressed and heated, melted, and then rise back to the surface. To study the history of the Earth and the formation of the solar system some 4000 to 5000 million years ago it is essential to study rocks which have changed little since their creation, i.e. those not affected by a rock cycle [Kuiper 1956]. The study of meteorites provides some insights, however, these can often be contaminated, making the study of comets and extraterrestrial planetary crusts essential to further our understanding of the solar system.

### 7.1.2 Extra Terrestrial X-ray Fluorescence

Extra terrestrial XRF requires two things: a thin atmosphere to allow low energy fluorescence X-rays to reach an orbiting detector and sufficient solar X-ray flux. Therefore detector response is linked to the mass of the body and proximity to the Sun of the target. Asteroids, Mercury and the Moon make excellent targets for extra terrestrial XRF, targeted by the Hayabusa [Okada 2007], MErcury Surface, Space ENvironment, GEOchemistry and Ranging mission (MESSENGER) and Chandrayaan-1 missions respectively. The main limitation in each case is that solar X-rays will only penetrate into the upper few micrometers of the target surface [Adler *et al.* 1972]. X-rays generated within the target layer may never escape, only allowing the surface properties to be identified, with impact sites providing an insight into what is below. This limitation requires the use of manned and robotic missions using drilling equipment, sample collection and return, and impacters to smash through the surface to material below. XRF can only provide elemental abundance and no information on the actual mineral species present which requires the use of X-ray diffraction.

A generalised expression for the number of characteristic photons  $N$  entering the detector as a result of XRF is given by [Adler 1966]:

$$N = \frac{\tau \Omega}{4\pi} \int_{E_o}^{E_m} c(E_i, E_s) J(E_i) dE_i \quad (7.1)$$

where  $\tau$  is the solid angle between the target and the X-ray source,  $\Omega$  is the solid angle subtended by the X-ray optics at the target,  $E_i$  is the energy of the incident X-ray beam,  $E_s$  is the energy of the secondary fluoresced X-rays,  $E_o$  and  $E_m$  are respectively the lowest and highest energies in the incident X-ray beam,  $J(E_i)$  is the number of photons. $\text{keV}^{-1}.\text{cm}^{-2}.\text{s}^{-1}$ , and  $c(E_i, E_s)$  is the conversion efficiency, i.e. the efficiency of  $E_i$  in producing secondary X-rays. To allow elemental abundances

to be identified, the geometry, the incident X-ray beam, and conversion efficiency must be understood, hence the requirement for the Swinyard code. The conversion efficiency,  $c(E_p, E_s)$ , is given by [Von Hamos 1945]:

$$c(E_p, E_s) = \frac{g X_Y \eta}{\mu_i} \times \left[ 1 + \left( \frac{\mu_s}{\mu_i} \right) \frac{\sin \Phi}{\sin \psi} \right]^{-1} \quad (7.2)$$

where  $\mu_s$  and  $\mu_i$  are the linear absorption coefficients of the specimen for the secondary X-rays and the incident X-rays respectively,  $\eta$  is the absorption coefficient of the spectra line  $E_s$ ,  $g$  is the relative weight (portion of emitted energy which goes into a particular series e.g. K and L),  $X_Y$  is the fluorescent yield,  $\Phi$  is the angle of incidence of the incident X-ray beam, and  $\psi$  is the emergence angle of the secondary X-rays, as shown in Figure 7.1 which compares the experimental setup with a simplified version of C1XS in orbit around the Moon. The transmission of the X-rays through the C1XS optical shielding and the surface properties of the Moon also have to be understood.

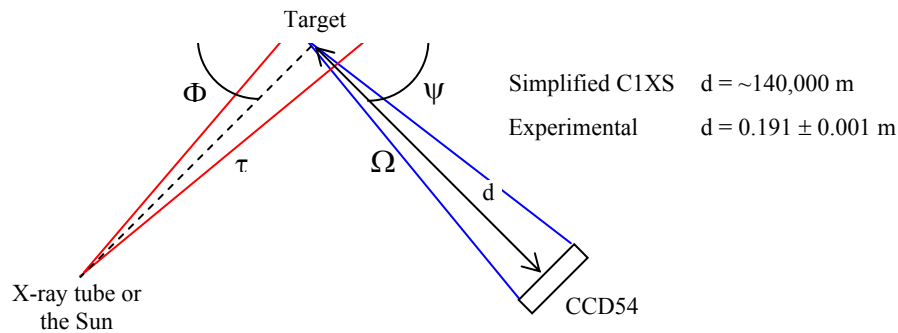


**Figure 7.1:** Geometry of the laboratory experiment with the angle of incidence and angle of emergence at  $45^\circ$

A polished smooth surface is understood to provide the best XRF response [Adler 1966], and similar work has demonstrated increased X-ray peak intensities with smaller grain size [Claisse 1956]. An uneven surface will result in more secondary X-rays stopped within the target and X-rays fluoresced and scattered along trajectories not incident on the detector. The surface of the Moon is far from a polished surface, as shown in Figure 7.2 [NASA image ID: 138623] with astronaut Harrison Schmitt standing next to a large boulder during Apollo 17 in 1972. The imperfections on the lunar surface will have some effect on the resulting secondary X-rays. Boulders like the one shown in Figure 7.2 will be negligible due to the wide field of view,  $25 \text{ km}^2$ , of the instrument. The mountains could be accounted for using radar mapping. It is more important to understand the response due to the surface material, which on the Moon is predominantly regolith, described in Chapter 1. Therefore the effect of grain size as briefly described in Section 7.3, angle of incidence and emergence, and incident X-ray spectra have to be understood.



**Figure 7.2:** Harrison Schmitt next to a large boulder on the lunar surface, Apollo 17 in 1972

[NASA]

The solar spectrum is dependant on solar activity as described in Section 3.2 and will have a large affect on the resulting X-ray spectrum detected by C1XS, as discussed in Section 7.4. The solar spectrum from the X-ray solar monitor onboard MESSENGER is shown in Figure 7.3, with the continuum spectrum and the total spectrum which consists of characteristic X-rays generated within the Sun. The pre-flare background spectrum can be compared with the solar spectrum illustrated in Figure 7.4 produced by the X-ray solar monitor mounted onboard Chandrayaan-1 on the 10<sup>th</sup> of January 2009, the intensity difference is due to the proximity to the Sun as the flux levels, measured by GOES, were comparable.

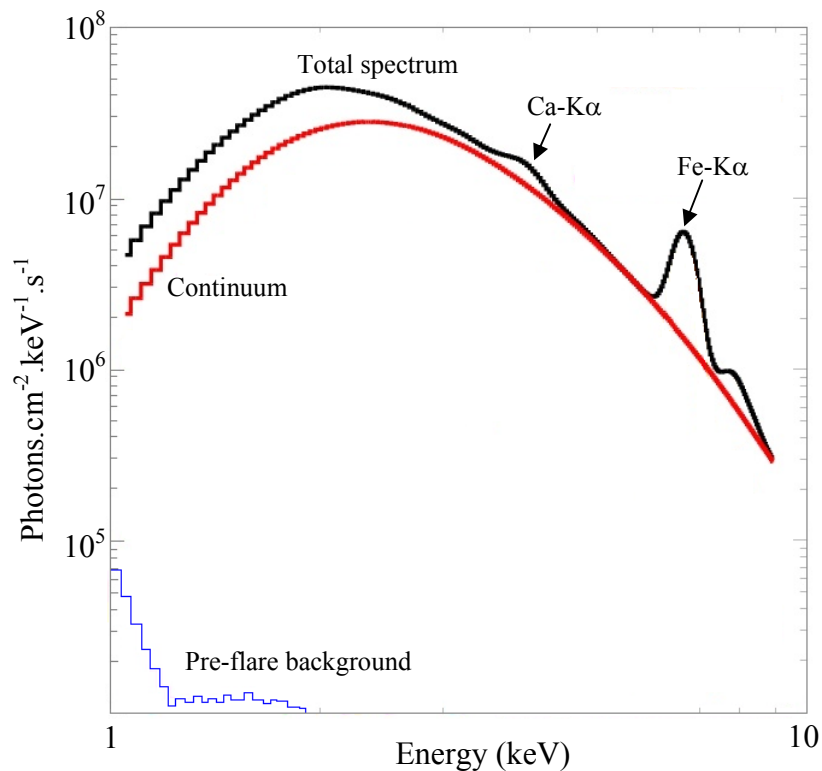


**Figure 7.3:** Solar spectrum from the Si PIN detector onboard MESSENGER, showing the pre-flare background and a solar flare which occurred on the 1<sup>st</sup> of June 2007 [adapted from Dennis 2008]

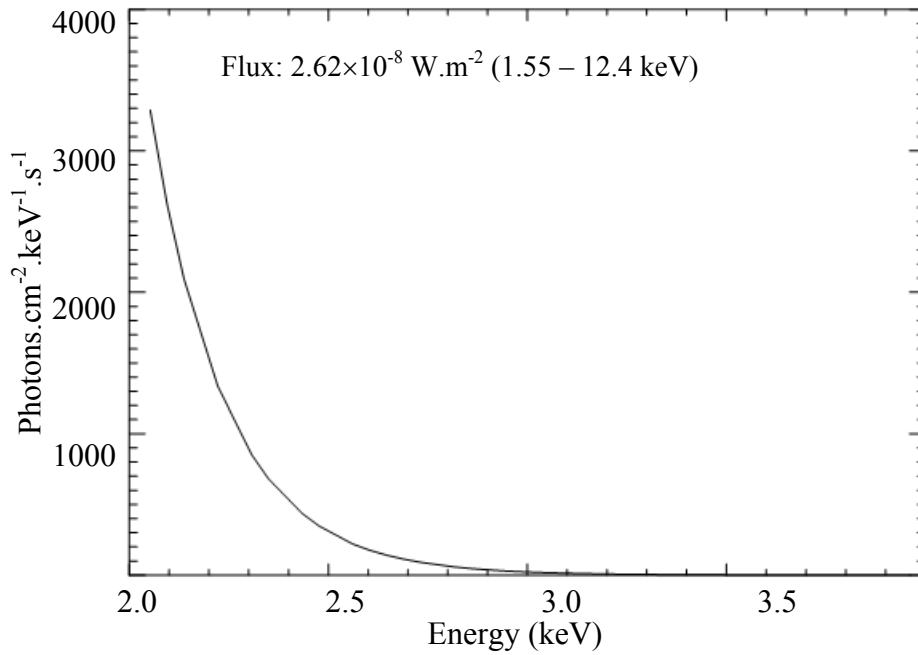


**Figure 7.4:** Solar spectrum recorded over 240 s using the XSM mounted onboard Chandrayaan-1 on the 10<sup>th</sup> of January 2009 [Alha 2009]

## 7.2 Experimental Arrangement and Procedure

This section describes the work to assist the C1XS science team, including the experimental arrangement and test procedure used to measure the X-ray tube beam profile, XRF response from different grain sizes and as a function of incident X-ray profile.

### 7.2.1 X-ray Beam Profile

The beam profile was recorded using an e2v scientific instruments Si(Li) detector, the same detector discussed in Chapter 4 for SCD QE measurements. The experimental arrangement used is shown in Figure 7.5. The setup was designed to hold the detector surface at the same distance from the X-ray source as that of the target surface shown in Figure 6.2, to within an accuracy of  $\pm 1$  mm. The X-ray spectrum was measured using tube voltages between 4 and 15 kV with a tube current of 0.002 mA. The tube current was also varied between 0.002 and 0.030 mA with the tube voltage held at 10 kV. An integration time of 30 minutes was for each test. After each change to the X-ray tube power supply, a settling time of 30 minutes was applied to ensure the beam was stable prior to data collection.

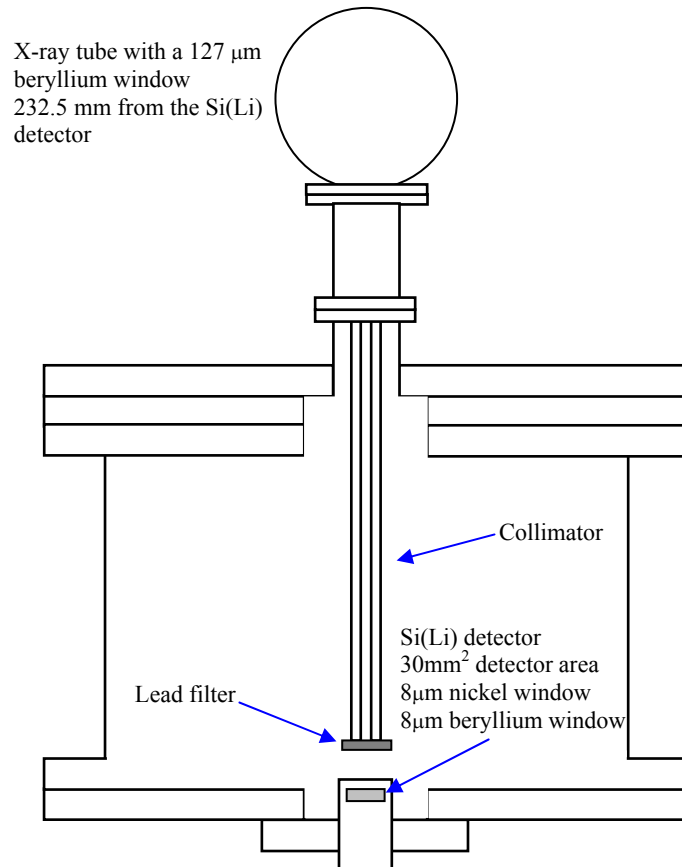


**Figure 7.5:** Schematic of the setup used to profile the X-ray beam using the Si(Li) detector

Initially, to ensure the detector was not saturated, varying thicknesses of aluminium foil were placed at the end of the collimator, removing the low end of the energy spectrum. Other filter materials were investigated based on their X-ray transmission values. All proved unsuitable as the X-ray spectrum would become too distorted. A lead shield with a small hole to further collimate the beam was selected, with the requirement that the detector not saturate. The size of hole required was determined experimentally, by starting at 1.00 mm and reducing the hole size, selecting a 0.25 mm diameter hole. To ensure the detector was not saturating the intensity as a function of current and voltage was recorded over the required test range. The results of the intensity as a function of current are shown in Figure 7.6, where above 0.008 mA the detector begins to saturate. The effect on the integrated intensity,  $I_{\text{int}}$ , is linear as given by the following equation [Adler 1966]:

$$I_{\text{int}} = 1.4 \times 10^{-9} i Z V^2 \quad (7.3)$$

where  $i$  is the electron current in amps,  $Z$  is the atomic number of the anode (Tungsten) and  $V$  is the potential difference on the tube in volts. Therefore, the actual number of X-ray photons incident onto the target using the setup in Figure 6.2 can be found by using a scaling factor based on the tube current, voltage, beam size, and QE of the Si(Li) detector.

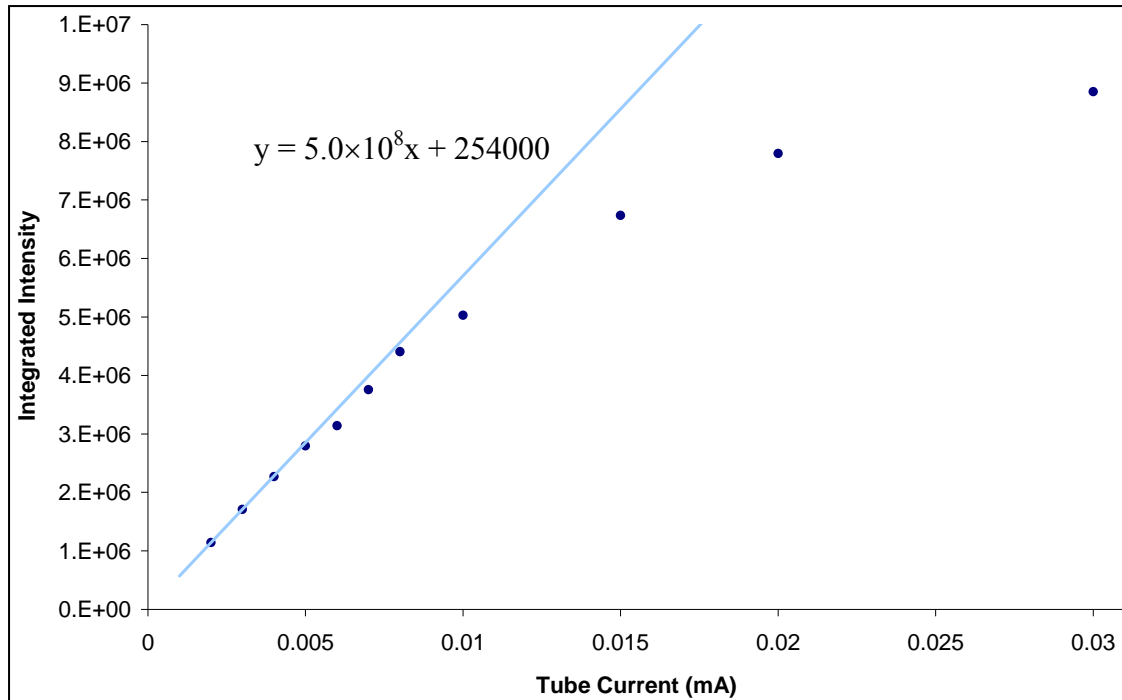


**Figure 7.6:** Integrated intensity as a function of X-ray tube current showing the initially linear increase of integrated intensity with increasing tube current and the onset of detector saturation

Three lead collimators, numbered 1 to 3 with 0.25 mm diameter holes, were produced to ensure repeatability. Shields 2 and 3 compared well, the results from shield 1 had a higher intensity. On inspection under a microscope it became apparent that the hole in shield 1 had been damaged during manufacture, most likely during the removal of the drill bit. The plot shown in Figure 7.7, which shows the number of counts as a function of tube power, is the result of the average spectra taken with shield 2 and 3. The characteristic X-ray peaks from the W target are clear, as are the Pb-M $\alpha$  line from the shield, and the Ni-K $\alpha$  and Ni-K $\beta$  lines from the window on the Si(Li) detector. The X-rays will also generate a number of Si-K $\alpha$  X-rays within the detector, un-resolvable from the W-M $\alpha$  line. The P-K $\alpha$  line is due to phosphorous present within the detector, used as a dopant in the manufacture of the detector. The main difference between the spectra in Figure 7.7 and the solar spectra in Figures 7.3 and 7.4 is due to the characteristic X-ray peaks, the continuum is similar. A copper anode would be more suitable to simulate solar flares. The Cu-L lines are below the energy required to fluoresce the elements of interest to C1XS and the Cu-K $\alpha$  line will have a negligible effect when producing spectra comparable to those in Figure 7.3. All incident and secondary X-ray spectra, including the un-modified incident spectra, were provided to RAL for the codes development. The data was held within Excel spreadsheets, with the raw data available upon request.

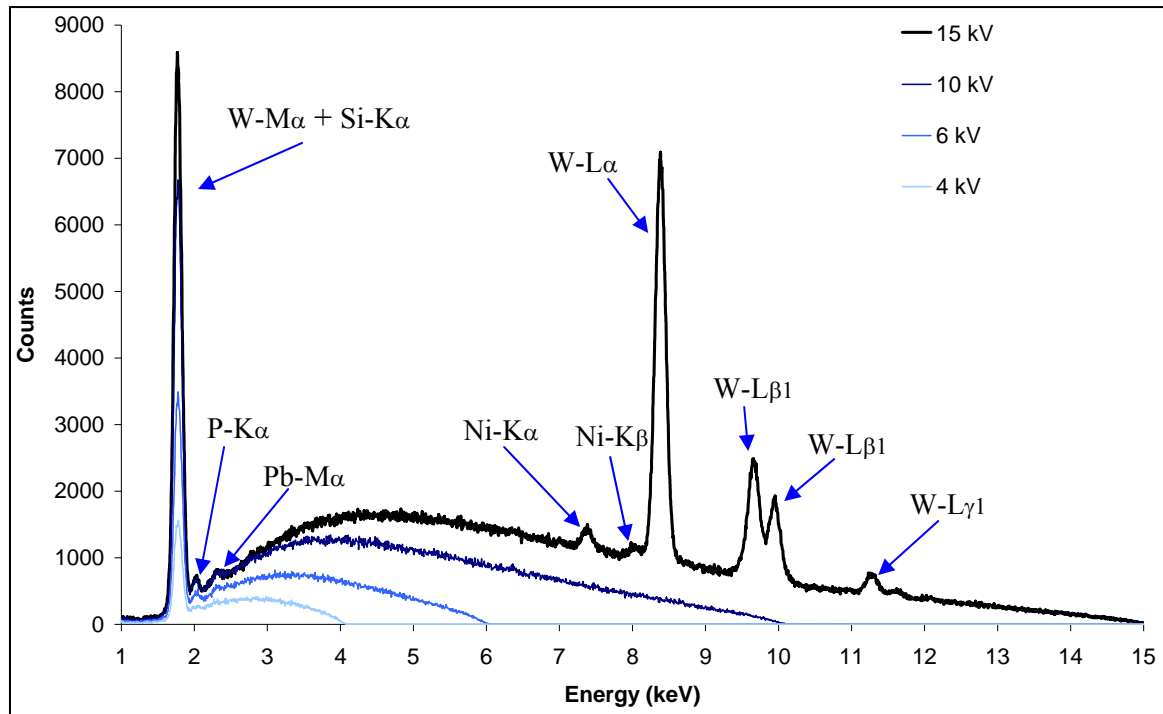


**Figure 7.7:** Incident X-ray spectra with varying tube potential

## 7.2.2 Geological Samples and Surface Type and Particle Size Comparison

During these tests a number of different target materials were used. Examples of three are given in Table 7.1. The elemental abundances were recorded by K. Joy for the samples provided by Birkbeck College UCL, sorted into grain size and mounted for testing by S. Weider, other samples were collected by the author from various locations. The Etna Basalt, Icelandite and Peridotite samples were prepared to produce five target types with grain sizes of:

- 250  $\mu\text{m}$  to 500  $\mu\text{m}$
- 125  $\mu\text{m}$  to 250  $\mu\text{m}$
- 75  $\mu\text{m}$  to 125  $\mu\text{m}$
- <75  $\mu\text{m}$  (comparable to lunar regolith)
- Polished solid sample

A layer of grain,  $\sim 2$  mm thick, was affixed to a glass slide with Gafchromic film used to ensure the incident X-ray beam was focussed solely on the target material. A sample of lunar regolith simulant (JSC-1) was donated by NASA/Orbitec, to provide data on the scattering effects of lunar regolith. JSC-1 was developed by NASA to simulate lunar regolith and is in the form of a powder [Carpenter 2006]. The elemental abundance of the regolith simulant is given in Table 7.1. The powder was formed into a pellet by mixing it with a binder and then moulding it at high pressure into a small disc, a process described in detail by Adler 1966. Although the most abundant element

within the lunar regolith simulant is oxygen due to the low fluorescent yield and the optical filters over the CCD54s mounted in the C1XS instrument, it will be unlikely that oxygen is detected.

<i>Element</i>	<i>K<math>\alpha</math> Energy</i>	<i>Fluorescent Yield</i>	<i>Regolith Simulant</i>	<i>Etna Basalt</i>	<i>Icelandite</i>	<i>Peridotite</i>
	(keV)	(%)	(%)	(%)	(%)	(%)
O	523.00	0.4%	44.71	43.99	43.45	45.02
Si	1740.00	3.7%	21.52	22.60	23.36	20.74
Al	1487.00	2.8%	8.63	9.21	7.27	0.55
Fe	6403.00	31.4%	8.53	7.46	11.30	5.69
Ca	3691.00	13.8%	6.91	7.35	6.90	0.45
Mg	1254.00	2.0%	5.10	3.19	3.09	26.97
Na	1041.00	1.4%	2.40	3.02	2.09	0.07
Ti	4510.00	19.0%	1.05	1.01	1.67	0.01
K	3313.00	11.5%	0.67	1.71	0.50	0.02
P	2015.00	4.8%	0.32	0.30	0.16	0.01
Mn	5898.00	28.1%	0.14	0.14	0.20	0.09
Cr	5414.00	24.9%	0.01	trace	trace	0.37

**Table 7.1:** Elemental abundance within the lunar regolith simulant JSC-1, Etna basalt, Icelandite, and Peridotite samples used during the particle size comparison

Data was acquired using a tube potential of 10 kV and a tube current of 0.20 mA, with integration times of 50 s, 300 s, and 600 s for each target type, with the CCD54 held at -30 °C and -50 °C. Targets were held in positions 1, 3, 5, and 7 as shown in Figure 6.2. The work involved a number of changes to the software used, including the inclusion of a spectrum integration feature to produce spectra over longer durations than the limit set by the XCAM software. The software has a maximum limit of 20 million pixels per readout, limiting the integration time to ~400 s. The software was also modified to include a variable time-out, after problems were experienced where a new set of read-outs were requested before the previous set was completed. The time-out was originally included to stop recording data if the readout process took over 30 s. The readout of a standard CCD can take ~10s, whereas the time the SCD is reading out is the integration time.

### 7.2.3 Varying the Incident X-ray Beam Intensity

The incident X-ray beam intensity was varied, by changing the tube potential and current, to demonstrate the importance of understanding the input X-ray spectrum. The targets used were the Al, Ca, and Cu combination target with a 60 s integration time. The tube potential was varied from 4 to 15 kV with the current held at 0.100 mA, shown in Figure 7.7. The tube current was varied from 0.002 mA to 0.150 mA with the potential held at 10.0 kV, shown in Figure 7.8. After each

change to the X-ray tube power supply, a settling time of 30 minutes was applied to ensure the beam was stable.

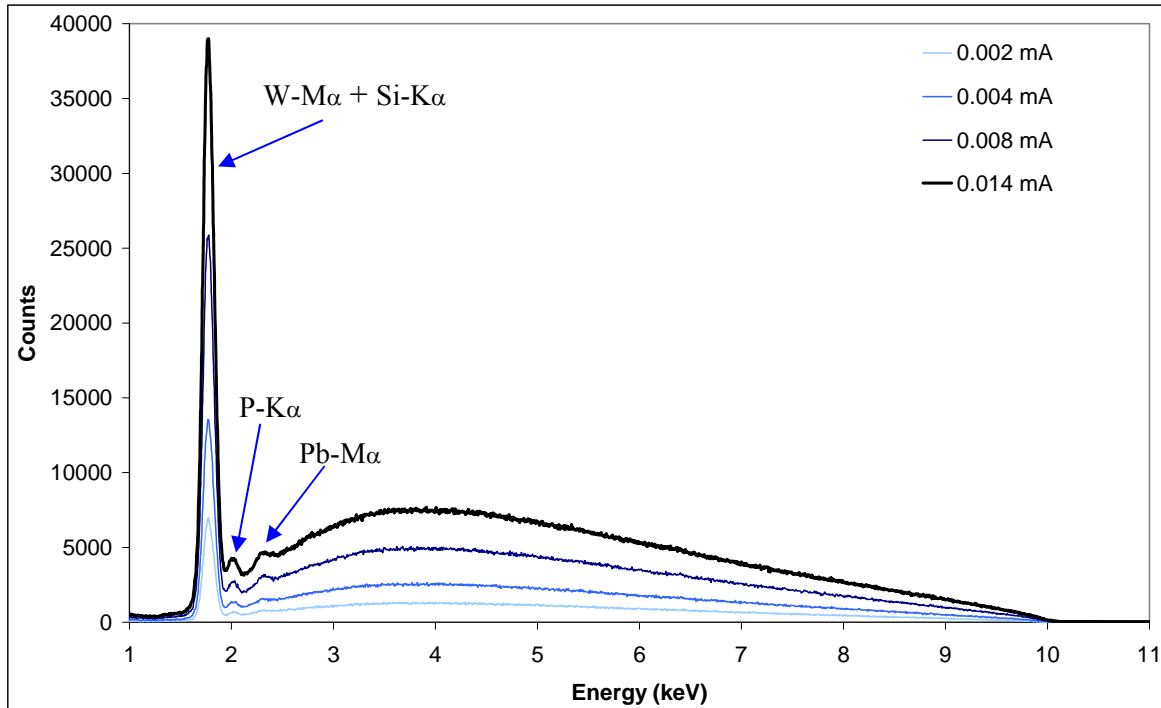


**Figure 7.8:** Incident X-ray spectra with varying tube current

### 7.3 XRF Modelling Code Development

This section describes the results from the work to assist the C1XS science team, including the effect of different grain size and incident X-rays profile, and presents the initial results from the XRF modelling code.

#### 7.3.1 Spectrum as a Function of Surface and Particle Size

The X-ray spectrum from the Etna basalt sample, collected using a 15 minute integration time, is shown in Figure 7.9. As expected the intensity of the X-ray peaks increased as the grain size was reduced with the highest intensity produced using the polished sample. The Cl line is as a result of weathering contamination. The weathering affects only the outer layers of rock, therefore the Cl peak has the lowest intensity after polishing where the outer layers have been removed, and the highest intensity for the large grain sizes which have undergone less grinding.

To compare the efficiency in which the different energy X-rays are generated, the peak intensity was normalised to that detected using the target with a grain size of 250 to 500  $\mu\text{m}$ , then normalised to 100, resulting in Figure 7.10 for the Etna basalt and Figure 7.11 for the Icelandite. A line has been added to show the trend. There is a clear increase in the response from lower energy X-rays.

This is as a result of fewer fluoresced X-rays stopping within the target, due to the reduced absorption depth of the incident X-rays within the sample. The results are comparable to those found by Maruyama *et al.* 2007. All data were provided to RAL in spectral form, in Excel spreadsheets.

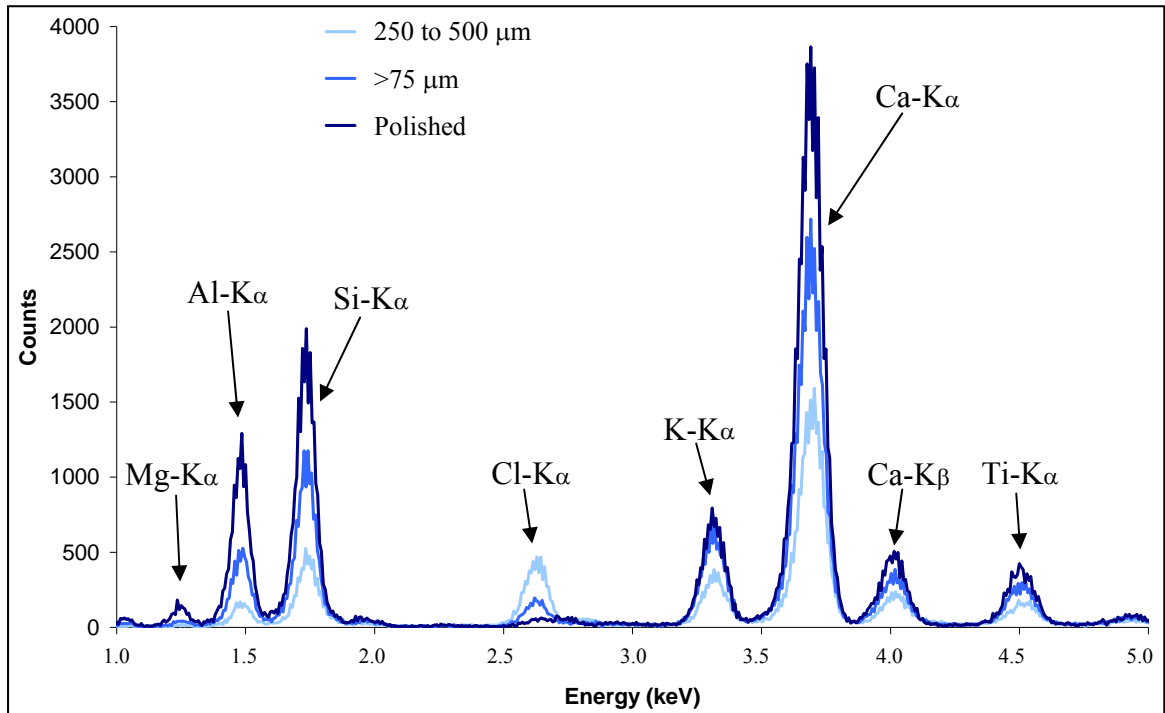


**Figure 7.9:** Spectra from different Etna basalt targets, with grain sizes between 250 and 500  $\mu\text{m}$ , >75  $\mu\text{m}$ , and a polished surface

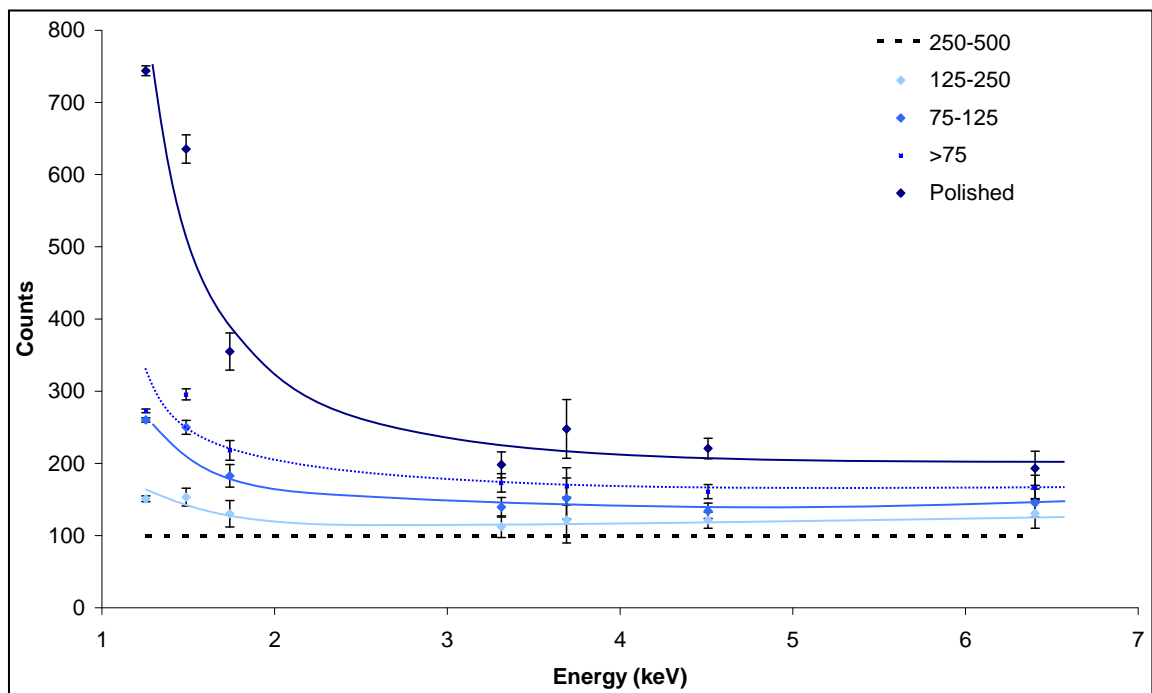


**Figure 7.10:** Counts in the X-ray peaks from different particle sizes of Etna basalt, normalised to provide 100 counts from the target with particles between 250 and 500  $\mu\text{m}$  in diameter

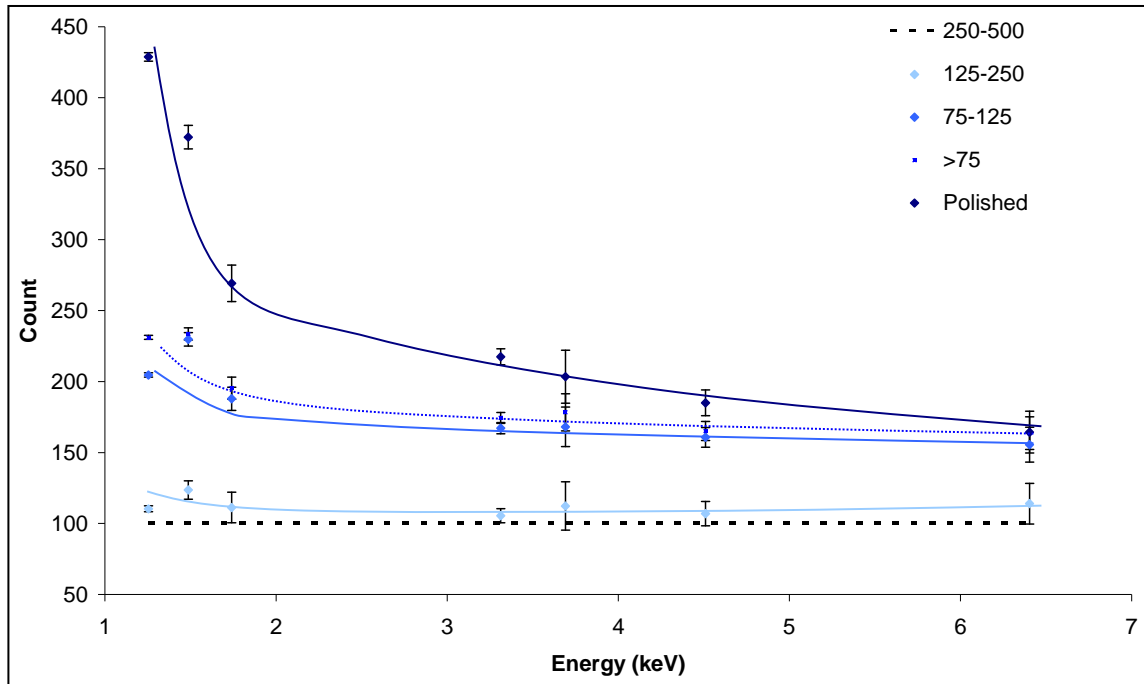


**Figure 7.11:** Counts in the X-ray peaks from different particle sizes of Icelandite, normalised to provide 100 counts from the target with particles between 250 and 500  $\mu\text{m}$  in diameter

### 7.3.2 Spectra as a Function of Incident X-ray Beam

When the number of incident X-ray photons that have sufficient energy to knock electrons from the shells of the target atoms decrease, the number of secondary X-rays reduces with a linear relationship with both tube potential and current. Every flare that occurs during C1XS operation will be different, not just increasing or decreasing in flux, controlled by tube current and potential, but changing in energy profile as well, controlled by tube potential. Hence the importance of providing the Swinyard code with X-ray spectra produced using a range of tube settings. It is essential that the input solar flare is recorded by the XSM, to determine the target composition. If the incident spectrum was not known it could be said that the spectra in Figure 7.12 were generated using multiple XRF targets, which was not the case. They were generated using different tube potentials, where the incident photons did not always possess sufficient energy to fluoresce each element within the target. Therefore the XSM data is essential to validate the C1XS spectra, showing which elements could be detected. Otherwise it could be said that certain areas have a low abundance of certain elements based on the C1XS spectra, when the solar flare possessed insufficient photons to fluoresce these elements.

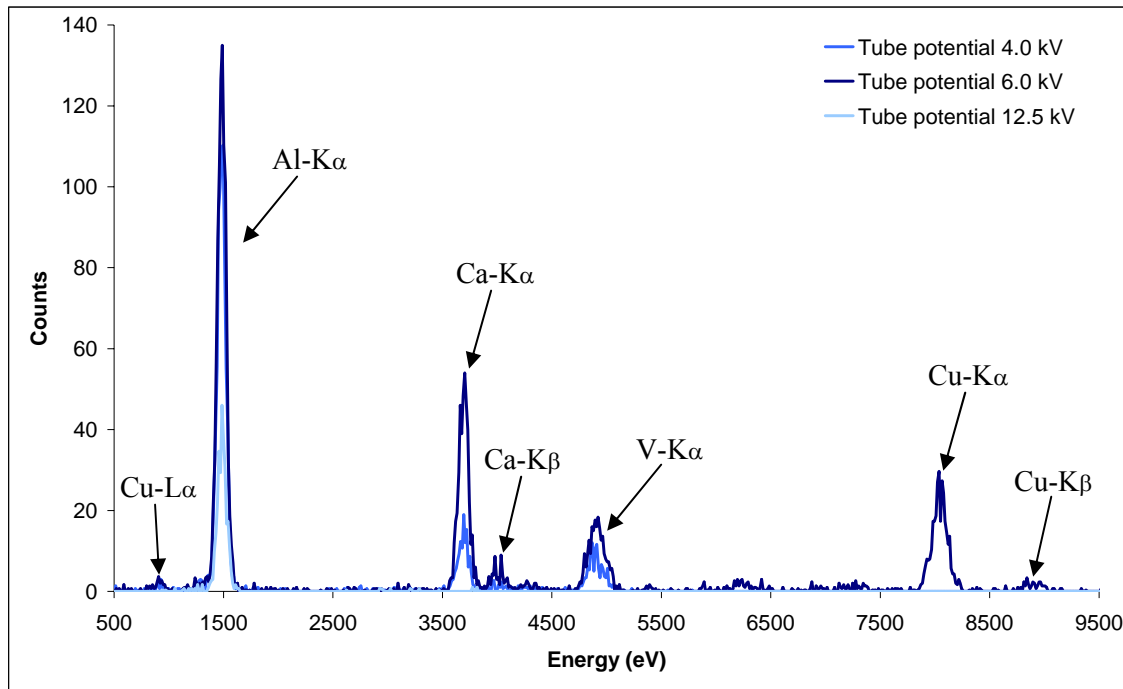


**Figure 7.12:** X-ray spectra taken using the same target with different tube potentials to demonstrate the importance of understanding the incident X-ray spectrum

Based on the GOES data in Figure 3.7 the solar flux in the energy range between 3.1 and 24.8 keV is 5 to 10 times lower than between 1.6 and 12.4 keV, therefore the largest amount of incident solar energy is below 3.1 keV. The spectra in Figure 7.3 shows that the largest amount of energy is below  $\sim 7$  keV, therefore it is unlikely that elements with atomic numbers greater than 30 (Zn) will be detected. The fluorescent yield of the L-shell X-rays is also very low. It is essential for the success of the C1XS instrument that the Swinyard XRF modelling code can successfully interpret the XSM data to provide information on the elemental abundances of lunar data. The data provided to RAL from the study presented above will be invaluable in achieving this goal.

### 7.3.3 Initial Results from the XRF modelling code

The initial results from data provided to RAL and placed into the XRF model by B. Swinyard, the results from the first version of the code are shown in Figure 7.13. The experimental data collected in the laboratory is shown in black and the modelled data, based on the incident X-ray spectra and the elemental abundance of the target, is shown in Green. The model provides a good approximation to the actual spectra, and is under continual development to improve the accuracy and provide some measure of error, and to incorporate the effect of phase angle and target roughness.

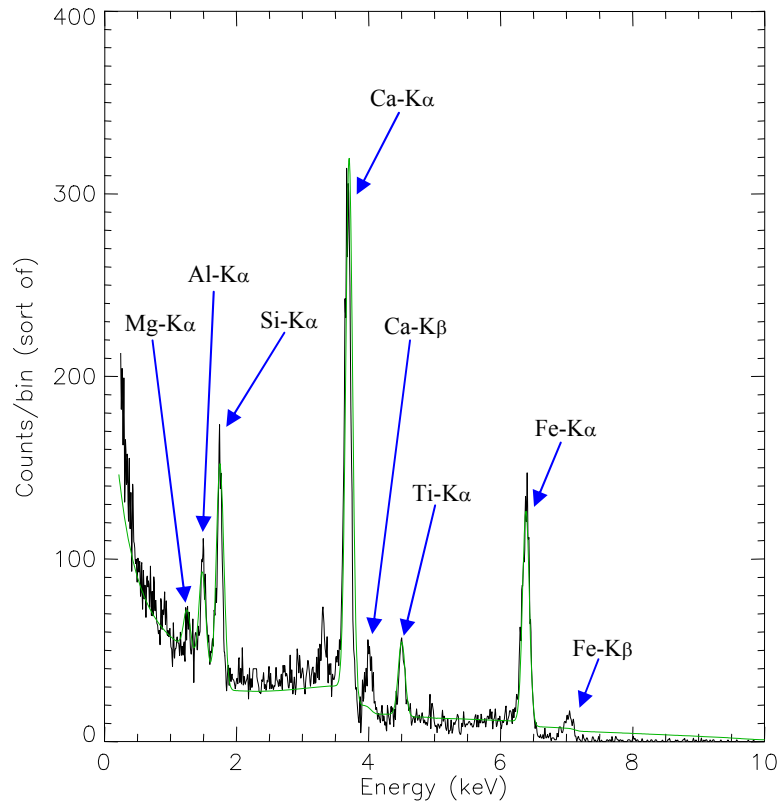


**Figure 7.13:** Initial results produced using the Swinyard code based on experimental data of the lunar regolith simulant [Swinyard 2008]

#### 7.4 Chandrayaan-1 Launch and Initial Results

On the 22<sup>nd</sup> of October 2008 Chandrayaan-1, shown in Figure 7.15, successfully launched using Polar Satellite Launch Vehicle (PSLV) C11 from Satish Dhawan Space Centre, as shown in Figure 7.16. The spacecraft achieved lunar orbit on the 12<sup>th</sup> of November.



**Figure 7.15:** The Chandrayaan-1 spacecraft [ISRO]



**Figure 7.16:** The launch of Chandrayaan-1 launched, using PSLV-C11, on the 22<sup>nd</sup> of October 2008 from the Satish Dhawan Space Centre [ISRO]

The first spectra from the calibration sources were received on the 21<sup>st</sup> of November, showing little sign of radiation damage with the measured energy resolution at Mn-K $\alpha$  increasing by 25 eV at -8 °C, equivalent to a 10 MeV equivalent proton fluence of  $\sim 0.5 \times 10^8$  protons.cm<sup>-2</sup>. The launch and transfer orbit occurred at solar minimum, as discussed in Section 6.1, therefore the actual worse case predicted fluence would be  $0.56 \times 10^8$  protons.cm<sup>-2</sup> based on an updated SPENVIS model, in close agreement with the received fluence based on the model. On the 12<sup>th</sup> of December while over the Apollo landing sites, shown in Figure 7.17, an A-class solar flare occurred, shown in Figure 7.18. The resulting XRF was detected by the C1XS instrument producing the X-ray spectrum shown in Figure 7.19, showing a large improvement over the D-C1XS spectrum shown in Figure 1.3. This is the first demonstration of the excellent performance and scientific data that C1XS will provide over the two years nominal mission duration and possibly beyond. The performance, when compared to Figures 5.21 and 6.23, is almost as good as that achieved in the laboratory!

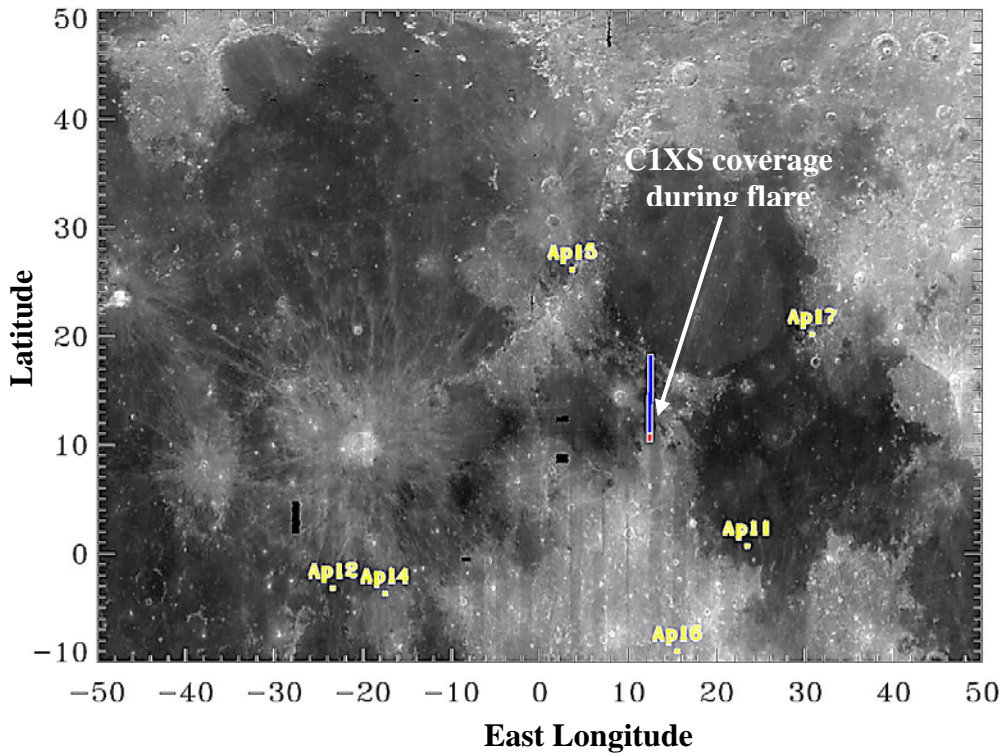


**Figure 7.17:** Photograph of the Apollo landing sites showing the ground track of C1XS during the integration of the first lunar spectra on the 12<sup>th</sup> of December 2008 [Kellet 2008]

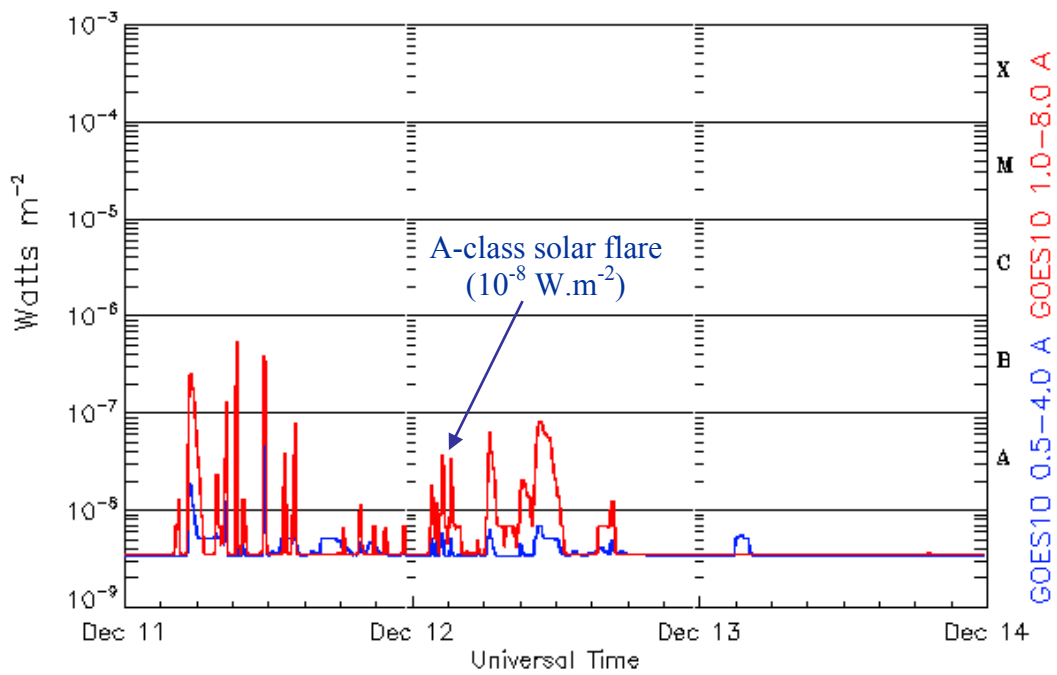


**Figure 7.18:** GOES data showing the solar flare responsible for the first lunar spectra recorded by C1XS

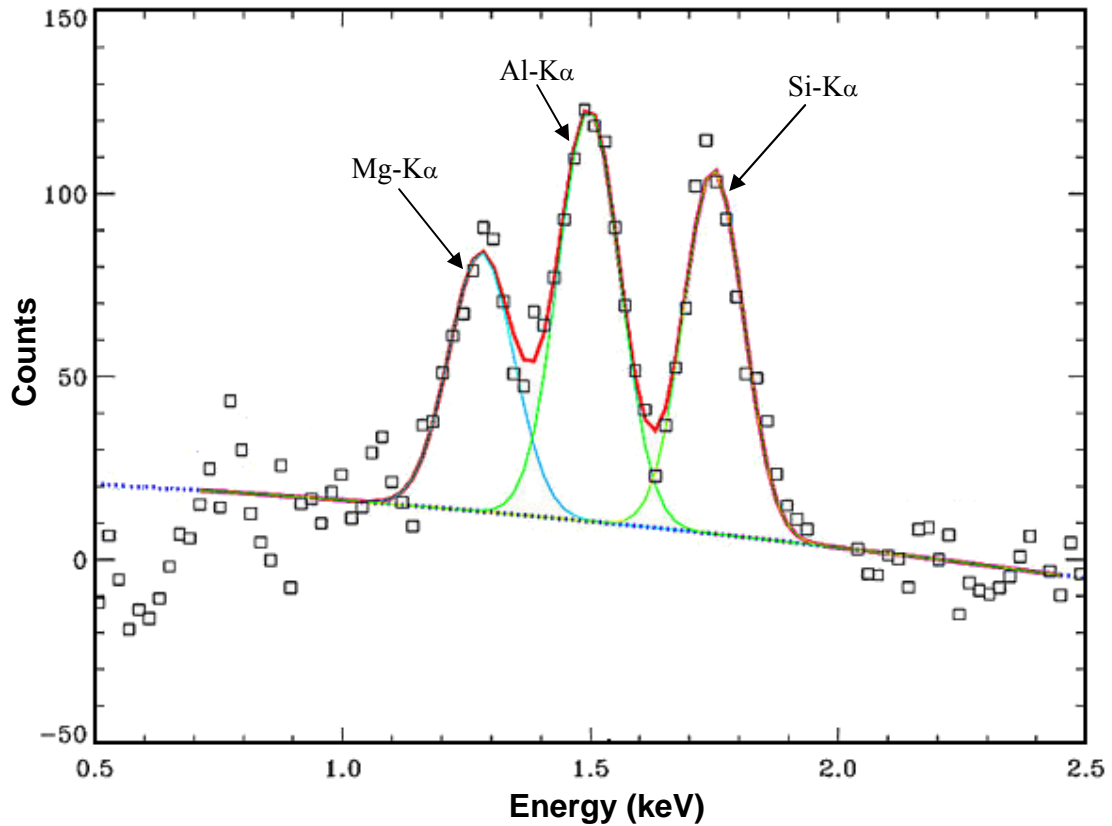


**Figure 7.19:** The first lunar spectrum recorded by C1XS on the 12<sup>th</sup> of December 2008 showing the Mg, Al and Si X-ray peaks fluoresced by an A-class solar flare [Kellet 2008]

## 7.5 X-ray Fluorescence Detector Comparison

During these experiments and previous testing, the CCD54 has proven itself to be an excellent XRF detector. The spectrum in Figure 7.14 was taken using the Icelandite polished sample recorded over 15 minutes with the SCD held at  $-50\text{ }^{\circ}\text{C}$ . The K-shell X-rays from the elements that form the major and minor elements, including oxygen, are resolved along with the Ca-L $\alpha$  line at 0.341 keV and sulphur present in only 354 parts per million. Below  $-15\text{ }^{\circ}\text{C}$  the measured energy resolution changes little, as demonstrated in previous chapters. The CCD54 can be operated using a low power TEC, allowing for the possibility of using it in a portable XRF kit.

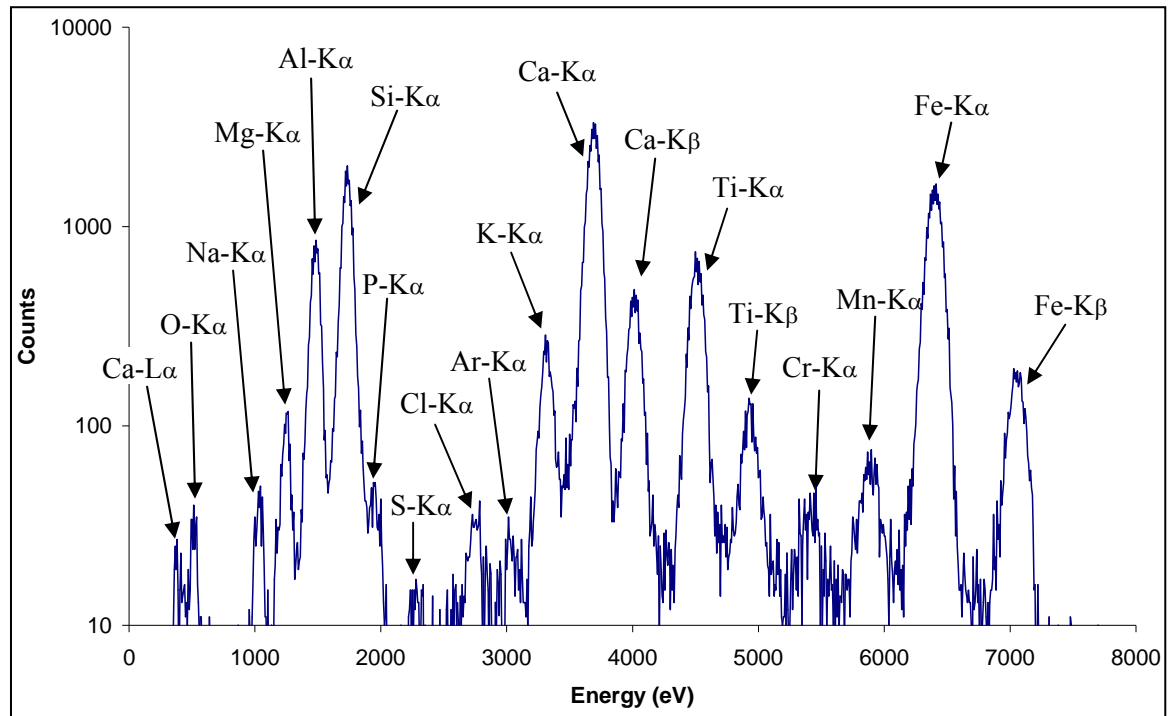


**Figure 7.14:** Icelandite spectrum recorded over 15 minutes with counts on a logarithmic scale

Using the methods discussed in Section 6.6 to improve CTE and reducing the imaging area to further decrease the dark current, would allow the SCD to be operated at warmer temperatures requiring less power for temperature control. Reducing the imaging area by 50% would reduce the dark current generated within the device by 50%. Therefore, with the dark current at  $-15\text{ }^{\circ}\text{C}$  of  $\sim 31\text{ electrons}\cdot\text{sample}^{-1}$  set as the requirement, different imaging areas of a CCD54 type device are given in Table 7.2 with the operational temperatures required to produce an energy resolution of  $\sim 135\text{ eV}$  at  $\text{Mn-K}\alpha$ , assuming no change in performance loss due to the reduction of charge transfers. A smaller device is less susceptible to performance loss from CTI due to the decreased number of charge transfers required to read-out the active area.

<i>Imaging Area</i> ( $\text{mm}^2$ )	<i>Temp</i> ( $^{\circ}\text{C}$ )
107.0	-15.0
85.6	-13.3
64.2	-11.2
53.5	-9.8
42.8	-8.1
32.1	-6.0
21.4	-3.0
10.7	2.2
5.4	7.4

**Table 7.2:** Imaging area required for a CCD54 type device to achieve an energy resolution of  $\sim 135\text{ eV}$  at  $\text{Mn-K}\alpha$ , and the required temperature of operation

A brief comparison of the measured energy resolution at Mn-K $\alpha$  was made using the Si(Li) detector discussed in Chapter 4, a number of SDD, and Si PIN diode detectors. The results of the study are shown in Table 7.3, listing the detector type, imaging area, cooling required, measured energy resolution and the source of the information. The SCD and the SDD are both capable of providing energy resolutions using TEC cooling which conventional detectors can only obtain using liquid nitrogen, with the SDD (SD<sup>3</sup>) capable of providing 128 eV at -10 °C [Lechner *et al.* 2004]. A CCD54 style device with an imaging area of 10 mm<sup>2</sup> could provide comparable performance at ~ +2 °C. The SCD is capable of providing excellent performance, while possessing a large active area when compared to the SDD.

<i>Detector Type</i>	<i>Imaging Area (mm<sup>2</sup>)</i>	<i>Cooling (°C)</i>	<i>Cooling Method</i>	<i>Energy resolution (eV)</i>	<i>Information Source</i>
Sirus Si(Li)	10	-196	Liquid Ni	130	e2v
Sirus Si(Li)	30	-196	Liquid Ni	136	e2v
Sirus Si(Li)	50	-196	Liquid Ni	139	e2v
Sirus Si(Li)	50	-196	Liquid Ni	139	e2v
Sirus SDD	10		TEC	123-133	e2v
Sirus SDD	30		TEC	131 - 139	e2v
XR-100 Si PIN	5	-55	TEC	145-170	AMPTEC
XR-100 Si PIN	13	-55	TEC	180-210	AMPTEC
XR-100 Si PIN	25	-55	TEC	190-230	AMPTEC
XR-100 SDD	7	-55	TEC	135-155	AMPTEC
12-element SDD	60	-10	TEC	172.7	Alberti <i>et al.</i> 2006
4-element SDD "Droplet" -type	50	-20	TEC	140	Alberti <i>et al.</i> 2006
SDD Droplet (SD <sup>3</sup> )	5	-10 to -20	TEC	128 to 124	Lechner <i>et al.</i> 2004
CCD54	107	-20 to -40	TEC	134 to 129	Chapters 5 and 6

**Table 7.3:** Comparison of the measured energy resolution at Mn-K $\alpha$  for different types of Si(Li), Si PIN, SDDs and the CCD54, recording the imaging area and operational temperatures

## 7.6 Chapter Summary

This chapter has presented work carried out to assist the C1XS science team by providing characterised incident X-ray spectra and the resulting spectra from various targets of different grain size. These results will form part of S. Weider's PhD thesis and the ongoing work of B. Swinyard, as a result it has not been discussed in detail in this thesis. The large affect of the incident X-ray flux on the resulting secondary X-ray spectrum was demonstrated by varying the incident X-ray flux by changing the tube potential and current. It is essential that the solar X-ray flux is well

characterised during data collection by the X-ray solar monitor onboard Chandrayaan-1. The final piece of work was to demonstrate the excellent performance of the CCD54 for possible use in other X-ray spectrometry applications. The SCD would be suitable to be used within a portable hand held XRF device similar to those used to analyse Stonehenge. The measured energy resolution of Mn-K $\alpha$  found using the CCD54 compared well to other XRF detectors including the SDD droplet and conventional Si(Li) and Si PIN detectors, especially considering  $\sim \times 3$  larger active area when compared to an SDD. It is hoped the work presented in this thesis will see SCDs developed and used in future space and terrestrial applications as the detector of choice.

## Chapter 8: Conclusions and Further Work

This chapter summarises the main conclusions of the studies carried out for this thesis and indicates directions for possible further work in each case.

### 8.1 Optimisation and Screening

To ensure that the CCD54 devices used in the C1XS instrument onboard Chandrayaan-1 performed better than the required operating performance, an optimisation study and flight device screening were performed, making recommendations for optimal device operating conditions and drive electronics settings. The optimisation and screening study demonstrated that the CCD54 is capable of providing excellent performance over the required energy range and at the operational temperature of the C1XS instrument. The main conclusions of the study are given below:

- The operational potentials and timings were optimised to minimise the dark current and provide the optimal energy resolution at Mn-K $\alpha$ . -20.0 °C was recommended as the C1XS operating temperature.
- The recommended operating voltages and timings were adopted for use on C1XS, with the exception of  $\phi R$ .
- A method for predicting device performance based on the gradient of the triangular leakage current profile, at 20.0 °C, was created.
- The modules recommended for flight were used onboard C1XS.
- Code was developed in MATLAB to analyse the CCD54 read-out, with analyse using isolated or combined events as recommended to RAL. Isolated and a combination of three events was adopted for use on C1XS.
- The QE of the CCD54 was measured to be 74% using combined events and 41% using isolated events, at Mn-K $\alpha$ , with a depletion depth of 42  $\mu m$ .

The need for a proton irradiation damage study was identified to assess the performance over the two year mission duration in orbit around the Moon.

### 8.2 CCD54 Proton Radiation Damage Assessment

Following this study and based on the recommendation of an operating temperature of -20.0 °C or less, the location of C1XS onboard Chandrayaan-1 was changed and the C1XS design modified to provide improved thermal isolation between the C1XS drive electronics and the CCD54s. The operating temperature will be less than -17 °C for ~90% of the mission. The shielding was also

increased to a 4 mm thick Al electronics box and 6 mm of Ta behind the CCD54 modules, with the window, shielding the detectors during the transfer orbit, reduced to 7 mm of Al due to the short amount of time spent within the belts. The gain provided by the electronics was increased to greatly improve upon the performance provided by D-CIXS, resulting in a read-out noise of 6 to 7 electrons r.m.s. [Howe *et al.* 2009]. The main conclusions of the study were:

- The predicted worst case end of life proton fluence was calculated to be  $5.5 \times 10^8$  protons.cm<sup>-2</sup>, based on the recommended shielding and a launch date of February 2008.
- The energy resolution was measured at Mn-K $\alpha$  demonstrating that the CCD54 would allow good quality scientific data to be collected throughout the two year mission.
- Radiation induced CTI within the central transport channels was identified as the main source of performance loss.
- The sample bin value was increased which led to an improvement in the measured energy resolution due to a decrease in dark current with the faster read-out. This could benefit mission performance towards the end of the two year C1XS mission.
- A combination Mg, Al and Si target was produced and fluoresced with X-rays to produce a set of spectra after irradiation to 0% and at 78% of the mission end of life proton fluence demonstrating that the instrument would achieve its scientific goals. The energy resolution towards the end of the mission will still outperform that of D-CIXS.

A reduction in the volume of the two central charge transport channels, a 2-phase clocking operation, the inclusion of a supplementary buried channel, or the use of a p-type buried channel would all improve the charge transfer efficiency in the development of future radiation hard SCDs. Increased sample size would also improve charge collection and event identification. As a result of a change to the launch date a further irradiation study was required.

### 8.3 Radiation Damage Study and Analysis Methods

The Chandrayaan-1 launch date was changed to the 22<sup>nd</sup> of October 2008, further into solar cycle 24. A further proton irradiation was performed, with the dose measured using Gafchromic HD-810 film. This study has allowed the performance degradation due to proton radiation damage to the CCD54s onboard Chandrayaan-1 to be fully characterised. CTI was identified as the main source of decreasing energy resolution over the operational temperature range of C1XS. The main findings of the investigation were as follows:

- The Earth to Moon transfer time was increased to ~17 days, resulting in a 10 MeV equivalent proton fluence of  $1.46 \times 10^8$  protons.cm<sup>-2</sup>. Due to the low solar activity it will more likely be  $0.56 \times 10^8$  protons.cm<sup>-2</sup>.

- The predicted worst case end of life proton fluence was calculated to be  $8.8 \times 10^8$  protons.cm<sup>-2</sup>, based on the recommended shielding and a launch date of October 2008.
- The increase in dark current was linear with proton fluence, with the main component arising from electrons generated from radiation induced defects within the bulk silicon. To account for the increase in voltage required to minimise the surface generated dark current, the preferred operational range of V<sub>ss</sub> should be within 9 to 10 V.
- The dominant trap level pre-irradiation is an unknown trap site at 0.32 eV, which compares well to a trap level at 0.30 eV identified by Holland 1993. After receiving a 10 MeV equivalent fluence of  $7.5 \times 10^8$  protons.cm<sup>-2</sup> the dominant trap site was measured to be 0.44 eV, corresponding to the E-centre, 0.42 eV [Holland 1993] and 0.44 eV [Janesick 2001].
- After irradiation with  $7.5 \times 10^8$  protons.cm<sup>-2</sup> the Al-K $\alpha$  peak location shifted by  $\sim 53$  eV as a result of the surface gain factor. The lunar regolith simulant spectra demonstrated that the change in linearity would not affect spectral analysis, as the effect is linear with fluence.
- The energy dependence of CTI dominance, to performance loss, was found to occur at around -21 °C, -13 °C and -6 °C for Al-K $\alpha$  (1,487 eV), Ca-K $\alpha$  (3,691 eV) and Cu-K $\alpha$  (8,047 eV) X-rays respectively. The energy resolution of Ca-K $\alpha$  and Cu-K $\alpha$  becomes CTI limited at around -25 °C, i.e. shows no improvement with further cooling.
- Spectra from lunar regolith simulant JSC-1 demonstrated that after  $7.5 \times 10^8$  protons.cm<sup>-2</sup> the low energy X-ray peaks can still be identified.
- A radiation damage model was produced to predict the energy resolution based on the proton fluence level and temperature using the quadrature summation of the X-ray Fano-limited statistics plus the measured noise and the CTI damage factor. The model compared well with the experimental data.

The clocking operation used in C1XS could be modified to increase the clock overlaps, or possibly have a larger area held under maximum potential, improving charge transport and storage, minimising the effects of radiation induced CTI. Further work should include a comparison of the predicted performance to the proton fluence recorded by the C1XS onboard dosimeter, and also to monitor the spectra produced over the entire mission to provide a large data set for quantifying radiation damage over a period of two years. Using the measured energy resolution of the Mn-K $\alpha$  X-ray peak on arrival at the Moon and the model the estimated fluence received was calculated to be  $\sim 0.5 \times 10^8$  protons.cm<sup>-2</sup>, which compares well to the predicted value of  $0.56 \times 10^8$  protons.cm<sup>-2</sup> for solar minimum conditions.

#### 8.4 XRF Modelling, C1XS Initial Results, and a XRF Detector Comparison

The data provided to RAL has proved invaluable in the development of the Swinyard XRF modelling code. Spectra collected from the lunar regolith simulant demonstrated the performance capabilities of the CCD54, and compares well to instrument performance in orbit around the Moon as demonstrated by the C1XS initial results. The recommendations to RAL have helped create an excellent X-ray spectrometer. C1XS will continue to provide excellent scientific data during the entire mission, through the understanding and minimising the radiation damage effects to the CCD54s. At the time of the submission of this thesis C1XS has observed X-rays from the lunar surface following a number of C-class solar flares with statistically significant detections of Ca and Fe, which will be the subject of future journal publications.

The final piece of work was to demonstrate that the SCD makes an excellent choice of detector for XRF, detecting the O-K $\alpha$  and Ca-L $\alpha$  X-ray peaks. The SCD is capable of providing energy resolutions with TEC cooling which conventional detectors can only obtain using liquid nitrogen, with the energy resolution at Mn-K $\alpha$  found using the CCD54 comparing very well to the other XRF devices investigated. The measured energy resolution of the CCD54 at Mn-K $\alpha$  compared to the other types of detector is excellent, considering that the surface area is greater than most of the other detectors which results in a larger dark current, and that the CCD54 was designed in 1997. The main advantage of the SCD over the SDD is the large active area.

Further work should include a detailed comparison of SCD technology and SDD technology, comparing the peak to background, QE, portability, energy resolution as a function of count rate and temperature while operating using the same experimental setup. The possibility of using the SCD in a portable XRF detector should also be investigated using the AMP TEK Mini-X or COOL-X X-ray generators.

## Bibliography

- Adler I. (1966) “X-ray *Emission Spectrography in Geology*”, Elsevier
- Adler I. and Gerard J. (1972) “The Apollo 15 X-ray fluorescence experiment”, *Proceedings of third Lunar Science Conference* (Supplement 3, *Geochimica et Cosmochimica Acta*), **no. 3**, pp. 2157-2178
- Alberti R., Buzzetti S., Fiorini C., Guazzoni C., Klatka T., Lechner P., Longoni A., and Strüder L. (2006) “Advanced monolithic arrays of Silicon Drift Detectors for elemental mapping applications”, SNIC Symposium, Stanford, California
- Alha L. (2009), C1XS email communication
- Alig R., Bloom S., and Struck C. (1980) “Scattering by ionisation and phonon emission in semiconductors”, *Phys. Rev. B.*, **vol. 22**, pp. 5565-82
- Alvarez L. W., Alvarez W., Asaro F., and Michel H. V. (1980) “Extraterrestrial Cause for the Cretaceous-Tertiary Extinction”, *Science*, **vol. 208**, no. 4448, pp. 1095-1108, 1980
- Ambrosi R. M., Short A. D. T., Abbey A. F., Wells A. A., and Smith D. R. (2002) “The effect of proton damage on the X-ray spectral response of MOS CCDs for the Swift X-ray telescope”, *Nucl. Inst. Meth.*, **A 482**, pp. 644-652, 2002
- Antcliffe G. A. (1975) “Development of CCD imaging sensors for space applications, phase 1”, Jet Propulsion Laboratory, ID: 19760019897
- Asimov I. (1975) “*The Tragedy of the Moon*”, Coronet Books, New edition
- Badhwar G. D. (1997) “Drift rate of the South Atlantic Anomaly”, *J. Geophysical Research*, **vol. 102**, noA2, pp. 2343-2349
- Beasley, D. and Weintraub R. (2005) “Solar Fireworks Signal New Space Weather Mystery”, NASA press release 05-132 [http://www.nasa.gov/vision/universe/solarsystem/solar\\_fireworks.html](http://www.nasa.gov/vision/universe/solarsystem/solar_fireworks.html)
- Bebek C., Groom S., Holland S., Karcher A., Kolbe W., Lee J., Levi M., Palaio N., Turko B., Uslenghi M., Wagner M., and Wang G. (2002) “Proton Radiation Damage in P-channel CCDs Fabricated on High-Resistivity Silicon”, *IEEE Trans. Nucl. Sci.*, **vol. 49**, no. 3, pp. 1221-1225
- Beckhoff B., Kanngießner B., Langhoff N., and Wedell, R. (2006) “*Handbook of Practical X-Ray Fluorescence Analysis*”, Springer, Illustrated Edition
- Belgium Institute for Space Astronomy, “SPENVIS-The Space Environment Information System”, <http://www.spennis.oma.be/intro.html>
- Bell labs <http://www.bell-labs.com>
- Bertolini G. and Coche A. (1968) “*Semiconductor Detectors*”, North Holland Pub. Co., Amsterdam
- Bethe H. A. (1932) “Bremsformel für Elektronen relativistischer Geschwindigkeit”, *Z. Phys.* **76**, pp 293
- Binder A. B. (1984) “The binary fission origin of the moon”, Origin of the moon; *Proceedings of the Conference*, Kona, HI, A86-46974 22-91
- Bragg W. L. (1975) “*The development of x-ray analysis*”, Bell
- Bredthauer R. A., Pinter J. H., Janesick J. R., and Robinson L. B. (1991) “Notch and large-area CCD imagers”, *Proc. SPIE*, **vol. 1447**, pp. 310-15

- Brophy J. J. (1969) "Variance Fluctuations in Flicker Noise and Current Noise", *J. Appl. Phys.*, **vol. 40**, Issue 9
- Brown W. L., Gabbe, J. D., and Rosenzweig, W. (1963) "Results of the Telstar Radiation Experiments", *Bell System Technical J.*, 42, pp. 1505
- Brown, J. G. (1975) "*X-rays and their applications*", Plenum/Rosetta
- Burke B. and Gajar S. (1991) "Dynamic suppression of interface state dark current in buried channel CCDs", *IEEE Trans. Electron Devices* **Vol. ED-38**, pp. 285-290
- Burke E. A. (1986) "Energy dependence of proton-induced displacement damage in silicon", *IEEE Trans. Nucl. Sci.*, **NS-33**, pp 1276-81
- Burt D. (2006) CCD Lecture Course
- Burt D. (2008), e2v technologies plc., Private Communication
- Claeys C. and Simoen E. (2002) "*Radiation effects in advanced semiconductor materials and devices*", Springer
- Claisse F. (1965) "Accurate X-ray fluorescence analysis without internal standards", Quebec, Dept. Mines, Preliminary Report
- Clark, P.E. and I. Adler (1978) "Utilization of independent solar flux measurements to eliminate non-geochemical variation in X-ray fluorescence data", *Proceedings Lunar Planetary Science Conference*, pp. 727-749
- Connors K. A. (1990) "*Chemical Kinetics: The Study of Reaction Rates in Solution*", Wiley
- De Monte B., Pool P., Turton J., Guyatt N., and King R. (2008), "Proton Irradiation Test – Summary Report", e2v internal report
- Defence Advanced Research Projects Agency (DARPA) (2005) "RDT&E budget item justification sheet for 2006/2007", **Vol. 1**, page 254
- Defise J. M., Berghmans D., Hochedez, J. F., Lecat J. H., Mazy E., Rochus P., Thibert T., Nicolosi P., Pelizzo M. G., Schühle U., Van der Linden R. A. M., Zhukov A. N. (2003) "SWAP: Sun Watcher using APS detector on board PROBA-II, a new EUV off-axis telescope on a technology demonstration platform", *Proc. SPIE conference*, **vol. 5171**, Telescopes and Instrumentation for Astrophysics
- Dennis B., and R. Starr (2008) "Flare Plasma Abundances - New X-ray Observations", rhesis nugget no. 84
- Dikpati M., Toma G., and Gilman P. A. (2006) "Predicting the strength of solar cycle 24 using a flux-transport dynamo-based tool", *Geographical Research Letters*, **vol. 33**, L05102
- Dolginov Sh., Yeroshenko E. G., Zhuzgov L. N., and Shulin I. A. (1967) "Possible interpretation of the results of measurements on the near lunar satellite", National Aeronautics and Space Administration Goddard Space Flight Centre, Contract N0.M-5-12487
- Dyer C. S. (1998) "Space Radiation Effects for Future Technologies and Missions", QINETIQ KI SPACE TR0106901/1.1
- e2v Technologies (1997) "CCD54 Design Details", Ref: ISDR 490/292, Issue 1
- Emery F. E. and Rabson T. A. (1965) "Average Energy Expended Per Ionized Electron-Hole Pair in Silicon and Germanium as a Function of Temperature", *Phys. Rev.*, **vol. 140**, A2089 - A2093
- European Space Agency (ESA), <http://www.esa.int/esaCP/index.html>

- Fano U. (1947) "Ionization Yield of Radiations. II. The Fluctuations of the Number of Ions", *Phys. Rev.*, **vol. 72**, pp. 26 - 29
- Feynman J., Spitale G., Wang J., and Gabriel S. (1993) "Interplanetary Proton Fluence Model: JPL 1991", *J. Geophys. Res.*, **vol. 98**, 13,281-13,294
- Foing B. H., Racca G.D., Marini A., Heather D.J., Koschny D., Grande M., Huovelin J., Keller H.U., Nathues A., Josset J.L., Malkki A., Schmidt W., Noci G., Birkel R., Iess L., Sodnik Z., and Mc Manamon P. (2002) "SMART-1 Mission to the Moon: Technology and Science Goals", *COSPAR*
- Fossum E. R. *et al.* (1994) "CMOS Active Pixel Sensor", *IEEE Trans. Electron Devices*, **vol. 41**, Issue 3, pp. 452-453
- Fossum E. R. (1998) "Digital Camera System on a Chip", *Micro IEEE*, **vol. 18**, Issue 3, pp. 8-15
- Galileo G. (1989) "*Sidereus Nuncius*" (Translated by Albert Van Helden), Chicago: University of Chicago Press
- Gatti E. and P. Rehak (1984) "Semiconductor drift chamber - an application of a novel charge transport scheme", *Nucl. Inst. Meth.*, **vol. 225**, pp. 608-614
- Glaser M. and Ravotti F., (2006) "Dosimetry Assessments in the Irradiation Facilities at the CERN-PS Accelerator", *IEEE Trans. Electron Devices*, **vol. 53**, Issue 4, pp. 2016-2022
- Goswami J. N., Thyagarajan K. and Annadurai M. (2006) "Chandrayaan-1: Indian Mission to Moon", *Lunar and Planetary Science XXXVII*
- Grande M. (2001) "The D-CIXS X-Ray Spectrometer on ESAs Smart-1 Mission to the Moon", *Earth, Moon, and Planets*, Springer, **vol. 85-86**, pp. 143-152
- Grande M., Browning R., Waltham N., and Parker D. (2003) "The D-CIXS X-ray mapping spectrometer on SMART-1", *Planetary and Space Science*, **vol. 51**, pp. 427-433
- Grande M., Kellett B.J., Howe C., Perry C.H., Swinyard B., Dunkin S., Huovelin J., Alha L., D'Uston L.C., Maurice S., Gasnault O., Couturier-Doux S., Barabash S., Joy K.H., Crawford I.A., Lawrence D., Fernandes V., Casanova I., Wiczorek M., Thomas N., Mall U., Foing B., Hughes D., Alleyne H., Russell S., Grady M., Lundin R., Baker D., Murray C.D., Guest J., and Christo A. (2007) "The D-CIXS X-ray spectrometer on the SMART-1 mission to the Moon – First results", *Planetary and Space Science*, **vol. 55**, pp. 494-502
- Grande M., Maddison B. J., Howe C. J., Kellett B. J., Sreekumar P., Huovelin J., Crawford I.A., Duston C.L., Smith D., Anand M., Bhandarij N., Cook A., Fernandes V., Foingo B., Gasnaut O., Goswami J.N., Holland A., Joy K.H., Kochneyo D., Lawrence D., Maurice S., Okadan T., Narendranath S., Pietersp C., Rothery D., Russell S.S., Shrivastava A., Swinyard B., Wilding M., and Wiczorek M. (2009) "The CIXS X-ray Spectrometer on Chandrayaan-1", *Planetary and Space Science*, **vol. 57**, Issue 7, pp 717-724
- Grove A. S. (1967) "*Physics and Technology of Semiconductor Devices*", Wiley
- Hall R. (1952) "Electron-hole combination in germanium", *Phys. Rev.*, **vol. 87**, pp. 387
- Hanley C. and Cawley L. (2000) "WFC3 Detector Characterization Report #1: CCD44 Radiation Test Results - CCD44V1", The Space Telescope Science Institute, Instrument Science Report WFC3
- Hanley C., and Cawley L. (2001) "WFC3 Detector Characterization Report #3: CCD44 Radiation Test Results - CCD44V1", The Space Telescope Science Institute, Instrument Science Report WFC3

- Hardy T., Murowinski R., and Deen M. J. (1998) "Charge Transfer Efficiency in Proton Damaged CCDs" *IEEE Trans. Nucl. Sci.*, **vol. 45**, pp. 154-163
- Hartmann, W. K. and Davis D. R. (1975) "Satellite-sized Planetesimals and Lunar Origin", *Icarus*, **vol. 24**, pp. 504-515
- Heiken G., Vaniman D., and French B. (1991) "*Lunar Sourcebook, a user's guide to the Moon*", Cambridge University Press
- Helmuth S. (2005) "*Semiconductor detector systems*", Oxford University Press
- Heynderickx D., Quaghebeur B., Speelman E., and Daly E. J. (2000) *Proc. AIAA* 0371
- Holland A. D. (1990) "*Radiation effects in CCD X-ray detectors*", Ph. D. Thesis, University of Leicester
- Holland A. D. (1991) "Annealing of proton-induced displacement damage in CCDs for space use", *Inst. Phys. Conf. Ser.*, **vol. 121**, pp. 33-40
- Holland A. D. (1993) "The effect of bulk traps in proton irradiated EEV CCDs", *Nucl. Inst. Meth., A*, **vol. 326**, Issue 1-2, pp. 335-343
- Holland A. D., Turner M. J. L., Burt D. J., and Pool P. (1993) "The MOS CCDs for the European Photon Imaging Camera", *Proc. SPIE*, **vol. 2006**, pp. 2-10
- Holland A. D. and Hutchinson I. B. (1998) "Testing Report for IMPACT ERD2 CCDs", Space Research Centre, Leicester University
- Holland A. D., Hutchinson I.B., Smith D.R., and Pool P. (2004) "Proton damage in the E2V swept charge device", *Nucl. Inst. Meth., A* **521**, pp. 393-398
- Holman G. and Benedict S. "Laboratory for Astronomy and Solar Physics, Solar Flare Theory", NASA's Goddard Space Flight Centre, <http://hesperia.gsfc.nasa.gov/sftheory/index.htm>
- Holmes-Siedle A. G. (2002) "*Handbook of radiation effects*", Oxford University Press
- Hopkins I. H., Hopkinson G. R., and Johlander B. (1994) "Proton-Induced Charge Transfer Degradation in CCDs for Near-Room Temperature Applications", *IEEE Trans. Nucl. Sci.*, **vol. 41**, no. 6
- Hopkinson G. R. and Lumb D. H. (1982) "Noise Reduction Techniques for CCD Image Sensors", *J. Phys. E: Sci. Instrum.*, **vol. 15**, pp. 1212
- Hopkinson G. R., Mohammadzadeh A., and Harboe-Sorensen R. (1994) "Radiation Effects on a Radiation Tolerant CMOS Active Pixel Sensor", *IEEE Trans. Nucl. Sci.*, **vol. 51**, Issue 5, pp. 2753-2762
- Horne R. B., Richard M., Thorne R. M., Shprits Y. Y., Meredith N. P., Glauert S. A., Smith A. J., Kanekal S. G., Baker D. N., Engebretson M. J., Posch J. L., Spasojevic M., Inan U. S., Pickett J. S., and Decreau P. M. E. (2005) "Wave acceleration of electrons in the Van Allen radiation belts", Nature Publishing Group, **vol. 437**
- Horowitz P. and Hill W. (1989) "*The art of electronics*", Cambridge University Press
- Hotston C. (2000) "Support for the CCD54 Sketch Sheet 1 of 2", Marconi
- Howe C. (2007), RAL, Private Communication
- Howe C.J., Drummond D. , Edeson R., Maddison B., Parker D. J., Parker R., Shrivastava A., Spencer J., Kellett B. J., Grande M., Sreekumar P., Huovelin J., Smith D. R., Gow J., Narendranath

- S., and d'Uston L. (2009) "Chandrayaan-1 X-ray Spectrometer (C1XS)—Instrument design and technical details", *Planetary and Space Science*, **vol. 57**, Issue 7, pp. 735-743
- Howes M. J. and Morgan D. V. (1979) "*Charge-Coupled Devices and Systems*", Wiley
- Hsu H., Chen J., and Vasilik G. (2001) "Photon radiation dose enhancement at material interfaces", *Applied Radiation and Isotopes*, **vol. 55**, pp. 323-326
- Hurst G. S. and Turner J. E. (1970) "*Elementary radiation physics*", Wiley
- Hynecek J. (1979) "Virtual phase CCD technology", *IEEE IEDM Tech. Dig.*, pp. 611-614
- International Commission on Radiation Units and Measurements (1993), ICRU Report 49, Stopping Powers and Ranges for Protons and Alpha Particles
- ISRO data sheet for MIP, the impacter
- Jacobs J. A., Russell R. D., and Wilson T. J. (1974) "*Physics and Geology*", McGRAW-Hill Inc.
- Janesick J. R. (2001) "*Scientific Charge Coupled Devices*", SPIE Press, Washington
- Jenkins R. (1967) "*Practical x-ray spectrometry*", Philips
- Jet Propulsion Laboratory, California Institute of Technology, <http://www.jpl.nasa.gov/>
- Johnson, J. B. (1928) "Thermal Agitation of Electricity in Conductors", *Phys. Rev.*, **vol. 32**, pp. 97-109
- Johnston A. H. (2002) "Space Radiation Effects on Microelectronics", Jet Propulsion Laboratory, Electronic Parts Engineering Office, Section 514
- Joy K. (2007), Birkbeck College UCL, Private Communication
- Kellett B. J. (2008) C1XS communication
- Kim C., Early J., and Amelio G. (1972) "Buried channel charge coupled devices", presented at NERM
- Kinchin G. H. and Pease R. S. (1995) "The Displacement of atoms in solids by Radiation", Atomic Energy Research establishment, Harwell
- Kiran Kumar A. S., and A. Roy Chowdhury (2005) "Terrain mapping camera for Chandrayaan-1", *J. Earth Syst. Sci.*, **vol. 114** (6), pp. 717-720
- Knoll G. F. (2000) "*Radiation Detection and Measurement*", Wiley
- Krane K.S. (1998) "*Introductory Nuclear Physics*", Wiley
- Kraner H. W. (1984) "Radiation damage in silicon detectors", *Nucl. Inst. Meth.*, **A225**, pp. 615-618
- Kuiper G. P. (1956) "The formation of the planets", *J. Roy. Astron. Soc. Cam.*
- Lechner P., Fiorini C., Longoni A., Lutz G., Pahlke A., Soltau H., and Strüder L. (2004) "Silicon Drift Detectors for High Resolution, High Count Rate X-ray Spectroscopy at Room Temperature", *Advances in X-ray Analysis*, **vol. 47**
- Levinson A. A. and Taylor S. R. (1971) "*Moon Rocks and Minerals*", Pergamon Press
- Li X. A., Chu J. C. H., Chen W., and Zusag T. (1999) "Dose enhancement by a thin foil of high-Z material: A Monte Carlo study", *Med. Phys.*, **vol. 26**, issue 7, pp. 1245-1251
- Li Z. (1995) "Experimental comparisons among various models for the reverse annealing of the effect concentration of ionized space charges of neutron irradiated silicon detectors", *IEEE Trans. Nucl. Sci.*, **vol. 42**, pp 224-234

- Lifshin E. (1999) “*X-ray characterisation of Materials*”, Wiley
- Litwiller D. (2001) “CCD vs. CMOS: Fact and Fiction”, Laurin Publishing Co. Inc. Photonics Spectra
- Lutz G. (1999) “*Semiconductor radiation detectors: device physics*”, Springer
- MacEvoy B., Hall G., and Gill K. (1996) “Defect evolution in irradiated silicon detector material”, *Nucl. Inst. Meth.*, **A374**, pp. 12-26
- MacKenzie W, S. (1994) “*A colour atlas of rocks and minerals in thin section*”, Manson Publishing
- Mapson-Menard H. C. (2003) “Performance evaluation of an Active Pixel Sensor Test Structure for space science applications”, *Nucl. Inst. Meth.*, **A513**, pp. 313-316
- Marshal C. J. and P. W. Marshall (2003) “CCD Radiation Effects and Test Issues for Satellite Designers”, NASA-GSFC Multi-Engineering Disciplinary Support Contract Task 1058m
- Maruyama Y., Ogawa K., Okada T., and Kato M. (2007) “Particle size effect in x-ray fluorescence and its implication to planetary XRF spectroscopy”, *Lunar and Planetary Science XXXVIII*, **No. 1186**
- Meidinger N., Schmalhofer B., and Strüder L. (2000) “Particle and X-ray damage in pn-CCDs”, *Nucl. Inst. Meth.*, **A439**, pp. 319-336
- Messenger G.C. (1992) “A summary review of displacement damage from high energy radiation in silicon semiconductors and semiconductor devices”, *IEEE Trans. Nucl. Sci.*, **vol. 39**, Issue 3, pp. 468-473
- Morishima R. and Watanabec S. (2004) “Co-accretion of the Earth–Moon system after the giant impact: reduction of the total angular momentum by lunar impact ejecta” *Icarus* **vol. 168**, Issue 1, pp. 60-79
- Murray N. J., Holland A. D., Smith D. R., Gow J., Pool P., Burt D. (2009) “The X-ray quantum efficiency measurement of high resistivity CCDs”, *Nucl. Inst. Meth.*, **A604**, pp. 180-182
- Nakamura J. (2005) “*Image sensors and signal processing for digital still cameras*”, CRC, 1st edition
- Narendranath S., Sankarsubramaniam K., and Choudhary P. (2006) “CIXS Radiation Environment Report for Chandrayaan-1”, ISAC internal document, ch1\_cixs\_radiation\_rpt\_1, version 1.0
- NASA, Tracking a Solar Storm, Storm Signals, viewed 4th July 2007, [http://son.nasa.gov/tass/radiowaves/sat\\_goes5.htm](http://son.nasa.gov/tass/radiowaves/sat_goes5.htm)
- Noble P. (1968) “Self-scanned image detector arrays”, *IEEE Trans. Elect. Dev.*, **vol. 15**, Issue 4, pp. 202-209
- Okada T. (2009), JAXA, C1XS Science Team Meeting
- Okada T., Shirai K., Yamamoto Y., Arai T., Ogawa K., Inoue T., and Kato M. (2007) “Elemental Composition of Asteroid Itokawa by Hayabusa XRF Spectrometry” *38th Lunar and Planetary Science Conference*, **no. 1338**, pp. 1287
- Oldham T. R. (1999) “*Ionizing radiation effects in MOS oxides*”, World Scientific
- Owens A., McCarthy, K. J., Wells A., Hajdas W., Mattenberger F., Zehnder A., and Terekhov O. (1995) “Measured radiation damage in charge coupled devices exposed to simulated deep orbit proton fluxes”, *Nucl. Inst. Meth.*, **A 361** pp. 602-610
- Pankove J. (1971) “*Optical Processes in Semiconductors*”, Dover Publications

- Pell E.M. (1960) "Ion drift in a n-p junction", *J. Appl. Phys.*, **vol. 31** No. 2, pp. 291-299
- Pfotzer, G. (1936) "Dreifachkoinzidenzen der Ultrastrahlung aus vertikaler Richtung in der Stratosphäre", *Z. Phys.*, **vol. 102**, pp 23-40 and 41-58
- Pickel J. C., Kalma A. H., Hopkinson G. R., and Marshall C. J. (2003) "Radiation Effects on Photonic Imagers-A Historical Perspective", *IEEE Trans. Nucl. Sci.*, **vol. 50**, Issue 3
- Pool P. J. (1997) "CCD54 Design Specifications", EEV Document No. DAS 544645 AN
- Reiff P. H. (1999) "The Sun-Earth Connection", Department of Space Physics and Astronomy
- Rieder R., Economou T., Wänke H., Turkevich A., Crisp J., Brückner J., Dreibus G., and McSween Jr. H. Y. (1997) "The chemical composition of the Martian soil and rocks returned by the mobile Alpha Proton X-ray Spectrometer: Preliminary results from the X-ray mode", *Science*, **vol. 278**, no. 5344, pp. 1771-1774
- Robbins M.S., Roy T., Watts S.J. (1991) "Degradation of the charge transfer efficiency of a buried channel charge coupled device due to radiation damage by a beta source" RADECS 91, *IEEE conference proceedings*, pp. 327-332
- Robbins M. S. (1992) "*Radiation Damage Effect in Charge Coupled Devices*", PhD Thesis, Brunel University
- Robbins M. S. (2004) "High-Energy Proton-Induced Dark Signal in Silicon Charge Coupled Devices", *IEEE Trans. Nucl. Sci.*, **vol. 47**, Issue 6
- Rodina P., Ebert U., Hundsdorfer W., and Grekhov I. (2002) "Tunnelling-assisted impact ionization fronts in semiconductors", *J. of Applied Physics*, **vol. 92**, number 2
- Roy T., Watts S. J., and Wright D. (1989) "Radiation damage effects in imaging charge coupled devices", *Nucl. Inst. Meth.*, **A275**, pp. 545-57
- Russell S. S., Zolensky M., Righter K., Folco L., Jones R., Connolly H. C., Grady M. M., and Grossman J. N. (2005) "The Meteoritical Bulletin, No. 89, 2005 September", *Meteoritics & Planetary Science* 40, Nr 9, Supplement, **A201–A263**
- Saks N. S. (1980) "A technique for suppressing dark current generated by interface states in buried channel CCD imagers", *IEEE Electron Device Lett.*, **vol. EDL-1**, pp. 131-133
- Sawyer D. M. and Vette J. I. (1976) "AP-8 Trapped Proton Environment for Solar Maximum and Solar Minimum", NSSDC/WDC-A-R&S 76-06
- Schove, D. J. (1983) "Sunspot Cycles", *Benchmark Papers in Geology*, **vol. 68**
- Seltzer S. M. (1980) "SHIELDOSE, A Computer Code for Space-Shielding Radiation Dose Calculations", National Bureau of Standards, *NBS Technical Note 1116*, U.S. Government Printing Office, Washington, D.C.
- Seltzer S. M. (1994) "Updated calculations for routine space-shielding radiation dose estimates: SHIELDOSE-2", *NIST Publication NISTIR 5477*, Gaithersburg, MD.
- Shiono N., Shimaya M., and Sano K. (1983) "Ionising radiation effects in MOS capacitors with very thin gate oxides", *Japanese J. App. Phys.*, **vol. 22**, no. 9, pp. 1430-35
- Shkuratova Y. G. and Bondarenkob N. V. (2001) "Regolith Layer Thickness Mapping of the Moon by Radar and Optical Data", *Icarus*, **vol. 149**, Issue 2, pp. 329-338
- Shockley W. and W. Read. (1952) "Statistics of recombination oh holes and electrons", *Physc. Rev.*, **vol. 87**, pp. 835

- Singer, S. F. (1984) "Origin of the moon by capture", Origin of the moon; *Proceedings of the Conference*, Kona, HI, A86-46974 22-91
- Smith D. R. (2003) "*Radiation Damage in Charge Coupled Devices*", Ph. D. Thesis, University of Leicester
- Smith D. R., Holland A. D., Hutchinson I., Abbey A. F., Pool P., Burt D., and Morris D. (2004) "Low Noise Charge Injection in the CCD22", *Proc. SPIE*, **vol. 5501**, pp. 189-196
- Smith D. R., Holland A. D., and Hutchinson I. B. (2004) "Random telegraph signals in charge coupled devices", *Nucl. Inst. Meth.*, **A 530**, pp. 521-535
- Smith R.W. and Tatarewicz, J.N. (1985) "Replacing a technology: The large space telescope and CCDs", *Proceedings of the IEEE*, **vol. 73**, Issue 7, pp. 1221-1235
- Sørensen J. (2005) "Chandrayaan-1: Environmental Specification", ESA internal document, TEC-EES-05-011/JS, issue 0.1
- Spratt J. P., Passenheim B. C., and Leadon, R. E. (1997) "The effects of nuclear radiation on P-channel CCD imagers", *Proc. IEEE Radiation Effects Data Workshop (NSREC) Rec.*, Snowmass
- Spudis P. D. (1998) "*Once & Future Moon*", Smithsonian Library of the Solar System
- Spudis P. D. (2004) "*Moon*" World Book Online Reference Centre.
- Srouf J. R. and Hartmann R. A. (1989) "Enhanced displacement damage effectiveness in irradiated silicon devices", *IEEE Trans. Nucl. Sci.*, **vol. 36**, pp. 1825-1830
- Srouf J. R. (2000) "Universal damage factor for radiation induced dark current in silicon devices", *IEEE Trans. Nucl. Sci.*, **vol. 47**, no. 6, pp. 2451-2459
- Srouf J. R., Marshall C.J., and Marshall P.W. (2003) "Review of Displacement Damage Effects in Silicon Devices", *IEEE Trans. Nucl. Sci.*, **vol. 50**, Issue 3
- Stassinopoulos E. G. and Raymond J. P. (1988), "The Space Radiation Environment for Electronics", *Proc. of the IEEE*, **vol. 76**, pp. 1423-42
- Stevanov K. D., Tsukamoto T., Miyamoto A., Sugimoto Y., Tamura N., Abe K., Nagaminc T., and Aso T. (2000) "Electron and Neutron Radiation Damage Effects on Two-Phase CCD", *IEEE Trans. Nucl. Sci.*, **vol. 47**, Issue 3
- Streetman B. G. (2000) "*Solid state electronic devices*", Prentice-Hall
- Swinyard B. (2008), RAL, Private Communication
- Sze S. M. (1981) "*Physics of Semiconductor Devices*", John Wiley and Sons Ltd., 2nd Edition
- Theuwissen A. and Roks E. (2001), "Building a better mousetrap – Modified CMOS processes to improve image sensor performance", *SPIE OE magazine*, pp. 29-32
- Thomson J. J. (1904) "On the Structure of the Atom: an Investigation of the Stability and Periods of Oscillation of a number of Corpuscles arranged at equal intervals around the Circumference of a Circle; with Application of the Results to the Theory of Atomic Structure", *Philosophical Magazine*, Series 6, **vol. 7**, pp. 237-265
- Thomson N. R., Rodger C. J., and Clilverd M. A. (2005) "Large solar flares and their ionospheric D region enhancements", *J. Geophysical Research*, **vol. 110**, A06306
- Tribble A. C. (2003) "*The space environment: implications for spacecraft design*" Princeton University Press

- Van Allen J. A. and Frank L. A. (1959) "Radiation around the Earth to a radial distance of 107,400 km", *Nature*, **vol. 183**, pp. 430-34
- Van Lint A.J. (1987) "The physics of radiation damage in particle detectors", *Nucl. Inst. Meth.*, **A253**, pp 453-459
- Vette J. (1991) "The AE-8 trapped electron model environment", National Space Science Data Centre, Report 91-24, Greenbelt, Maryland
- Von Hamos, L. (1945) "The determination of very small quantities of substances by the X-ray microanalyser", *Arkiv. Mat., Aston. Fysik*, 31:1-11
- Warren P. H. and Wasson J. (1979) "The origin of KREEP", *Rev. Geophys. Space Phys.*, 17, 73
- Warren P. H. (1985) "The magma ocean concept and lunar evolution", *Annual Review of Earth and Planetary Sciences*, **vol. 13**, pp. 201-240
- Webster J. G. (1999) "*The Measurement Instrumentation and Sensors Handbook*", Springer
- Weidenschilling S. J., Greenberg R., Chapman C. R., Davis D. R., and Hartmann W. K. (1984) "Origin of the moon from a circumterrestrial disk", Origin of the moon; *Proceedings of the Conference*, Kona, HI, A86-46974 22-91
- Weider S. Z., Gow J., Crawford I. A., Joy K. H., Smith D. R., Holland A. D., and Swinyard B. M. (2008) "X-ray Fluorescence Particle Size and Scattering Angle Considerations Preparatory Experiments for the Calibration and Interpretation of C1XS Data" Poster presentation at the *Lunar and Planetary Science XXXIX*, No. 1098
- Williams D. R. (2006) "Moon Fact Sheet", NASA Fact sheets
- Winglee R. M. and Harnett E. M. (2007) "Radiation mitigation at the Moon by the terrestrial magnetosphere", *Geophysical research letters*, **vol. 34**, L21103
- Yongliao Z. and Lin X., Ziyuan O. (2004) "KREEP Rocks", *Chinese Journal of Geochemistry*, **vol. 23**, Number 1, pp. 65-70